*Acoustical Physics, Vol. 51, Suppl. 1, 2005, p. S1. Translated from Akusticheskiĭ Zhurnal, Vol. 51, Suppl., 2005, p. 5.*


# Dear Readers!

We have the pleasure of bringing to your notice a special issue of *Acoustical Physics*, which is devoted to the problems of geoacoustics. Today, these problems are much discussed in the scientific literature. *Acoustical Physics* also regularly publishes papers devoted to this subject. A specific feature of the issue is that it combines papers written by researchers who specialize in seismoacoustics and physical acoustics but work at institutions involved in different kinds of scientific and engineering activities. The interest in geoacoustics is connected not only with the physical processes that accompany the propagation and interaction of waves but also with the practical applications of the results of research. For example, seismic activity manifests itself primarily in the generation of elastic waves, which travel long distances. On the other hand, seismoacoustic methods are much used as a sounding technique in Earth studies and in seismic prospecting. In the last few years, special interest has been attracted to studying the mechanisms of acoustic intensification of oil production. Such investigations have been carried out for 40 years, but the mechanisms underlying this effect are still not clearly understood. The problems of geoacoustics are closely related to the problems of nondestructive testing of granular media, which are also discussed in this issue. A granular medium with cracks is often considered as a model of rock. It is well known that randomly inhomogeneous granular media can not always be described in terms of the classical models of continuous media. A granular medium possesses a mesoscale structure, which can be modified under the effect of a load. Rock in a stressed state is the origin of acoustic emission. The parameters of the latter can be used as a source of information for finding mineral resources, including hydrocarbon deposits. Moreover, rock features an anomalously strong nonlinearity. For example, the value of the nonlinear parameter typical of a granular medium is 2–3 orders of magnitude greater than that of a homogeneous medium. This fact is important for describing the nonlinear processes that determine the acoustic effect on a medium. For example, according to the papers presented in this issue, the effect of sound of even a relatively low (medium) amplitude gives rise to the "slow dynamics" of individual grains and cracks. In addition to nonlinear problems, this issue presents papers devoted to studying the propagation of seismic waves in layered structures of rock, in particular, in application to earthquake forecasting.

We hope that such a topical approach to representing the results of research in geoacoustics will be of interest for the readers from the point of view of developing new ideas and solutions in this important area of research.

*I.B. Esipov and A.V. Nikolaev*
*(Compilers of the Issue)*

1063-7710/05/51S1-S0001$26.00 

*Acoustical Physics, Vol. 51, Suppl. 1, 2005, pp. S102–S114. Translated from Akusticheskiĭ Zhurnal, Vol. 51, Suppl., 2005, pp. 118–131.*


# Modeling of the Intensification of Oil Production by an Acoustic Action on the Oil Pool from the Borehole

**G. A. Maximov and A. V. Radchenko**

*Moscow Engineering Physics Institute (State University), Kashirskoe sh. 31, Moscow, 115409 Russia*

*e-mail: maximov@dpt39.mephi.ru*

Received August 10, 2004

**Abstract**—An improved model of physical processes that occur under an acoustic action (AA) is presented in the context of both thermal AA mechanism and its nonthermal alternatives. It is assumed that the fluid in an oil pool consists of light and heavy hydrocarbon phases, which are in thermodynamic equilibrium. External actions, such as filtration or AA, can shift the point of equilibrium of the fluid fractions in such a way that the heavy fraction may deposit on the pore walls or dissolve. In this case, the process of long-term mudding is governed by the inhomogeneity of the pressure field around the borehole and, correspondingly, by the change in the equilibrium concentration of the heavy impurity in the course of filtration. In the framework of the proposed model, the effect of an acoustic action can manifest itself both indirectly, as a heating of the surrounding medium because of sound absorption (which also changes the equilibrium concentration of impurity), and directly, as the dependence of the equilibrium concentration and relaxation time on the average density of acoustic energy of ultrasonic vibrations. The proposed model makes it possible to reproduce the characteristic features of the fluid filtration from the borehole before and after the AA, including the long-term intensification of petroleum recovery from the collector with a gradually decreasing recovery rate. © *2005 Pleiades Publishing, Inc.*

## 1. INTRODUCTION

Although applied geophysics is in obvious need of powerful physical methods aimed at the intensification of petroleum extraction from boreholes under development, it seems that none of the existing physical means of enhancing the productive capacity of a reservoir has been studied exhaustively. The difficulty of such a study follows from the insufficient understanding of processes occurring in the porous permeable space of collectors. This difficulty is in full measure inherent in the method of acoustic action (AA). The success of using the AA depends on many factors, which include the filtration and capacity properties of the medium, the viscosity of reservoir fluid, the initial and current values of the reservoir pressure, and the history of borehole production rate variation. However, even ample statistical data on the use of the AA method and the experience of specialists cannot guarantee a positive result of ultrasonic treatment (to our knowledge, the success of the method is below 60–70%), not to mention a quantitative evaluation of the effect of a possible use of AA.

Thus, there is an actual need to understand the physical mechanisms intensifying petroleum production under an acoustic action on an oil pool from the borehole.

At the moment, a number of different physical processes and phenomena are being discussed that could under certain conditions be responsible for the intensification of petroleum production under AA [1–6]. Among the most probable action mechanisms, one usually mentions thixotropic variations in the reservoir fluid, cavitation, and heating [3–6]. However, the existing appraisals of the roles that specific mechanisms play in the intensification effect most often have a qualitative rather than a quantitative nature because of the lack of a complete model of the intensification phenomenon (the existing models deal with only certain elements of the phenomenon).

In a recent paper [1], we attempted to quantitatively estimate the net result of the AA, i.e., the increase in the borehole production rate. In that paper, we considered the simplest physical mechanism of such intensification; namely, we assumed that petroleum viscosity decreases solely due to heating caused by the action of the acoustic source. To obtain a quantitative estimate, we nevertheless had to model the whole set of physical phenomena accompanying the acoustic impact in the context of the thermal mechanism. Formulating the unified sequence of physical problems, we took into account the fact that the borehole source of acoustic vibrations radiates acoustic waves to the surrounding medium. Because of the absorptive property of the medium, a portion of the mechanical energy is dissipated and appears in the form of thermal energy. As a result, a thermal source with certain thermal density arises around the borehole and heats the surrounding medium. As is known [2], the viscosity of hydrocar-

bons depends on temperature according to an exponential law; correspondingly, an increase in temperature decreases the viscosity and increases the rate of percolation around the borehole. Estimates given in [1] showed that, in the framework of the thermal mechanism, AA increases the temperature of the borehole environment by 10–13°C, which has an experimental support [7] and increases the borehole production rate by 5–12% [1]. However, the relatively fast relaxation (6–7 days) of the temperature field offers only a short time for the positive effect.

Nevertheless, successful borehole experiments with ultrasonic cleaning showed a long-term (several months) increase in the borehole production rate. Figure 1 shows the characteristic average production rate variation after AA as a function of time, which was obtained from the data collected over ten boreholes. This curve was constructed using the production rates measured at ten boreholes of NGDU Izhevskneft' after the ultrasonic treatment of the bottom-hole region with the goal of oil inflow intensification. The squares show the normalized data on the production rate of one of the boreholes, which offers a possibility to estimate the quality of the initial data. As can be seen, the initial data hardly can be considered as high-quality onnes; however, they are sufficient for judging the magnitude and duration of the intensification caused by the AA. The solid curve in Fig. 1 represents the average of the production rates normalized by the initial value for ten boreholes. The dashed line is the root-mean-square approximation of the above curve with the exponential function $Q/Q_0 = A\exp(-t/\tau)$, where the parameters have the following values: $A = 1.23$ and $\tau = 150$ days.

From the data of Fig. 1 it follows that the average production rate increase amounts to 30% and the average duration of the positive effect of AA amounts to 1.5–2 months.

It may seem that such experimental data are definite evidence in favor of the fact that heating caused by the AA is an insignificant mechanism among other phenomena used in literature [3–6] to explain the long-term effect of AA. The calculated values of the borehole production rate increase because of the heating of the fluid [1] support on the whole the widespread opinion of specialists in petroleum production intensification that heating gives only short-term and, hence, small effect manifesting itself as a relatively small amount of additionally accumulated petroleum due to the decreasing viscosity of the reservoir fluid.

However, the dependence of hydrocarbon viscosity on temperature is only one of the consequences of heating of the borehole environment under the action of acoustic radiation.

In this paper, we give an improved model of the physical processes occurring under AA in the framework of the thermal mechanism. We assume that the

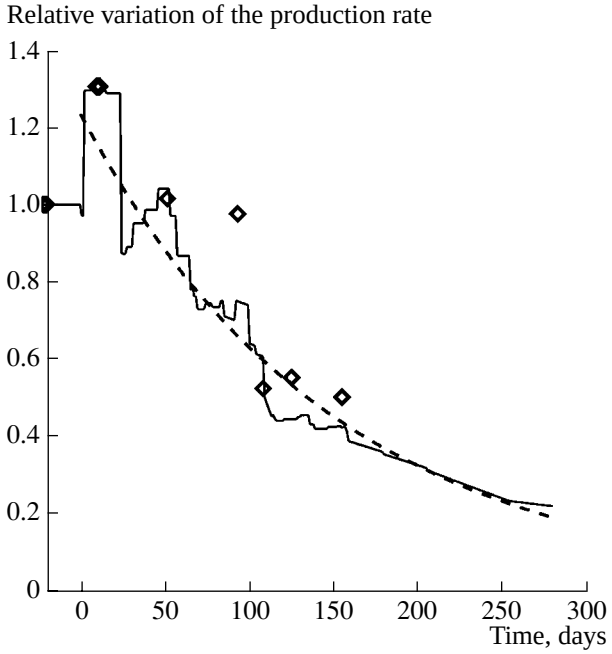


**Fig. 1.** Variation of the borehole production rate after the AA. The production rate is normalized by its value before the AA. The solid line corresponds to the data averaged over 10 boreholes, the squares correspond to the data of a single borehole, and the dashed line corresponds to the exponential approximation.

reservoir fluid is composed of light and heavy hydrocarbon phases and these phases are in thermodynamic equilibrium. External actions, such as filtration and AA, can shift the point of equilibrium between fractions in such a way that the heavy fraction can deposit on pore walls or dissolve. In the framework of this model, we managed to reproduce the features of the fluid filtration from the borehole before and after the AA, including the long-term increase in petroleum recovery from the collector with a gradually decreasing recovery rate. An important feature of the model is that it describes not only the effect of AA and its consequences but also the preceding processes of mudding of the borehole environment, which make it necessary to apply the AA.

## 2. MODEL OF PHYSICAL PHENOMENA OCCURRING UNDER AA

The reservoir fluid is a very inhomogeneous medium composed of different substances, such as gas, water, light hydrocarbons, gums, oils, and pyrobitumens. In the course of the fluid filtration, heavy hydrocarbons slowly deposit on the walls of the pore space in the form of a solid substance, which gradually reduces the diameter of pores and, consequently, the conductivity and porosity of the medium. The proposed model assumes that the reservoir fluid is composed of light and heavy fractions of hydrocarbons. The concentra-

tion of the heavy fraction (considered as an impurity) is the ratio of the number of molecules of the dissolving substance to the number of molecules of the solvent per unit volume, $C = N_B/N_A$. At thermodynamic equilibrium, the relative concentrations of both phases are in a certain balance. The state of thermodynamic equilibrium is characterized by the impurity equilibrium concentration $C_*$. It is obvious that variations of thermodynamic conditions in the collector should vary the impurity equilibrium concentration, thus causing the current concentration to relax to the equilibrium value. For example, a pressure drawdown in the oil pool during the well development varies the pressure field and, consequently, the equilibrium concentration. A decrease in $C_*$ means that the current concentration of impurity $C$ will tend to the equilibrium value at which excessive liquid fraction of heavy hydrocarbon begins to deposit in the form of a solid substance on the walls of the pore space, thus degrading the filtration and capacity properties of the medium. A decrease in the pore radius reduces the porosity and conductivity of the medium, especially in the borehole environment, and appreciably affects the velocity of the fluid flow, thereby gradually decreasing the petroleum production rate. The speed of this process can vary over an extremely wide range, depending on the physical chemical properties of the solvent and impurity, the stage of well development, and the level to which the borehole production rate has been reduced to the moment. Such a mudding may continue for weeks, if not months.

In turn, an excess of the impurity equilibrium concentration over the current concentration (this effect occurs under AA) stimulates the dissolution of the solid phase of heavy hydrocarbons and the cleaning of the pore channels. In particular, the acoustic waves generated by an ultrasonic borehole radiator are absorbed in the surrounding medium thus forming a thermal source distributed around the borehole. As a consequence, the surrounding medium is heated and the fluid temperature changes, which, in turn, changes the equilibrium concentration $C_*$, causes heavy hydrocarbon fraction to dissolve, cleans the pore channels, and improves the filtration characteristics.

Thus, the cleaning of pores under AA, which is a rapid process, especially in comparison with the preceding process of mudding, can explain the long-term effect of AA in the framework of the same simple thermal mechanism.

Consequently, the complete modeling of the production rate behavior under the AA assumes the consideration of the behavioral features of the fluid in a porous permeable medium both without ultrasonic treatment and under the conditions of stimulated petroleum production. In the framework of the proposed model, the following processes are to be simulated:

(i) the propagation of ultrasonic waves generated by the borehole source (the simulation of this process is accompanied by the corresponding calculation of the distribution of sound energy density around the borehole and by the evaluation of the distribution of thermal sources);

(ii) the variation of the temperature field around the borehole under the AA;

(iii) the fluid filtration and the evaluation of the fluid flow through the borehole perforated interval;

(iv) the variation of the impurity concentration;

(v) the evaluation of the degree of either settling or dissolution of the heavy hydrocarbon fraction and the evaluation of the corresponding variations of the pore radii, conductivity and porosity.

Certain characteristic times are inherent in all the above processes. For example, if we assume that the characteristic size of the problem (borehole diameter) is $L$, then, the time of sound wave propagation will be $\tau_s = L/c$, where $c$ is the sound velocity; the characteristic heating time will be described by the expression $\tau_h = L^2/\chi$, where $\chi$ is the thermal diffusivity; the filtration time will have the order of magnitude $\tau_f = (L^2\eta m)/(\rho c^2 k)$, where $\rho$ and $\eta$ are the density and viscosity of the fluid, respectively, and $k$ and $m$ are the permeability and porosity of the medium; the characteristic time of impurity diffusion will be $\tau_D = L^2/D$, where $D$ is the diffusion coefficient; the time of impurity transfer will be $\tau_t = (L^2\eta)/(k\Delta P)$, where $\Delta P$ is the pressure differential; and the settling or dissolution time $\tau_c$ will be given by a function of thermodynamic parameters. Using the characteristic size of the problem $L \sim 1$ m (this value is characteristic of boreholes) and setting the values typical of productive oil pools for other parameters, we estimate the above characteristic times as follows: $\tau_S \sim 10^{-3}$ s, $\tau_f \sim 1$ s, $\tau_t \sim 10^3$ s $\sim 1$ h, and $\tau_h \sim \tau_D \sim 10^6$ s $\sim 10$ days. These estimates suggest the following order of temporal scales of the above physical processes: $\tau_s \ll \tau_f \ll \tau_t \ll \tau_D \sim \tau_h \ll \tau_c$. The difference in these temporal scales makes it possible to divide the complex problem into a number of independent problems that are mutually connected only through coefficients. In accordance with the above ideas of the physical processes occurring under the AA, below we formulate and solve a number of problems, the solution to each of them being a necessary component of understanding the whole the complex phenomenon, which allows a qualitative evaluation of the effect of AA.

## 3. PROPAGATION OF ACOUSTIC WAVES AND DISTRIBUTION OF ACOUSTIC ENERGY

The problem on the distribution of acoustic energy density produced by an ultrasonic acoustic source in the borehole environment was considered in papers [1, 8]. The acoustic field excited by a monochromatic source

can be completely and exactly calculated for both an elastic medium with absorption [1] and Biot's porous permeable medium [8].

The term Biot's medium refers to a fluid-saturated permeable porous two-phase continuum composed of an elastic skeleton and a fluid, which occupy connected and interpenetrating regions. Let $\vec{u}$ represent the average displacements in a certain macroscopic volume that contains both solid and liquid components and $\vec{U}$ represent the average displacements of the continuous liquid phase in this volume. In the case of Biot's medium, the system of equations of motion has the form [9]

$$\begin{aligned}\rho_{11}\ddot{\vec{u}} + \rho_{12}\ddot{\vec{U}} - b\left(\dot{\vec{U}} - \dot{\vec{u}}\right) &= P\,\mathrm{grad}\,\mathrm{div}(\vec{u}) + Q\,\mathrm{grad}\,\mathrm{div}(\vec{U}) - \mu\,\mathrm{curl}\,\mathrm{curl}(\vec{u}),\\ \rho_{21}\ddot{\vec{u}} + \rho_{22}\ddot{\vec{U}} + b\left(\dot{\vec{U}} - \dot{\vec{u}}\right) &= Q\,\mathrm{grad}\,\mathrm{div}(\vec{u}) + R\,\mathrm{grad}\,\mathrm{div}(\vec{U}),\end{aligned} \tag{1}$$

where we used the following notation:

$$\rho_{11} = \rho + m\rho_f(a-2), \quad \rho_{12} = \rho_{21} = m\rho_f(1-a),$$
$$\rho_{22} = am\rho_f$$
$$b = \frac{m^2\eta}{k}, \quad P = \lambda_f + 2\mu + Mm(m-2\beta),$$
$$Q = Mm(\beta - m), \quad R = Mm^2.$$

Here, $\rho$ is the average density of the porous medium ($\rho = (1-m)\rho_s + m\rho_f$), $\rho_f$ is the density of the fluid, $\rho_s$ is the density of the elastic skeleton material, $m$ is the porosity, $k$ is the permeability, $\eta$ is the dynamic viscosity of the fluid, and $a$ is the twisting parameter. Other parameters ($\lambda_f$, $\mu$, $M$, and $\beta$) characterize the elastic properties of the skeleton and the fluid forming the permeable medium; these parameters can be determined by testing the compressibility of stratum samples in laboratory experiments [9, 10].

If we decompose each of the vector fields $\vec{u}$ and $\vec{U}$ in Eq. (1) into the potential and solenoidal components by introducing longitudinal and transverse potentials according to the formulas

$$\begin{aligned}\vec{u} &= \mathrm{grad}\,\varphi + \mathrm{curl}\,\vec{\psi}\\ \vec{U} &= \mathrm{grad}\,\vartheta + \mathrm{curl}\,\vec{\chi},\end{aligned} \tag{2}$$

we can diagonalize the system of equations (1) and reduce it to the system of independent wave equations in transverse potential $\vec{\psi}$ (or potential $\vec{\psi}$, which is proportional to $\vec{\chi}$) and a pair of longitudinal potentials $\varphi_+$ and $\varphi_-$, which are linear combinations of potentials $\varphi$ and $\vartheta$. In the frequency domain, the corresponding equations have the form

$$\begin{aligned}\Delta\varphi_+ + \left(\frac{\omega^2}{c_+^2(\omega)} + i\alpha_+(\omega)\right)\varphi_+ &= 0,\\ \Delta\varphi_- + \left(\frac{\omega^2}{c_-^2(\omega)} + i\alpha_-(\omega)\right)\varphi_- &= 0,\\ \Delta\vec{\psi} + \left(\frac{\omega^2}{c_s^2(\omega)} + i\alpha_s(\omega)\right)\vec{\psi} &= 0,\end{aligned} \tag{3}$$

where $c_+(\omega)$ and $c_-(\omega)$ are the phase velocities of longitudinal waves of the first and second kinds; $c_s(\omega)$ is the complex velocity of transverse waves; and $\alpha_+(\omega)$, $\alpha_-(\omega)$, and $\alpha_s(\omega)$ are the corresponding attenuation coefficients. We illustrate the behavior of these quantities in Fig. 2, which shows the frequency-dependent phase velocities and the attenuation coefficients of different waves for different porosities $m$ = 10, 20, 30, and 40%. In Fig. 2, the frequency $f = \omega/2\pi$ is normalized by Biot's characteristic frequency

$$f_{\mathrm{bio}} = \frac{1}{2\pi}\frac{m}{a}\frac{\eta}{k\rho_f}. \tag{4}$$

To make the comparison of the quantities corresponding to media with different porosities, we fixed low-frequency limits of phase velocities.

From the above curves (and the corresponding asymptotic expressions) it follows that, in the framework of Biot's model considered here, both phase velocities and attenuation coefficients of all originating waves behave as functions monotonically increasing with frequency and approaching a certain finite limit. In the low-frequency limit $f \ll f_{\mathrm{bio}}$, the phase velocity and the attenuation coefficient of the longitudinal wave of the second kind exhibit a behavior different from that of the phase velocity and attenuation coefficient of the longitudinal wave of the first kind and the transverse wave. In the latter case, the attenuation coefficient in the low-frequency limit is quadratic in frequency and the phase velocity tends to a finite limit. In contrast to this behavior, both phase velocity and attenuation coefficient of the longitudinal wave of the second kind are proportional to the square root of frequency, which, at low frequencies, transforms this wave into a filtration process [9, 10].

Let us consider a fluid-filled borehole of radius $R$ in an external permeable Biot's medium and let a monochromatic point source be located at the axis of this borehole. In this case, the acoustic field inside the borehole is described by the ordinary wave equation and the fields outside the borehole are described by Eqs. (3). Owing to symmetry, the vector $\vec{\psi}$ in the cylindrical

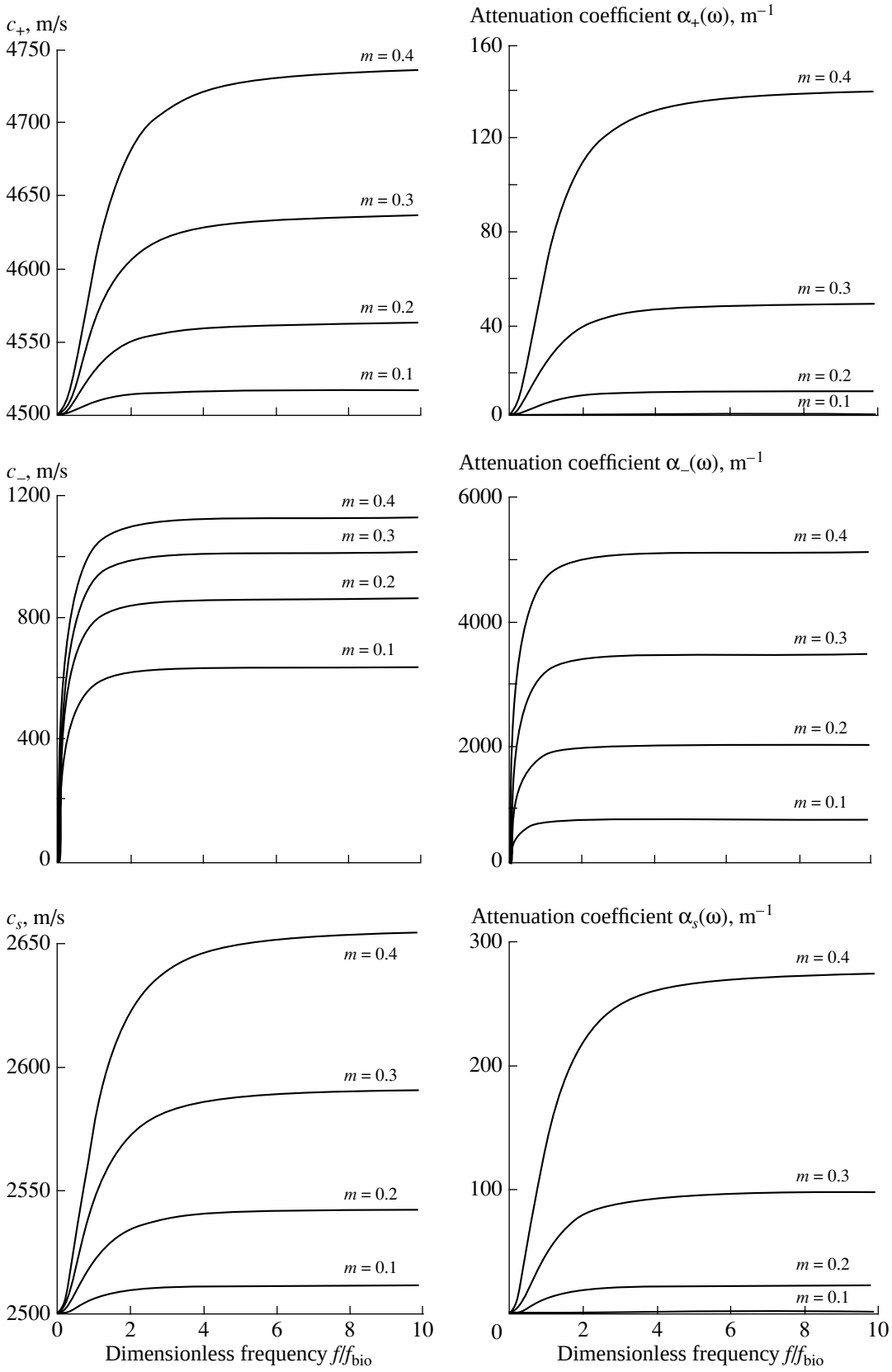


**Fig. 2.** Frequency dependent phase velocities (left) and absorption coefficients (right) of the longitudinal waves of the first (top) and second (middle) kinds and the transverse wave (bottom) for different porosities $m$ = 10, 20, 30, and 40%.

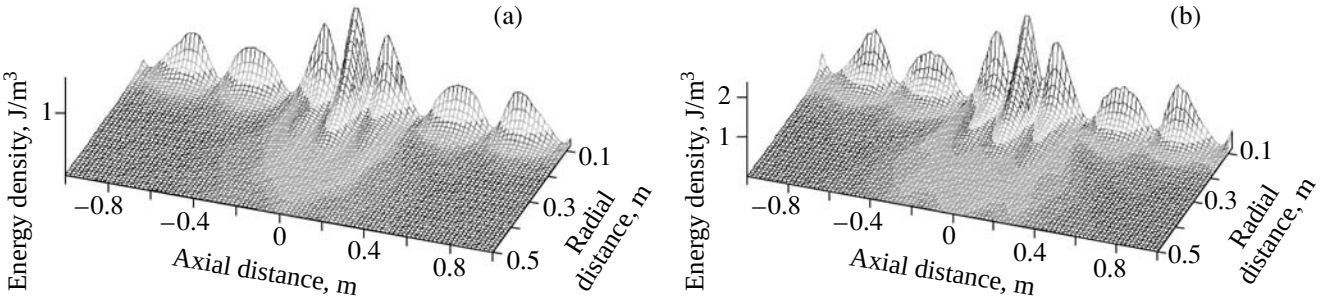


**Fig. 3.** Distribution of the acoustic energy density for (a) the elastic model of the medium and (b) Biot's model of a permeable medium with $m = 0.2$ and $k = 0.1$ D.

coordinate system $\{r, \varphi, z\}$ has only the azimuth component $\vec{\psi} = (0, \psi, 0)$.

The boundary conditions at the borehole surface consist in the continuity of the averaged normal stresses, the absence of tangential stresses, the continuity of the fluid pressure, and the continuity of the averaged normal displacements. The solutions in the external medium must tend to zero at infinity and the singularity of the solution at the borehole axis must correspond to the source singularity.

The solution to these equations satisfying the boundary conditions at the borehole axis and at infinity can be expressed in terms of cylindrical functions multiplied by arbitrary constants. Substituting this solution into boundary conditions at the borehole surface, we can determine both the potentials introduced above and the vectors of average displacements of the elastic skeleton $\vec{u}$ and the fluid $\vec{U}$; in the coordinate representation, these quantities are expressed in the form of Fourier integrals over the wave number and are calculated numerically.

At a given frequency, the distribution of acoustic energy density around the borehole is given by the expression

$$E = \frac{1}{2}\rho_0\omega^2|\vec{u}(\vec{r}, \omega)|^2, \quad (5)$$

while the dissipated power equal to the power of thermal sources is described by the dissipative function [9, 10] that can be represented in the form

$$D = \frac{1}{2}\frac{\eta}{k}\omega^2 m^2|\vec{U}(\vec{r}, \omega) - \vec{u}(\vec{r}, \omega)|^2. \quad (6)$$

Note that, in the framework of the elastic statement of the problem, the dissipative function can be estimated through the acoustic energy density $\alpha cE$ if the absorption coefficient $\alpha$ is known from experiments.

Not going into the details of numerical algorithm, we present the comparison of the resulting distributions of acoustic energy density and thermal source density in the borehole environment for the models of an elastic absorbing medium and the Biot's porous permeable medium model.

Figure 3 shows the calculated distributions of acoustic energy density in the borehole environment. The problem's statement corresponds to an ultrasonic point source with power $I = 1$ kW at a frequency of 20 kHz located at the axis of a fluid-filled borehole of radius $R = 8$ cm. The parameters characterizing the elastic properties of the surrounding medium and the properties of the reservoir and borehole fluids are identical for both models (see table). The porosity and the permeability of Biot's medium amount to 20% and 100 mD, respectively.

As may be seen from Fig. 3, the distribution of acoustic energy density calculated for Biot's medium is almost identical to the result obtained for the elastic model with absorption in both shape and scale (one to several joulllles per cubic meter within ten centimeters from the borehole).

However, the distributions of thermal source density around the borehole appear to be drastically different for these two models because of the different physical mechanisms underlying the acoustic energy dissipation in the elastic and Biot's models. In the calculations, we assumed that the energy of longitudinal and transverse waves in the elastic medium is dissipated with the absorption coefficient $\alpha = 1$ m$^{-1}$ at a frequency of 20 kHz. On the contrary, in Biot's model, the energy dissipation is caused by the motion of the reservoir fluid saturating the permeable medium relative to the elastic skeleton. Motion of this type corresponds to Biot's wave of the

**Table**

| Parameters | Fluid | | Elastic medium | |
|---|---|---|---|---|
| Density (kg/m$^3$) | $\rho_f$ | 1000 | $\rho$ | 2100 |
| Velocity (m/s) | $c_f$ | 1500 | $c_I$ | 4500 |
| | | | $c_s$ | 2500 |
| Dynamic viscosity (Pa s) | $\eta_f$ | 0.01 | | |

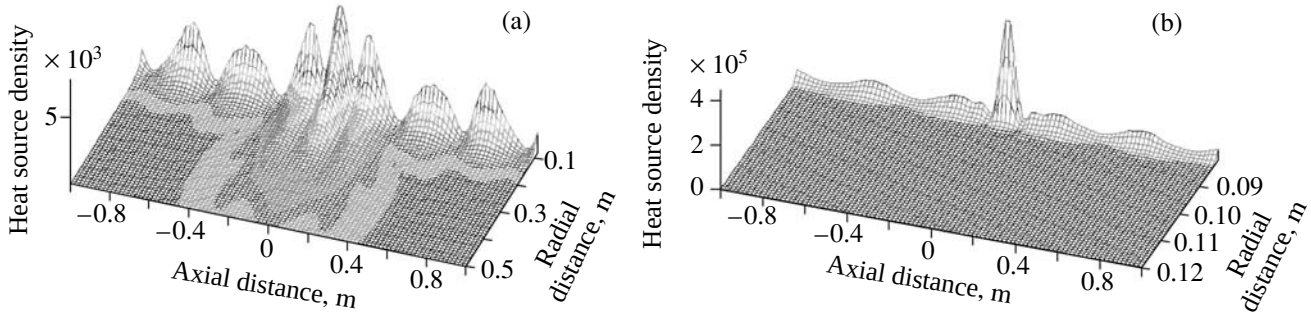


**Fig. 4.** Distribution of the heat source density for (a) the elastic model of the medium and (b) Biot's model of a permeable medium with $m = 0.2$ and $k = 0.1$ D.

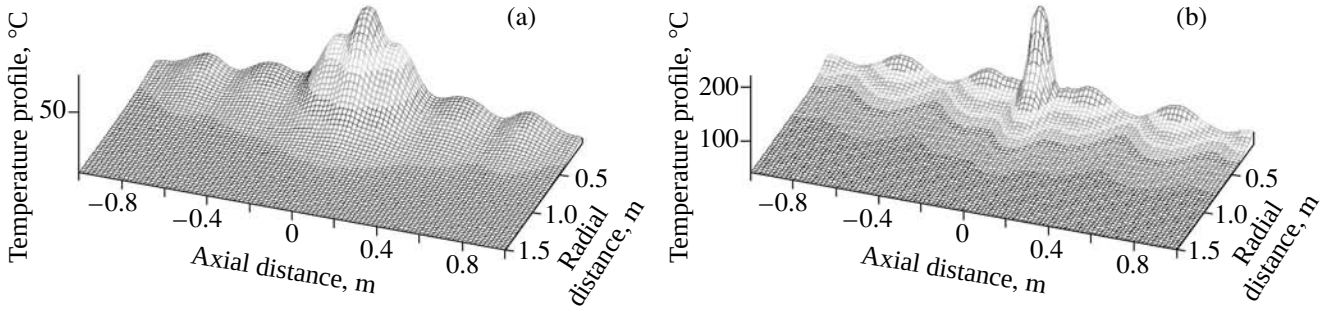


**Fig. 5.** Temperature field around the borehole after a 10-h-long treatment for (a) the elastic model of the medium and (b) Biot's model of a permeable medium.

second kind, which rapidly decays with distance from the borehole (within few first centimeters for the parameters used in the calculation). As a result, the thermal source density is predominantly concentrated in the immediate vicinity of the borehole (see Fig. 4b).

## 4. TEMPERATURE FIELD AROUND THE BOREHOLE UNDER THE AA

The time-dependent temperature field in the course of borehole radiator operation, as well as in the course of medium cooling after AA, can be obtained from the predetermined distribution of thermal sources using a finite-difference technique. The dynamics of the temperature field after the AA was adequately studied in papers [1, 8], and we will not dwell here on the details of the problem's statement and the solution techniques.

Figure 5 shows a typical distribution of the temperature field around the borehole against the background level of 40°C in the case of a one-point ultrasonic action during 10 h. The temperature field was calculated for the thermal sources that were obtained by solving the problem on the acoustic energy distribution in the elastic medium and in Biot's permeable medium (see Fig. 4). In the first case, we found that the increase in temperature at the borehole boundary after the 10-hour operation of the radiator comes to nearly 10°C, which agrees well with experimental data [7]. It should be noted that Biot's model gives rise to a thermal source density exceeding by a factor of ten the corresponding values for the elastic medium model, and it may seem that this must lead to a much stronger heating (according to calculations, the temperature field can reach hundreds of degrees). However, experimental data show no such great increase in temperature. The origin of this disagreement possibly consists in the necessity to distinguish between open and closed porosities in the permeable medium. Calculating the dissipated energy, one must take into account only the contribution corresponding to the open porosity. In view of the strong dependence of the calculated results on porosity and permeability, this fact can noticeably reduce the level of thermal sources. Another reason possibly lies in the fact that the acoustic action is usually realized in cased boreholes, where the fluid cross-flow between reservoir and borehole is weaker because of the partial borehole perforation, which also considerably (by a factor of ten or more) reduces the efficiency of Biot's wave generation because of different boundary conditions.

## 5. FLUID FILTRATION

In the problem at hand, the fluid filtration is the central process and other processes are accompanying. The equation describing the fluid motion in a porous permeable medium can be derived from the equation of continuity for the fluid in the pore space, the Darcy law that relates the filtration mass velocity $\vec{V}$ to the gradient of pressure $P$, and the linearized equation of the fluid state that relates the density and pressure deviations from the equilibrium values through the square of sound velocity $c$:

$$m\frac{\partial P}{\partial t} - \mathrm{div}\frac{k\rho_0 c^2}{\eta}\mathrm{grad}P = 0. \quad (7)$$

Despite the fact that the model under consideration treats the permeability $k$, porosity $m$, and viscosity $\eta$ as functions of coordinates and time, this equation considers the filtration as a process independent of variations of these parameters, because it is assumed that the rate of their variations is small, so that one can substitute the current parameter values in the final result.

Supplementing Eq. (7) with the corresponding initial and boundary conditions, we obtain the problem on the fluid filtration from the borehole of radius $R$ through the perforated interval of length $h$. The boundary condition on the perforated interval of the borehole corresponds to the pressure drawdown $\Delta P$, the boundary condition on the cased segment of the borehole is formulated as the requirement that the normal component of velocity be equal to zero (an, correspondingly, the radial gradient of pressure), and the boundary condition on the remainder of the calculation region is formulated as the condition of free flow. With the pressure field being calculated, one can determine the velocity field using the Darcy law.

As in paper [1], the total production rate of liquid is determined as the integral of the normal component of the substance flow $\rho_f(\vec{V}\vec{n}) = \rho_f V_n$ over the surface of the perforated segment of the borehole of radius $R$:

$$Q = 2\pi R\rho_f\int_0^h dz V_n(R, z, t). \quad (8)$$

## 6. TRANSFER AND DIFFUSION OF HYDROCARBON IMPURITY

In the process of petroleum production, a pressure drawdown springs up around the perforated segment of the borehole, which gives rise to the macroscopic transfer of the reservoir fluid with a touch of heavy hydrocarbons. An inhomogeneous distribution of impurity concentration in the solution causes the impurity to diffuse from areas with higher impurity concentration to areas with lower impurity concentration. In addition, a portion of impurity can settle or dissolve at the walls of the pore space. Thus, we can formulate three main mechanisms that vary the concentration of heavy hydrocarbon impurity: the transfer with the flow of the solution, the diffusion, and the settling/dissolution at the walls of the pore space. Correspondingly, the equation of impurity concentration transfer in the reservoir fluid can be represented in the form [12]

$$\frac{\partial C}{\partial t} + \vec{V}\nabla C - D\Delta C = \frac{1}{\tau_c}(C - C_*(P, T)), \quad (9)$$

where $\vec{V}$ is the fluid filtration (transfer) rate and $D$ is the diffusion coefficient. The right-hand side of Eq. (9) describes the relaxation (with characteristic time $\tau_c$) of the current impurity concentration in the solution to the equilibrium concentration $C_*(P, T)$ due to the impurity settling or dissolution at the walls of the pore space.

In the general case, the current and equilibrium concentrations do not coincide, which initiates the processes of either heavy fraction settling, or dissolution on the walls of the pore space. The impurity equilibrium concentration in the solution $C_*(P, T)$ determines the direction and rate of the dissolving–settling process; it is a function of fundamental thermodynamic parameters such as, for example, pressure $P$ and temperature $T$. Within the framework of the linear approximation valid for not very large deviations from the corresponding equilibrium values, the equilibrium concentration can be approximated by the linear function

$$C_* = C_0\left(1 + A\frac{P - P_0}{P_0} + B\frac{T - T_0}{T_0}\right), \quad (10)$$

where $C_0$ is the equilibrium concentration at reservoir pressure $P_0$ and reservoir temperature $T_0$; the dimensionless parameters $A$ and $B$ are fixed in this model so as to fit the calculated decrease in the oil production rate before and after AA to experimental data.

## 7. CHANGES IN THE PORE RADIUS, PERMEABILITY, AND POROSITY

The amount of the impurity locally deposited or dissolved at pore walls in volume $V_0$ per unit time is given by the formula

$$\frac{dM}{dt} = \rho_f^0 m V_0\frac{(C - C_*)}{\tau_c}. \quad (11)$$

In the form of solid phase with density $\rho_s$, this amount must occupy a volume $dV_s$ per unit time:

$$\frac{dM}{dt} = \rho_s\frac{dV_s}{dt}. \quad (12)$$

This volume increment must cause a change in the pore space volume at the expense of the substance deposited at the pore walls. To determine the variation of the pore radii (and, hence, porosity and permeability), we consider the simplest model of a porous

medium in the form of cylindrical pore channels. Within the framework of this model, the volume porosity of the medium coincides with the open porosity and is determined by the formula $m = n\pi R^2$, where $n$ is the number of open pore channels per unit area. The permeability of the medium in this model is determined by the formula $k = mR^2$.

Thus, in the model under consideration, the surface density of pore channels remains intact and is determined by the formula $n = m_0^2/(\pi k_0)$, where $m_0$ and $k_0$ are the initial porosity and permeability of the layer. Correspondingly, the initial radius of pore channels is given by the formula $R_0 = \sqrt{k_0/m_0}$.

Under the condition that all dissolved or condensed impurity is dissolved or deposited on the pore channel walls uniformly, the change in the pore volume can be represented as

$$dV_s = -nV_0 \times 2\pi R dR. \quad (13)$$

Thus, in view of Eqs. (11)–(13), the kinetic equation for the pore radius variation can be represented in the form

$$\frac{dR}{dt} = -\frac{1}{2}R\frac{\rho_f^0}{\rho_s}\frac{(C - C_*)}{\tau_c}. \quad (14)$$

As can be seen from Eq. (14), the rate of pore radius variation has the sign opposite to the sign of the difference between the current and equilibrium concentrations, which corresponds to pore channel mudding in the case of excess impurity concentration and pore channel cleaning in the opposite case.

If the current concentration deviates from the equilibrium value by a constant, then, as it follows from Eq. (14), the variation of the pore radius in time is described by the exponential law

$$R = R_0 \exp(-t/\tau_{\text{eff}}), \quad (15)$$

where

$$\tau_{\text{eff}} = \tau_c \frac{\rho_s}{\rho_f^0}\frac{2}{(C - C_*)}. \quad (16)$$

The above kinetic equation (14) for the pore radius variation was obtained within the framework of the simplest model of porous medium. If necessary, one can use more complicated models, such as, for example,

$$m = m_0 F(R/R_0), \quad k = k_0 G(m/m_*),$$

where the functions $F(R/R_0)$ and $G(m/m_*)$ can take into account other geometry of the pore space and the percolation effects.

## 8. RESULTS AND DISCUSSION

In the preceding sections, we considered the basic points of the construction of an adequate mathematical model for describing the physical processes that occur under AA. The validity of a model can be proved or disproved by experimental data. In our case (see Fig. 1), experimental data form evidence in favor of a prolonged (about 2 months) positive effect consisting in the increased reservoir fluid income to the borehole under AA. Let us show how such an effect can be obtained from simulations with the use of the proposed model.

In the proposed model, the key point that distinguishes it from the earlier model [1] consists in the inclusion of the dynamics of the impurity settling–dissolving processes arising due to the difference between the current impurity concentration and the equilibrium impurity concentration for local thermodynamic conditions. As we mentioned earlier, two circumstances cause the change in these conditions in space and time, namely, variations of the pressure distribution in the fluid flow due to the slow dynamics of porosity and variations of the temperature field under the AA.

In calculating the pressure field, we used the boundary conditions corresponding to the reservoir pressure $P_0 = 13$ MPa and the pressure drop in the borehole $\Delta P = 4.4$ MPa. The dynamics of the temperature field corresponds to the results obtained in Sections 3 and 4 for the acoustic action of the source with a power of 1 kW during $t_a = 10$ h. The reservoir temperature was set to $T_0 = 40°C$. The environment is considered as an elastic medium with the absorption coefficient $\alpha = 1$ m$^{-1}$ at a frequency of 20 kHz. With these parameters, the pressure distribution before, during, and after the AA varies only slightly (by few percents). The temperature near the borehole increases during the AA by 16°C; within 80 days after the termination of the AA, the temperature relaxes to the initial level.

Figure 6a shows the radial distribution of equilibrium concentration occurring in the central plane of the borehole perforated interval in accordance with the current thermodynamic conditions in the fluid flow before AA, during AA, and 80 days after AA. Figure 6b shows the corresponding distributions of the current concentration. We used the following parameters in the equation of equilibrium concentration (10): $C_0 = 0.2, A = 0.5$, and $B = 8$. The values of the diffusion coefficient and relaxation time in Eq. (9) are $D = 10^{-9}$ m$^2$/s and $\tau_c = 1 \times 10^5$ s [12]. We selected the values of parameters $A$ and $B$ from considerations of qualitative agreement with the data given in Fig. 1.

Indeed, if we use Eq. (16) for the effective time of pore channel radius variation and estimate the nonequilibrium state of concentration from the first term of Eq. (10) for the specified parameters $C_0$, $A$, $P_0$, and $\Delta P$, then we easily obtain the estimate $C - C_* = C_0 A(P - P_0)/P_0 = 0.03$, which, in view of the relationship $\rho_s/\rho_f^0 = 2$, yields the relationship $\tau_{\text{eff}} = 130\tau_c$. Because $\tau_c = 1 \times 10^5$ s $\approx 1.15$ days, this relationship pre-

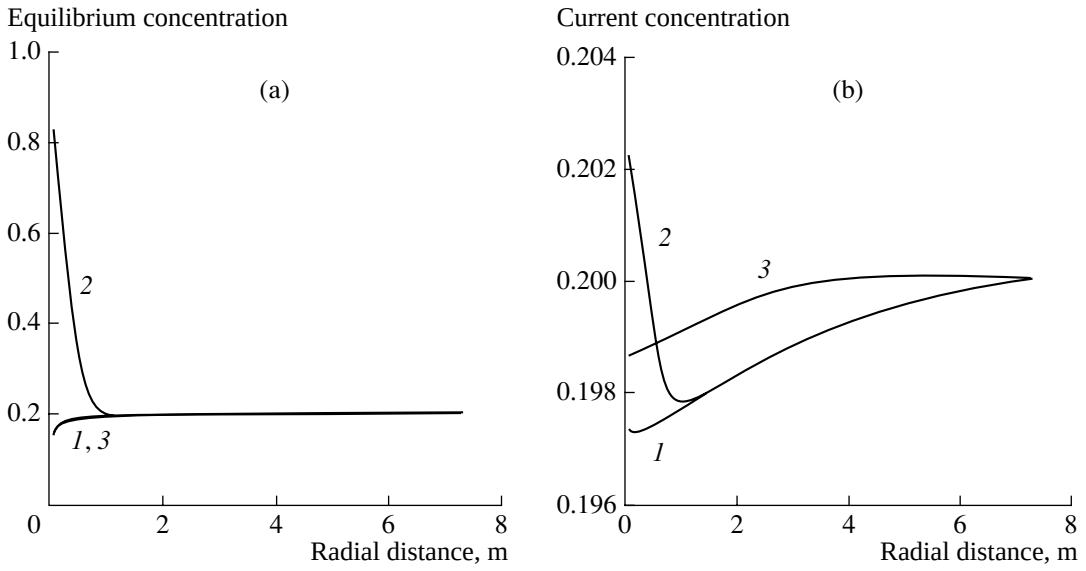


**Fig. 6.** Radial distributions of (a) the equilibrium concentration and (b) the current concentration of impurity at the center of the borehole perforated interval; curves *1*, *2*, and *3* correspond to the instants before AA, immediately after AA, and 80 days after AA.

cisely gives the experimentally observed duration $\tau$ = 150 days.

In the model under consideration, parameters *A* and *B* are the fitting parameters. Parameter *B* is determined from the characteristic time of the borehole production rate degradation, while parameter *B* is determined from the relative production rate increase after the AA. As may be seen from Fig. 6a, for the parameters chosen, the distributions of the equilibrium concentration before AA and 80 days after AA (when the temperature field is completely relaxed—see Fig. 5b) are both determined by the deviation of the current pressure in the borehole environment from the reservoir pressure and appear to be very similar, decreasing toward the borehole. This fact results in a gradual settling of the impurity at the pore walls. At the same time, the equilibrium concentration in the borehole environment immediately after the AA considerably (by a factor of four) exceeds the equilibrium reservoir concentration, which is conditioned by the temperature term in Eq. (10). Note that, qualitatively, the current concentration (Fig. 6b) behaves similar to the equilibrium concentration; the only difference consists in the much smaller (by two orders of magnitude) scale of variation and in the more prominent difference between the concentration values before and after the AA (the latter effect is caused by change in the fluid flow velocity).

Figure 7 shows the radial distribution of porosity for the same instants before and after the AA. In calculations, we set the reservoir porosity $m_0 = 0.2$ and permeability $k_0$ = 0.1 D. According to the relationship $R_0 = \sqrt{k_0/m_0}$, these values correspond to the pore channel radius $R_0$ = 1 μm.

Finally, Fig. 8 shows the net curves of the borehole production rate variation before and after the AA for different regimes of environment heating. The lower curve *1* corresponds to the production rate dynamics without AA and exhibits an exponential decrease. Other curves in Fig. 8 show how this dynamics is changed if the AA is carried out on the 45th day.

Curve *2* corresponds to the production rate variation related to heating of the borehole environment in the framework of the elastic model with absorption. Curve *3*

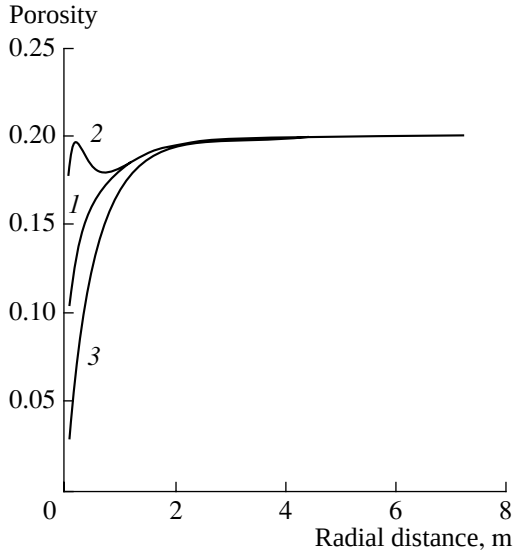


**Fig. 7.** Radial distributions of porosity at the center of the borehole perforated interval; curves *1*, *2*, and *3* correspond to the instants before AA, immediately after AA, and 80 days after AA.

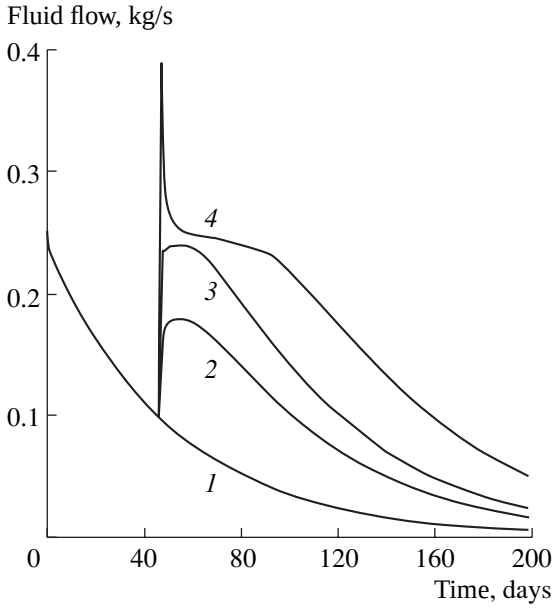


**Fig. 8.** Dynamics of the fluid flow from the borehole (production rate) before and after the AA for different regimes of heating of the environment. The lower curve *1* corresponds to the production rate dynamics without AA. Curve *2* corresponds to the heating according to the elastic model with absorption. Curve *3* corresponds to heating in Biot's model with open porosity $m = 0.05$ and permeability $k = 0.1$ D. The upper curve *4* differs from curve *3* by the assumption that all of the porosity is open, $m = 0.2$.

corresponds to heating in the framework of Biot's model with open porosity $m = 0.05$ and permeability $k = 0.1$ D. The upper curve *4* differs from curve *3* by the assumption that the whole of porosity is assumed to be open with $m = 0.2$. The sharp peak arises in this curve due to the significant decrease in the fluid viscosity under the conditions of a fast heating of the borehole environment by more than 200 degrees, which occurs for the specified model parameters. Integrally, the qualitative production rate behavior shown in Fig. 8 agrees well with the experimental data given in Fig. 1.

Thus, we showed that the proposed model representing the physical phenomena accompanying the AA in the framework of the thermal mechanism is able to explain the long-term effect of AA.

## 9. CONSIDERATION OF NONTHERMAL MECHANISMS UNDER AA

An important feature of the model is that this model includes the mechanism of slow mudding of the borehole environment and, consequently, allows one to investigate alternative mechanisms of AA.

As an example of a nonthermal mechanism of AA, we consider one of the models related to the dependence of the equilibrium concentration and relaxation time of the intensity of AA. Here, one must take into account two circumstances.

First, the process of heavy impurity deposition on the pore walls can be considered as a second-order phase transition related to of the change in the order parameter of the impurity. In this case, relaxation time $\tau_c$ in Eq. (9) becomes a function of temperature and external acoustic field and can be represented in the form [13]

$$\frac{1}{\tau} = \frac{1}{\tau_k}\frac{|T - T_k|}{T_k} + \frac{1}{\tau_0} + \frac{1}{\tau_E}\frac{E}{E_0}. \qquad (17)$$

Here, according to the Landau theory of the second-order phase transitions, the first term describes the temperature dependent behavior of relaxation time near the critical point $T_k$, the second term corresponds to the effective contribution of spatial fluctuations, and the last term corresponds to the contribution of the external acoustic field with normalized energy density $E/E_0$.

Second, the impurity equilibrium concentration in the solution $C_*$ that determines the direction and rate of the dissolving–settling process is, in the equilibrium state, a function of fundamental thermodynamic parameters, such as pressure $P$ and temperature $T$; under the conditions of the ultrasonic radiator operation, it additionally depends on the acoustic energy density. We can illustrate this fact as follows. Linear expansion (10) holds for the conditions of quasi-static equilibrium. In the presence of rapidly varying acoustic fields, one must average the corresponding expansion over the oscillation period. This averaging results in zero values of linear terms, so that the expansion of the average equilibrium concentration in the field of an acoustic wave will start from the terms quadratic in pressure, which, being averaged over time, will be proportional to the acoustic energy density. Taking this fact into account, we can represent the expansion of the equilibrium concentration in the form

$$C_* = C_0\left(1 + A\frac{P - P_0}{P_0} + B\frac{T - T_0}{T_0} + D\frac{E}{E_0}\right), \qquad (18)$$

where dimensionless parameters $A$, $B$ and $D$ are fixed in this model so as to fit the calculated decrease in the petroleum production rate before and after AA to experimental data.

Figure 9 shows the characteristic distribution of parameter $\tau_c$ around the borehole under ultrasonic treatment. In the calculations, we used the following parameters in Eq. (18): $T_c = 313$ K (40°C), $\tau_c = 10^3$ s, $\tau_0 = 10^6$ s, $\tau_E = 10^3$ s, and $E_0 = 1$ J/m$^3$. It may be seen that, for these parameters, the acoustic field can reduce the relaxation time by two or three orders of magnitude. Such a decrease in relaxation time can significantly increase the speed of pore channel cleaning in the permeable medium in the course of AA.

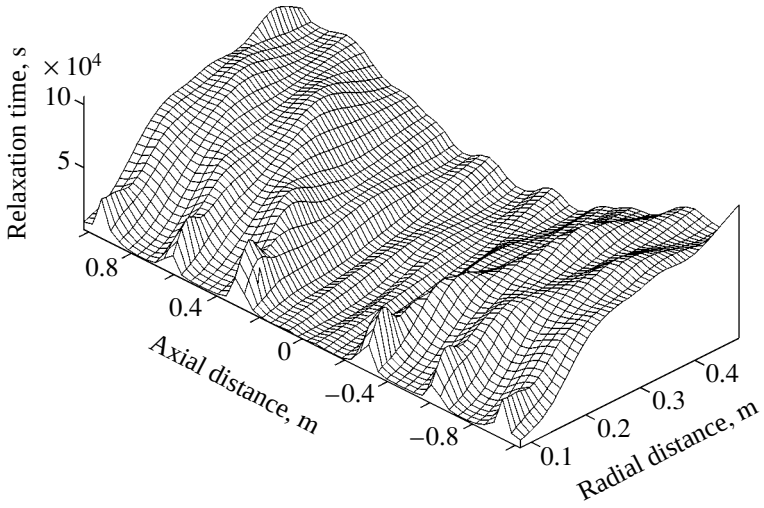


**Fig. 9.** Distribution of relaxation times in the borehole environment during the operation of the borehole ultrasonic radiator.

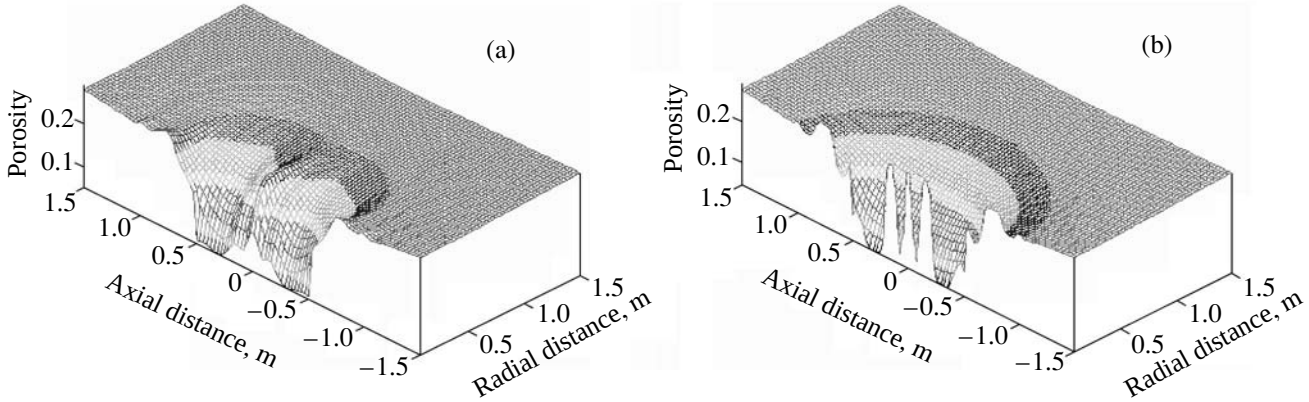


**Fig. 10.** Spatial distribution of porosity for (a) thermal and (b) nonthermal mechanisms immediately after a 10-h-long AA.

Figures 10a and 10b show the spatial distributions of porosity in the borehole environment that was calculated for thermal and nonthermal mechanisms of action on the oil pool from the borehole for the moment immediately following a 10-h ultrasonic treatment of the collector's perforated interval.

Figure 11 shows the comparison of the production rates of a producing borehole that were calculated for thermal and nonthermal mechanisms according to the procedure of calculating the AA efficiency given in the foregoing sections. The solid lines corresponds to the production rate variation related to heating of the borehole environment in the framework of the elastic model with absorption with fitting parameters $A = 0.5$ and $B = 12.0$ for one of the solid lines and $B = 8.0$ for the other. The dashed line corresponds to the problem with a nonthermal mechanism with parameters $A = 0.5$ and $D = 0.01$.

One can see from Fig. 11 that the agreement between the calculated and experimental dynamics of the borehole production rate variation can be achieved using the corresponding parameters in Eqs. (17) and (18) in the framework of both thermal and nonthermal mechanisms of AA. This agreement is determined by the identity of the behavior of the long-term process of mudding. The difference consists in different sluggishness of the processes occurring immediately after AA. In the case of the thermal mechanism, the production rate dynamics appears to be relatively long (several days), which is related to the thermal field relaxation in the borehole environment; in contrast, in the case of the nonthermal mechanism of AA, the nondelay transition to the mudding regime occurs immediately after the termination of AA.

Thus, we proposed a complex model that is able to quantitatively reproduce the long-term effect of AA in the framework of both thermal and nonthermal mecha-

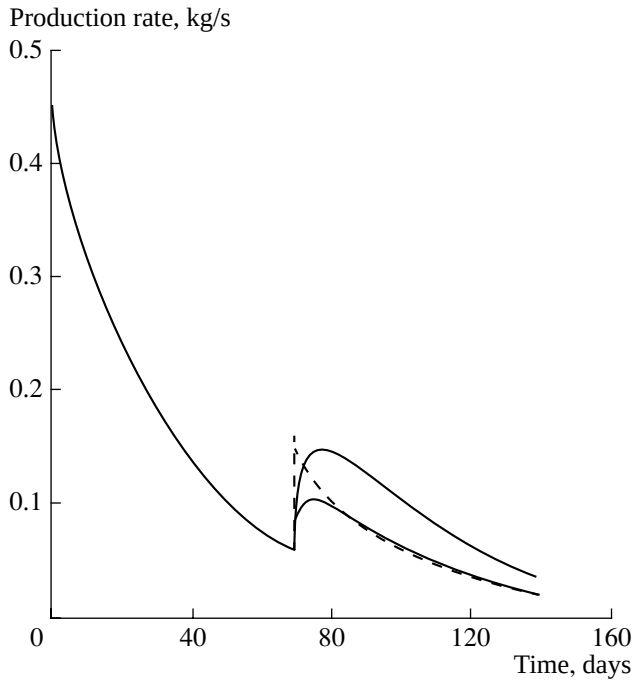


**Fig. 11.** Borehole production rate as a function of exploitation time for AA carried out on the 60th day. The solid lines show two versions of calculations according to the thermal mechanism with coefficients $B = 12.0$ and $B = 8.0$ ($A = 0.5$ in both versions). The dashed line corresponds to the nonthermal mechanism of AA with a relaxation time depending on the acoustic energy density and with $D = 0.01$.

nisms with the appropriate choice of parameters. At the same time, we emphasize that this model includes a number of fitting parameters ($A$, $B$, $D$, and $\tau_c$), whose values are specified only from the condition of fitting the result with experimental data. However, these parameters are determined by the physical chemical properties of petroleum and allow an independent evaluation. The consideration of this fact can give a more objective estimate of the role of both thermal and alternative nonthermal mechanisms of AA.

## REFERENCES

1. G. A. Maksimov and A. V. Radchenko, Geofizika, No. 6, 38 (2001).
2. *Handbook of Physical Quantities*, Ed. by I. S. Grigor'iev and E. Z. Meĭlikhov (Énergoatomizdat, Moscow, 1991; CRC Press, Boca Raton, 1997).
3. Yu. I. Gorbachev, Geoinformatika, No. 3, 7 (1998).
4. Y. I. Gorbachev, R. S. Rafikov, V. Rok, and A. A. Pechkov, First Break **17** (10), 331 (1999).
5. O. L. Kuznetsov, É. M. Simkin, and G. V. Chilingar, *Physical Grounds of Acoustic Effects on Oil and Gas Deposits* (Mir, Moscow, 2001) [in Russian].
6. O. L. Kuznetsov and S. F. Efimova, *Application of Ultrasound in Oil Industry* (Nedra, Moscow, 1983) [in Russian].
7. A. A. Pechkov and A. V. Shubin, Geoinformatika, No. 3, 16 (1998).
8. S. E. Elias, D. G. Kirnos, G. A. Maksimov, and A. V. Radshenko, in *Proceedigns of Scientific Session of Moscow Engineering Physic Institute, MIFI, Moscow, 2002* (Moscow Inzhenern. Fiz. Inst., Moscow, 2002), Vol. 5, pp. 84–86 [in Russian].
9. M. A. Biot, J. Acoust. Soc. Am. **34**, 1254 (1962).
10. T. Bourbie, O. Coussy, and B. Zinszner, *Acoustics of Porous Media* (Paris, 1987).
11. G. A. Maksimov and A. V. Radchenko, in *Proceedings of XI Session of Russian Acoustical Society* (GEOS, Moscow, 2001), p. 67 [in Russian].
12. R. Ewing, Mat. Model. **13** (2), 117 (2001).
13. E. M. Lifshitz and L. P. Pitaevskiĭ, *Course of Theoretical Physics*, Vol. 10: *Physical Kinetics* (Nauka, Moscow, 1979; Pergamon, New York, 1982).

*Translated by A. Vinogradov*

*Acoustical Physics, Vol. 51, Suppl. 1, 2005, pp. S115–S121. Translated from Akusticheskiĭ Zhurnal, Vol. 51, Suppl., 2005, pp. 132–139.*


# Propagation of Longitudinal Elastic Waves in a Fluid-Saturated Porous Medium with Spherical Inclusions

**M. G. Markov**

*Instituto Mexicano del Petróleo, Eje Central Lázaro Cárdenas 152, CP 07730, México, DF*

*e-mail: mmarkov@imp.mx*

Received April 23, 2004

**Abstract**—The Frenkel–Biot theory is used to study the propagation of a longitudinal harmonic wave of the first kind in an isotropic porous matrix with inclusions contrasting in elastic properties and hydrodynamic permeability. The generation of elastic waves of the second kind at the boundaries of inclusions is taken into account. The effective wave number of the longitudinal wave is calculated using the equations of multiple scattering theory. The characteristic size of inhomogeneities is assumed to be much greater than the size of pores. The parameters of the model used for calculations correspond to sandstone with centimeter-scale inhomogeneities. The presence of such inhomogeneities is typical of sedimentary rocks. Calculations show that, in the frequency range of acoustic logging, the effective attenuation factor of the longitudinal wave may noticeably exceed the attenuation factors of longitudinal waves of the first kind in both matrix and inclusions. From the results obtained, it follows that, when studying the propagation of elastic waves in fluid-saturated porous media, it is necessary to take into account the hydrodynamic effects associated with the filtration overflows that arise at the boundaries of inhomogeneities. © *2005 Pleiades Publishing, Inc.*

## INTRODUCTION

Many rocks contain mobile fluids in their pores. The propagation of elastic waves in such media has a number of distinctive features as compared to a single-phase elastic medium. A correct description of these features is possible in the framework of the Frenkel–Biot theory [1–5]. According to the latter, two longitudinal waves propagate in a fluid-saturated porous medium. The longitudinal wave of the first kind in the geoacoustic frequency range is associated with in-phase oscillations of the solid skeleton and the fluid in the pores. The longitudinal wave of the second kind corresponds to antiphase particle displacements of the solid and fluid phases, and, hence, this wave is characterized by strong attenuation. As a rule, only longitudinal waves of the first kind are recorded in geoacoustic measurements. However, in an inhomogeneous medium, the generation of the rapidly attenuating longitudinal waves of the second kind at the boundaries of inclusions leads to an additional energy dissipation and to changes in the amplitudes of the observed waves.

The propagation of elastic waves in a fluid-saturated porous medium containing a crack in the form of a plane-parallel liquid layer was studied in [6]. The crack model in the form of a Biot medium with a very high porosity was considered in [7, 8]. In [6, 7], it was shown that the attenuation of elastic waves may be caused by filtering flows of the fluid near the boundaries of inclusions. The effective wave numbers of elastic waves propagating in a periodically layered fluid-saturated porous medium were calculated in [9–12]. The propagation of longitudinal waves in a medium containing spherical inclusions that differ in the properties of the fluid was first considered by White [13]. The results obtained by White were refined in [14], where the effective compressibility was determined for a water-saturated medium containing spherical gas-filled inclusions whose size was much greater than the characteristic size of the pores. A complete solution to the problem of elastic wave scattering by a fluid-filled cavity in a fluid-saturated porous medium was obtained in [15, 16], and the solution for the case of porous inclusions with contrasting elastic properties, in [17, 18]. B.Ya. Gurevich and his coauthors considered the propagation of elastic waves in fluid-saturated porous media with weak-contrast spherical [19] and spheroidal [20] inclusions. In [15], the multiple scattering theory version proposed by Chaban [21] was used to calculate the effective wave number of a longitudinal wave of the first kind propagating in a medium with pores and cavities.

This paper presents the calculation of the effective wave number of a longitudinal wave of the first kind propagating in a fluid-saturated porous medium with spherical inclusions on the basis of the equations of the multiple scattering theory [22]. The characteristic size of inclusions is assumed to be much greater than the size of pores. The inclusions differ from the matrix in elastic and hydrodynamic properties. The second section of the paper briefly describes the solution of the

problem of elastic wave scattering by a single inclusion in a fluid-saturated porous medium. The third section presents the equations of the multiple scattering theory and the results of calculations for inhomogeneous rocks. The calculations are performed for the frequency range typical of acoustic logging.

## SCATTERING OF LONGITUDINAL ELASTIC WAVES BY A SPHERICAL INCLUSION IN A FLUID-SATURATED POROUS MEDIUM

Consider a fluid-saturated porous medium (matrix) containing a spherical inclusion with a radius $a$ and with elastic and hydrodynamic parameters different from those of the medium. To describe the elastic wave propagation in the saturated porous medium, we use the equations of the dynamics of saturated porous media. With thermoelastic effects being ignored, these equations have the form [2]

$$\begin{aligned}\rho_{11}\frac{\partial^2 U_i}{\partial t^2} + \rho_{12}\frac{\partial^2 V_i}{\partial t^2} &= b\frac{\partial(V_i - U_i)}{\partial t} + \frac{\partial \tau_{ij}}{\partial x_j},\\ \rho_{12}\frac{\partial^2 U_i}{\partial t^2} + \rho_{22}\frac{\partial^2 V_i}{\partial t^2} &= b\frac{\partial(U_i - V_i)}{\partial t} + \frac{\partial s}{\partial x_j},\end{aligned} \tag{1}$$

where $U_i$ and $V_i$ are the components of the displacement vectors of the skeleton and the fluid in the pores, respectively; $\omega$ is the cyclic frequency; $\rho_{11}$ is the effective density of the elastic skeleton; $\rho_{22}$ is the effective density of the fluid; $\rho_{12}$ is the apparent density of the fluid;

$$\tau_{ij} = \delta_{ij}A\nabla\cdot\mathbf{U} + 2Ne_{ij} + \delta_{ij}Q\nabla\cdot\mathbf{V};$$

$$s = -mp = Q\nabla\cdot\mathbf{U} + R\nabla\cdot\mathbf{V};$$

and

$$e_{ij} = (\partial U_i/\partial x_j + \partial U_j/\partial x_i)/2.$$

The coefficient $b$ characterizes the friction associated with the motion of the fluid relative to the skeleton: $b = \dfrac{m^2}{\eta K_{pr}}$, where $\eta$ is the dynamic viscosity of the fluid, $m$ is the porosity, and $K_{pr}$ is the permeability; $A$, $N$, $Q$, and $R$ are the elastic constants of the Biot theory; and $p$ is the pressure in the liquid. In what follows, we consider only harmonic waves propagating with a frequency $\omega$.

Equations (1) have solutions in the form of one transverse wave and two longitudinal waves. The displacements of the skeleton and the fluid filling the pores can be described by the scalar potentials, $\varphi_1$ and $\varphi_2$, of the longitudinal waves and by the vector potential $\mathbf{\Psi} = \psi\mathbf{e}_\varphi$ of the transverse wave [4, 23, 24]:

$$\begin{aligned}\mathbf{U} &= \nabla\varphi_1 + \nabla\varphi_2 + \nabla\times\mathbf{\Psi},\\ \mathbf{V} &= M_1\nabla\varphi_1 + M_2\nabla\varphi_2 + M_3\nabla\times\mathbf{\Psi},\end{aligned} \tag{2}$$

where

$$M_j = \frac{\gamma_{12} - \xi_j\sigma_{12} + i\gamma}{-\gamma_{22} + \xi_j\sigma_{12} + i\gamma}, \quad j = 1, 2$$

$$M_3 = \frac{\gamma_{12} + i\gamma}{-\gamma_{22} + i\gamma},$$

$\gamma_{11} = \rho_{11}/\rho$, $\gamma_{12} = \rho_{12}/\rho$, $\gamma_{22} = \rho_{22}/\rho$, $\gamma = -b/(\rho\omega)$,

$\sigma_{11} = (A + 2N)/H$, $\sigma_{12} = Q/H$, $\sigma_{22} = R/H$,

$\rho = \rho_{11} + 2\rho_{12} + \rho_{22}$,

$H = A + 2N + 2Q + R$, $\xi_j = k_j^2 H/(\rho\omega)$.

Here, $k_j$ ($j = 1, 2$) are the wave numbers of the longitudinal waves of the first and second kinds, respectively; $\xi_j$ satisfies the quadratic equation

$$\begin{aligned}&(\sigma_{11}\sigma_{12} - \sigma_{12}^2)\xi_j^2\\ &+ (\sigma_{11}\gamma_{22} + \sigma_{22}\gamma_{11} - 2\sigma_{12}\gamma_{12} + i\gamma)\xi_j\\ &+ \gamma_{11}\gamma_{22} - \gamma_{12}^2 - i\gamma = 0;\end{aligned}$$

$\mathbf{e}_\varphi$ is the unit azimuth vector in the direction; and the factor $\exp(-i\omega t)$ is everywhere omitted.

The substitution of Eqs. (2) into system of equations (1) yields a system of Helmholtz equations [4, 16, 23, 24] for the potentials of the two longitudinal and one transverse waves:

$$\begin{aligned}\Delta\varphi_j + k_j^2 &= 0, \quad j = 1, 2;\\ \Delta\psi - \frac{1}{r^2\sin\theta}\psi + k_3^2\psi &= 0,\end{aligned} \tag{3}$$

where $k_3^2 = \dfrac{\omega^2\rho}{N}[\gamma_{11} + \gamma_{12} + i\gamma(M_3 - 1)]$.

The solutions to Eqs. (3) that are finite at the origin of coordinates (inside the inclusion) and satisfy the

absorption condition away from the inclusion have the form [16]

$$\begin{aligned}
\varphi_j^{\text{int}} &= \sum_{n=0}^{\infty} A_n^{(j)} j_n(k_j^{\text{int}} r) P_n(\cos\theta), \quad j = 1, 2;\\
\psi^{\text{int}} &= \sum_{n=0}^{\infty} B_n^{(j)} j_n(k_3^{\text{int}} r) P_n^{(1)}(\cos\theta), \quad r \le a,\\
\varphi_j^{\text{out}} &= \sum_{n=0}^{\infty} C_n^{(j)} h_n^{(1)}(k_j^{\text{out}} r) P_n(\cos\theta), \quad j = 1, 2;\\
\psi^{\text{out}} &= \sum_{n=0}^{\infty} D_n^{(j)} h_n^{(1)}(k_3^{\text{out}} r) P_n^{(1)}(\cos\theta), \quad r \ge a,
\end{aligned} \tag{4}$$

where $h_n^{(1)}(x)$ and $j_n(x)$ are spherical Hankel functions of the first kind and Bessel functions and $P_n(\cos\theta)$ and $P_n^{(1)}(\cos\theta)$ are Legendre functions of a real argument.

An incident plane longitudinal wave of the first or second kind also can be described by a series expansion in spherical functions:

$$\begin{aligned}
\varphi_0 &= \exp(ik_j^{\text{out}} r\cos(\theta))\\
&= \sum_{n=0}^{\infty} i^n (2n+1) j_n(k_j^{\text{out}} r) P_n(\cos\theta), \quad j = 1, 2.
\end{aligned} \tag{5}$$

At the boundary $r = a$ of the porous media, the following conditions should be satisfied [24–26]:

$$\begin{aligned}
&\sigma_{rr}^{\text{out}} + s^{\text{out}} = \sigma_{rr}^{\text{int}} + s^{\text{int}}, \quad p^{\text{out}} = p^{\text{int}},\\
&\sigma_{r\theta}^{\text{out}} = \sigma_{r\theta}^{\text{int}}, \quad U_r^{\text{out}} = U_r^{\text{int}},\\
&(1-m)U_r^{\text{out}} + mV_r^{\text{out}} = (1-m)U_r^{\text{int}} + mV_r^{\text{int}},\\
&U_\theta^{\text{out}} = U_\theta^{\text{int}},
\end{aligned} \tag{6}$$

where the first and second conditions express the continuity of the normal component of the total stress tensor and the continuity of pressure in the pores; the third condition is the continuity of the tangential stress in the skeleton; the fourth and fifth conditions describe the continuity of the normal displacements of the skeleton and the continuity of total displacements; and the sixth condition expresses the continuity of the tangential displacements of the skeleton.

Substituting Eqs. (4) and (5) into Eqs. (6), we obtain a system of linear equations for determining the amplitudes of scattered waves. The resulting solution is the basic one for the equations of multiple scattering theory, which will be used below to calculate the velocity and attenuation of the effective longitudinal wave in an inhomogeneous porous medium.

## CALCULATIONS OF THE VELOCITY AND ATTENUATION OF THE EFFECTIVE LONGITUDINAL WAVE PROPAGATING IN AN INHOMOGENEOUS FLUID-SATURATED POROUS MEDIUM

To calculate the effective wave number, we use the classical Waterman–Truell theory [22]. This theory gives the following expression for the effective wave number $k_{\text{eff}}$ of an elastic wave propagating in a medium with spherical inclusions:

$$\begin{aligned}
k_{\text{eff}}^2 &= (k_f^{\text{out}})^2\\
&\times\left(1 + \frac{4\pi n_0}{k_j^2} f(0) - \frac{4\pi^2 n_0^2}{k_j^4}[f^2(0) - f^2(\pi)]\right).
\end{aligned} \tag{7}$$

Here, $n_0$ is the density of the scattering centers, which is related to the volume concentration of inclusions $\Phi$ by the formula $\Phi = \frac{4\pi R^3}{3} n_0$, and $f(0)$ and $f(\pi)$ are the forward and backward scattering amplitudes obtained from the solution of the single-particle problem, respectively.

The scattering amplitudes are expressed through the coefficients $C_n^{(j)}$ determined in the previous section:

$$\begin{aligned}
f(0) &= \frac{1}{ik_j^{\text{out}}} \sum_{n=0}^{\infty} (2n+1) C_n^{(j)},\\
f(\pi) &= \frac{1}{ik_j^{\text{out}}} \sum_{n=0}^{\infty} (-1)^n (2n+1) C_n^{(j)}.
\end{aligned} \tag{8}$$

Let us consider examples of calculation with Eqs. (7) and (8) for specific types of fluid-saturated porous media. The calculation of the effective wave number of the longitudinal wave of the first kind is of most practical interest. Therefore, precisely this case will be considered below and the term “effective longitudinal wave” will imply the effective longitudinal wave of the first kind.

Consider the first example: the propagation of waves in a porous medium containing inclusions that differ in porosity and permeability from the matrix. We assume that pores in the matrix and in the inclusion are filled with the same fluid. The properties of rock are assumed to be those of water-saturated sandstone. The

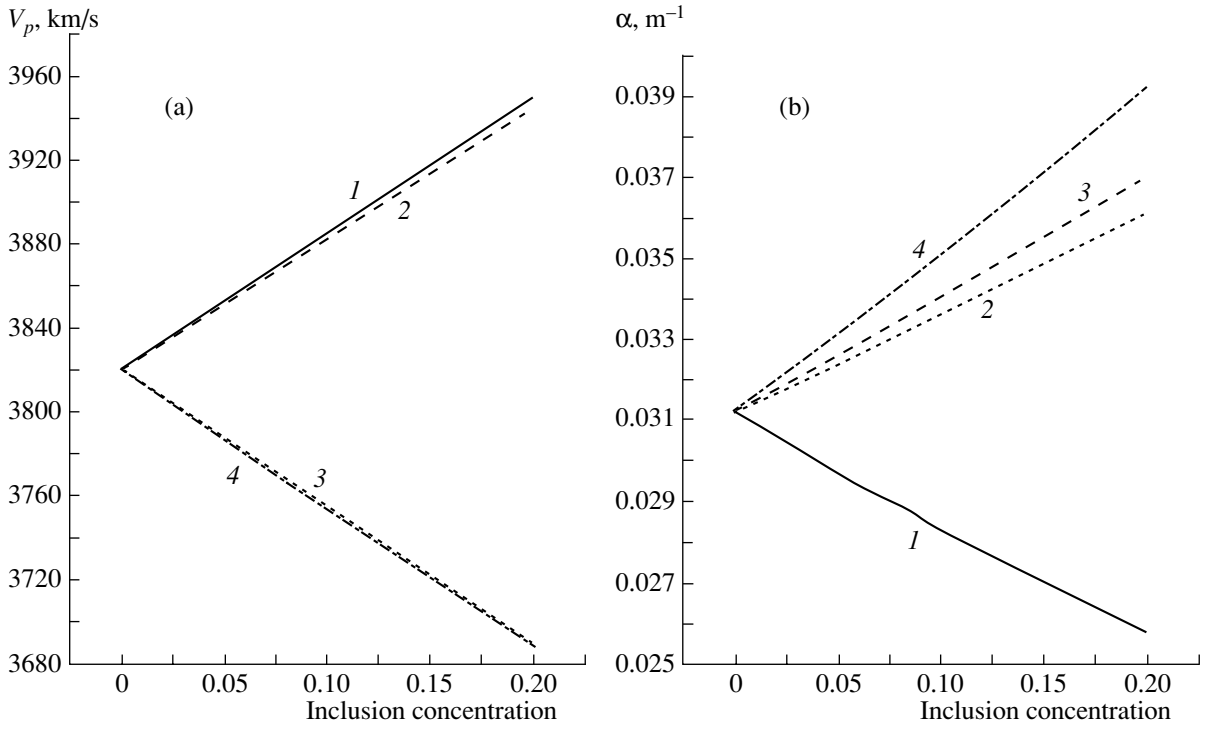


**Fig. 1.** Dependences of (a) the velocity and (b) the attenuation factor of the effective longitudinal wave on the volume concentration of inclusions. The porosity of inclusions is (*1*, *2*) 0.1 and (*3*, *4*) 0.3; the permeability of inclusions is (*1*, *2*) $5 \times 10^{-15}$ and (*3*, *4*) $1 \times 10^{-12}$ m$^2$; the radius of inclusions is (*1*) 0.01, (*2*) 0.025, (*3*) 0.01, and (*4*) 0.025 m.

elastic constants $A$, $N$, $Q$, and $R$ are calculated using the known relations [4, 24]

$$A = \lambda + K_0 a_0^2 S_0/m, \quad N = \mu,$$
$$Q = a_0 K_0 S_0, \quad R = mK_0 S_0, \tag{9}$$

where $a_0 = 1 - m - K_s/K_r$, $S_0 = mK_r/(mK_r + a_0 K_0)$, $\lambda_s$ and $\mu_s$ are Lame constants of the skeleton with empty pores, $K_s$ is the bulk modulus of the porous skeleton with empty pores, $K_r$ is the true bulk modulus of the solid phase, and $K_0$ is the bulk modulus of the fluid. The elastic moduli of the skeleton with empty pores were calculated by the self-consistent EMA method [27, 28]. The longitudinal wave velocity in the skeleton material was taken to be equal to 5.5 km/s, the ratio between the longitudinal and transverse wave velocities was 1.65, the density of the skeleton material, 2.65 g/cm$^3$, the longitudinal wave velocity in the fluid, 1.5 km/s, the density of the fluid, 1 g/cm$^3$, and the viscosity, 0.001 Pa s.

Figure 1 shows the calculated dependences of the velocity and attenuation factor of the effective longitudinal wave on the volume concentration of inclusions. The porosity and the permeability of the matrix are 0.2 and $5 \times 10^{-13}$ m$^2$, respectively, and the frequency is $\omega = 2\pi 10000$ s$^{-1}$. The calculations show that the velocity of the effective elastic wave weakly depends on the permeability of rock and can be calculated with an acceptable accuracy by using a simpler model of a single-phase elastic medium, at least in the geoacoustic frequency range $|k_1 a| < 1$. The attenuation factor of the effective longitudinal wave (Figs. 1b and 2) strongly depends on both the concentration and size of the inclusions. The attenuation of the effective longitudinal wave is associated with the energy transfer from the longitudinal waves of the first kind to the rapidly attenuating longitudinal waves of the second kind and strongly depends on two diffraction parameters, $|k_1 a|$ and $|k_2 a|$. In the frequency range under consideration, the inequality $|k_1 a| < 1$ is satisfied; however, for the longitudinal wave of the second kind, in the same frequency range we have $|k_2 a| \geq 1$, and the effective attenuation factor strongly depends on the radius of inclusions and may exceed the attenuation factor of the longitudinal wave of the first kind in both matrix and inclusion. In this situation, the presence of inclusions with porosity and permeability both higher and lower than those of the matrix may lead to an increase in the effective attenuation factor of the longitudinal wave in the inhomogeneous medium. Note that the presence of inhomogeneities on the order of centimeters in size is typical of sedimentary rocks [29]. It is of interest to study the frequency dependence of the attenuation factor. Figure 3 shows the frequency dependences of the attenuation factor of the effective longitudinal wave. The calculations were performed for water-saturated

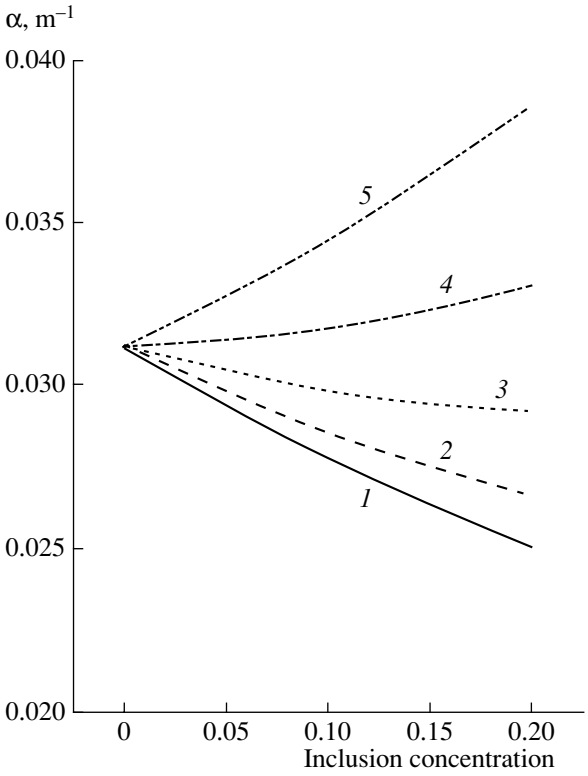


**Fig. 2.** Dependences of the attenuation factor of the effective longitudinal wave on the volume concentration of inclusions. The radius of inclusions is (*1*) 0.005, (*2*) 0.01, (*3*) 0.015, (*4*) 0.02, and (*5*) 0.025 m.

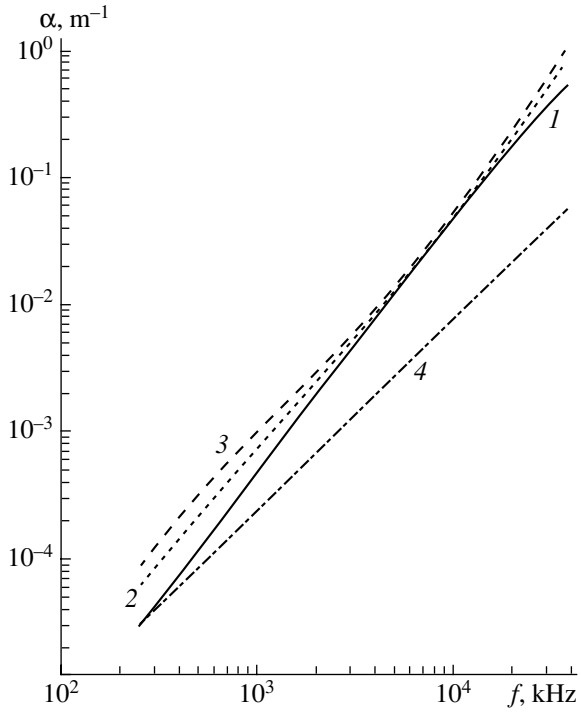


**Fig. 3.** Frequency dependences of the attenuation factor of the longitudinal wave of the first kind: the attenuation factor (*1*) for the matrix without inclusions and for the inclusion concentrations of (*2*) 0.1 and (*3*) 0.2; (*4*) the curve calculated by the formula $\alpha = \alpha_0^{3/2}$, where $\alpha_0$ is the attenuation factor at a given frequency.

porous sandstone with the matrix and inclusion porosities being 0.3 and 0.1, respectively, and the matrix and inclusion permeabilities being $10^{-12}$ m$^2$ and $5 \times 10^{-15}$ m$^2$, respectively. The estimates obtained in [19] by using the Born approximation for weak-contrast inclusions showed that, in the region of very low frequencies, where $|k_1 a| \ll 1$ and $|k_2 a| \ll 1$, the attenuation factor of the effective longitudinal wave is $\alpha_{\text{eff}} \propto \omega^{5/2}$, and in the higher frequency region, where $|k_1 a| \ll 1$ and $|k_2 a| \gg 1$ – $\alpha_{\text{eff}} \propto \omega^{3/2}$. In the major part of the frequency range under study, the second condition is satisfied and the effective attenuation factor is $\alpha_{\text{eff}} \propto \omega^{3/2}$ (see the interval 700–6000 Hz in Fig. 3). The latter law is of a rather general character: for example, the same law describes the frequency dependence of the attenuation factor for the Rayleigh and Stoneley surface waves propagating along the boundary of a fluid-saturated porous medium [30, 31]. In the region of very low frequencies, where $|k_1 a| \ll 1$ and $|k_2 a| \ll 1$, the medium is described by the equations of a fluid-saturated porous medium with a certain effective permeability. In this case, the effective attenuation factor is $\alpha_{\text{eff}} \propto \omega^2$, as in the conventional Frenkel–Biot model. Note that, in [19], the wave numbers of both the longitudinal wave of the first kind and the transverse wave were assumed to be real and the aforementioned mechanism was not taken into account.

As the second example, let us consider the situation where the inhomogeneities differ from the medium in only the properties of the fluid filling the pores. Let the inclusions be filled with a fluid whose compressibility is much greater than that of the fluid in the surrounding medium (the White model). This situation corresponds to, e.g., gas bubbles in water or in oil. Figure 4 shows the frequency dependences of the velocity and attenuation factor of the effective longitudinal wave propagating in a water-saturated porous medium with gas-filled inclusions. The properties of the skeleton correspond to those of sandstone with a porosity of 30% and a permeability of $5 \times 10^{-13}$ m$^2$. The longitudinal wave velocity in gas is 500 m/s, and the density and viscosity of gas are taken to be equal to 0.1 g/cm$^3$ and 0.0001 Pa s, which corresponds to, e.g., methane. Since the filler of inclusions is much softer than that of the matrix, intense hydrodynamic flows arise at the boundaries of inclusions, which are associated with the energy transfer from the longitudinal waves of the first kind to rapidly attenuating longitudinal waves of the second kind. These effects lead to a considerable velocity dispersion, up to 30%, and a considerable (more than an order of magnitude) increase in the attenuation factor of the effective longitudinal wave in comparison with the

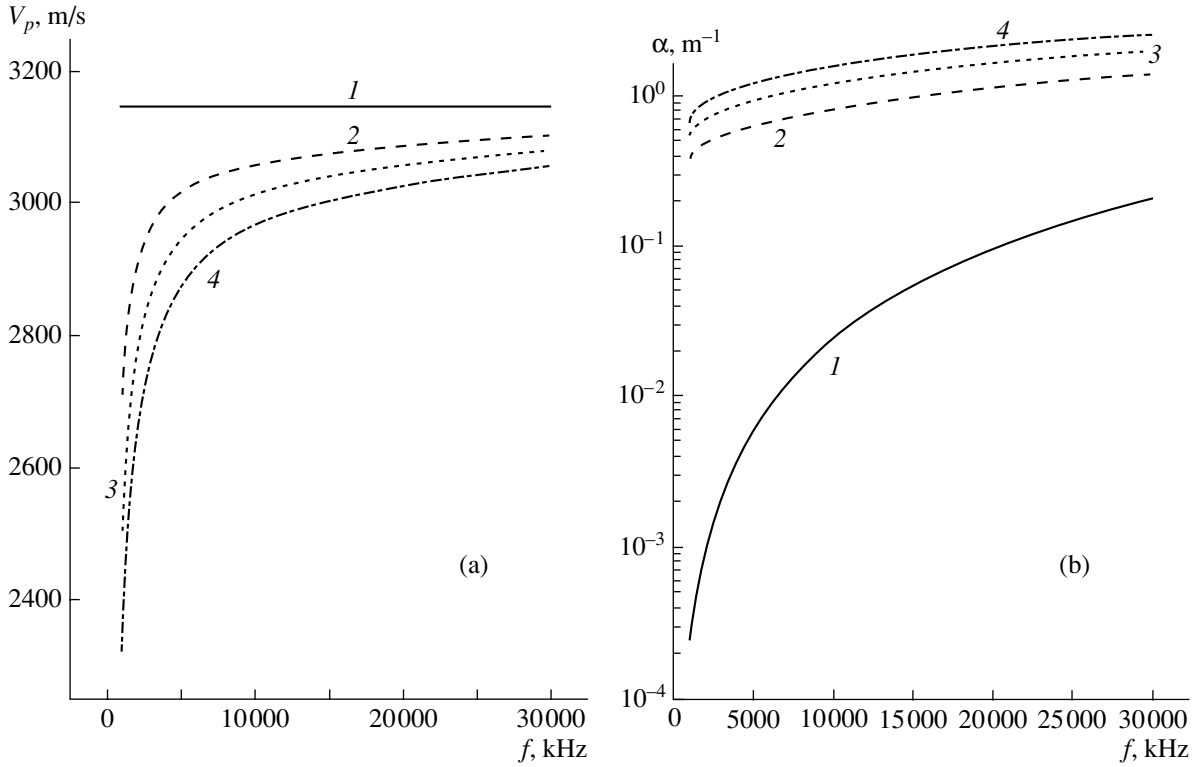


**Fig. 4.** Frequency dependences of the (a) velocity and (b) attenuation factor of the effective longitudinal wave in a medium with gas-filled inclusions: (*1*) the matrix without inclusions; the inclusion concentrations are (*2*) 0.1, (*3*) 0.15, and (*4*) 0.2.

attenuation factors of longitudinal waves of the first kind in the matrix and in the inclusions.

## CONCLUSIONS

It is well known that rocks are rather complicated objects of investigation, and this complexity is largely determined by the presence of inhomogeneities of different scales. In this paper, in the framework of the Frenkel–Biot theory, we considered the propagation of longitudinal elastic waves in rock containing mesoscale inhomogeneities [29], whose size was assumed to be greater than the characteristic pore size and smaller than or comparable to the acoustic wavelength. It was shown that the presence of such inhomogeneities may lead to considerable changes in the kinematic and especially the dynamic parameters of elastic waves. In this situation, the effective attenuation factor of the longitudinal wave may noticeably exceed the attenuation factors of the longitudinal waves of the first kind propagating in the matrix and in the inclusions. Evidently, the aforementioned mechanism of acoustic wave attenuation in rock is not unique but is quite important. It should be taken into account in interpreting the data of geoacoustic measurements along with other hydrodynamic mechanisms of elastic wave attenuation [29, 32–24].

## ACKNOWLEDGMENTS

I am grateful to my colleagues V.M. Levin, E.D. Kazachenko, and A.A. Musatov from the Mexican Petroleum Institute (IMP), V.N. Krutin from VNIIGEOSISTEM, A.Yu. Yumatov from NEFTEGAZGEOFIZIKA, and B.Ya. Gurevich from Curtin University of Technology, Australia, for useful discussions. This work was carried out under The Program “Naturally Fractured Reservoirs” (YNF) of the Mexican Petroleum Institute.

## REFERENCES

1. Ya. I. Frenkel’, Izv. Akad. Nauk SSSR, Ser. Geogr. Geofiz. **8** (4), 133 (1944).
2. M. A. Biot, J. Acoust. Soc. Am. **28**, 168 (1956).
3. V. N. Nikolaevskiĭ, *Mechanics of Porous and Cracked Media* (Nedra, Moscow, 1984) [in Russian].
4. V. N. Nikolaevskiĭ, K. S. Basniev, A. T. Gorbunov, and G. F. Zotov, *Mechanics of Saturated Porous Media* (Nedra, Moscow, 1970) [in Russian].
5. T. Bourbie, O. Coussy, and B. Zinzner, *Acoustics of Porous Media* (Gulf Publ., Houston, 1987).
6. M. G. Markov and A. Yu. Yumatov, Prikl. Mekh. **20** (8), 116 (1984).
7. A. Yu. Yumatov and M. G. Markov, Geol. Geofiz., No. 3, 98 (1987).

8. A. V. Bakulin and L. A. Molotkov, *Effective Seismic Models of Cracked and Porous Media* (Izd. St.-Peterburg. Univ., St. Petersburg, 1998) [in Russian].
9. M. G. Markov and A. Yu. Yumatov, Zh. Prikl. Mekh. Tekh. Fiz., No. 1, 115 (1988).
10. B. Ya. Gurevich, S. L. Lopatnikov, and O. S. Vinogradova, Geol. Geofiz. **44** (1), 95 (1990).
11. A. N. Norris, J. Acoust. Soc. Am. **94** (1), 359 (1993).
12. B. Gurevich and S. Lopatnikov, Geophys. J. Int. **121**, 933 (1995).
13. J. E. White, Geophysics **40** (2), 224 (1975).
14. D. J. Dutta and H. Ode, Geophysics **44** (11), 1777 (1979).
15. A. Yu. Yumatov and M. G. Markov, Izv. Akad. Nauk SSSR, Fiz. Zemli **20** (1), 62 (1984).
16. V. N. Krutin, M. G. Markov, and A. Yu. Yumatov, Prikl. Mat. Mekh. **48** (2), 333 (1984).
17. J. G. Berryman, J. Acoust. Soc. Am. **91**, 551 (1992).
18. C. Zimmerman, J. Acoust. Soc. Am. **94**, 527 (1993).
19. B. Gurevich, A. Sadovnichaya, S. Lopatnikov, and S. Shapiro, Appl. Phys. Lett. **61**, 1275 (1992).
20. B. Gurevich, A. P. Sadovnichaya, S. L. Lopatnikov, and S. Shapiro, Geophys. J. Int. **133** (1), 91 (1998).
21. I. A. Chaban, Akust. Zh. **10**, 351 (1964) [Sov. Phys. Acoust. **10**, 298 (1964)].
22. P. C. Waterman and R. Truell, J. Math. Phys. **2** (2), 512 (1961).
23. L. Ya. Kosachevskiĭ, Prikl. Mat. Mekh. **25** (6), 1076 (1961).
24. V. M. Seĭmov, A. E. Trofimchuk, and O. A. Savitskiĭ, *Vibrations and Waves in Layered Media* (Naukova Dumka, Kiev, 1990) [in Russian].
25. H. Deresiewicz and R. Scalak, Bull. Seismol. Soc. Am. **53** (4), 783 (1963).
26. B. Gurevich and M. Schoenberg, J. Acoust. Soc. Am. **105**, 2585 (1999).
27. J. G. Berryman, J. Acoust. Soc. Am. **68**, 1809 (1980).
28. E. Kazachenko and M. Markov, Geofizika, No. 1, 32 (2003).
29. S. R. Pride, J. G. Berryman, and J. M. Harris, J. Geophys. Res. **109** (1), 1 (2004).
30. M. F. Foda and C. C. Mei, Int. J. Soil. Dyn. Earthquake Eng. **2** (2), 62 (1983).
31. M. G. Markov and A. Yu. Yumatov, Akust. Zh. **33**, 293 (1987) [Sov. Phys. Acoust. **33**, 172 (1987)].
32. J. Dvorkin, R. Holen-Hoeksema, and A. Nur, Geophysics **59** (2), 428 (1994).
33. J. A. Hudson, E. Liu, and S. Crampin, Geophys. J. Int. **124**, 105 (1996).
34. S. R. Tod, Geophys. J. Int. **149** (1), 149 (2002).

*Translated by E. Golyamina*

*Acoustical Physics, Vol. 51, Suppl. 1, 2005, pp. S12–S22. Translated from Akusticheskiĭ Zhurnal, Vol. 51, Suppl., 2005, pp. 19–30.*


# A Possible Mechanism of the Acoustic Action on Partially Fluid-Saturated Porous Media

**A. A. Abrashkin, V. S. Averbakh, S. N. Vlasov, Yu. M. Zaslavskiĭ, I. A. Soustova, R. A. Sudarikov, and Yu. I. Troitskaya**

*Institute of Applied Physics, Russian Academy of Sciences, ul. Ul'yanova 46, Nizhni Novgorod, 603950 Russia*

*e-mail: abrash@hydro.appl.sci-nnov.ru*

Received August 16, 2004

**Abstract**—The motion of a liquid drop under the action of acoustic vibration is studied for two limiting cases: the high-frequency case, when the effect of viscous forces can be ignored, and the low-frequency case, when the viscosity is significant. Equations describing the motion of a drop in an axially symmetric capillary with a varying cross section are derived by taking into account the hysteresis of the wetting angle. Numerical calculations are performed for cylindrical, conic, and corrugated capillaries. © *2005 Pleiades Publishing, Inc.*

In the last few years, the interest in the problem of vibration-wave action on porous media has quickened. This is primarily related to the problem of increasing the permeability of geological strata to oil. By now, the physical basis of the vibration-wave action on porous media is sufficiently well understood. A number of monographs (e.g., [1–4]) and a comprehensive review [5] were devoted to this subject. At the same time, the specific physical mechanisms responsible for the changes in the permeability of the medium, the roles of these mechanisms, and their relative efficiencies are still vague and, in the case of low-frequency vibrations, largely unclear.

The efficiency of the known physical mechanisms that increase the permeability of the oil pool structure under the effect of acoustic fields with frequencies of 5–50 kHz is estimated in [6]. These mechanisms include e.g., the change in the viscosity of free oil, the acoustic flows in pore channels, and the excitation of Biot waves of the second kind [7, 8], which give rise to the motion of the fluid relative to the skeleton. Generally speaking, all of these mechanisms manifest themselves the stronger the higher the amplitude and frequency of the acoustic action are. However, ultrasonic waves are strongly attenuated in the medium and the region of their action on the medium is very limited.

Low-frequency acoustic waves exhibit a much weaker attenuation. Beginning in 1960s, the action of low-frequency elastic vibrations on the face zone of an oil pool by means of intrawell vibrators has found application in oil production [2]. By now, ample experimental data testifying to an increase in the permeability of oil-containing strata under the effect of acoustic waves are available (see [1–4, 9–12] and Proceedings of the Workshop "Effect of Elastic Vibrations on Liquid Flows in Porous Media" held within conference [13]). However, the physical mechanisms underlying a similar effect in the low-frequency region are still unknown.

The character of the liquid motion in a crack depends on the frequency of vibration of the crack walls. In the low-frequency limit, the depth to which vibrations penetrate into the liquid (the thickness of the liquid skin layer) is usually much greater than the characteristic thickness of cracks. In this case, the liquid moves together with the crack surface as a single whole and no mass transfer of the liquid phase occurs in the solid matrix. Therefore, the problem of explaining the increase observed in the permeability of the medium under the action of low-frequency vibrations seems to be nontrivial. To explain this effect, the theory of dominant frequencies was proposed in [14–16]. This theory is based on the assumption that a low-frequency seismic wave may effectively generate ultrasonic vibrations in the medium. However, in this case, it is necessary to assume that the stresses and strains of the geological medium are related in a very particular way, through an unusual relationship that is difficult to explain. This assumption considerably reduces the number of physical situations where such a mechanism can be realized.

In the present paper, we study another possible mechanism that may cause an increase in permeability. This mechanism can be realized only in a partially fluid-saturated porous medium. As is known, in oil production, the basic method is the displacement of oil from the porous collector by water, which is supplied under pressure through the injection wells. This process is accompanied by a number of adverse effects that reduce the discharge of the oil well. In particular, these effects include the formation of water films on the pore walls and the appearance of trapped water drops in the narrowed portions of the pores. The water films reduce

the effective radii of capillaries through which the oil flows, while the trapped drops may completely block the oil's motion through the capillaries. The process of eliminating the water films and drops from the intrapore space may be called "water unclogging." The mechanisms of breaking submicron water films and a systematic evaporation of trapped drops under the effect of vibration were considered in [17]. Below, we study in detail the mechanism of motion of individual drops in capillaries of different shapes under the effect of acoustic vibration.

The motion of trapped drops in a capillary under vibration was first considered in [18]. Its essence is as follows. Assume that a single drop is in the field of a static force (e.g., pressure gradient or gravity), which, however, does not exceed the static friction force. In this case, the drop remains immobile. Now, let a low-frequency alternating acoustic field be superimposed on the given static field. Because a moving meniscus exhibits a hysteresis of the wetting angle [19–21], the dependence of the wetting angle on the velocity magnitude is of an ambiguous (hysteretic) character. The capillary forces acting on the positive and negative menisci of a drop are different. As a result, the initially immobile drop moves in the direction of the aforementioned static force. Thus, the effect of vibration is equivalent to a reduction of the static friction [22]. Experimentally, the motion of drops under vibration was observed for a glycerin drop [23], a drop of 50% aqueous solution of glycerin, and a water drop [24].

The formulation of the hydrodynamic problem in the case of wetting a solid body when the meniscus, i.e., the line of contact between three phases, moves over a solid surface is complicated by the stress singularity at this line [25]. The dynamic wetting angle is determined by the structure of the flow with a free surface in the vicinity of the moving contact line. The determination of the dependence of this angle on the velocity of the meniscus motion presents an individual complicated problem in each specific case [26]. We will consider this dependence to be known and, for simplicity, assume that the value of the wetting angle only depends on the direction of motion and does not depend on the velocity, i.e., that the change of the direction of motion is accompanied by a jumplike change in the wetting angle from one constant value to another.

An important factor that determines the motion of the drop along a capillary under vibration is the viscosity of the liquid. If the frequency of vibration is sufficiently high and the depth of vibration penetration into the liquid is small compared to the capillary radius, the effect of viscous forces can be ignored. In this case, the drop will move as a solid particle under the effect of the static, oscillating, and capillary forces. Its motion can be analyzed by considering an ordinary differential equation of the second order with a hysteretic nonlinear force. If the thickness of the skin layer is comparable to or on the order of the capillary thickness, the viscosity of the liquid should be taken into account. In this case, the motion of the drop should be studied in terms of hydrodynamic equations. In the Stokes approximation, the motion of the drop is described by a differential equation of the first order. In this paper, we present a theoretical description of both situations: with and without considering the viscous effects. We indicate the necessary conditions for the drift of the drop in the presence of vibration. We present analytical solutions for specific regimes of the drop motion. We perform a numerical study of the drop motion in cylindrical, conic, and corrugated capillaries.

## STATEMENT OF THE PROBLEM AND BASIC EQUATIONS

Consider a drop in an axially symmetric capillary with a varying cross section of radius $r = R(z)$, where $z$ is the coordinate along the capillary axis. Let the walls of the capillary perform harmonic vibrations in the direction of the $z$ axis according to the law

$$\xi = \xi_0 \cos \omega t. \tag{1}$$

Owing to the symmetry of the problem, the velocity of the liquid $\vec{v}$ and the pressure $p$ are independent of the polar angle. We assume that the liquid is incompressible.

To describe the motion of the liquid, it is convenient to use the noninertial frame of reference, in which the walls of the channel are at rest. In the cylindrical coordinate system, the set of hydrodynamic equations has the form

$$\frac{1}{r}\frac{\partial}{\partial r}(r v_r) + \frac{\partial v_z}{\partial z} = 0, \tag{2}$$

$$\begin{aligned} &\frac{\partial v_r}{\partial t} + v_r\frac{\partial v_r}{\partial r} + v_z\frac{\partial v_r}{\partial z} \\ &= -\frac{1}{\rho}\frac{\partial p}{\partial r} + \nu\left[\frac{\partial}{\partial r}\left(\frac{1}{r}\frac{\partial r v_r}{\partial r}\right) + \frac{\partial^2 v_r}{\partial z^2}\right], \\ &\frac{\partial v_z}{\partial t} + v_r\frac{\partial v_z}{\partial r} + v_z\frac{\partial v_z}{\partial z} \\ &= -\frac{1}{\rho}\frac{\partial p}{\partial z} + \nu\left[\frac{1}{r}\left(\frac{\partial}{\partial r}r\frac{\partial v_z}{\partial r}\right) + \frac{\partial^2 v_z}{\partial z^2}\right] - \ddot{\xi} + G. \end{aligned} \tag{3}$$

Here, $G$ is the constant external force, which can be, e.g., the gravitational force if the capillary is in the vertical position.

The boundary conditions for the set of equations (2), (3) include the conditions of no leaks and sticking to the capillary walls:

$$v_r|_{r = R(z)} = 0; \quad v_z|_{r = R(z)} = 0. \tag{4}$$

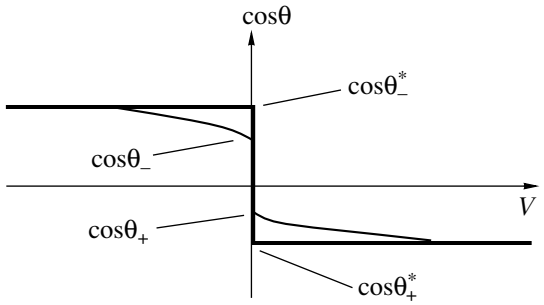


**Fig. 1.** Hysteresis of the wetting angle.

At the free surfaces $\Sigma_1$ and $\Sigma_2$, conditions for the normal stress jump are satisfied:

$$p_n|_{\Sigma_{1,2}} = \frac{2\sigma}{R'(\Sigma_{1,2})} + P_{1,2}; \quad R'(\Sigma_{1,2}) = \frac{R(z_{1,2})}{\cos\theta_{1,2}}, \quad (5)$$

where $\sigma$ is the surface tension, $R'(\Sigma_{1,2})$ is the curvature radius of the meniscus of the drop, $P_{1,2}$ are the pressures on different sides of the meniscus, $z_1$ and $z_2$ are the coordinates of the left and right ends of the drop, and $\theta_1$ and $\theta_2$ are the wetting (contact) angles for the left and right menisci [20].

For a moving drop, in the general case, the wetting angles of the positive and negative menisci are different. Figure 1 shows, as an example, the result of an experimental study of the hysteresis of the angles $\theta_+$ and $\theta_-$ of the positive and negative menisci for the case of an incomplete wetting in the water–paraffin system [19]. One can see that the wetting angles depend on the velocity of the meniscus motion relative to the wall. This curve has an ambiguity region at zero velocity of meniscus motion $V = 0$ (the so-called wetting angle hysteresis). In the case of $V \neq 0$, the wetting angle is uniquely related to the velocity of motion and, at a certain velocity value, flattens out reaching constant values $\theta_+^*$ and $\theta_-^*$ for the positive and negative menisci, respectively. The values of $\theta_+^*$ and $\theta_-^*$ are determined by both the sign and the velocity of the meniscus motion. For simplicity, we assume that the wetting angle rapidly reaches its limiting value (this idealization corresponds to a $Z$ characteristic of the hysteresis curve). The expressions for $\theta_1$ and $\theta_2$ are determined as follows:

$$\begin{aligned}\cos\theta_1 &= \cos\theta_+^* + 1(V_1)(\cos\theta_-^* - \cos\theta_+^*)\\ \cos\theta_2 &= \cos\theta_-^* + 1(V_2)(\cos\theta_+^* - \cos\theta_-^*),\end{aligned} \quad (6)$$

where $\theta_+^*$ and $\theta_-^*$ are empirical constants and $V_1$ and $V_2$ are the velocities of the menisci.

The mass of the drop $m$ is expressed as

$$m = \rho\int_{z_1}^{z_2}\pi R^2(z)dz. \quad (7)$$

For the purpose of investigation, it is convenient to represent the continuity equations (2) in an integral form. Integrating Eq. (2) with respect to $r$ from the center of the capillary to its wall with allowance for boundary conditions (4), we obtain the equality

$$Q(t) = 2\pi\rho\int_0^{R(z)} r v_z dr. \quad (8)$$

Here, the flux $Q(t)$ plays the role of an auxiliary function.

Assume that the characteristic longitudinal dimension of the drop, $L$, far exceeds its transverse dimension $R_0$ (the characteristic thickness of the capillary): $L \gg R_0$. In this case, the liquid motion in the drop can be considered as quasi-parallel (except for the small regions on the order of the capillary thickness near the ends of the drop). From the first equation of set (3), it follows that, to an accuracy of about $R_0/L$, the pressure is independent of $r$. With all of the aforementioned assumptions, the set of equations (3) is reduced to a single equation for the longitudinal velocity:

$$\begin{aligned}&\frac{\partial v_z}{\partial t} + v_z\frac{\partial v_z}{\partial z} + v_r\frac{\partial v_z}{\partial r} + \frac{1}{\rho}\frac{\partial p}{\partial z}\\ &\quad = \nu\frac{1}{r}\frac{\partial}{\partial r}\left(r\frac{\partial v_z}{\partial r}\right) - \ddot{\xi} + G.\end{aligned} \quad (9)$$

In combination with continuity equations (8) and boundary conditions (4)–(6), it forms a set of equations that will be solved below.

The problem contains two characteristic time scales: the time of vorticity diffusion within a distance of about the characteristic capillary radius $R_0$, which is determined as $\tau_d = R_0^2/\nu$, and the period of vibrations of the channel walls $T = 2\pi/\omega$. The problem can be simplified in two limiting cases: in the case of high-frequency vibrations, when $\varepsilon = \tau_d/T = R_0^2\omega/\nu \gg 1$, and in the case of low-frequency vibrations, when $\varepsilon = \tau_d/T \ll 1$. The first of these inequalities describes the case of a skin layer that is thin compared to the capillary thickness, and the second inequality, the case of a thick skin layer.

## THE MOTION OF DROPS UNDER HIGH-FREQUENCY VIBRATIONS

Let $\varepsilon \gg 1$. We solve the problem without considering the viscosity. In this case, the hydrodynamic equations have a solution in which $v_z$ does not depend

on $r$. Equations (8) and (9) are simplified and take the form

$$\frac{\partial v_z}{\partial t} + v_z\frac{\partial v_z}{\partial z} + \frac{1}{\rho}\frac{\partial p}{\partial z} = -\ddot{\xi} + G, \tag{10}$$

$$Q(t) = \pi\rho v_z R^2(z). \tag{11}$$

Integrating Eq. (10) over $z$ within the drop with allowance for Eqs. (5) and (11), we obtain

$$\frac{1}{\pi\rho}\frac{dQ}{dt}\int_{z_1}^{z_2}\frac{dz'}{R^2(z')} + \frac{1}{2}\frac{Q^2}{(\pi\rho)^2}\left(\frac{1}{R^4(z_2)} - \frac{1}{R^4(z_1)}\right) + \frac{2\sigma}{\rho}\left(\frac{\cos\theta_2}{R(z_2)} - \frac{\cos\theta_1}{R(z_1)}\right) = (G - \ddot{\xi})(z_2 - z_1) + \frac{P_2 - P_1}{\rho}. \tag{12}$$

We take into account that, by definition, we have

$$v_z\big|_{z = z_{1,2}} = \frac{dz_{1,2}}{dt}.$$

Then, with allowance for Eq. (11), we obtain

$$\frac{dz_1}{dt} = \frac{Q(t)}{\pi\rho R^2(z_1)}; \quad \frac{dz_2}{dt} = \frac{Q(t)}{\pi\rho R^2(z_2)}. \tag{13}$$

Equations (12) and (13) form a closed set of three equations in three unknowns: $z_1$, $z_2$, and $Q$. If the length of the drop $l = z_2 - z_1$ is small compared to the characteristic scale of the capillary radius variation (a short drop), this set is reduced to a single equation. Indeed, we denote $z = (z_1 + z_2)/2$; then,

$$R(z_{1,2}) = R(z) \mp \frac{dR}{dz}l/2 + \ldots$$

and, after some transformations, we obtain

$$\frac{d^2z}{dt^2} + \frac{2\sigma}{R(z)\rho l}(\cos\theta_2 - \cos\theta_1) + \frac{\sigma}{2\rho}(\cos\theta_1 + \cos\theta_2)\frac{d}{dz}\left(\frac{1}{R(z)}\right) = G - \ddot{\xi} + \frac{P_2 - P_1}{\rho l}. \tag{14}$$

For $\theta_1$ and $\theta_2$, we use Eq. (6), where $v_1 = v_2 = dz/dt$. The condition of mass conservation for the drop is expressed as

$$\pi\rho R^2(z)l(z) = m,$$

and Eq. (14) takes the form

$$\frac{d^2z}{dt^2} + \frac{2\pi}{m}\sigma R(z)(\cos\theta_+^* - \cos\theta_-^*)\operatorname{sgn}\left(\frac{dz}{dt}\right) + \frac{\sigma}{2\rho}(\cos\theta_+^* + \cos\theta_-^*)\frac{d}{dz}\left(\frac{1}{R(z)}\right) = G - \ddot{\xi} + \frac{P_2 - P_1}{\rho l}. \tag{15}$$

Let us introduce the dimensionless drop displacements, time, and capillary radius:

$$\eta = \frac{z}{R_0}; \quad \tau = \omega t; \quad \hat{R}(\eta) = \frac{R(z)}{R_0}. \tag{16}$$

In terms of the new variables, Eq. (15) takes the form

$$\frac{d^2\eta}{d\tau^2} + b\hat{R}(\eta)\operatorname{sgn}\left(\frac{d\eta}{d\tau}\right) + \gamma\frac{d}{d\eta}\left(\frac{1}{\hat{R}(\eta)}\right) = g + a\cos\tau. \tag{17}$$

The parameters involved in this equation are determined by the formulas

$$a = \frac{\xi_0}{R_0}; \quad b = \frac{2\pi\sigma}{m\omega^2}(\cos\theta_+^* - \cos\theta_-^*);$$

$$\gamma = \frac{\sigma}{2R_0^3\rho\omega^2}(\cos\theta_+^* + \cos\theta_-^*); \tag{18}$$

$$g = \frac{G}{\omega^2 R_0} + \frac{P_2 - P_1}{\rho l\omega^2 R_0}.$$

Parameter $a$ determines the intensity of the vibration action on the capillary, $b$ and $\gamma$ determine the capillary forces, and $g$, the static (gravitational) force.

Now, we proceed to considering the drop motion in capillaries with cross sections of different shapes. Depending on the frequency of vibration action, the regime realized in the capillary will be either nonviscous, when the drop displacement is described by the second-order equation (17), or viscous (this case will be analyzed below). The boundary between the regimes is determined by the value of $\varepsilon$. Let us estimate the parameters of the capillaries and the fluid that are typical of oil pools. For example, for the radius of the capillary cross section $R_0 = 10^{-3}$ cm, the threshold frequency is $f_0 = \dfrac{\nu}{2\pi R_0^2} \sim 10^3$ Hz (the kinematic viscosity of the fluid is $\nu = 10^{-2}$ cm$^2$/s). For such a capillary, the nonviscous approximation is applicable for vibration frequencies higher than 1 kHz, i.e., for high-frequency sound and ultrasound, and the Stokes approximation is applicable for $f \ll 10^3$ Hz, i.e., for low-frequency sound.

### *A Cylindrical Capillary (Nonviscous Approximation)*

Assume that the capillary radius $R(z) = r_0$ is independent of $z$. Then, in Eq. (17), $\hat{R} = 1$, and this equation takes the form

$$\frac{d^2\eta}{d\tau^2} + b\operatorname{sgn}\left(\frac{d\eta}{d\tau}\right) = g + a\cos\tau. \tag{19}$$

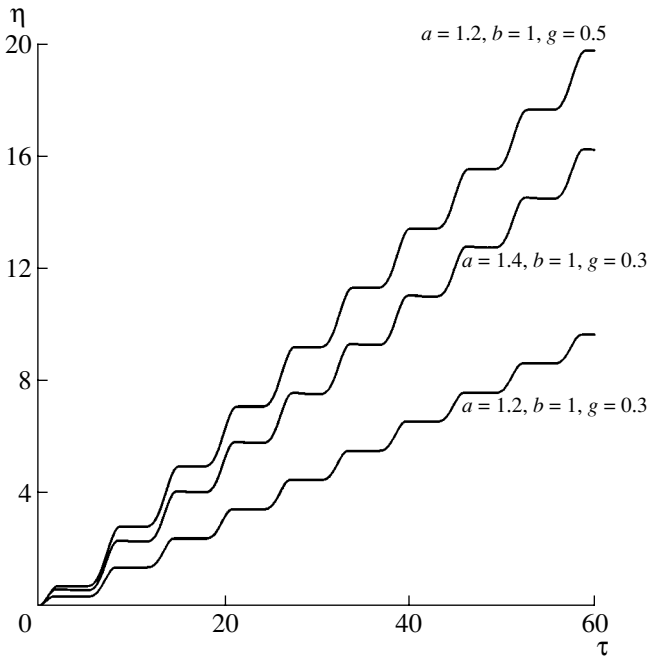


**Fig. 2.** Drop displacement versus time in a cylindrical capillary.

We first consider the simplest case of $g = 0$. In this case, Eq. (19) has the form

$$\frac{d^2\eta}{d\tau^2} = a\cos\tau - b\,\mathrm{sgn}\frac{d\eta}{d\tau}.$$

The second term on the right-hand side of this equation represents the static friction force. Although this force acts only when the drop moves, to set the drop in motion, it is necessary that the amplitude of the vibration action becomes greater than *b.* In view of the expressions for *a* and *b*, we easily derive the condition for the threshold amplitude of vibration:

$$\xi_0 > \frac{\sigma(\cos\theta_+^* - \cos\theta_-^*)}{\rho l R_0 \omega^2}. \quad (20)$$

Evidently, for high-frequency vibrations, much smaller vibration amplitudes are necessary to initiate the drop motion, as compared to the case of low-frequency vibrations. When the vibration is sufficiently intense ($a > b$), the drop behavior within one period of vibration is as follows: first, the drop is immobile, then it is shifted in one direction, remains for some time in the extreme position, and then returns to its initial position. On the whole, it is clear that, in the absence of the static force, the vibration does not cause any systematic displacement of the drop.

In the presence of a mean external force acting on the drop ($g \neq 0$), the condition for the beginning of the drop motion is less stringent:

$$|g| + |a| > |b|.$$

It can be represented in the form

$$\xi_0 > \frac{1}{\omega^2}\left(\frac{\sigma}{\rho l R}(\cos\theta_+^* - \cos\theta_-^*) - G - \frac{P_2 - P_1}{\rho l}\right). \quad (21)$$

One can assume that the fluid motion in an oil pool terminates when the external pressure in capillaries is counterbalanced by the capillary pressure, i.e., when the right-hand side of Eq. (21) is close to zero. Under these conditions, for the drop motion to begin, a relatively small vibration amplitude is required even at low frequencies. Since low-frequency sound is characterized by weak attenuation, one can expect an increase in the permeability of oil pool structures as a result of the beginning of the drop motion at large distances (several hundreds of meters) from the source of low-frequency acoustic vibrations.

Figure 2 shows the displacement of a drop with time for different combinations of the values of three parameters: *a*, *b*, and *g*. One can see that, all other conditions being the same, the displacement of the drop is greater when the vibration amplitude is higher (compare the lower and intermediate plots) or the static force is stronger (compare the intermediate and upper plots).

In the case of $g = b$, it is easy to obtain the solution to equation (19) of the drop motion in a cylindrical capillary. The solution has the form

$$\eta = a(\tau - \sin\tau).$$

The corresponding average velocity of drop displacement is

$$\langle v\rangle = R_0\omega\left\langle\frac{d\eta}{d\tau}\right\rangle = \xi_0\omega. \quad (22)$$

Let us analyze the dependence of the dimensionless parameters *a*, *b*, and *g* on the drop length *l*. According to Eq. (18), the quantity *a* does not depend on *l*, whereas *b* is inversely proportional to *l*. If we assume that the static force *G* is the nonzero projection of the gravity force and that $P_1 = P_2$, the quantity *g*, as the quantity *a*, will be independent of *l*. Thus, the only parameter that depends on the drop length is the parameter *b*, which determines the beginning of the drop motion at a given *a*. This means that, at a given level of vibration action, long drops will begin moving earlier and stop later than short drops. Since the parameter *g* is the same for different drops, the average velocity of long drops will be higher than that of short drops. The effect of coalescence of two different drops under the effect of vibration was studied in [27].

### *A Conic Capillary*

Let us consider a conic capillary. In this case, we have

$$\hat{R} = 1 + \delta\eta,$$

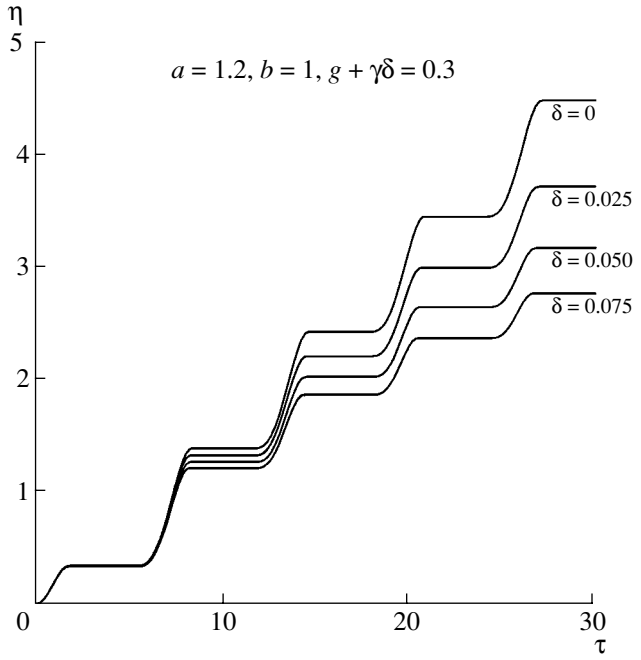


**Fig. 3.** Drop displacement versus time in a conic capillary (the static force is directed toward the vertex).

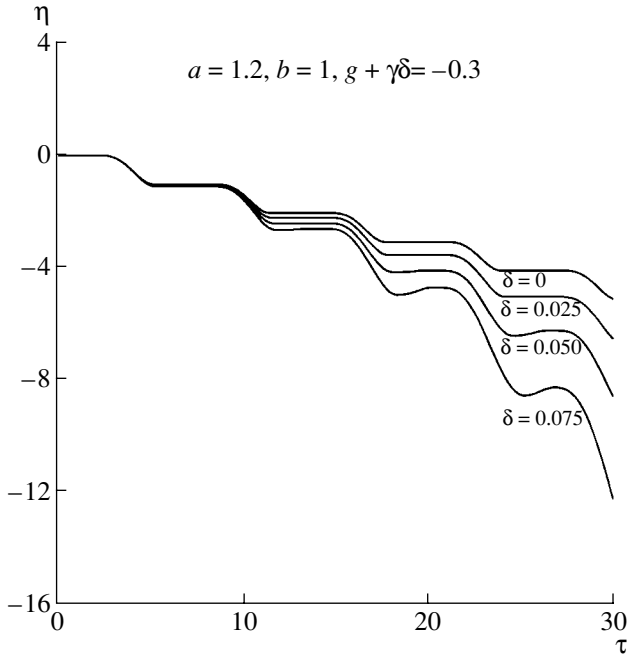


**Fig. 4.** Drop displacement versus time in a conic capillary (the static force is directed from the vertex).

where $\delta = \tan 2\alpha$ and $\alpha$ is the cone angle. We assume that $\delta \ll 1$. In this case, Eq. (17) takes the form

$$\frac{d^2\eta}{d\tau^2} + b(1 + \delta\eta)\operatorname{sgn}\left(\frac{d\eta}{d\tau}\right) = g + \gamma\delta + a\cos\tau. \quad (23)$$

One can see that, in the presence of conicity, an additional average force arises in addition to $g$. The direction of this force is determined by the sign of the cone angle $\alpha$. It may enhance the effect of the mean pressure gradient or reduce it. Under actual conditions, one can expect that the conicity of capillaries will reduce the threshold amplitudes of vibrations that are necessary to begin the filling of the capillaries in which the additional force is added to the external pressure gradient.

Figures 3 and 4 represent the numerical study of the time dependence of the drop displacement in a conic capillary for different values of the cone parameter $\delta$. The values of $a$ and $b$ were taken to be constant, and for the static force two values were used: 0.3 (Fig. 3) and –0.3 (Fig. 4). This corresponds to the direction of the force action along the axis from the cone vertex and to the vertex, respectively. In the first case, the drop leaves the narrow part of the capillary faster when the cone parameter is smaller. In the second case, the drop approaches the vertex faster when the cone parameter is greater.

### *A Capillary with a Periodically Varying Radius*

One can assume that, under actual conditions, the radius of the capillary cross section may nonmonotonically depend on the longitudinal coordinate. Let us consider the effects that arise in this case. As a model, we consider a capillary whose radius varies according the harmonic law

$$\hat{R} = 1 + \alpha\sin kz. \quad (24)$$

We assume that the wavelength is $\frac{2\pi}{k} \gg R_0$; i.e., the radius of the capillary varies slowly. For this capillary, Eq. (17) takes the form

$$\frac{d^2\eta}{d\tau^2} + b(1 + \alpha\sin\mu\eta)\operatorname{sgn}\frac{d\eta}{d\tau} - \frac{\gamma\mu\alpha\cos\mu\eta}{(1 + \alpha\sin\mu\eta)^2} = g + a\cos\tau. \quad (25)$$

One would expect that, in the absence of external action, the drops will tend to occupy the positions corresponding to stable equilibrium. For a capillary with a cross section varying according to Eq. (24), these positions are determined by the condition

$$kz = \pm\frac{\pi}{2} + 2\pi n.$$

In the case when the constant external pressure gradient $g$ is nonzero, the drop will stay in this position as long as

$$g < b(1 + \alpha);$$

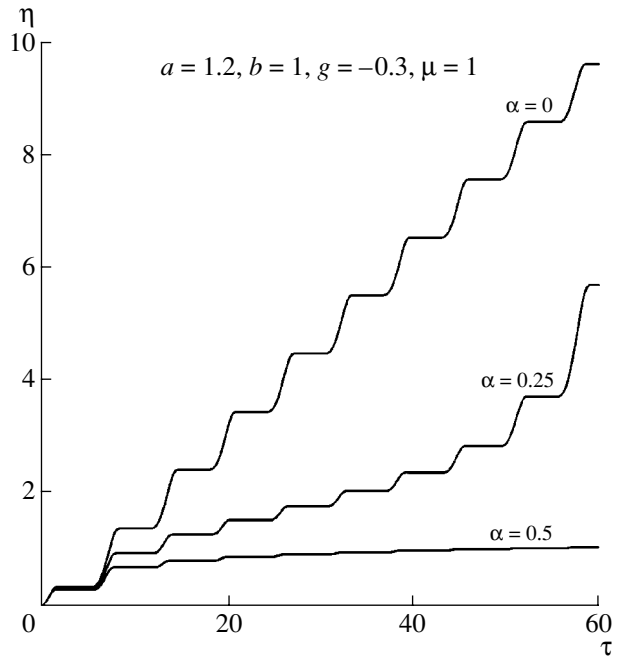


**Fig. 5.** Drop displacement versus time in a capillary with a sine-shaped boundary.

i.e., $g = b(1 + \alpha)$ corresponds to the threshold value for the beginning of motion. If a vibration is superimposed, the drop begins moving.

Figure 5 shows the time dependence of the drop displacement in a capillary with sine-shaped walls for different values of the corrugation parameter. One can see that, as this parameter increases, the motion of the drop in the direction of the static force becomes progressively less effective (the initial position of the drop corresponds to $z = 0$). At $\alpha = 0.5$, starting from a certain instant, the drop ceases moving.

## THE MOTION OF DROPS UNDER LOW-FREQUENCY VIBRATIONS

Consider now the case of vibrations with a sufficiently low frequency, so that the time of vorticity diffusion within a distance of about the characteristic capillary radius is much smaller than the vibration period; i.e., $\varepsilon = \dfrac{R_0^2\omega}{\nu} \ll 1$. This condition means the smallness of the Reynolds number for the flow under study.

We seek the solution in the form of a series expansion in the small parameter ε:

$$v_z = v_0 + v_1 + \ldots$$

$$p = p_0 + p_1 + \ldots,$$

where $v_1/v_0 \sim \varepsilon$ and $p_1/p_0 \sim \varepsilon$.

*Equation of the Inertialess Approximation*

In the zeroth order in ε, Eq. (9) takes the form

$$\frac{1}{\rho}\frac{\partial p_0}{\partial z} = \nu\frac{\partial}{\partial r}\left(\frac{1}{r}\frac{\partial(rv_0)}{\partial r}\right) - \ddot{\xi} + G.$$

Its integration with allowance for boundary condition (4) yields the expression for the velocity of the liquid:

$$v_0 = \frac{1}{4\mu}\left(\frac{\partial p_0}{\partial z} + \rho(\ddot{\xi} - G)\right)(r^2 - R^2).$$

Substituting this expression into Eq. (8), we determine the relation between the liquid flow and the pressure gradient:

$$\frac{\partial p_0}{\partial z} = -\frac{8\nu}{\pi}\frac{Q_0}{R^4} - \rho(\ddot{\xi} - G). \tag{26}$$

Here, $Q_0$ is the mass flux to zeroth order in ε. Then, we integrate Eq. (26) with respect to $z$ with allowance for the dynamic boundary condition (5). As a result, we obtain

$$-2\sigma\left(\frac{\cos\theta_2}{R(z_2)} - \frac{\cos\theta_1}{R(z_1)}\right) = \frac{4\nu Q_0(t)}{\pi}\int_{z_1}^{z_2}\frac{dz}{R^4(z)} + \rho\left((\ddot{\xi} - G)(z_2 - z_1) - \frac{P_2 - P_1}{\rho}\right). \tag{27}$$

This equation corresponds to Eq. (12).

Since the transverse dimension of the drop is much smaller than the longitudinal dimension, the velocities of the displacements of the drop ends can be determined as the average velocities in the corresponding cross sections:

$$\frac{1}{S}\int_0^S v_0 ds = \frac{Q(t)}{\pi\rho R^2(z)}.$$

As a result, we obtain a set of equations for determining the positions of the ends of the drop:

$$\frac{dz_1}{dt} = \frac{Q_0(t)}{\pi R^2(z_1)}; \quad \frac{dz_2}{dt} = \frac{Q_0(t)}{\pi R^2(z_2)}. \tag{28}$$

The set of equations (27), (28) is analogous to set (13), (14) obtained in the absence of viscosity.

By analogy with Eq. (14), in the short drop approximation, from Eqs. (27) and (28) we obtain one equation for determining the coordinates of the center of mass of the drop. This equation has the form

$$\frac{dz}{dt} = \frac{\pi\sigma}{2\nu m}R^3(z)(\cos\theta_+^* - \cos\theta_-^*)\,\mathrm{sgn}\left(\frac{dz}{dt}\right)$$

$$+\frac{\sigma R^2(z)}{4\nu\rho}(\cos\theta_+^* + \cos\theta_-^*)\frac{d}{dz}\left(\frac{1}{R(z)}\right) \qquad (29)$$

$$+\frac{1}{4\nu}R^2(z)\left(\ddot{\xi} - G - \frac{P_2 - P_1}{\rho l}\right).$$

Unlike Eq. (14), Eq. (29) is a first-order equation. This reflects the fact that, in the Stokes approximation, the inertial force acting in the noninertial frame of reference is counterbalanced by the viscous force, which is proportional to the velocity of the drop motion.

Changing to dimensionless variables (16), we represent Eq. (29) in the form

$$\frac{d\eta}{d\tau} = b\hat{R}^3(\eta)\,\mathrm{sgn}\left(\frac{d\eta}{d\tau}\right) + \gamma\hat{R}^2(\eta)\frac{d}{d\eta}\left(\frac{1}{\hat{R}(\eta)}\right)$$

$$-a\hat{R}^2(\eta)\cos\tau - g\hat{R}^2(\eta),$$

$$b = \frac{\pi\sigma}{2\nu m\omega}R_0^2(\cos\theta_+^* - \cos\theta_-^*), \qquad (30)$$

$$\gamma = \frac{\sigma}{4\nu\rho\omega R_0}(\cos\theta_+^* + \cos\theta_-^*);$$

$$a = R_0\omega\sigma/4\nu; \quad g = \frac{R_0}{4\nu\omega}\left(G + \frac{P_2 - P_1}{l\rho}\right).$$

*A Cylindrical Capillary (Viscous Approximation)*

For a cylindrical capillary, Eq. (30) takes the form

$$\frac{d\eta}{d\tau} = b\,\mathrm{sgn}\left(\frac{d\eta}{d\tau}\right) - g - a\cos\tau. \qquad (31)$$

Again, we first consider the simplest case of $g = 0$. For the drop to begin moving (i.e., for $dv/d\tau$ to become nonzero), the normalized vibration amplitude $a$ should exceed $b$. This leads to the necessity of satisfying condition (20), which requires much smaller vibration amplitudes for high-frequency vibrations, as compared to low-frequency ones. In the presence of an external force acting on the drop ($g \neq 0$), the condition for the beginning of the drop displacement is less stringent (condition (21)).

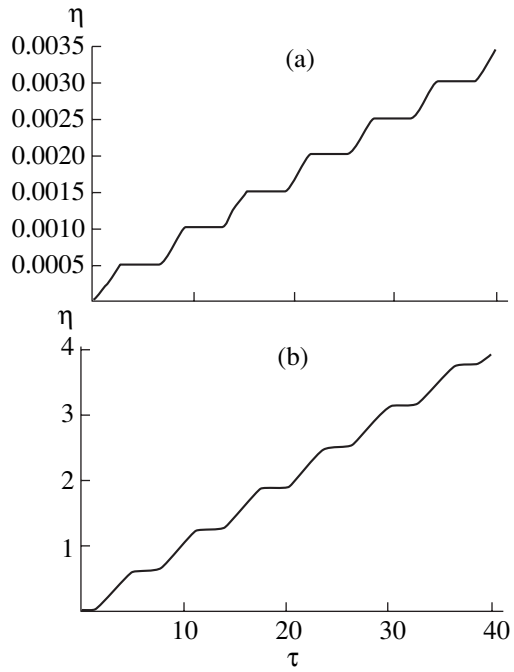


**Fig. 6.** Drop coordinate versus time in a cylindrical capillary: calculations with the (a) viscous and (b) nonviscous models. The parameters of the liquid and the capillary dimensions are as follows: $\xi_0 = 10^{-4}$ cm, $\omega = 10^2$ s$^{-1}$, $R_0 = 10^{-3}$ cm, $l = 10^{-1}$ cm, $\sigma/\rho = 74$ cm$^3$/s$^2$, $\nu = 10^{-2}$ cm$^2$/s, and $b = g$.

To estimate the average velocities of the drop displacement in the capillary, we numerically solve Eqs. (19) and (31) with the following values of the parameters: $\omega = 10^2$ s$^{-1}$; $R_0 = 10^{-3}$ cm, $\nu = 10^{-2}$ cm$^2$/s, $\sigma/\rho = 74$ cm$^3$/s$^2$, $l = 10^{-1}$ cm, and $\xi_0 = 10^{-4}$ cm. We assume that $G + \frac{P_2 - P_1}{l\rho} = \frac{\sigma}{\rho l R}(\cos\theta_+^* - \cos\theta_-^*)$, i.e., $b = g$. Let us compare the results of calculating the drop motion in a cylindrical capillary near the displacement threshold in the frameworks of the nonviscous and viscous models. The results are shown in Figs. 6a and 6b, respectively.

One can see that the character of the drop motion calculated with the given parameters is qualitatively the same for the two models. However, considerable quantitative differences are observed. From Fig. 6a, one can see that the average velocity of the drop displacement is $10^{-2}$ cm/s. In the Stokes model, the average velocity is about $10^{-4}$ cm/s. Thus, viscosity noticeably reduces the average velocity of the drop motion. At the same time, the nonviscous model allows one to analyze all the main features of the drop behavior in a vibrating capillary.

In the case of $g = b$, one can easily find the solution to the equations of the drop motion in a cylindrical capillary.

In the Stokes approximation, Eq. (31) can be represented in the form

$$\frac{d\eta}{d\tau} = a\begin{cases}\sin\tau & \text{for } \sin\tau > 0\\ 0 & \text{for } \sin\tau < 0.\end{cases}$$

This yields the average velocity

$$\langle v\rangle = \frac{a}{\pi}R_0\omega = \frac{R_0^2\omega^2\xi_0}{4\pi\nu}. \quad (32)$$

Now, let the external force be not compensated for by the dry friction force; i.e., $g \neq b$. We assume that the external force is sufficiently strong, so that the condition $g > a$ is always satisfied (this corresponds to a sufficiently small amplitude of acoustic vibrations). In this case, Eq. (32) can be represented as

$$\frac{d\eta}{d\tau} = \begin{cases}0, \text{ when } b-g \geq a\\ \left\{a\sin\tau - (b-g) \text{ in the interval } \arcsin\dfrac{b-g}{a} < \tau < \pi\right.\\ \left. -\arcsin\dfrac{b-g}{a}\right\},\\ 0, \text{ for } \tau \text{ outside the interval when } |b-g| < a\\ a\sin\tau - (b-g) \text{ when } b-g \leq -a.\end{cases} \quad (33)$$

Averaging Eq. (33) over the vibration period, we obtain the expression for the average velocity of the drop motion:

$$\left\langle\frac{d\eta}{d\tau}\right\rangle = \begin{cases}0 \text{ for } b-g \geq a\\ \dfrac{\sqrt{a^2-(b-g)^2}}{\pi} - \dfrac{b-g}{2},\\ +\dfrac{b-g}{\pi}\arcsin\dfrac{b-g}{a} \text{ for } |b-g| < a,\\ g-b \text{ for } b-g \leq -a.\end{cases} \quad (34)$$

Within the vibration period, the drop displacement does not exceed $|g - b|$. If the characteristic scale of the capillary radius variation $\eta$ is great compared to $|g - b|$, i.e., $\eta_0 \gg |g - b|$, expression (34) can be used to analyze the drop motion in a capillary with a varying cross section.

### *The Motion of a Drop in a Quasi-Cylindrical Capillary (Viscous Limit)*

Under actual conditions, capillaries have complex shapes; in particular, bends and deviations from axial symmetry are typical. Here, we ignore such complex distortions of capillary shapes and consider the influence of the simplest distortion: the dependence of the radius of the capillary cross section on the longitudinal coordinate. In this case, the motion of a drop is described by Eq. (31), and, for the average displacement velocity, we can use expression (34) with the following substitutions:

$$b \longrightarrow b\hat{R}^3(\eta),$$
$$a \longrightarrow a\hat{R}^2(\eta), \quad (35)$$
$$g \longrightarrow g\hat{R}^2(\eta) + \gamma\frac{d\hat{R}}{d\eta}.$$

The expression for the effective average force acting on the drop involves the additional term $\gamma\dfrac{d\hat{R}}{d\eta}$ caused by the conicity of the capillary. This force represents the effect of pulling the drops of wetting liquids into narrower capillaries and pushing the drops of nonwetting liquids out toward the expanded capillary portions. This means that, in a capillary of varying cross section, the stable equilibrium position of a wetting liquid drop corresponds to the minimum capillary radius while the equilibrium position of a nonwetting drop corresponds to the maximum radius. A drop remains near the equilibrium position in the presence of an average pressure gradient if the condition

$$b\hat{R}^3(\eta_e) > g\hat{R}^2(\eta_e)$$

is satisfied, where $\eta_e$ is the coordinate of the corresponding extremum.

Let us assume that a drop is near an extremum and the external force corresponds to the displacement threshold. If $\hat{R}(\eta_e) = 1$ (which is preset by the choice of normalization), we have $b = g$. The motion of drops

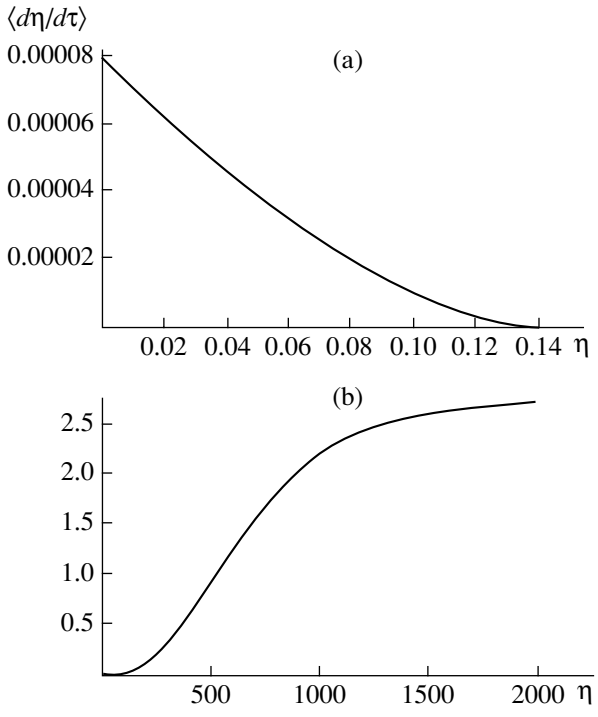


**Fig. 7.** Average velocity of the drop displacement versus coordinate in a capillary with the cross section radius varying as $\hat{R}(\eta) = \frac{1 + q/\cosh^2(\eta/\eta_0)}{1 + q}$, where $q = 0.5$ and $\eta_0 = 1000$: (a) a wetting drop and (b) a nonwetting drop.

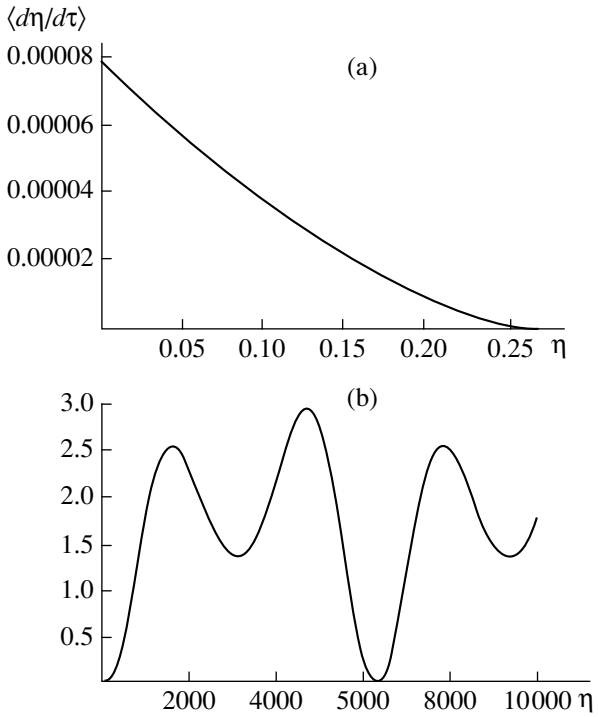


**Fig. 8.** Average velocity of the drop displacement versus coordinate in a capillary with the cross section radius varying as $\hat{R}(\eta) = \frac{1 + q\cos(\eta/\eta_0)}{1 + q}$, where $q = 0.5$ and $\eta_0 = 1000$: (a) a wetting drop and (b) a nonwetting drop.

under vibration is different for wetting and nonwetting liquids. In the case of a wetting drop, $\hat{R}(\eta)$ near its minimum is an ascending function of $\eta$. According to Eqs. (34) and (35), the motion of the drop occurs until the following condition is satisfied:

$$(\hat{R}(\eta) - 1) - \frac{\gamma \frac{d\hat{R}}{d\eta}}{R^2(\eta)} \geq a. \qquad (36)$$

If, near the equilibrium position, condition (36) fails, the drop begins moving. As the distance from the point of equilibrium increases (the drop deviates from the point of minimum $\hat{R}(\eta)$), condition (36) begins to be satisfied and the drop stops.

In the case of a nonwetting drop, its equilibrium position is near the maximum of $\hat{R}(\eta)$. If the drop is displaced from the equilibrium position under the effect of vibration, condition (36) is not satisfied for smaller values of $\hat{R}(\eta)$ and, hence, the drop will continue moving away from the point of equilibrium. Thus, by applying a vibration, it is possible to eliminate a trapped drop of a nonwetting liquid, whereas a drop of a wetting liquid will remain near its stable equilibrium position. Examples of such drop motion are shown in Fig. 7 for a capillary with a monotonically varying radius

$$\hat{R}(\eta) = \frac{1 + q/\cosh^2(\eta/\eta_0)}{1 + q}, \quad q = 0.5, \quad \eta_0 = 1000$$

and in Fig. 8 for a capillary with a periodically varying radius

$$\hat{R}(\eta) = \frac{1 + q\cos(\eta/\eta_0)}{1 + q}, \quad q = 0.5, \quad \eta_0 = 1000.$$

From Figs. 7a and 8a, one can see that the vibration pushes a wetting drop out of the narrowed portions of the capillary; the drop then stops at some distance from its initial position. In the case of a nonwetting drop (Figs. 7b and 8b), under vibration it may infinitely move away from the equilibrium position. This motion will be of a monotonic character in a capillary with a monotonically varying cross section and of oscillating character in a capillary with a periodically varying cross section.

## CONCLUSIONS

Thus, we analyzed the motion of individual drops in a porous medium under the effect of a low-frequency

vibration. We assumed that the liquid wets the walls of the pores. At the same time, it is well known that oil is a nonwetting liquid for most rock types. Therefore, it is necessary to separately specify the conditions under which the mechanism considered above can lead to an increase in the velocity of the oil flow. Three situations are possible:

(i) Oil is mixed with water, and a suspension flows through the capillaries. Unlike pure oil, the suspension wets the walls of the capillaries. Thus, the vibration action stimulates the flow of the suspension drops trapped in the pores;

(ii) Water drops fill part of the pore volume and prevent the flow of the oil phase (or suspension). In this case, the vibration action cleans the pores;

(iii) If the seam pressure decreases, heavy oil fractions deposit on the walls of the capillaries and the surface of the collector becomes wetted.

The mechanism of drop motion under vibration that was considered above is of a threshold character (the sound wave amplitude should exceed a certain critical value). At first glance, one may expect that this mechanism manifests itself only under an intense acoustic action on the oil pool. (For intrawell acoustic radiators, the region of effective action is the near-well zone.) However, it should be noted that, in our model, the threshold level proves to be lower the larger (longer) the drop is. Large drops may begin their motion even at a relatively low vibration level at which smaller drops are yet unable to move. If small drops occur in the way of moving large drops, they will be gradually absorbed by large drops and carried along by them. Hence, a moving drop will grow and its velocity will increase. This scenario of mass transfer seems to be quite realistic. In our opinion, this is the most efficient physical mechanism that allows one to explain the observed intensification of the oil flow under a low-frequency vibration action on an oil pool.

## ACKNOWLEDGMENTS

This work was supported by the Russian Foundation for Basic Research (project nos. 02-02-17089, 03-05-64993, and NSh-1637.2003.2); it was carried out under the program of the Presidium of the Russian Academy of Sciences “Mathematical Methods in Nonlinear Dynamics.”

## REFERENCES

1. O. L. Kuznetsov, É. M. Simkin, and G. V. Chilingar, *Physical Grounds of Acoustic Effects on Oil and Gas Deposits* (Mir, Moscow, 2001) [in Russian].
2. V. P. Dyblenko, R. N. Kamalov, I. A. Sharifullin, and I. A. Tufanov, *Production Increase and Revival of Wells by Vibrowave Action* (Nedra, Moscow, 2000) [in Russian].
3. M. L. Surguchev, O. L. Kuznetsov, and É. M. Simkin, *Hydrodynamic, Acoustic, and Thermal Cyclic Actions on Oil Pools* (Nedra, Moscow, 1975) [in Russian].
4. G. G. Vakhitov and É. M. Simkin, *Application of Physical Fields for Oil Extraction from Oil Pools* (Nedra, Moscow, 1985) [in Russian].
5. I. A. Beresnev and P. A. Johnson, Geophysics **59** (6), 1000 (1994).
6. Yu. I. Gorbachev, O. L. Kuznetsov, R. S. Rafikov, and A. A. Pechkov, Geofizika, No. 4, 5 (1998).
7. M. A. Biot, J. Acoust. Soc. Am. **28**, 168 (1956).
8. M. A. Biot, J. Acoust. Soc. Am. **34**, 1254 (1962).
9. A. V. Nikolaev, in *Seismic Vibration Action on an Oil Pool* (Izd. Obshch. Inst. Fiz. Zemli, Moscow, 1993), pp. 7–13 [in Russian].
10. A. N. Ryashentsev and N. P. Ryashentsev, in *Acoustics of Inhomogeneous Media*, Vol. 112: *Dynamics of Continua* (Izd. Inst. Geofiz. Sibir. Otdel. RAN, Novosibirsk, 1997) [in Russian].
11. B. N. Bogolyubov, V. N. Lobanov, L. S. Brilliant, *et al.*, Neft. Khoz., No. 9, 80 (2000).
12. L. S. Brilliant, B. N. Bogolyubov, I. V. Tsykin, *et al.*, Neft. Khoz., No. 9, 86 (2000).
13. *Nonlinear Acoustics at the Begining of the 21st Century*, Ed. by O. V. Rudenko and O. A. Sapozhnikov (Mosk. Gos. Univ., Moscow, 2002), Vol. 2, pp. 1169–1264.
14. V. N. Nikolaevskiĭ, Dokl. Akad. Nauk SSSR **307** (3), 570 (1989).
15. V. N. Nikolaevskiĭ, Izv. Akad. Nauk, Mekh. Zhidk. Gaza, No. 5, 110 (1992).
16. A. L. Krylov, V. N. Nikolaevskiĭ, and G. A. Él’, Dokl. Akad. Nauk SSSR **318** (6), 1340 (1991).
17. A. A. Abrashkin and M. A. Raevskiĭ, Izv. Akad. Nauk, Ser. Fiz. **66** (12), 1730 (2002).
18. V. S. Averbakh, S. N. Vlasov, and Yu. M. Zaslavskiĭ, Radiofizika **43** (2), 155 (2000).
19. B. V. Zheleznyĭ, Dokl. Akad. Nauk SSSR **207** (3), 647 (1972).
20. A. W. Adamson, *The Physical Chemistry of Surfaces* (Wiley, New York, 1982; Mir, Moscow, 1979).
21. P.-G. de Gennes, Usp. Fiz. Nauk **151** (4), 619 (1987).
22. I. I. Blekhman, *Vibration Mechanics* (Nauka, Moscow, 1994) [in Russian].
23. V. S. Averbakh, S. N. Vlasov, and Yu. M. Zaslavskiĭ, in *Proceedings of X Session of Russian Acoustical Society, Moscow, 2000* (Moscow, 2000), p. 91.
24. Yu. M. Zaslavskiĭ, Akust. Zh. **48**, 56 (2002) [Acoust. Phys. **48**, 50 (2002)].
25. H. K. Moffatt, J. Fluid Mech. **18**, 1 (1964).
26. O. V. Voinov, Dokl. Akad. Nauk **343** (5), 627 (1995).
27. A. A. Abrashkin, V. S. Averbakh, and S. N. Vlasov, Izv. Vyssh. Uchebn. Zaved., Radiofiz. **46**, 235 (2003).

*Translated by E. Golyamina*

*Acoustical Physics, Vol. 51, Suppl. 1, 2005, pp. S122–S130. Translated from Akusticheskiĭ Zhurnal, Vol. 51, Suppl., 2005, pp. 140–149.*


# Geoacoustic Monitoring as a Means for Investigating the State of the Lithosphere and for Earthquake Forecasting

**A. V. Nikolaev*, A. S. Belyakov*, V. S. Lavrov*, and A. D. Zhigalin****

** Schmidt Joint Institute of Physics of the Earth, Russian Academy of Sciences, ul. Bol'shaya Gruzinskaya 10, Moscow, 123995 Russia*

*e-mail: nikavs@comail.ru*

*** Institute of Geoecology, Russian Academy of Sciences, Moscow, Russia*

Received October 7, 2004

**Abstract**—The existing approach to mitigating earthquakes and other catastrophic geological processes stipulates the determination of the site, time, and strength of the anticipated event. However, the disastrous earthquakes of recent years clearly demonstrate that even the most advanced systems of monitoring and warning for seismic and other geological hazards are insufficiently effective. However, by adding the monitoring of the Earth's acoustic field to the existing systems of observation of so-called precursors and by restricting the observations to a certain region (thus excluding the task of determining the site), it is possible to provide a more adequate forecast of earthquakes and other catastrophic geological processes in this particular region.


Numerous victims, huge destruction, and vast economic losses caused by seismic impacts and other catastrophic geological processes are determined to a considerable extent by incorrect selection of the site, design, and technology of construction of houses and public and technical buildings. It is impossible to avoid destruction of buildings constructed at sites with "poor" geology unless the structure possesses a sufficient strength reserve. Nor it is possible to eliminate the loss of life if a disastrous earthquake takes them unawares and if unexpected secondary catastrophes arise on ecologically hazardous objects. Therefore, the main task of hazard forecasting is to provide a reliable warning concerning the exact place and time of a disastrous earthquake or other geological cataclysm. This is a very complicated problem; however, it can be simplified if we exclude the task of determining the site of a possible event by *a priori* selecting a certain region and carrying out long-term observations of the seismic and geological situation in this region. Then, the main effort can be concentrated on determining the time of the onset of a catastrophic development in this region. The corresponding algorithm can be realized by organizing the appropriate observation system, for example, within the boundaries of a big city, industrial region, or a local object of special importance—that is, immediately in the vicinity of a site where a catastrophic geological event has to be forecasted and mitigated.

In order to solve the problem of determining the onset of a catastrophic event (e.g., an earthquake) in such a preselected region, it is necessary to choose a set of reliable and informative prognostic signs and adapt the observation systems to monitoring the corresponding characteristics. In the case of observations in large cities, one important prognostic sign is underground acoustic noise, which can be monitored in deep wells, on the Earth's surface, and at the sea and ocean bottom. The acoustic noise, representing stochastic oscillations in a frequency range from 16 to $10^4$ Hz, has a mechanical nature, appears in the Earth's solid crust at random sites and at arbitrary moments of time, and generates pulses of acoustic radiation (acoustic emission). The frequent weak pulses merge into continuous noise, from which narrow (1/3 octave wide) bands of the underground hum (UH) can be separated with the aid of analog filters. Such signals are usually very difficult to detect because of their extremely low intensity. However, the recent progress in measuring equipment offers a possibility to measure the previously inaccessible UH parameters.

Acoustic signals have been successfully used for a long time in seismic prospecting and in nondestructive testing of materials and engineering structures. Instruments employed in seismic prospecting are capable of measuring the displacement velocities in a range of frequencies below 200 Hz, while the nondestructive testing involves the measurement of accelerations in the ultrasonic frequency range (above 20 kHz). However, the measurements of the UH in these frequency intervals are not very effective. From the standpoint of solving the main problem posed above—to monitor UH for seismic hazard warning—the most informative spectral interval is the initial part of the acoustic frequency range, which extends from 16 to 2500 Hz. Higher UH frequencies are still difficult to observe, because the amplitudes of displacements in a longitudinal acoustic wave are extremely small—on the order of femtome-

ters (~$10^{-15}$ m)—and rapidly decrease with increasing frequency.

The detailed analysis of the UH and the detection of its small variations have become possible owing to the creation of geophones based on magnetoelastic acoustic crystal sensors. Using these devices, it is possible to measure acoustic signals within 1/3 octave band at 30, 160, 500, and 1200 Hz. A special feature of such geophones is a steep frequency characteristic, which provides for an increase in the sensitivity with the frequency (60 dB per decade). This behavior is analogous to the variation of the UH level. For this reason, the new devices are capable of reliably detecting the character of variation of even very low UH in the indicated frequency bands. In an automated regime, geophones measure the amplitudes of the particle velocity acceleration [m/s$^3$] (averaged over a minute time interval) in a longitudinal acoustic wave of the UH. In the course of processing, the data are averaged and compared with a model process parameter—the calculated absolute rate of variation of the relative volume strain of the Earth's crust under the action of the solar tide component, which is used as an estimate for the energy of the solar tide-induced deformation component and as an energy model of the process modulating or initiating the UH, which is separated from the total seismoacoustic noise.

As is known, the earthquakes are generated by mechanical displacements in the Earth's crust. Such processes take place continuously, and their intensities and amplitude–frequency characteristics depend on the properties of the geophysical medium and the character of variation of its stressed state. Tectonic processes lead to the formation of large zones with significantly anisotropic concentrations of internal stresses, which results in the fracture of blocks in the Earth's crust that is accompanied by the liberation of mechanical energy in the form of earthquakes. Precursors and the onset of this fracture manifest themselves as changes in the intensity of acoustic emission and can be revealed from the related UH characteristics.

It should be noted that the difference between the acoustic emission and the UH is rather conventional. The concept of acoustic emission is somewhat broader and refers to the entire spectrum of acoustic energy radiated in the pulse form, whereas the UH implies a conditionally separated average amplitude of harmonic components of the acoustic emission in narrow bands of the initial part (from 16 to 2500 Hz) of the acoustic frequency range. Both the acoustic emission and the UH are highly sensitive to changes in the stressed state of the Earth's crust, which accompany the geodynamic processes. Assuming that the interactions involving the rock pressure and the long-term compression of platforms moving in the Earth's crust are accompanied by energy accumulation, we may conclude that a nonuniform unloading and the resulting anisotropic stress distribution in the foci prepare the conditions for a possible earthquake. These assumptions do not contradict the well-known Gilbert–Reid model. Therefore, we may ascertain that the liberation of acoustic energy must take place primarily in the course of an anisotropic change (decrease) of stresses in the Earth's crust. This is confirmed by the results of numerous experimental investigations of a variable acoustic emission in the regions with different characters of seismic activity, such as central Russia, Belarus, California, North Caucasus, and Kamchatka.

The underground sound always accompanies and, probably, precedes all seismic and large exogenous geological events. A description of the underground sound observations made in Italy at the end of the 19th century was reproduced by G.H. Darwin in his book "Tides and Kindred Phenomena in the Solar System." In particular, he wrote: "one de Rossi of Rome arranged a microphone in a lone place 20 m deep under the ground. The next night, he heard sounds that, in his opinion, belonged to 'natural telluric phenomena.' De Rossi described these sounds as 'noises, shots fired separately and a volley, metal clangs, and ring bells.' All these sounds were absolutely incomprehensible and mixed to reach maximum strength in irregular time intervals. These noises sometimes became intolerably loud, in particular, once in the midnight, half an hour before a significant earthquake." This is historical evidence, but more than a century had to pass before investigations of the underground noise became possible.

Nowadays, some witnesses of earthquakes also recall strange acoustic sensations related to such events. For example, intense vibrations of the Earth's surface in the acoustic range were observed in the village of Garm in Tajikistan two hours before the disastrous 1950 earthquake. Based on such evidence, Prof. Rikitaka from the Institute for Earthquake Investigations (Tokyo) suggested that the monitoring of vibrations in the acoustic frequency range might be useful for earthquake forecasting. Witnesses also recalled "auditory impressions" from catastrophic giant landslides, sinks, and the like.

The natural underground sound appears as a sequence of various acoustic signals differing in rhythm, level, and frequency, rather than a monotonous noise. These sounds mostly resemble knocking, thunder, grinding, hum, rustle, and so on. Therefore, it is not surprising that separating components from this chaos which are capable of notifying us about a forthcoming seismic or other hazardous event is a very difficult task. Apparently, this direction of research did not find practical development, because the relevant acoustic signals mostly fall outside the sensitivity range of instruments traditionally used in seismic and engineering investigations. For this very reason, the existing prognostic testing grounds are still not equipped with instrumentation for underground sound detection and recording.

Changes in the parameters of acoustic emission and UH, as a kind of response to seismic events, tides, exogenous processes, and technogeneous impacts on the

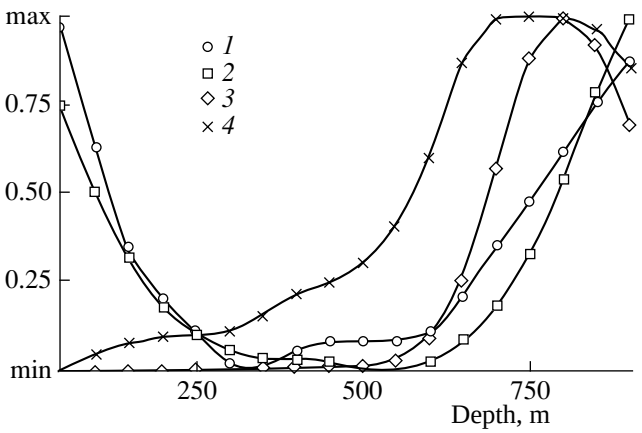


**Fig. 1.** Noise amplitude measured in 1/3 octave bands at (*1*) 33, (*2*) 160, (*3*) 580, and (*4*) 1250 Hz in a 930-m-deep well (Pervomaĭskaya, Belarus Republic).

lithosphere, offer an important characteristic of the geophysical medium. Recording and analysis of variations in the UH provide the possibility to detect the very onset in the development of rock degradation, which is a precursor of catastrophic earthquakes, rock shocks, and other exogenous geological processes. Profound UH investigation, including the online monitoring and analysis of such signals by qualified specialists in acoustics and seismology, offers essentially a new approach to short-term hazard warning for earthquakes and other geological events. Using electric signal records carrying information abut the underground sound, it is possible to build unconventional monitoring systems—for example, utilizing multimedia computer networks to image the volume sound—and to employ the broad possibilities offered by the Web as a communication means for involving large number of experts in the evaluation of the current seismic and geological situation.

The phenomenon of variation of the acoustic emission parameters can be used as an identification sign in geophysical (in particular, seismic) monitoring of the upper part of the Earth's crust at sites most susceptible to tectonic and exogenous processes, as well as at sites of high technogenic activity, such as a megapolis, big city, or a large industrial object.

Until recently, most specialists in geophysics and seismology believed (and many still do) that the acoustic signal of natural origin detected in the upper part of the Earth's crust consists for the most part of an exogenous noise. Indeed, for a long period of time, this delusion did not meet any convincing objections. In order to evaluate the ratio of exogenous and endogenous noise in the upper part of the Earth's crust, a large series of experimental investigations was carried out and a number of relations concerning the laws of acoustic emission have been established, including those accompanying the mechanical action upon the lithosphere in the upper part of the Earth's crust. The experiments performed in various regions, including the tests with high-power vibrators, provided new data indicative of the intensification of endogenous high-frequency noise (i.e., of the natural acoustic emission) in response to strong action upon the lithosphere. The results of these investigations showed that geoacoustic monitoring can be used as a means for the investigation of the state of lithosphere, the evaluation of the level of technogenic action, and the earthquake forecast.

The experimental measurements of acoustic signals in a 930-m-deep well drilled in a homogeneous sedimentary rock, which were performed in 1995 on the territory of Belarus at a site remote from industrial noise sources, objectively confirmed the existence of a natural endogenous high-frequency noise. The variation of the amplitude of the underground acoustic signal in the frequency range from 33 to 1250 Hz was measured along the depth of the well at 50-m intervals. It was found that the noise level variations at 33 and 160 Hz were relatively small (not exceeding 3–4% of the minimum noise level). In the vicinity of 580 Hz, the deviations increased to 11%, and at 1250 Hz they exceeded 100%. The low frequency noise decreased with the depth, whereas the high-frequency noise was minimum at the surface and significantly increased on moving downward, especially at 1250 Hz (Fig. 1).

Similar data were obtained in the study of acoustic emission signals in a well at Petropavlovsk-Kamchatski. The measurements were performed at 30, 160, 560, and 1200 Hz over a range of depths down to 1035 m. By analogy with the results described above, the amplitude of low-frequency (30 and 160 Hz) components initially decreased with increasing depth, while the high-frequency (560 and 1200 Hz) components remained at a low level. This behavior was observed down to a depth of about 600 m. From this point downward, the acoustic signal intensity increased in the entire spectral range. The growth continued down to a depth of about 900 m and then decreased again.

An analysis of the results of experiments described above showed that the character of changes in the acoustic signal intensity with increasing depth had much in common at all sites where the measurements were carried out. This similarity was especially pronounced at sites where the geological medium was not subjected to significant technogenic action, which is additional evidence for the natural origin of the acoustic emission. In practically all cases, the noise level initially decreased and then increased with increasing depth. The noise measured at different sites varied in amplitude, but this behavior remained the same. The minimum noise level was virtually always observed at a depth of 250–500 m. This result indicates that the "exogenous" signal exhibits a decay with increasing depth, which is accompanied by the appearance and growth of an "endogenous" signal. Thus, acoustic sensors occurring at a depth in excess of 250–500 m are capable of detecting the acoustic emission (and the UH)

free of both technogenic and exogenous interference. In contrast, acoustic measurements at a relatively small depth can be used to assess the state of the lithosphere in its upper layers, which is especially important for monitoring disastrous technogenic and natural exogenic geological processes.

A good illustration of the seismoacoustic emission response to a technogenic action is offered by the results of experiments performed in spring 2002 on an oil field in Western Siberia. The experiments were aimed at assessing changes in the endogenous acoustic signal in the presence of surface vibrations. The geological section of the field mostly comprised clays, shingle, sandstone, and aleurolites with collector beds at a depth of 1650 and 1750 m. The acoustic emission measurements were performed in a 1780-m-deep well. The surface vibrations at a frequency varying from 10 to 33 Hz were generated by seismic sources of the SVS24/RS27 type, whose synchronous operation provided a vertical vibrational load of 20 ts. The results of these measurements confirmed that the internal acoustic vibrations could be initiated by an external vibrational action applied at the surface. As can be seen from the data presented in Fig. 2, the external mechanical action produced a severalfold increase in the natural seismoacoustic emission intensity at certain frequencies (11 and 22 Hz at a depth of 1650 m; 10 and 20 Hz at 1740 m).

By extrapolating the obtained experimental data, one may expect that a technogenic physical (mechanical) action upon a geological substrate in big cities, which is mediated by the fields of vibrations and natural and technogenic microseismic oscillations, is also capable of generating acoustic emission in the uppermost layers of the Earth's crust (i.e., in the geological medium). Taking into account the considerable inhomogeneity of the geological basis of big cities, which is related to large variations in the geoengineering, hydrogeological, and geocryological (for northern regions) conditions, we may expect that investigations into seismoacoustic emission will provide a basic knowledge for the understanding of the laws governing both endogenous and exogenous geological processes in such cities.

Variations of the acoustic emission can be also used as an identification sign in the monitoring of distant earthquakes. The results of experimental monitoring of surface technogenic noise performed at the Moscow Seismic Station by the Geophysics Service of the Russian Academy of Sciences showed that distant earthquakes influence the character of the acoustic emission. The aim of these experiments was to assess the ability to detect manifestations of endogenous and exogenous processes by monitoring the variations in the background microseismic vibrations. The success was provided by the possibility of detecting seismic waves propagating due to a distant earthquake.

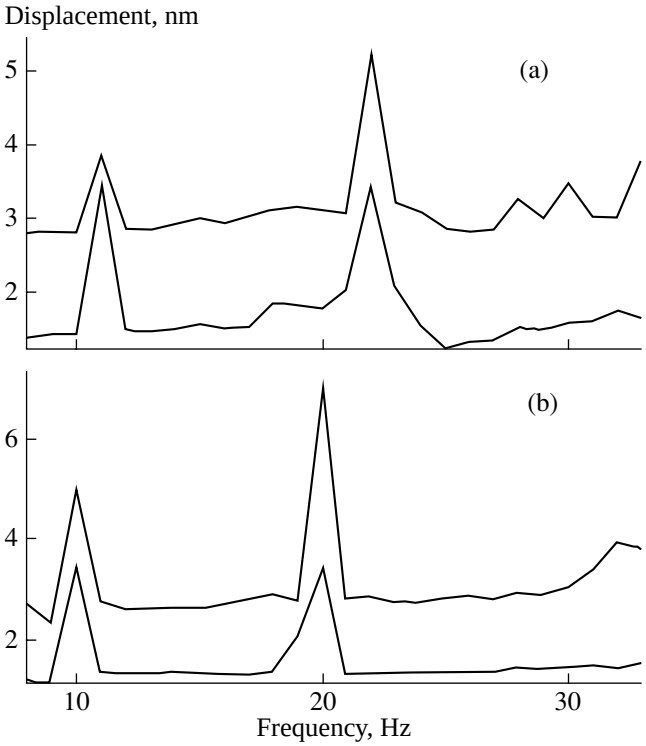


**Fig. 2.** Acoustic frequency characteristics measured at a depth of (a) 1650 and (b) 1750 m in a 1780-m-deep well (No. 3306, Gubkinskoe oil field) in response to the surface vibration action (10–33 Hz): signals in the vertical and horizontal directions.

Seismic waves caused by earthquakes can play the role of natural sources of underground acoustic vibrations (underground noise). This phenomenon is well known at the epicenter and in the adjacent regions. However, until very recently, there was some doubt concerning the possibility that such seismic waves may induce vibrations in the acoustic frequency range at a significant distance from the epicenter. The results of continuous monitoring of surface noise at the Moscow Seismic Station provided convincing evidence for this possibility.

The probability that a seismic wave from a strong distant earthquake will pass through a seismic station in a big city in the night (i.e., when technogenic noise is minimal) is very small. Nevertheless, such an event was recorded in the night on February 16–17, 1998. The instruments detected a seismic wave caused by an earthquake with a magnitude of 6.4–6.6 and a hypocenter situated at a depth of 18 km in the northern part of the Atlantic Ocean, which was accompanied by a "powerful" outburst of acoustic emission in the four 1/3-octave low-frequency bands (30, 160, 500, and 1000 Hz). The arriving wave induced vibrations of the base of the Moscow Seismic Station equipped with standard seismometers of the SKD type (measuring seismic waves in the traditional low-frequency range) and a MAG-3S device operating in the acoustic fre-

Characteristics of the seismic background signal and induced seismoacoustic emission

| Parameter | Frequency, Hz | | | |
|---|---|---|---|---|
| | 30 | 160 | 500 | 1000 |
| Seismic background signal, $10^{-6}$ m/s$^2$ | 15 | 6 | 0.6 | 0.05 |
| Seismoacoustic emission, $10^{-6}$ m/s$^2$ | 24 | 8 | 0.7 | 0.1 |
| Relative increase, % | 60 | 33 | 16 | 100 |

quency rage. The vibrations induced by the passage of the seismic wave continued for more than 30 min. The amplitude of vertical vibrations with a period of up to 20 s reached 40 μm at a maximum acceleration of $3.8 \times 10^{-6}$ m/s$^2$. The acceleration of horizontal vibrations was somewhat lower, not exceeding $3.0 \times 10^{-6}$ m/s$^2$ (north–south) and $2.0 \times 10^{-6}$ m/s$^2$ (west–east). The seismic low-frequency vibrations induced an increase in the acceleration of vertical high-frequency background vibrations, which exceeded the corresponding component in the initiating wave (see table).

An analysis of the results of these measurements showed that the induced acoustic emission process in all four low-frequency bands exhibited a 10–30 min lag behind the initiating seismic wave. The maximum lag (30 min) was observed at 30 Hz, and the minimum (10 min), at 1000 Hz (Fig. 3). Similar results were obtained on the Borovoe Seismic Station (Northern Kazakhstan), where the measurements were performed in a 5–25 Hz band with the aid of a laser strain meter arranged at a depth of 16 m in granite rock.

As can be seen from the results presented above, observations in the continuous regime provided a record of the acoustic emission induced by a remote earthquake and confirmed the possibility of acoustic emission generation by seismic waves propagating over large distances from the epicenter. The results obtained are interesting and even surprising, not only because the effect was detected at a very large epicentral distance and the measurements were performed on the territory of a megapolis (under conditions of strong technogenic activity). The main unusual result is that the acceleration of the induced vibrations in the geophysical medium exceeded that in the initiating seismic wave. Thus, the acoustic emission response to a seismic action is an important characteristic of a solid medium, which can be used as a criterion during a seismic monitoring of the upper part of the Earth's crust and in the assessment of the seismic and geological risk at a given site. Even separate cases of observations of such extraordinary events can provide grounds for the formulation of working hypotheses and planning the corresponding verification experiments.

The results of numerous, albeit short-term and rather fragmentary investigations of the seismoacoustic emission and the UH, which have been performed since 1985 at various sites with the aid of magnetoelastic acoustic geophones, were a base for undertaking long-term (possibly "secular") observations. Such experiments were initiated in 1999–2000 at Obninsk, Petropavlovsk-Kamchatski, and Kislovodsk. The latter two sites—Petropavlovsk-Kamchatski and Kislovodsk, at which the seismoacoustic monitoring is planned on a secular basis—are located in regions of elevated seismic activity, where catastrophic earthquakes are possible. This circumstance increases the probability of observing the phenomena preceding earthquakes on the background of regular UH variations, which can therefore serve as prognostic signs for short-term hazard warning. The results of observations at Obninsk will provide data on the UH variations under conditions of a relatively low seismic activity, which must help in elucidating the geophysical factors responsible for these variations.

In order to establish the relationship between acoustic noise variations and seismic activity, the vertical noise component has been continuously monitored since the end of 2000 in a 70-m-deep well near Kislovodsk (Northern Caucasus). Continuous monitoring of acoustic noise (vertical component) in a 90-m-deep well in Obninsk was started in September 2003. The characteristics of the latter well are analogous to those of the well in Kislovodsk. In the future, the acoustic noise databases simultaneously accumulated in the regions with low (Obninsk) and high (Kislovodsk) seismic activities will provide a basis for the comparative analysis, which will probably reveal synchronous variations of the seismoacoustic parameters of records made at the two sites with significant latitudinal spacing. These experiments are also expected to give information on the influence of remote technogenic activity on the seismicity. Figure 4 shows fragments of the acoustic emission records made in Kislovodsk during military operations in Iraq. A comparative analysis of the acoustic emission variations in the bands at 30 and 160 Hz in a period between March 17 and April 12, 2003, showed evidence for correlations between the UH variations and the intense bombardments that took place in the foothill regions of Iraq. These results lead to the conclusion that even remote technogenic mechanical action on the lithosphere can lead to an increase in the seismoacoustic emission.

However, the description and formalization of the signs of changes in the seismic and tectonic situation, as correlated with the underground sound variations, encounters considerable difficulties. The problem is additionally complicated by the still limited possibilities of recording and imaging of acoustic signals. Overcoming these difficulties would provide for the possibility of objectively detecting even very small changes in the character of the underground sound preceding earthquakes and other disastrous exogenous geological processes. On this basis, it will be possible to create an algorithm of recognition of the onset and development

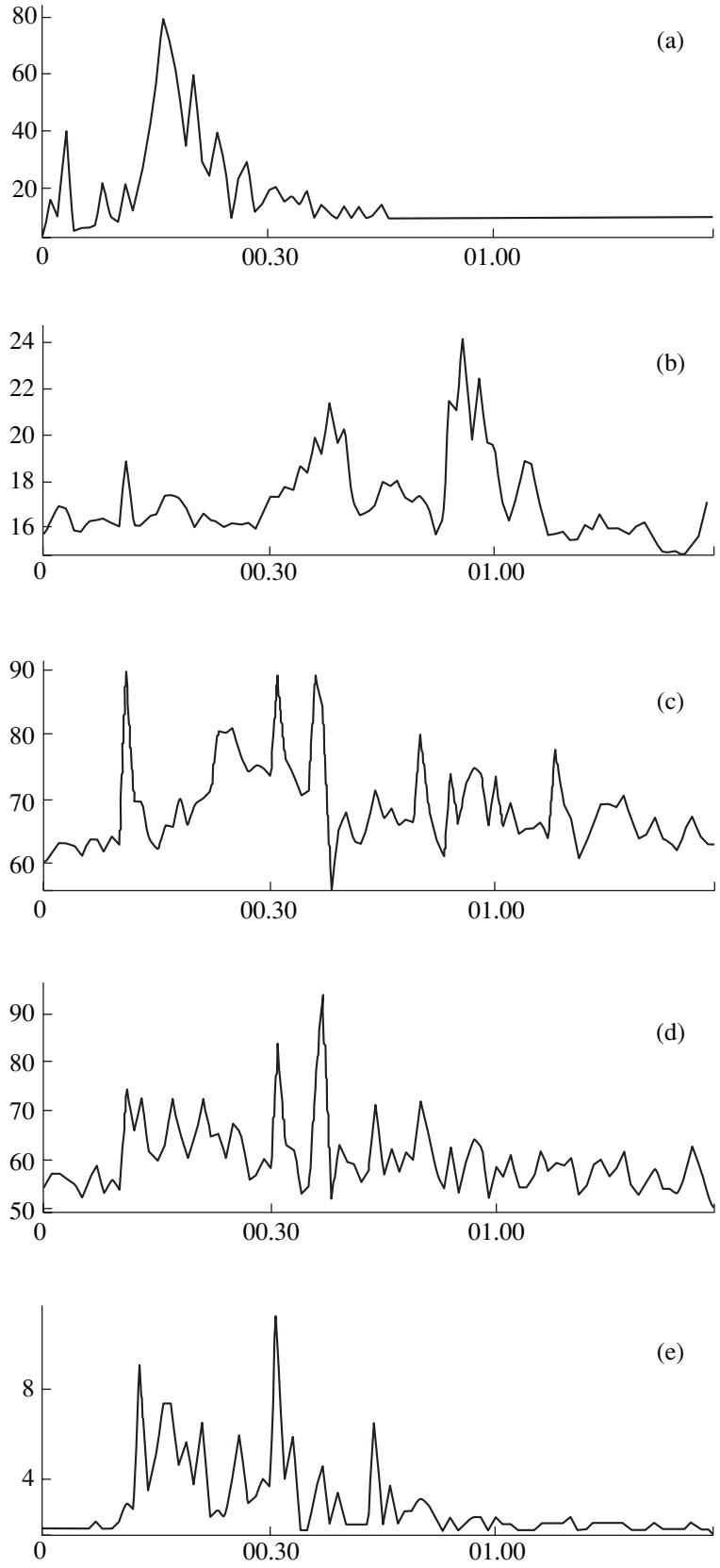


**Fig. 3.** Vertical components of (a) the seismic signal from a remote earthquake and (b–e) the induced seismoacoustic emissions in the 1/3 octave bands at 30, 160, 500, and 1000 Hz, respectively, measured at the Moscow Seismic Station (February 16–17 night, 1998).

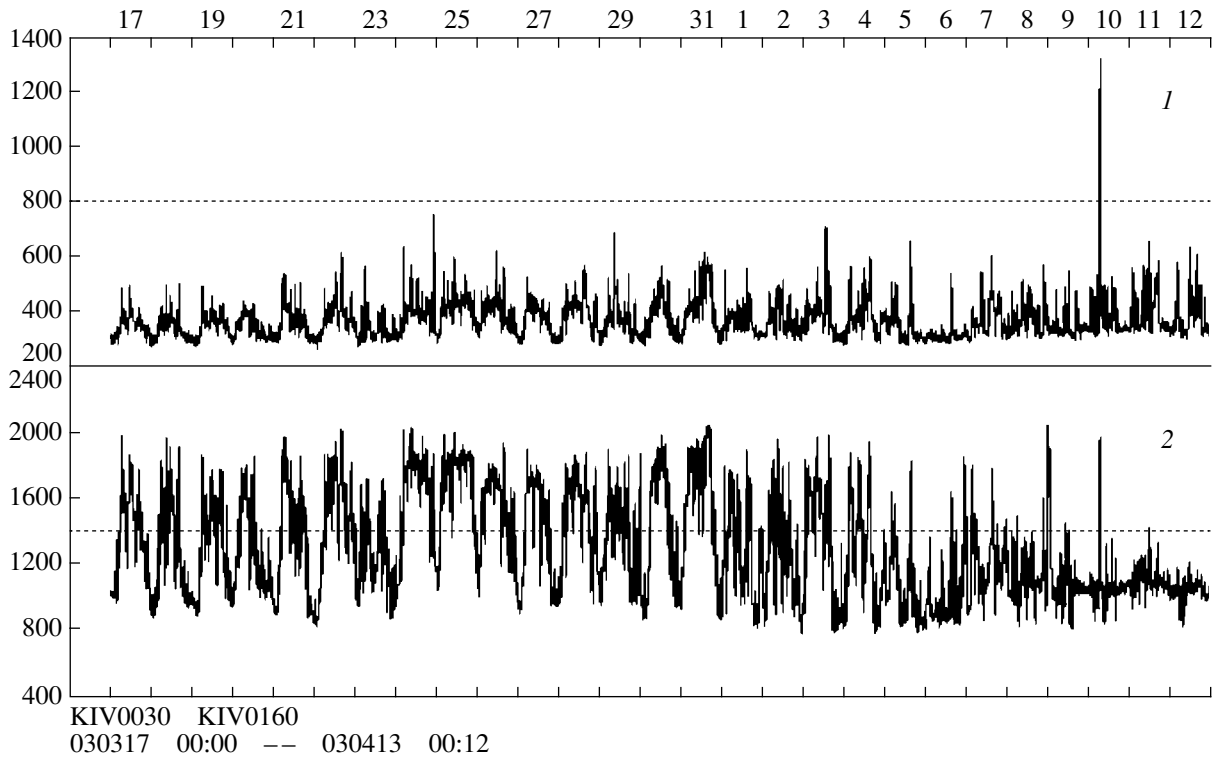


**Fig. 4.** Fragments of time series of the seismoacoustic emission measured in 1/3 octave bands at (*1*) 30 and (*2*) 160 Hz in a 70-m-deep well in Kislovodsk during military operations in Iraq.

of such critical events. In connection with this, we can only regret that UH investigations have not been properly developed for a long time and hope that modern professional equipment created for the detection, recording, processing, and display of acoustic signals (in particular, their spectra) in the online regime, in combination with novel geophones, will provide a means for objective recording of even the finest changes in the character of underground sound and make possible the extraction of objective information from these data. It should be noted that the aforementioned equipment is already available from many well-known companies but is still not used in practical seismology.

The phenomenon of significant temporal variation in the UH, which sometimes (but not always) follows tidal variations of gravity, has not been given an acceptable description for quite a long time. Such a description was obtained only when a model (image) of the initiating process was taken in the form of a plot of the time series of the absolute rate of variation of the relative volume strain of the Earth's crust caused by the solar component of tidal forces. The absolute rate of variation of the relative volume strain serves as a conditional measure of the liberated energy (work) spent for the deformation of the medium under the action of tidal forces. The proposed energy model is quite well correlated (correlation coefficient, $r = 0.6$–$0.8$) with the background variations of the underground sound in the upper part of the Earth's crust. It should be noted, however, that this correlation decreases and even vanishes for certain periods of time in the vicinity of the vernal and autumnal equinox days. Since the tidal strain is stable and can be calculated, the proposed energy model can be used for evaluating the related UH variations. On the background of these variations, all other possible changes can be recognized and identified. In particular, an increase in the UH intensity can be detected in some frequency bands, which is probably related to a change in the stressed state of a local volume of the Earth's crust immediately before earthquakes and other exogenous geological processes. The observed changes, representing direct consequences of disturbances in the Earth's crust, can be considered as reliable early forerunners of such disastrous events.

The continuous series of data provided by the results of acoustic monitoring in Obninsk and Petropavlovsk-Kamchatski confirmed the existence and allowed the evaluation of the relationship between the UH variations and the lunar and solar components of tidal strain in the vicinity of two characteristic points of the annual cycle—the vernal and autumnal equinox days.

Synchronous phase variation of the UH intensity and the energy model parameter before and after the equinox days cannot be related to any known exogenous process. Moreover, the observed 12-h phase shift excludes the possible influence of thermal stresses (whose extrema are related either to the diurnal maxi-

mum or to the nocturnal minimum of the Earth's surface temperature) and cannot change on the equinox days. The coefficient of correlation between the UH and the energy model parameters is 0.82 before the vernal equinox and 0.81 after this day, while decreasing to –0.13 on this day. A similar pattern is observed for the autumnal equinox day, whereby the correlation coefficient is 0.63 one month before the equinox, drops to 0.02 on the equinox day, and increases to 0.87 in one month after this day. Thus, the UH intensity variations at the end of March, the beginning of April, the end of September, and the beginning of October are not correlated with the energy model, while a high correlation with $r = 0.63–0.87$ is observed over all the remaining time of the year.

A comparative analysis of the results of the UH measurements in Obninsk and Petropavlovsk-Kamchatski to the energy model calculations revealed regular and stable (from the standpoint of a stochastic noise process) coincidences of the amplitude and phase. Depending on the site of measurements, these coincidences ($r = 0.6–0.8$) are observed in various frequency bands. This correlation is significantly improved for the results of observations at greater depths, especially in the high-frequency bands of the interval under consideration. An analysis of data in comparison with the energy evaluation of the lunar component of the tidal wave revealed no stable correlations (the average correlation coefficient was close to zero).

New experimental data obtained by seismoacoustic monitoring in Obninsk and Petropavlovsk-Kamchatski made it possible to check the adequacy of the proposed energy model to the observed UH variations. For this purpose, we used (i) a comparative and correlation analysis of the results of UH measurements in the vicinity of the vernal and autumnal equinox points and the results of model calculations, (ii) the equinox day test, and (iii) a comparative analysis of the periodograms constructed for the new data. The aforementioned similarity of the frequency spectra of the underground sound in the frequency band at 1250 Hz and the spectra of the solar tidal strain component (which appear much like the power spectra of electric circuits with active resistances) was also confirmed for the bands at 160 and 30 Hz. Then, it was natural to suggest that the work of the tidal wave, which is continuously spent for the deformation of the Earth's crust, is converted into thermal and acoustic energy. These energies must be proportional to the square of the strain rate (i.e., to the strain energy) rather than to the linear strain. However, there is no principal error in using the absolute value of the rate of variation of the relative volume strain of the model medium (instead of the energy) for the qualitative analysis of causal relations.

It should be noted that we failed to reveal a stable relationship between the UH amplitude and the lunar component of the tidal volume strain (whose amplitudes are on the average two times greater than those for the solar tidal strain), which has not yet been given an acceptable explanation. It is hoped that the continuously increasing volume of seismoacoustic data gained in Obninsk, Petropavlovsk-Kamchatski, and in the Northern Caucasus will help to remove this discrepancy and provide additional information necessary for improving and refining the proposed energy model and for formulating reliable prognostic criteria.

At the same time, the adequacy of the proposed energy model to the seismoacoustic process under consideration is reliably confirmed by the coincidence of the composition of predominating periods in the real spectra of the UH variations (measured in various frequency bands) and in the calculated energy of the solar component of the tidal-wave-induced straining. The main advantages of the proposed model are its simplicity and the clear sense. This model must be helpful in explaining some nonlinear stationary processes of energy supply, conversion, and dissipation in the Earth's crust. In particular, this energy is partly liberated in the form of "microscopic" earthquakes, which superimpose to form the underground sound. The same model can be used for developing a prognostic criterion for the earthquake forecast. On the background of the stationary UH variation process, which is close to the proposed model, it is possible to reveal and evaluate the anomalies preceding disastrous earthquakes.

Using the continuous and sufficiently long series of data on the UH amplitude variation obtained at the seismic stations in Obninsk and Petropavlovsk-Kamchatski, we have performed a mode detailed spectral analysis of the acoustic oscillations. This analysis revealed contrast differences in amplitudes of the main periods, 12 and 24 h. The main periods of the UH amplitude variations agree well with those in the proposed energy model, a difference not exceeding fractions of a percent. An analogous coincidence with the main periods was also found using the data obtained previously for a high-frequency band (1250 Hz) observed over a 30-day period in a 930-m-deep well in the Pripyat trough (Belarus). When the observation time was increased up to 3 months, the same main periods were revealed for the low-frequency bands (30 and 160 Hz). In addition, separate frequency analysis of the new 30-day intervals showed that the periodograms of data obtained in Obninsk and Petropavlovsk-Kamchatski immediately on the vernal and autumnal equinox days of 2000 significantly differ in amplitudes of the main periods from the analogous periodograms obtained in the subsequent periods of time.

According to the results of observations in Obninsk, the amplitudes of the diurnal and semidiurnal periods in the periodograms for the days close to the vernal equinox (March 15 to April 15) are 236 and 38 times lower, respectively, than those in the periodograms obtained in the next month (April 15 to May 15) and are 294 and 69 times lower, respectively, than those in the periodograms obtained in the following month (May 15 to

June 15). Analogous differences in the amplitudes are characteristic of the periodograms obtained using the data for September and October, 2000, in Petropavlovsk-Kamchatski. Indeed, the amplitudes of the diurnal and semidiurnal periods in the periodograms in September are 13.5 and 14.7 times lower, respectively, than in October. The amplitude of shorter periods after the equinox days also significantly increased: by a factor of 1.7 to 32 in Obninsk, and 6 to 55 in Petropavlovsk-Kamchatski. These significant variations in the amplitude composition of harmonics of the UH variations are evidence that these variations are caused by the solar tidal strain component rather than related to the thermal noise or some antropogenous factor. The antropogenous factors cannot vary as significantly within two months (from March to April and May) or even within one month (from September to October) as does the UH variation amplitude. The diurnal temperature gradients in these periods are also relatively small and cannot account for significant variations in the main UH harmonic amplitudes. Analogous changes are observed in periodograms calculated for the proposed energy model. Therefore, we may suggest that the UH arises from telluric processes and, hence, bears new, important independent information concerning changes in the stressed state of the Earth's crust. This information can and must be used for forecasting earthquakes and other disastrous exogenous geological processes.

A system of the seismoacoustic monitoring for a megapolis, a big city, or a special industrial object should be based on a measuring network including a series of geophones arranged in deep (deeper than 1000 m) wells. The maximum prognostic effect of the UH monitoring can be obtained in combination with alternative methods of hazard assessment for earthquakes and other disastrous exogenous geological processes. On the other hand, the use of the UH monitoring data in the general system of seismic and geoengineering monitoring will increase the reliability of currently developed algorithms of evaluation of the degree of seismic and other hazardous factors for the objects of protection. Therefore, the optimum monitoring scheme stipulates the creation of complex centers for forecasting earthquakes and other disastrous exogenous geological processes, which would ensure fast an effective organization of the necessary methodological and research works. An example is offered by the testing ground in Parkfield (California, USA), whose control center collects and analyses the whole body of seismic information about the surrounding region. This allows the epicenter to be determined and the shock intensity to be evaluated within three to five minutes after the earthquake onset.

Although no testing grounds like that in California have been created in Russia, there are many possibilities for rapidly organizing a deep-well monitoring system using acoustic detectors with the corresponding characteristics. The development of a UH monitoring system is currently in progress in Petropavlovsk-Kamchatski, which is the region of maximum seismic risk in Russia. This gives hope for a revival of the state forecast service on the new, advanced methodological and technical level, and for the organization, already in the nearest future, of a reliable system of early warning and hazard mitigation in cases of earthquakes and other disastrous exogenous geological processes.

*Translated by P. Pozdeev*

*Acoustical Physics, Vol. 51, Suppl. 1, 2005, pp. S131–S139. Translated from Akusticheskiĭ Zhurnal, Vol. 51, Suppl., 2005, pp. 150–159.*


# Nonlinear Seismics and the Acoustic Action on the Oil Recovery from an Oil Pool

**V. N. Nikolaevskiĭ* and G. S. Stepanova****

** Schmidt Joint Institute of Physics of the Earth, Russian Academy of Sciences, ul. Bol'shaya Gruzinskaya 10, Moscow, 123995 Russia*

*e-mail: viktor@ifz.ru*

*** Krylov Institute of Oil Research, Dmitrovskiĭ proezd 10, Moscow, 127422 Russia*

Received August 17, 2004

**Abstract**—At the first stage of seismic action, the attenuation of acoustic waves in real (porous, creviced) rocks is always related to the energy pumping to high-frequency (ultrasonic) modes, and only at the next stage are these waves converted into chaotic thermal oscillations, so that the entire phenomenon refers to a basic problem of nonlinear seismics. Several physical phenomena related to the excitation of ultrasound and the corresponding transformations of the wave spectrum (including the dry friction in contacts, the instability of viscoelastic oscillations, the seismic energy pumping to the rotational modes, and the resonance of gas bubbles in natural oil) are considered in relation to the development of vibroseismic methods of acting upon a producing oil pool. The results of experiments on the ultrasound-stimulated water displacement of natural (gas-saturated) oil from a porous medium are presented, in which the oil recovery reached up to 90%. © *2005 Pleiades Publishing, Inc.*

## INTRODUCTION

The vibroseismic method of residual oil withdrawal from a water-encroached oil pool was originally developed at the Schmidt Joint Institute of Physics of the Earth [1]. This method is based on selecting a frequency of the external acoustic action (typically within 6–20 Hz) capable of changing the oil–water balance in the running well production rate, predominantly toward increasing the oil yield. The observed effect is indicative of variations in the water and oil phase conductivities. In addition, the field tests also showed significant gas evolution, although variations in the average pressure level were rather insignificant. The two phenomena seem to be interrelated, and both are probably caused by the action of ultrasound. Although the acoustic wave energy in the course of the vibroseismic action is supplied to the oil pool predominantly with low-frequency modes, the final effect is related to the acoustic action and, hence, the operation of a commercial vibrator must be accompanied by the corresponding evolution of the wave spectrum. This circumstance requires the development of nonlinear mathematical models, while retaining the wave front propagation according to the linear elasticity theory.

The vibroseismic method finds increasing use in oil fields for the improvement of productivity. In applying this method, it is important to select the optimum frequency of the acoustic action. If the task is to provide for the acoustic cleaning of the bottom-hole zone (e.g., removal of the skin zone [2]), it is recommended to use ultrasonic frequencies. In contrast, the optimum working frequency for a heavy vibrator operating at the free surface of a pool area [1, 3] is much lower and usually falls within 10–20 Hz. In the case of an immersed radiator operating at the well bottom, preferred frequencies are on the order of 200 Hz [4]. In each particular case, the optimum frequency should be adjusted *in situ* [5]. Practical experience showed that the vibroseismic method provides for an increase in the oil yield in the total production of water-encroached pool regions.

An increase in the oil yield is possible, in particular, when the seismic waves reaching an oil pool induce ultrasonic oscillations with a wavelength comparable to the average oil drop size [3]. Indeed, strains in such a wave are realized only as a result of the relative displacement of the edges of microcracks or collector grains, which (according to the laws of dry friction) are generating ultrasound. Another important factor is that ultrasound stimulates the gas evolution from natural oil, in particular, by increasing the oil saturation pressure [6]. The appearance of a large amount of gas in the pool favors an increase in the total pore pressure.

In a water-encroached oil pool, the evolved microscopic gas bubbles are concentrated at the interface between water and oil drops, which leads to an increase in the mobility of oil drops in the water flow. In a fresh oil pool, the gas bubbles predominantly stick to the solid walls or pores, which results in a short-term increase in the oil yield [7]. However, the subsequent growth of bubbles and their coalescence reduce the oil phase conductivity, while a long-term depletion of the reservoir is additionally accompanied by an increase in the oil viscosity. Therefore, it is necessary to keep the gas as long as possible in the form of microscopic bubbles with the aid of surfactants (including the natural ones) [8].

1063-7710/05/51S1-S0131$26.00 

The above considerations show the importance of the laboratory investigations into the properties of oil–water flows under the action of ultrasound. Such experiments elucidate the nature of events taking place in an oil pool under the dynamic action in the course of oil withdrawal. Below, we will summarize the main results of the physical modeling of the process of ultrasound-stimulated water displacement of oil.

## BASIC CONCEPTS

As is well known [9], wave energy is effectively transferred into soils at low frequencies on the order of 20–30 Hz. This can be related both to the stratification of the surface layers and to the existence of dominant resonance frequencies in sands and clays [10, 11]. On the other hand, according to elasticity theory, the stratification resonances of a geological section occur in the region of 100–400 Hz [12], and the waves propagating in an oil pool (as in a waveguide, which is softer than the surrounding medium) must fall in the same frequency interval. This implies that, in selecting the working frequency, it is necessary to take into account the position of the radiator (vibrator).

The experiments with wet sand on a seashore [10, 11, 13] showed that an acoustic source generated two waves in this medium: fast and slow. The fast wave had a higher frequency and a velocity of ~2 km/s, which corresponded to a "frozen" state of the medium. However, this wave could not be unambiguously interpreted as the first Frenkel–Biot wave, since the sand was only partly saturated with water.

The main part of the strain energy was carried by the slow wave propagating at ~200 m/s, whose spectrum gradually transformed to a certain dominant frequency component (~25 Hz), and it is this component that propagates over large distances. The slow wave spectrum also contains high-frequency noise (~1 kHz), which can be explained as being due to dry friction at rough contacts between grains or crack edges. We identify the slow wave (which is the only wave observed at long distances) with the second Frenkel–Biot wave [10, 13, 14]. This wave corresponds to developed deformations of the porous matrix and is observed in a system of pores filled with air at a low pressure. Thus, the presence of a dominant frequency in the wave spectrum may serve as additional evidence (besides the low velocity) of the characteristic low-frequency wave of the second type. Since the deformations in real geological media necessarily involve relative displacements at the contacts between structural fragments, they are always accompanied by the generation of high-frequency oscillations. It was found that the dominant frequency corresponds to that of the acoustic emission from the same sand. An external acoustic action upon the sand at the dominant frequency leads to degradation of the initial structure, whereby water-saturated sand exhibits liquefaction. For comparison, the dominant frequency of gravel is on the order of 10 Hz, while that of clay is about ~40 Hz.

It was established that, during the operation of a heavy vibrator at a selected low frequency in the region of an oil pool [1], deep layers were "filled" with high-frequency noise. This noise was added to the characteristic noise of liquid flows accompanying the oil recovery, where the latter noise was probably related to the presence of gas bubbles in natural oil. Note that the oil pools are always "noisy," in contrast to water pools where the gas content is extremely low [15].

The presence of gases is a very important factor for the propagation of waves in rocks saturated with liquids. The first fraction of gas saturation is always represented by bubbles. The presence of gas bubbles dramatically changes the situation for high-frequency modes. Indeed, the propagation of a wave of the second type involves the deformation of the porous matrix and, hence, the modification of accompanying liquid flows in the system of pores. However, in the presence of compressed gas bubbles, such flows (absorbing the wave energy due to viscosity) are no longer necessary. Under conditions of the gas bubble resonance, the second wave acquires [16] the resonance frequency of these bubbles and, hence, has a higher velocity. On the contrary, the velocity of the first wave decreases as a result of an increase in the effective compressibility of the liquid medium, and this wave exhibits stronger attenuation [16]. The results of model experiments [17] showed that the seismic waves propagated at the second characteristic wave velocity (~200 m/s) at frequencies below the resonance, whereas, at higher frequencies, they propagated at the first characteristic wave velocity (~1500 m/s).

Another source of high-frequency noise can be related to the dry friction, which is mathematically equivalent [18] to the action of an oscillator. Richard and Detournay [19] proposed a bidirectional oscillator model describing intermittent slippage, in which the relation between the normal and tangential stresses on the friction surface corresponded to the limiting cycles of high-frequency noise depending on the velocity of particle displacements in the incident wave. It is also known that perturbations introduced by a source of the Van der Pol type (as well as of some other types) give rise to a chaotic noise smearing the spectra of acoustic signals [20]. These considerations agree with the aforementioned experiments. As for the relationship between the normal and tangential stresses, this hypothesis is necessary to explain the fact that the dissipation coefficient is proportional to the wave frequency due to the dry friction [11] at a dilatant displacement of contacting hard particles.

## GENERALIZED VISCOELASTIC MODEL

It should be noted that the size of sand grains is too small to explain the low dominant wave frequency in terms of their natural frequencies. It is more reasonable to attribute the observed effect to a resonance viscoelas-

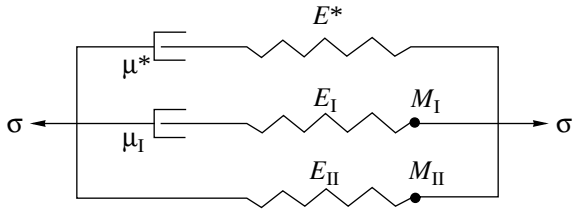


**Fig. 1.** The model of a viscoelastic medium with internal oscillators.

tic interaction in a system of agglomerated wet grains. Figure 1 shows a generalization of the rheological Maxwell–Voigt model developed in [13, 21], where it was originally suggested to add masses to the elastic elements of a rheological scheme. According to Gamburtsev [22], an analogous combination underlies the calculations of mechanical seismographs and their electromechanical analogues.

The proposed model includes two elements with viscosities $\mu_1$ and $\mu^*$, three elastic springs (with the elastic moduli $E_\mathrm{I}$, $E_\mathrm{II}$ and $E^*$), and two oscillating masses ($M_\mathrm{I}$ and $M_\mathrm{II}$). According to the laws of rheology, this scheme corresponds to the following relation between stress $\sigma$ and strain $e$:

$$\left(b_0 + \sum_{p=1}^{m} b_p \frac{D^p}{Dt^p}\right)\sigma = \left(a_0 + \sum_{p=1}^{m} a_p \frac{D^p}{Dt^p}\right)e; \qquad (1)$$
$$m = 3, \quad n = 5; \quad b_0 = 1, \quad a_0 = E^*, \ldots,$$

where $p$ is the running index of summation. Restricting our consideration to the case of a planar one-dimensional dynamics and passing to the time and coordinates in a frame moving at an elastic velocity of $c = (E_\mathrm{II}/\rho)^{1/2}$ ($\rho$ is the density) in Eq. (1), we obtain an equation describing the $P$-wave evolution:

$$\frac{\partial v}{\partial t} + v\frac{\partial v}{\partial x} = \sum_{p=1}^{n} (-1)^{p+1} A_{p+1} \frac{\partial^{p+1} v}{\partial x^{p+1}}. \qquad (2)$$

Equation (1) is a generalization of the Burgers–Korteweg–de Vries and Kuramoto–Sivashinsky equations well known in the nonlinear wave theory. The selection of relation (1) and, hence, Eq. (2), can be rationalized as follows. The dispersion curve of Eq. (2) has two roots corresponding to the dependence of the damping factor ($\mathrm{Im}\,\omega$) on the wave number $\chi$, where

$$\omega = \chi v^* - |A_3|\chi^2 + |A_5|\chi^5 + i\chi^2(|A_2| - |A_4|\chi^2 + |A_6|\chi^4) \equiv \mathrm{Re}\,\omega + i\mathrm{Im}\,\omega. \qquad (3)$$

If the coefficients $A_J$ are selected so that the sum in parentheses is negative between the two roots, the corresponding interval of wave numbers (Fig. 2) represents a region where the oscillations are unstable and their amplitudes exhibit unlimited growth. However,

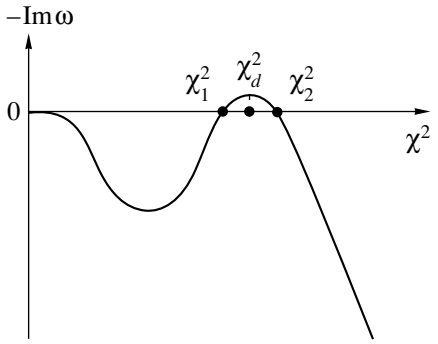


**Fig. 2.** A dispersion curve with an instability interval $\chi_1 < \chi < \chi_2$.

the nonlinear term in Eq. (2) limits this growth due to the energy pumping to high-frequency modes, where a positive damping factor is ensured. This requires a special selection of the parameters:

$$A_2 = \frac{E_\mathrm{I}\theta + E^*\theta^*}{\rho}; \quad A_3 = -c\left(\frac{E_\mathrm{I} + E^*}{\rho}\theta\theta^* + \kappa_\mathrm{II}^2\right);$$
$$A_4 = c^2\left(\kappa_1^2\frac{E^*\theta^* + E_\mathrm{I}\theta}{E_\mathrm{I}} + \kappa_\mathrm{II}^2(\theta + \theta^*)\right);$$
$$c = \sqrt{\frac{E_\mathrm{II}}{\rho}}; \quad \kappa_{11} = \sqrt{\frac{M_\mathrm{II}}{\rho_0}}; \quad \kappa_1 = \sqrt{\frac{M_\mathrm{I}}{\rho}}; \qquad (4)$$
$$\theta_J = \frac{\mu_J}{E_J}, \quad A_5 = -c\kappa_\mathrm{I}^2(c^2\theta\theta^* + \kappa_\mathrm{II}^2);$$
$$A_6 = c^2\kappa_\mathrm{I}^2\kappa_\mathrm{II}^2\theta^*\frac{E_\mathrm{II}}{E_\mathrm{I}},$$

where $\theta$ is the relaxation time and $\kappa$ is the internal length (corresponding to a continuous description [13, 21] of the fragmentary medium). In the case of wet clayey sand, the following estimates are valid: the water-saturated clay viscosity, $\mu_\mathrm{I} = 1$–$10^2$ Pa s, and the wet sand matrix viscosity, $\mu^* = 10^4$–$10^5$ Pa s. The ratio of elastic moduli (quartz grains and sand particles) is on the order of $\sim 10^{-4}$ (the same as the viscosity ratio), which implies that the model has a small parameter. Malomed [23] wrote Eq. (2) in the following form:

$$\frac{\partial v}{\partial t} + v\frac{\partial v}{\partial x} + \beta_1\frac{\partial^3 v}{\partial x^3} + \beta_2\frac{\partial^5 v}{\partial x^5} = \frac{\partial^2}{\partial x^2}\left[\left(\frac{\partial^2}{\partial x^2} + 1\right) - \varepsilon\right]v, \qquad (5)$$

where $\varepsilon$ is a small parameter and $\Delta\chi \sim \varepsilon$ is the width of the instability interval. Let the instability center $\chi_d$ correspond to the dominant frequency: $\omega_d = \chi_d c \sim \Delta c/\kappa_\mathrm{II} \sim$

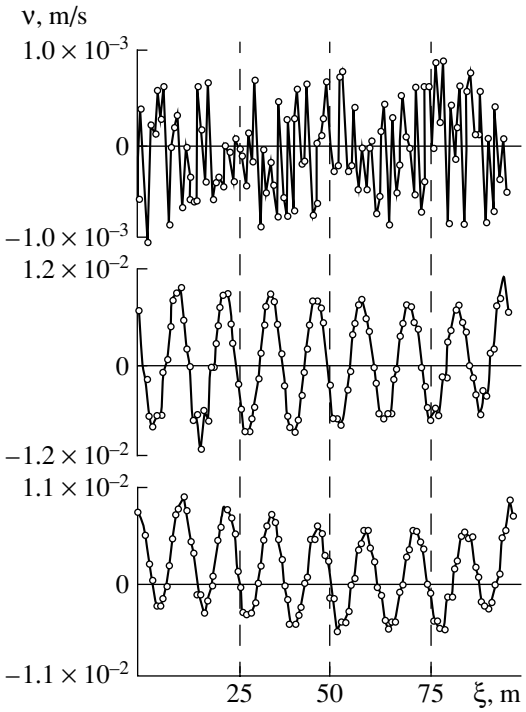


**Fig. 3.** Transformation of white noise [34] into the wave with a frequency of 12 Hz at $t = 0$, $5/\mathrm{Im}\,\omega$, and $7/\mathrm{Im}\,\omega$.

$(c/\kappa_{II})(\mu_I/\mu^*)$, where $\Delta c$ is the dispersion (close to insignificant for geomaterials).

With neglect of the odd-order derivatives (dispersion), Eq. (2) simplifies to yield

$$\frac{\partial v}{\partial t} + v\frac{\partial v}{\partial x} = \frac{\partial^2}{\partial x^2}\left[\left(1 + \frac{\partial^2}{\partial x^2}\right)^2 - \varepsilon\right]v. \qquad (6)$$

In this form, the *P*-wave evolution equation was used in [24–33], where the following important result was obtained: long waves are unstable and give rise to high-frequency chaotic oscillations (related to the Goldstone mode). This instability, called the soft turbulent mode (STM), leads to the intense spatiotemporal chaos. There was a discussion [24–33] concerning the possibility of finding a form of the Ginzburg–Landau equation equivalent to Eq. (6), for which a wave with a dominant frequency $\omega_d$ would be stable over a certain time interval. However, within the framework of this study, it is sufficient that oscillations with a dominant frequency $\omega_d$ be accompanied by high-frequency noise, in agreement with the experimental data [1, 3, 10].

In this respect, only one nontrivial numerical solution of Eq. (2) with retained dispersion term of the third order was successful [34]. The results presented in Fig. 3 show the transformation of the initial white noise into a regular wave structure with a frequency of $\omega_d \sim 12$ Hz existing for a certain finite period of time. This pattern resembles the evolution of a seismic signal to a dominant frequency in the case of wet sand [10]. After the third time interval (indicated in Fig. 3), the wave structure lost stability and exhibited degradation.

Probably, STM instability accounts for the unsuccessful attempts to follow, by means of numerical simulations using Eq. (2) with dispersion, the evolution of an arbitrary harmonic wave to a dominant frequency. The results of direct calculations using Eq. (6) performed on a CRAY C-90 supercomputer [30] showed that the instability is related to the appearance of high-frequency limiting cycles.

## THE LONG–SHORT WAVE RESONANCE MODEL

Sand grains in a weakly connected granular medium are capable of kinematic rotation, even in the course of wave-caused deformation. In this case, it is necessary to use the Cosserat theory involving the angular moment balance in addition to the momentum conservation. For the *P*-waves, the two balances are related as [35]

$$\frac{\partial^2 u}{\partial t^2} - c_1^2\frac{\partial^2 u}{\partial x^2} - \nu\frac{\partial u}{\partial x}\frac{\partial^2 u}{\partial x^2} - \delta\frac{\partial^4 u}{\partial x^4} + \beta\frac{\partial \Phi^2}{\partial x} = 0; \qquad (7)$$

$$\frac{\partial^2 \Phi}{\partial t^2} - c_2^2\frac{\partial^2 \Phi}{\partial x^2} + a\Phi - \left(c_2^2\frac{\partial^2 \Phi}{\partial x^2} - a\Phi\right)\frac{\partial u}{\partial x} = 0, \qquad (8)$$

where $\Phi$ is the angle of grain rotation; $u$ is the displacement; $\nu$, $\delta$, $\beta$, and $a$ are the elastic constants; $c_1$ and $c_2$ are the wave velocities of the translational and rotational modes,

$$\nu = c_1^2 + 2\frac{B}{\rho_0}; \quad \delta = \frac{c}{\rho_0}; \quad a = \frac{\gamma}{\rho J};$$
$$c_1^2 = \frac{E}{\rho_0}; \quad c_2^2 = \frac{A}{\rho_0 J}; \qquad (9)$$

$J$ is the moment of inertia per unit grain volume; and $A$ and $\gamma$ are the elastic moduli for the moment and antisymmetric stress components, respectively.

In Eqs. (7) and (8), the nonlinear terms correspond to the elastic coupling:

$$\sigma = E\frac{\partial u}{\partial x} + C\frac{\partial^3 u}{\partial x^3} + B\frac{\partial u}{\partial x}\frac{\partial u}{\partial x} - \beta\rho_0\Phi\Phi. \qquad (10)$$

Since the $J$ value is small (being on the same order of magnitude as the water conductivity of the medium), the rotational mode can be identified with ultrasound, while the translational mode corresponds to the seismic wave. Figure 4 shows the dispersion curves for the linear variants of Eqs. (7) and (8):

$$\omega_s^2 = c_1^2\chi_s^2 + \delta\chi_s^4, \quad \omega_{us}^2 = c_2^2\chi_{us}^2 + 2\omega_0^2, \qquad (11)$$

where

$$\omega_0 = \frac{\sqrt{a}}{2}; \quad c_g = \frac{d\omega}{d\chi}, \quad \Theta = \chi\xi - \omega\tau.$$

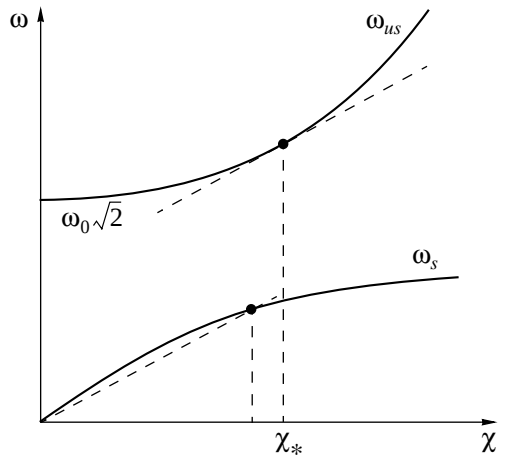


**Fig. 4.** Dispersion curves for seismic and ultrasonic waves showing the long–short wave resonance conditions [35].

The energy transfer between various wave modes is possible in the case of the so-called long–short wave resonance (LSWR). In particular, it was suggested [35] that the pumping of seismic energy to ultrasonic oscillations can be realized provided that the group velocity of ultrasound ($c_g$) is equal to the seismic wave velocity ($c_1$): $c_g = c_g \approx c_1$ (at a wave number of $\chi_{us} = \chi^*$).

The LSWR is usually considered from the standpoint of the modulation of short-wave (optical) oscillations [36]. However, the inverse situation, whereby short waves (high frequencies) are excited due to long waves (low frequencies), is possible as well. As was pointed out by V.I. Erofeev (private communication), the excitation of ultrasound at the expense of the energy of short waves requires the presence of another ultrasound oscillation. As can be seen from the above considerations, this possibility is ensured in real oil pools. The corresponding energy exchange coefficient (~0.001) was calculated in [37].

The Cosserat mechanics in a viscoelastic variant was also used for the generation of subharmonics [38], when the resultant system corresponded to the Duffing equation. This effect was experimentally observed both under laboratory conditions [39] and in the field test [10]. If the translational mode is viscous while the rotational mode is elastic, the rheological model corresponds to a slow creep of the rock massive, in which the noise generation has the form of a strange attractor [40].

## LABORATORY INVESTIGATION OF THE ULTRASOUND ACTION ON THE OIL RECOVERY FROM AN OIL POOL

Under laboratory conditions, natural oil was modeled by a transformer oil saturated with natural gas (propane) and containing (in some tests) surfactant additives. The model oil was saturated with gas at a pressure of $P$ = 0.8–1.0 MPa and a temperature of $T$ = 20–25°C. The gas factor $G$ (defined as the gas volume per unit oil volume under normal conditions) was on the average about 9.6 $m^3/m^3$. The oil saturation pressure was determined both without ultrasound and under (weak or strong) acoustic action [6].

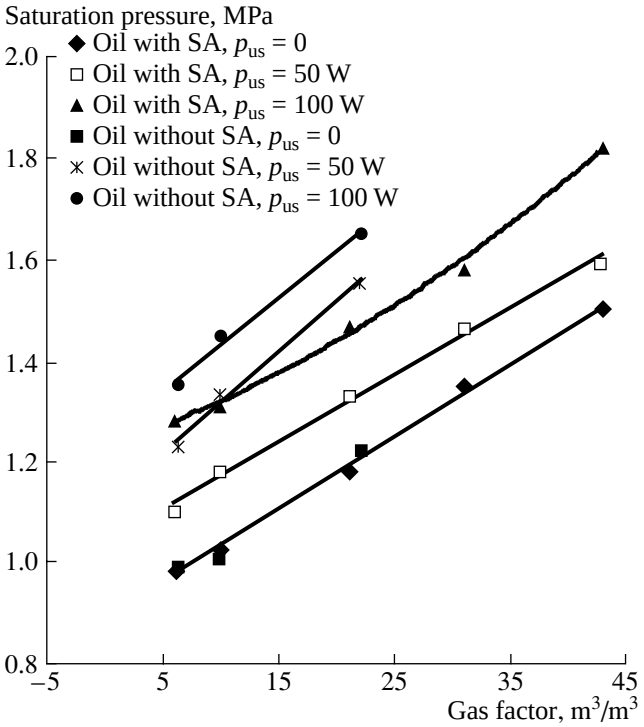


**Fig. 5.** Saturation pressure versus the gas factor for oil with and without surfactant (SA) under weak ($p_{us}$ = 50 W) and strong ($p_{us}$ = 100 W) acoustic action.

Figure 5 presents the plots of the saturation pressure versus the gas factor obtained under various conditions and shows the corresponding linear (or polylinear) approximations. As can be seen, the saturation pressure in pure oil at the same gas factor increases with the intensity of acoustic action, while the presence of a surfactant reduces this pressure by 0.1–0.2 MPa. Thus, the introduction of foaming surfactants decreases the free gas evolution from oil and retains gas in the form of fine-disperse bubbles. However, at a high gas factor ($G > 35$ $m^3/m^3$) and strong acoustic action, the presence of foaming surfactants cannot prevent the conversion of a fine foam into free gas. Under such conditions, the saturation pressure significantly increases (the gas factor is doubled).

The producing oil pool was modeled (Fig. 6) by a metal cylinder *5* filled with sand. The ultrasound was generated by a source *12* positioned at the cylinder input. Receiver *14* was placed at the output and inside the cylinder. The model oil pool had a length of 0.495 m, a diameter of 3.2 cm, a pore volume of 170 $cm^3$, and a permeability of 0.478 $\mu m^2$. The ultrasound power in the regimes of weak and strong acoustic action was 50 and 100 W, respectively. The pressure amplitude measured

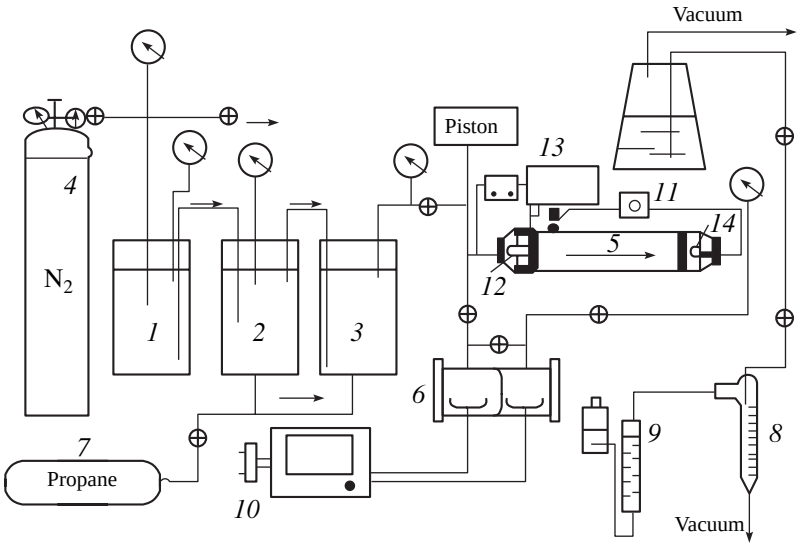


**Fig. 6.** Schematic diagram of the experimental setup: (*1–3*) interconnected gas cylinders; (*4*) compressed nitrogen; (*5*) model oil pool; (*6*) differential pressure gauge; (*7*) compressed propane; (*8*) gas/oil separator; (*9*) gas trap; (*10*) manifold; (*11*) cooler; (*12*) ultrasound radiator; (*13*) generator; (*14*) ultrasound receiver.

by the output ultrasonic receiver in the regimes of weak and strong action was 20 and 50 KPa, respectively. The temperature during the experiment was maintained at a constant level of 25°C.

The model pool *5* was initially washed, conditioned, and filled with gas-free oil. Then, the gas pressure in the cylinder was increased with the aid of piston up to a typical reservoir pressure level of 1.2–1.25 MPa. First, gas-free oil was displaced by the model gas-saturated oil, and then the latter oil was displaced by water. The model gas-saturated oil was prepared taking into account that the propane vapor pressure at room temperature (22°C) is 0.82 MPa. In order to accelerate the saturation process, the gas pressure was increased to 1.82 MPa.

The conditions and results of all experiments are summarized in the table. In the initial control experiment (test 1/2) without acoustic action, the model pool was flooded with water at a constant input pressure (Figs. 7 and 8, curves *1*, *3*, *5*, *7*). Then the water supply was terminated and the withdrawal was carried out under conditions of reservoir pressure drop (the oil pool depletion stage, curves *2*, *4*, *6*, *8*).

The subsequent experiments on the ultrasound-stimulated water displacement of oil were performed using the acoustic source at the pool input. In test 3/4, the source was periodically switched on for 15–60 s every 15 min over a total time of 7 h. Then, the ultrasound action was terminated and the withdrawal was continued without external action. Tests 5/6 and 7/8 were conducted without large intervals between the impulses of acoustic action: ultrasound was applied for 15 or 60 s every 15 min throughout the experiment.

Each impulse increased the reservoir pressure by 10–50%, depending on the impulse duration. This pressure growth in the course of action led to the counterflow of water. In order to prevent this counterflow, the water supply was interrupted during the acoustic impulse (but the output fluid withdrawal was continued until the pressure reached a reservoir level). The pressure jump under the acoustic action, which was related to the evolution of gas bubbles from oil and to an

**Table**

| Test | Ultrasonic action | Surfactant | Gas factor *G* | | Displacement coefficient *K* upon breakthrough | Final *K* |
|---|---|---|---|---|---|---|
| | | | upon breakthrough of water | final | | |
| **1/2** | No ultrasound | No | Maximum | Not reached | 37% | 42% |
| **3/4** | 60 s (aperiodic) | No | Sharp peak | Minimum | 48% | 53% |
| **5/6** | 15 s (15-min interval) | No | Moderate | Maximum | 38% | 56% |
| **7/8** | 60 s (15-min interval) | 0.1 % | Maximum | Moderate | 38% | ~90% |
| **9** | No ultrasound; oil with $CO_2$ displaced by $N_2$ | 3 % in oil | Irregular pulsations of $CO_2$ and $N_2$ | | 38% | 40% |

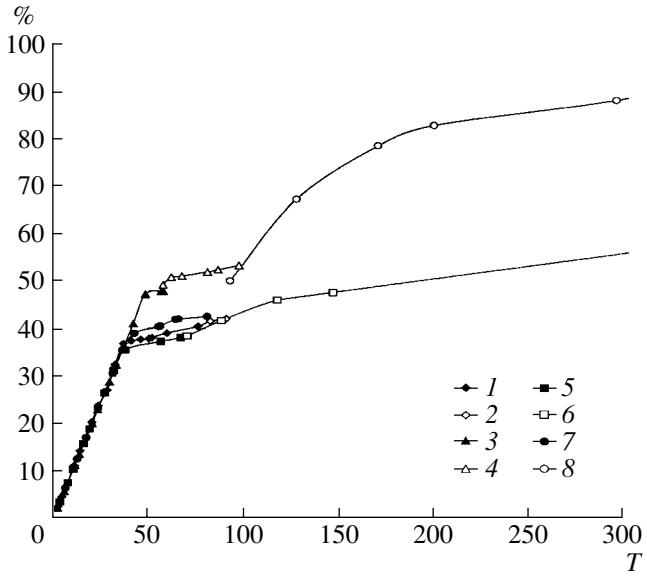


**Fig. 7.** Oil displacement coefficient $K$ versus the ratio $T$ of the product volume to the initial pore volume occupied by the model oil in the pool (see the text for explanations).

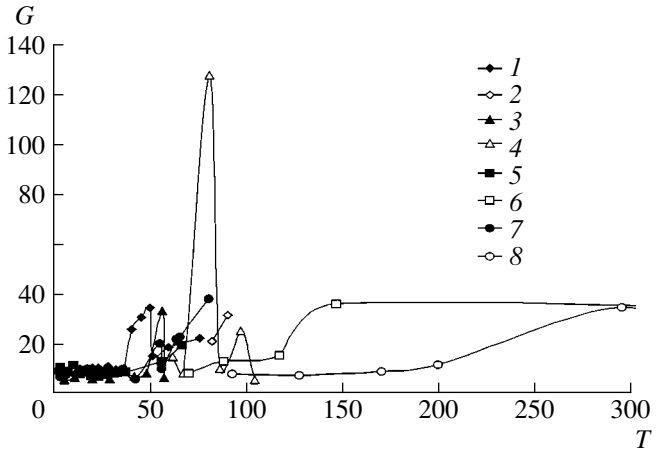


**Fig. 8.** Current gas factor $G$ versus the ratio $T$ of the product volume to the initial pore volume occupied by the model oil (see the text for explanations).

increase in the total volume of the mixture) amounted to 7%. Thus, oil was displaced from the pool not only by the injected water but by the gas evolving from oil as well.

Figure 7 shows typical plots of the oil displacement coefficient $K$ versus the ratio of the product volume to the initial pore volume occupied by the model oil in the pool. As can be seen, the acoustic action and water supply after water breakthrough were terminated (at $K$ = 0.49), as reflected by the passage from curve *3* to curve *4*. Subsequently, in the regime of pressure drop and pool depletion, the output fluid consisted predominantly of water with oil and gas admixtures, and the total yield (0.53) was 8% higher than that in the reference test 1/2. This gain in the total yield can be explained using the data of Fig. 8, which shows the variation of the current gas factor $G$. As can be seen, the gas factor was significant at the water breakthrough moment (33.5 $m^3/m^3$) and increased to 127 $m^3/m^3$ upon the pressure drop. Apparently, the acoustic action led to the formation of a foamy layer consisting of microscopic gas bubbles at the displacement front. In tests 3/4, there was virtually no gas breakthrough under the acoustic action. At the pool depletion stage, the gas bubbles merged into a free volume and evolved from the bed.

In the reference tests 1/2 (Fig. 7, curve *1*), the water front reached the output at $K$ = 0.37, while the gas factor was somewhat lower than in the previous case (26 $m^3/m^3$). The final displacement coefficient was $K$ = 0.42, which is 11% lower than in the case of water displacement with a periodic acoustic action (curve *2*). The absolute maxima in the gas breakthrough are observed in the depletion stage (decrease in the reservoir pressure) and are not accompanied by an increase in the oil yield (Fig. 8), so that the energy of compressed gas in this case was spent in vain.

The subsequent experiments (tests 5/6 and 7/8) were performed in the presence of bound water, which occupied 13.5% of the pore volume. Both experiments were performed under the acoustic action over the entire displacement period (i.e., until the water breakthrough moment and the pool depletion onset). Note that the intensity of the acoustic action was somewhat higher than that in tests 3/4. When the reservoir pressure exceeded 1.25 MPa as a result of the ultrasonic impulse application, the water supply was terminated. The relative duration of the period of increased pressure (with respect to the total flooding period) was within 0.15–0.2.

Test 7/8 differed from test 5/6 in that an aqueous layer containing a foaming surfactant (similar to that present in the natural oil) was introduced into the oil pool. These experiments are illustrated by curves *5*, *6* and *7*, *8* in Figs. 7 and 8. The water breakthrough moment corresponded to $K$ = 0.37–0.4. When the water front approached the output, the gas factor increased only slightly: to 13.2 $m^3/m^3$ in tests 5/6 and to 20.2 $m^3/m^3$ in tests 7/8.

The results can be summarized as follows. The gas saturation pressure in the pure oil and that with surfactant for equal gas factors were virtually the same. This fact, as well as the early water breakthrough in tests 5/6 and 7/8 as compared to tests 1/2 and 3/4, can be explained by the presence of bound water in front of the displaced oil. We may suggest that the acoustic action leads to a partial restoration of the bound water mobility, which also accounts for the relative decrease in the final displacement coefficient in tests 5/6, as compared to tests 3/4 (compare curves *4* and *6* in Fig. 7).

In addition, the approach of the flooding front was accompanied by a lower increase in the gas factor in tests 5/6 (20 $m^3/m^3$), as compared to tests 3/4 (33.5 $m^3/m^3$),

where a foamy layer consisting of microscopic gas bubbles was present at the displacement front. Apparently, the enhancement of ultrasound at the oil pool input in tests 5/6 led to the growth of gas bubbles and their coalescence into a free volume outside the front, which was confirmed by the reduced signal of the ultrasonic receiver. For this reason, the gas factor at the water breakthrough moment was lower in tests 5/6 than in tests 3/4.

In tests 7/8, the gas factor at the water breakthrough moment increases to 38 $m^3/m^3$, which means that the surfactant stabilizes microscopic gas bubbles and prevents this foam from degradation in the layer at the displacement front under the acoustic action. At the depletion stage, the gas factor was significantly lower in tests 7/8 than in tests 5/6 (compare curves *8* and *6* in Fig. 8), which is naturally explained by the presence of the surfactant (retaining the gas in the liquid phases, predominantly in oil). It should be recalled that the effect of ultrasound on the oil saturation pressure decreases in the presence of the surfactant. As a result, the oil displacement coefficient in tests 7/8 reached almost 90% (more precisely, 87%) against 54% in tests 5/6.

For comparison, the table shows the results of an experiment (test 9) modeling an alternative technology, whereby $CO_2$-saturated oil is displaced by a nitrogen ($N_2$) layer in a flow of poly(isobitylene). This process may also involve the formation of microscopic gas bubbles, but the comparison with the results of tests 7/8 shows the significant advantages of the ultrasonic action.

## CONCLUSIONS

Real rocks, especially the porous collectors of oil and gas, possess complicated rheological properties, which clearly manifest themselves under the action of ultrasonic and seismic waves. The related factors include the dry friction at contacts, the viscoelastic dynamic deformation, and the presence of internal oscillators in the form of gas bubbles and solid fragments. The resulting dynamics leads to characteristic changes in the spectrum of acoustic vibrations, which are very important from the standpoint of their dynamic action upon underground objects, including oil and gas bearing formations.

Ultrasound generated by a vibroseismic action upon a producing oil pool stimulates the gas evolution from natural oil, thus increasing the mobility of the residual oil. The released gas forms a layer of microscopic gas bubbles at the displacement front, thus enhancing the displacement process. The higher the gas factor, the more effective the ultrasound-stimulated oil outgassing. The presence of foaming surfactants reduces this effect. On the other hand, small additives of a foaming oil and water soluble agent stabilize the microscopic gas bubbles both at the displacement front and in oil at the depletion stage, which sharply increases the final oil recovery (up to 90%). The main problem arising in the implementation of the proposed technology is to provide the effective generation of ultrasound in the oil pool under a vibroseismic action.

## ACKNOWLEDGMENTS

We are grateful to T.L. Nenartovich and G.N. Yagodov for participation in the experiments.

## REFERENCES

1. A. G. Asan-Dzhalalov, V. V. Kuznetsov, I. G. Kissin, *et al.*, SU Patent No. 1596081, Bull. Izobret., No. 36 (1990).
2. O. L. Kuznetsov, É. M. Simkin, and G. V. Chilingar, *Physical Grounds of Acoustic Effects on Oil and Gas Deposits* (Mir, Moscow, 2001) [in Russian].
3. V. N. Nikolaevskiĭ, Izv. Ross. Akad. Nauk, Mekh. Zhidk. Gaza, No. 5 (1992).
4. *Nonlinear Acoustics at the Beginning of the 21st Century*, Ed. by O. V. Rudenko and O. A. Sapozhnikov (Moscow State Univ. Press, Moscow, 2002), Vols. 1–2.
5. *Seismic Vibration Action on an Oil Pool*, Ed. by M. A. Sadovskiĭ and A. V. Nikolaev (Inst. Fiz. Zemli Ross. Akad. Nauk, Moscow, 1993) [in Russian].
6. G. S. Stepanova, T. L. Nenarnovich, G. N. Yagodov, and V. N. Nikolaevskiĭ, Burenie Neft' (Leningrad), Nos. 7–8, 36 (2003).
7. A. T. Gorbunov, Izv. Akad. Nauk SSSR, Mekh. Mashinostr., No. 1 (1962).
8. V. N. Nikolaevskiĭ and G. S. Stepanova, in *Nonlinear Acoustics at the Beginning of the 21st Century*, Ed. by O. V. Rudenko and O. A. Sapozhnikov (Moscow State Univ. Press, Moscow, 2002), Vol. 2.
9. K. Terzagi, *Theoretical Soil Mechanics* (Wiley, New York, 1943; Gosstroĭizdat, Moscow, 1961).
10. N. A. Vil'chinskaya and V. N. Nikolaevskiĭ, Izv. Akad. Nauk SSSR, Fiz. Zemli, No. 5, 91 (1984).
11. V. N. Nikolaevskiĭ, *Mechanics of Porous and Cracked Media* (Nedra, Moscow, 1984) [in Russian].
12. O. Yu. Dinariev and V. N. Nikolaevskiĭ, Izv. Ross. Akad. Nauk, Mekh. Tverd. Tela, No. 3, 88 (2001).
13. V. N. Nikolaevskiĭ, *Geomechanics and Fluid Dynamics* (Nedra, Moscow, 1996) [in Russian].
14. M. A. Biot, J. Acoust. Soc. Am. **28**, 168 (1956).
15. *Atlas of the Time Variations of Natural Processes* (Ob'edin. Inst. Fiz. Zemli Ross. Akad. Nauk, Moscow, 1994), Vol. 1 [in Russian].
16. S. Z. Dunin, D. Mikhailov, and V. Nikolaevskiy, in *Proceedings of 2nd Biot Conference on Poromechanics, Grenoble, France, 2002* (Grenoble, 2002), p. 633.
17. T. N. Gardner, J. Acoust. Soc. Am. **107**, 163 (2000).
18. A. A. Andronov, A. A. Vitt, and S. É. Khaĭkin, *Theory of Oscillations* (Fizmatgiz, Moscow, 1959; Pergamon Press, Oxford, 1966).
19. T. Richard and E. Detournay, Acad. Sci., Paris **328** (IIb), 671 (2000).
20. G. Chen, S.-B. Hsu, and J. Zhou, Int. J. Bifurcation Chaos **12** (3), 535 (2002).

21. V. N. Nikolaevskiĭ, in *Lecture Notes in Engineering*, Ed. by C. A. Brebbia and S. A. Orszag (Springer, Berlin, 1989), Vol. 29, pp. 210–221.
22. G. A. Gamburtsev, *Selected Works* (Nauka, Moscow, 2003), Vol. 2 [in Russian].
23. B. A. Malomed, Phys. Rev. A **45** (2), 1009 (1992).
24. H. Fujiaka and T. Yamada, Prog. Theor. Phys. **106** (2), 315 (2001).
25. H. Fujiaka, T. Honkawa, and T. Yamada, Prog. Theor. Phys. **109** (6), 911 (2003).
26. I. L. Kliakhandler and B. A. Malomed, Phys. Lett. A **231**, 191 (1997).
27. P. C. Mathews and S. M. Cox, Phys. Rev. E **62** (2), R1473 (2000).
28. D. Tanaka and Y. Kuramoto, Phys. Rev. E **68**, 026219 (2003).
29. R. Toral, G. Xiong, J. D. Gunton, and H. Xi, J. Phys. A: Math. Gen. **36**, 1323 (2003).
30. M. I. Tribelsky, Int. J. Bifurcation Chaos **7** (5), 997 (1997).
31. M. I. Tribelsky and K. Tsuboi, Phys. Rev. Lett. **76** (10), 1631 (1996).
32. M. I. Tribelsky and M. G. Velarde, Phys. Rev. E **54** (5), 4973 (1996).
33. H.-W. Xi, R. Toral, J. D. Gunton, and M. I. Tribelsky, Phys. Rev. E **62** (1), R17 (2000).
34. I. A. Beresnev, V. S. Mitlin, and V. N. Nikolaevskiĭ, Dokl. Akad. Nauk SSSR **317** (10), 1103 (1991) [Sov. Phys. Dokl. **36** (10), 701 (1991)].
35. A. L. Krylov, N. G. Mazur, V. N. Nikolaevskiĭ, and G. A. Él', Prikl. Mat. Mekh. **57** (6), 100 (1990).
36. M. I. Rabinovich and D. I. Trubetskov, *Introduction to the Theory of Oscillations and Waves* (Nauka, Moscow, 2001) [in Russian].
37. N. G. Mazur, V. N. Nikolaevskiĭ, and G. A. Él', Prikl. Mat. Mekh. **61** (2), 336 (1997).
38. O. Yu. Dinariev and V. N. Nikolaevskiĭ, Izv. Ross. Akad. Nauk, Mekh. Tverd. Tela, No. 6, 78 (1997).
39. V. V. Gushchin, Yu. M. Zaslavskiĭ, and S. N. Rubtsov, Fiz. Zemli, No. 5, 92 (1998).
40. O. Yu. Dinariev and V. N. Nikolaevskiĭ, Dokl. Akad. Nauk **331** (6), 739 (1993).

*Translated by P. Pozdeev*

*Acoustical Physics, Vol. 51, Suppl. 1, 2005, pp. S140–S148. From Akusticheskiĭ Zhurnal, Vol. 51, Suppl., 2005, pp. 160–168.*


# Laboratory Observations of Altered Porous Fluid Flow Behavior in Berea Sandstone Induced by Low-Frequency Dynamic Stress Stimulation[1]

**P. M. Roberts**

*Los Alamos National Laboratory, Earth and Environmental Sciences Division EES-11, Mail Stop D443 Los Alamos, NM 87545, USA*

*e-mail: proberts@lanl.gov*

Received July 10, 2004

**Abstract**—It has been observed repeatedly that low-frequency (1–500 Hz) seismic stress waves can enhance oil production from depleted reservoirs and contaminant extraction from groundwater aquifers. The physics coupling stress waves to fluid flow behavior in porous media is not understood, although numerous physical mechanisms have been proposed to explain the observations. To quantify the effects of low-frequency, dynamic-stress stimulation on multiphase fluid flow and *in situ* particle behavior in porous media, laboratory experiments were conducted with a core flow stimulation apparatus that allows for precise control and measurement of applied stress and strain, static confinement, and fluid flow parameters. Results are reported for experiments on stimulated single-phase and two-phase fluid flow behavior in 2.54-cm-diameter Berea sandstone cores. For all experiments, stimulation was applied to the cores in the form of sinusoidal, axial, mechanical stress coupled to the solid porous matrix at frequencies of 25 to 75 Hz. Applied stress RMS amplitudes ranged from 300 to 1200 kPa and, at these levels, produced coupled, pore-pressure fluctuations of much less than 1.2 to 4.8 kPa, respectively. During single-phase brine flow, stimulation increased the absolute permeability of the rock by 10–20%. This was caused by mobilizing *in situ* clay particles that were partially plugging the pore throats. During two-phase, steady-state, constant-rate flow of oil–brine and decane–brine mixtures, stimulation caused significant changes in the bulk fluid pressure drop across the core. The pressure changes showed a strong dependence on the viscosity of the nonwetting fluid phase (oil or decane) relative to the wetting phase (brine). This may indicate that relative changes in the mobility of wetting versus nonwetting fluid phases were induced by the dynamic stress. Under the specific experimental conditions used, pore-scale particle perturbation and altered wettability are possible physical mechanisms that can explain the results. © *2005 Pleiades Publishing, Inc.*

## INTRODUCTION

Numerous investigations have shown that seismic waves (low-amplitude stress waves at frequencies of 1 to 500 Hz) can selectively increase the mobility and transport of multiphase fluid components in porous media such as rocks and soils [1–5]. Most of the prior and ongoing research in this area has been focused on increasing production from declining oil and gas reservoirs during field deployments of various surface and downhole seismic sources. During several field tests by the oil and gas industry [1, 2, 5], increases in oil production rates by 20% or more have been reported. However, the majority of oil-field tests to date have been performed with little or no guidance from laboratory experimental data or theoretical predictions. Thus, field tests have yielded mixed and unpredictable results, mainly because the underlying physical mechanisms for seismically enhanced fluid transport are not adequately understood.

More recently, research has also begun to examine the possibility of using seismic wave stimulation to enhance the extraction of *dense* nonaqueous-phase liquid (DNAPL) contaminants from groundwater aquifers. In contrast to the numerous field tests already performed on stimulated flow of oil, which is a *light* nonaqueous-phase liquid (LNAPL), no field tests have been performed yet on enhancing DNAPL extraction at groundwater remediation sites in the United States. Furthermore, only a limited number of laboratory experiments have been performed on enhanced DNAPL transport in unconsolidated sands or soils [6, 7]. The obvious practical value of harnessing the stress-stimulated flow phenomenon has, over the past ten years, motivated increased research interest in the subject. Despite this growth, the scientific community is far from fully understanding the phenomenon.

Recent laboratory experiments on stimulated two-phase fluid flow in rocks and sands [6–9] and theoretical studies on coupled stress/fluid flow dynamics [10–15] have confirmed that the stress-stimulation phenomenon is observable at the bench scale, is reproducible,

[1] This article was submitted by the author in English.

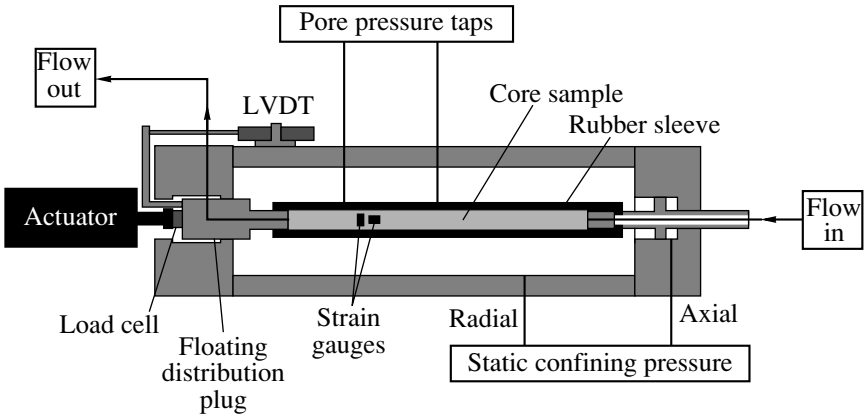


**Fig. 1.** Schematic diagram of dynamic-stress core flow stimulation apparatus.

and can be modeled. However, lab experiments have produced mostly empirical data, and theoretical models are still in the initial stages of development. Numerous physical mechanisms have been proposed to explain seismically enhanced NAPL mobilization, but no conclusive experimental laboratory or field data have been collected that can prove *which* mechanisms dominate under the widely varying physical conditions typically encountered in the Earth.

Although "stress-wave propagation in saturated porous media" and "multiphase porous fluid flow dynamics" are each well-developed individual scientific fields, they have not yet been cross-coupled successfully. Initial theoretical work indicates that cross coupling of stress waves with fluid flow can be modeled using simplified physical conditions [10, 13, 15]. Under more realistic conditions like those in the Earth, the coupling is likely controlled by a combination of several different mechanisms, each operating over a different range of scale lengths. The stress-wave stimulated porous flow phenomenon, then, needs to be understood from the subpore scale (nm to μm) to the field scale (m to km). This would allow the stimulated flow response to be predicted for different combinations of physical conditions and applied dynamic stress parameters.

This paper reports recent laboratory experimental results of tests on core samples of Berea sandstone; these results provide further evidence that low-frequency stress stimulation can alter porous fluid flow behavior. The data were obtained with a high degree of accuracy and precision and demonstrate that the phenomenon is readily induced and can be quantified. The observed core-scale (cm) behavior supports two physical mechanisms that are likely to be important for understanding how to predict and control the stress-stimulated flow phenomenon on larger scales as well. These are (1) *in situ* clay particle mobilization and (2) pore fluid wettability alteration. Because the results are still largely empirical, no proof can be presented yet that other physical mechanisms do not also partially contribute to the observations.

## LABORATORY APPARATUS

To investigate the effects of low-frequency stress stimulation on porous fluid flow behavior in the laboratory, a specialized core flow apparatus was constructed (Fig. 1). This apparatus is part of a unique, state-of-the-art facility designed specifically for this purpose. The main component of the system is a triaxial core holder capable of applying up to 70 MPa axial and radial confining pressure to a cylindrical core sample. The sample is placed inside a horizontal Viton rubber sleeve designed to hold cores 2.54 cm in diameter and up to 60 cm long. Distribution plugs at each end of the sleeve accommodate fluid flow through the core. Radial confining pressure is applied to the main hydraulic-fluid chamber surrounding the sleeve. Static axial confinement is applied separately by a hydraulic piston attached to the inlet distribution plug (at the right end in Fig. 1).

The apparatus was designed to study a wide range of physical conditions under which stress stimulation may prove to be a useful application. Specifically, the pressure ratings are appropriate for simulating *in situ* overburden and pore-pressure conditions at crustal depths of up to approximately 3 km. During the experiments, constant-flow-rate pumps are used to produce pulse-free flow of fluids through the core at flow rates ranging from 0.02 to 200 mL/min. A back-pressure regulator at the fluid outlet end of the apparatus provides precise control over the static pore pressure during flow. The permeability along the core sample is measured using differential pressure gauges connected by tubing to taps located every 5 cm along the length of the rubber confining sleeve. The measured pressure drop across the core is converted to permeability using Darcy's law [16].

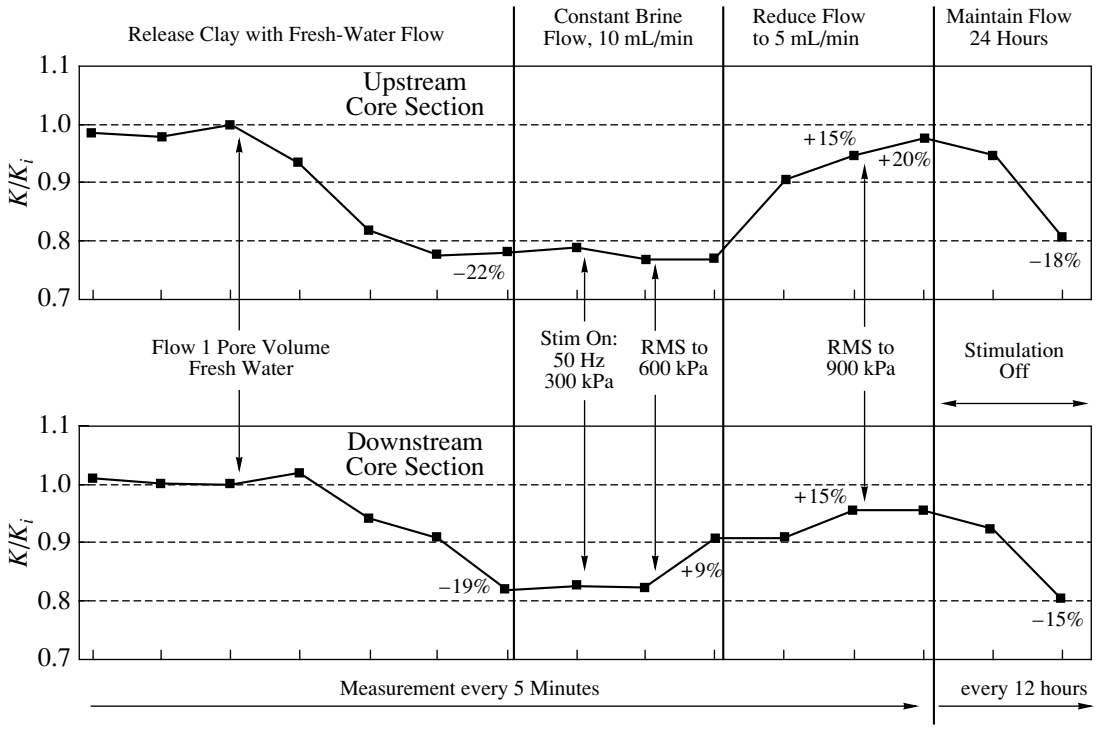


**Fig. 2.** Permeability changes during single-phase brine flow caused by release of *in situ* clay fines and subsequent mobilization by low-frequency stress stimulation.

To dynamically stimulate the core samples, axial stress cycling at frequencies from 1 to 500 Hz is produced by direct mechanical coupling of the core sample to a Terfenol-D magnetostrictive actuator. The actuator can deliver a dynamic force with a peak amplitude as high as 900 N with a maximum displacement of 70 microns, producing axial strains as high as $10^{-4}$. A load cell in series with the actuator, an LVDT attached to the floating distribution plug, and strain gauges attached to the core provide calibrated stress and strain data during stimulation. The fluid-pressure gauges are also used to estimate dynamic pore-pressure fluctuations induced by the stimulation.

Another mode of stimulation that has been investigated by other researchers [7, 8] is vibrating porous samples during flow using shaker tables. The apparatus used here (Fig. 1) has been designed to minimize this type of excitation because it causes translational, nonstrain energy that does not typically occur at significant depth in the Earth when a seismic wave propagates through it. To maximize the mechanical stress component of the dynamic stimulation and minimize the vibrational component, the axial load piston at the inlet (right) end of the core holder is locked in place mechanically after the desired static axial confinement is applied. This immobilizes the inlet end of the core, and the particle acceleration induced by the actuator effectively vanishes there. Thus, wave propagation does not occur during stress stimulation because the core is simply being compressed and expanded like a spring. This, in turn, partly avoids wavelength scaling issues when comparing laboratory and field results.

## EXPERIMENTAL RESULTS

### *Single-Phase Flow Experiments*

Experiments were performed to investigate a physical mechanism proposed for increasing absolute permeability: mobilization of *in situ* clay particles by stress stimulation. This mechanism has previously been demonstrated as feasible using ultrasonic energy at 10 kHz and above [17–19] but had not been observed at seismic frequencies of 100 Hz and lower. A Berea sandstone core sample, 2.54 cm in diameter and 32 cm long, with an initial permeability of approximately 800 millidarcies (md), was confined at 7 MPa static radial and 5.5 MPa static axial pressures. Constant flow of a 3 wt % brine solution was then initiated at a rate of 10 mL/min. Brine was used to stabilize *in situ* clay particles (fines) during permeability measurements. At lower salinity, clay fines that are normally attached to the pore walls will be released and plug the pore throats during flow, thus decreasing the rock's permeability. The permeability measurements for this experiment are plotted in Fig. 2 for two separate 5-cm-long sections of the core sample. The top plot is for an "upstream" section closest to the fluid inlet, and the bottom plot is for a "downstream" section closest to the fluid outlet and the stimulation source. The measured

permeability K is normalized by the baseline permeability $K_i$ obtained during the initial brine flow.

To induce a controlled release of clay particles, one pore volume of fresh water was flowed through the core. This resulted in a decrease in absolute permeability of approximately 20% across the entire core. The upstream section was affected sooner than the downstream section because of the flow direction. After returning to the 3 wt % brine flow and establishing a new stabile permeability, continuous sinusoidal stress cycling was initiated at 50 Hz and 300 kPa RMS stress amplitude. No change in permeability was observed in either core section until the stress amplitude was increased to 600 kPa RMS, after which an increase of 9% was observed in the downstream core section. No change was observed in the upstream core section until the brine flow rate was dropped from 10 ml/min to 5 ml/min. At the lower flow rate, the upstream permeability rose by 15%, and the downstream permeability increased an additional 6% to a final value of 15%. This means that the ability to mobilize clay particles that are plugging pore throats is sensitive to the absolute pore pressure and/or the fluid pressure gradient in the rock as a function of length along the core. When the RMS stimulation amplitude was increased to 900 kPa, an additional 5% permeability increase was observed in the upstream core section but not in the downstream section. After turning off the stimulation and maintaining constant brine flow, the permeability of the entire core gradually dropped back to the prestimulation values over a period of 24 hours. This occurred because the stimulation was not applied long enough to expel the mobilized clay particles, and they subsequently replugged the pore throats during continued flow.

### *Two-Phase Steady-State Flow Experiments*

Experiments were performed to investigate dynamic stress effects on steady-state, two-phase immiscible fluid flow through Berea sandstone. The cores used were again 2.54 cm in diameter and 32 cm long but had an initial intrinsic permeability of 100 md. The samples were confined at 7 MPa radial pressure and 4 MPa axial pressure. Two constant-rate fluid pumps were used to flow both immiscible phases through the core simultaneously at different flow-rate ratios. For the first experiment, decane was used as the nonwetting fluid phase and brine as the wetting phase. The second experiment used ten-weight vacuum pump oil as the nonwetting phase instead of decane. The reason for this was to determine whether the viscosity of the nonwetting phase has an effect on two-phase flow behavior induced during dynamic stress stimulation. Decane was chosen because it has a viscosity (approximately 0.9 cP) lower than water (1.0 cP), and ten-weight oil, because its viscosity (approximately 90 cP) is higher than that of water. A different 100-md Berea core sample was used for each experiment.

During two-phase flow, the total bulk fluid flow rate was held constant, but the ratio of decane (or oil) to brine flow rates was varied to investigate the dependence of the stimulated flow behavior on water saturation. For the decane–brine experiment, the bulk flow rate used was 2.0 mL/min. To achieve similar pressure drops for the oil–brine experiment, the bulk flow rate was dropped to 0.5 mL/min. The procedure for both experiments was to start the two fluids flowing at a given flow-rate ratio and, then, wait until the bulk-fluid pressure drop across the entire core stabilized at a constant value, indicating that steady-state conditions were achieved. Then, sinusoidal mechanical stimulation was applied as before, and induced changes in the bulk-fluid pressure drop were recorded. Stimulation frequencies and RMS stress amplitudes were varied during the decane–brine experiment while holding the flow-rate ratio constant. During the oil–brine experiment, however, the same frequency and RMS amplitude were used throughout.

The results for the decane–brine experiments are shown in Fig. 3. Bulk-fluid pressure drops are plotted versus flow time for the entire 32-cm core length (top plot) and for a 5-cm-long section in the middle of the core (bottom plot). The left half of each plot shows the results when the decane fractional flow rate was 25% of the combined bulk flow rate of 2.0 mL/min, and the right half shows the results for 10% decane flow. Stress stimulation treatments are indicated by the arrows, and the frequency and RMS amplitudes used are labeled.

In general, stress stimulation caused the bulk fluid pressure drop across the core to decrease. During 25% decane flow, the pressure drops behaved erratically, but there is a correlation between applied stress and sudden decreases in pressure. During 10% decane flow, the correlation is much clearer and the magnitude of the pressure change increases with applied RMS stress amplitude. Also, when the stimulation is turned off, the pressure drops return rapidly toward their prestimulation values. This behavior was not observed during flow runs (not shown) where the decane fractional flow rate was 50% or less. Figure 3 shows results only for stimulation at 50 Hz. Additional runs (not shown) for 10% decane flow were performed where the stimulation frequency was varied from 25 Hz to 75 Hz while holding the stress amplitude constant. The largest decrease in bulk-fluid pressure drop was observed at 25 Hz, and the smallest, at 75 Hz. Thus, lower frequencies were most effective at inducing the observed pressure changes.

The results for the oil–brine experiment are shown in Fig. 4. Bulk-fluid pressure drops across the entire 32-cm core length are plotted for four different oil fractional flow rates (10, 30, 50, and 70% of the combined bulk flow rate of 0.5 mL/min), indicated above each plot. The plots are shifted to line up at the times when stress stimulation was applied at 25 Hz and 1000 kPa RMS stress amplitude. In contrast to the decane–brine behavior (see Fig. 3), stimulation caused the pressure

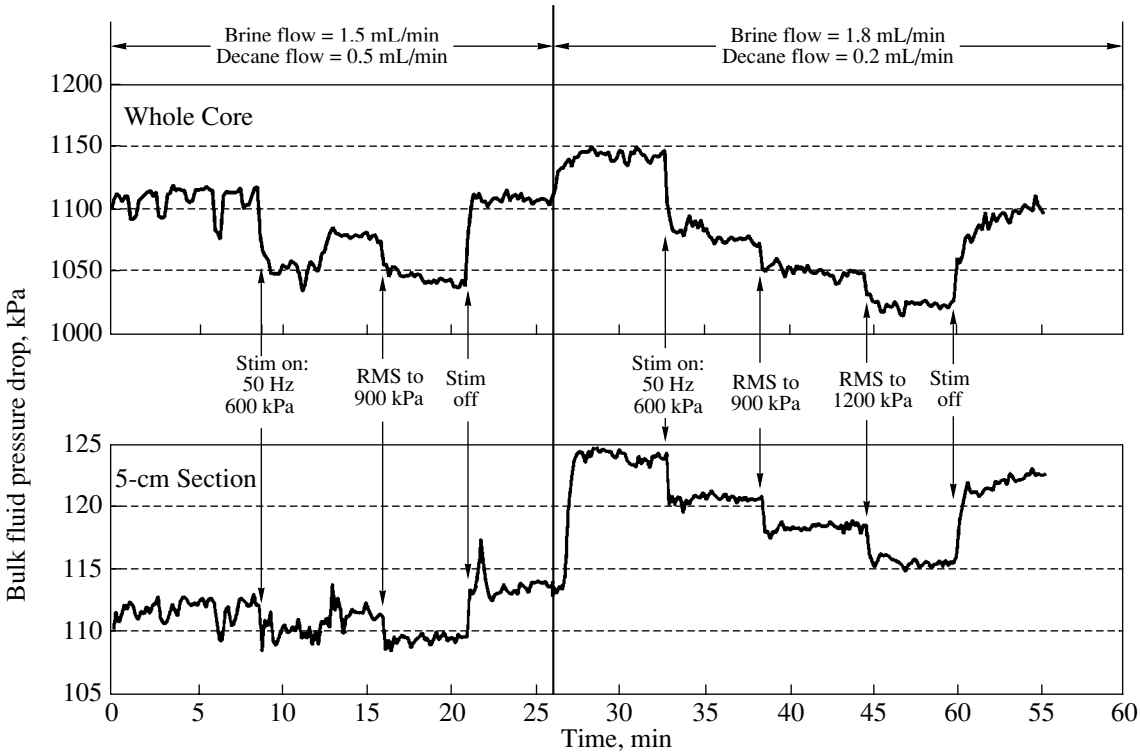


**Fig. 3.** Changes in bulk-fluid pressure drop during steady-state two-phase flow of decane–brine, induced by 50-Hz stress stimulation at varying amplitudes.

drop across the core to increase when flowing oil–brine, and this behavior was observed for all fractional oil flow rates. At each flow-rate ratio, stimulation was applied continuously and turned off when the fluid pressure drop leveled off at the new value, as indicated by the "off" arrows. The pressures then decreased toward the prestimulation values. These stimulation cycles were repeated at least three times for each flow rate, and the same behavior was observed each time. The plot for 50% oil flow shows two of these cycles to demonstrate the repeatability of the behavior. The results for both sets of two-phase steady-state flow experiments indicate that the wetting-phase and nonwetting-phase relative fluid distribution may have been changed during stress stimulation.

### *Stress/Strain and Pore Pressure Measurements*

The various transducers described previously were used to measure the static radial and axial confining stresses and the applied dynamic axial stress during core stimulation. Using strain-gauge measurements on the core, estimates of the static and dynamic values for Young's modulus and Poisson's ratio were obtained for dry and saturated Berea sandstone. Pore pressure was also monitored using an absolute-fluid-pressure gauge connected to one of the taps on the rubber confining sleeve.

Figure 5 shows one example of stress–strain measurements obtained for a Berea sandstone core sample before it was saturated with brine. The static axial stress was increased in four increments up to a maximum of approximately 1400 kPa and, then, reduced back to zero in four similar increments. At each static stress level, dynamic axial stress was applied at 10 Hz and 250 kPa RMS amplitude. The plot shows axial stress versus axial strain during this stress cycling. The solid curve represents increasing static stress up to the maximum, and the short-dashed curve shows the return to zero. The open circles dots on the static curve indicate when dynamic stress was turned on, and the black dots indicate when it was turned off. The inset at the bottom right shows one example of the dynamic stress–strain, after removing the DC components, measured during each of the eight stimulations. All eight dynamic loops were nearly identical. The open circle in the dynamic data corresponds to the start points on the static curve. When the dynamic stress is turned off, the new static values (black dots) fall inside the main static stress–strain loop. When the static stress is then increased or decreased, however, the values return to the main static loop. This type of nonlinear hysteretic behavior is typical of rocks [20].

The dashed lines through the static and dynamic stress-strain curves show linear fits to the measured data. The slopes of these lines were used to estimate Young's modulus (E) for this sample of dry Berea sand-

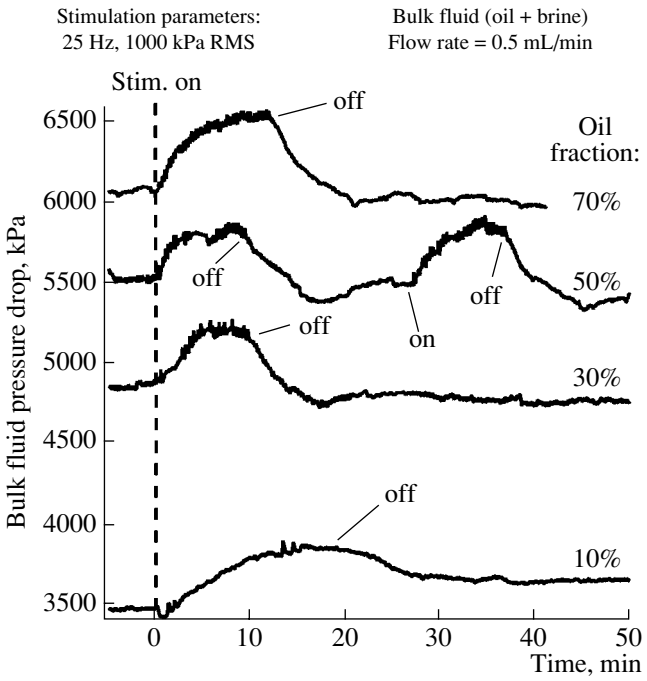


**Fig. 4.** Changes in bulk-fluid pressure drop during steady-state two-phase flow of ten-weight oil–brine, induced by 25-Hz stress stimulation for different oil-to-water ratios.

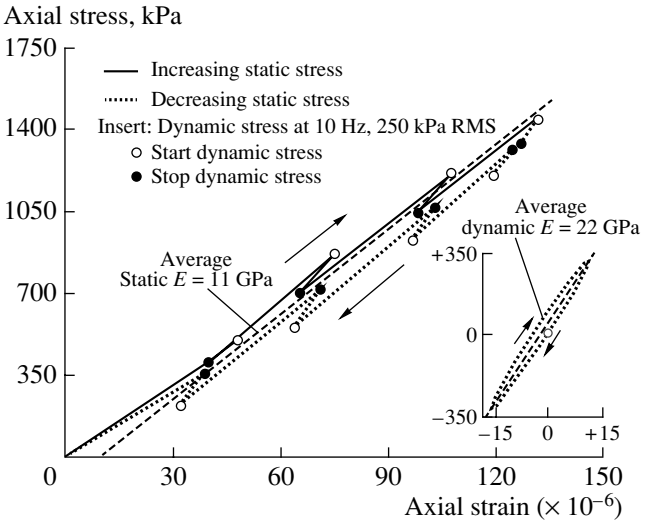


**Fig. 5.** Static and dynamic axial stress vs. strain data obtained for dry Berea sandstone.

stone. The dynamic Young's modulus is twofold larger than the static value, as has been noted by others [21]. Similar data for radial versus axial strain also show hysteresis, but the static and dynamic Poisson's ratios are nearly identical. Additional dynamic measurements obtained at different frequencies and amplitudes showed that the dynamic Young's modulus varies only with applied strain amplitude and not with frequency, whereas the dynamic Poisson's ratio varies only with frequency. When the sample is saturated with brine, both the static and dynamic Young's moduli are three- to fourfold lower than their corresponding values for the dry case. Clearly, the elastic properties of the rock are strongly influenced by the frequency and amplitude of dynamic stress oscillations as well as by the fluid content of the pore space.

A major practical purpose of the stress, strain, and pore-pressure measurement systems is to provide estimates of stimulation parameters that cause observable changes in fluid flow behavior under laboratory conditions. Downhole stimulation sources to be used for field testing can then be designed to generate similar mechanical stress and/or pore-pressure perturbations within the Earth's crust. The mechanical-stress levels used in the laboratory tests ranged from 300 to 1200 kPa RMS, and the equivalent axial strains induced in the core were roughly $3 \times 10^{-5}$ to $8 \times 10^{-5}$, respectively. Altered flow behavior was observed only at RMS stress levels of 600 kPa and above. Because the stimulation was primarily mechanical, pore-pressure oscillations are induced through pore volume changes caused by deformational strain of the core's solid matrix. Measuring dynamic pore pressure during stimulated fluid flow is difficult because the tubing connecting the core confinement sleeve to the pressure transducers attenuates the signal when the frequency is higher than about 1 Hz. Instead, estimates for induced pore-pressure oscillations were obtained by measuring the fluid pressure near the center of the core at numerous static axial stress values. To get accurate measurements, the fluid flow inlet and outlet had to be closed to prevent fluid leakage from the core. Figure 6 shows the pore-pressure data obtained. Closed-system pressure is lower by a factor of 0.004 than the applied axial stress, as indicated by the linear fit to the data. The coupling between matrix deformation and pore pressure will be much weaker when fluid is allowed to escape from the core. Thus, the closed-system measurements represent upper bounds for pore-pressure oscillations during stimulated fluid flow, when the system is open at each end of the core. In other words, during steady-state fluid flow, dynamic axial stress stimulation at a RMS amplitude of 600 kPa (the threshold level at which altered flow behavior was observed) will induce pore-pressure oscillations much lower than 2.4 kPa in a 100-md Berea sandstone core.

## DISCUSSION

The laboratory results presented here provide compelling new evidence that low-frequency stress stimulation can strongly influence both single-phase and two-phase porous fluid flow behavior in sandstone cores. Depending on the physical conditions, both long-term (Fig. 2) and short-term (Figs. 3 and 4) changes in permeability and/or fluid mobility can be induced. This variable behavior is similar to that observed during numerous field tests on enhancing oil production with downhole seismic sources. Clearly, the stimulated flow

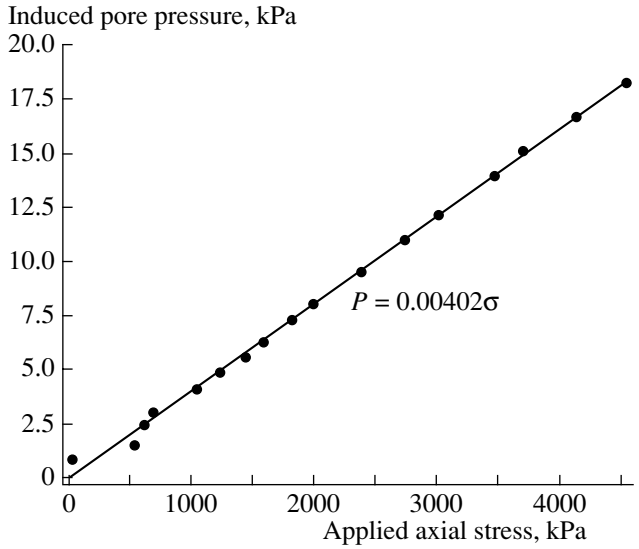


**Fig. 6.** Pore pressure versus static, axial, mechanical stress for brine-saturated Berea sandstone. Measurements were made with the fluid flow system closed.

phenomenon can be observed over a wide range of size scales, but major questions persist about what the possible physical mechanisms are that control the phenomenon and whether or not they are scale-independent. The core flow tests reported here partially bridge the scale range gap by investigating stress stimulation frequencies below 100 Hz, which is where, in the field, virtually all of the successful long-range reservoir stimulation tests have been conducted.

The clay-fines mobilization experiment is a good example of this. It is well known that ultrasonic waves at 20 kHz and above are effective at removing clay particles from porous rocks. This phenomenon has been investigated before [17, 19] and shown to depend on the wavelength of the excitation relative to the sample's size, geometry, and acoustic properties. Thus, it is somewhat surprising that 50-Hz stress cycling can produce similar effects on core samples that are roughly the same size as those used in the ultrasonics experiments. Because the wavelength at 50 Hz is orders of magnitude larger than the sample size, wave propagation does not occur. The core is simply being strained uniformly, as if it were a spring. Motion of clay particles relative to the fluid or porous matrix can occur, however, if local fluid pressure differentials or particle momentum perturbations are being generated within the pore space. Two possible mechanisms that could generate these dynamic effects are (1) phase delays between the solid-matrix, clay-particle, and fluid motions due to fluid viscoelastic effects and (2) pore-scale turbulence generated by transient fluid motion around the clay particles themselves. Both mechanisms are supported by the observation that particle mobilization is more effective at either lower absolute pore pressures or lower fluid pressure gradients during flow. This may indicate that a fluid-dynamics-based mechanism is more likely than a mechanical-strain-based mechanism (i.e., pore expansion). Additional modeling and new experiments will be needed to adequately investigate these speculations.

A major practical implication of low-frequency particle mobilization is that a phenomenon that was previously thought to occur only at high frequencies and at very short distances (10–20 cm or less) may prove to be useful for improving formation permeability at much larger distances, perhaps up to 1000 m from the stimulation source. This could be used, for instance, to improve the hydrodynamic conductivity of silty groundwater aquifiers using a low-frequency seismic source in a single water well.

The two-phase flow experiments demonstrated that (i) low-frequency stress stimulation changes the bulk-fluid pressure drop across porous core samples during steady-state flow and (ii) the viscosity of the nonwetting phase relative to the wetting phase determines whether the pressure drop will increase or decrease. Because of the imposed constant-rate steady-state flow conditions, the pressure changes are in the directions one would expect for increased nonwetting-phase saturation in the core; that is, the ratio of flowing decane (or oil) to flowing brine is increased inside the core by dynamic stress stimulation, even though the injected fluid composition is fixed by the pumps.

One possible explanation for this behavior is that stimulation mobilizes the nonwetting fluid at the expense of previously mobile wetting fluid, thereby increasing the nonwetting-phase saturation of the bulk fluid flowing through the core. Thus, decane–brine pressures decrease because decane is less viscous than brine, and oil–brine pressures increase because ten-weight oil is more viscous than brine. This is speculation, because the actual mobile-fluid saturation in the core before and during stimulation could not be measured in these experiments. The data support this hypothesis, however, if we assume that a single physical mechanism (one that controls fluid phase mobility or, equivalently, the relative permeability of the rock to the nonwetting phase) is responsible for both the decane–brine and oil–brine observations.

One such mechanism is altered matrix wettability. Berea sandstone is a highly water-wet rock, meaning that water will spontaneously imbibe into and flow through the rock more readily than decane or oil. Thus, the connected flow paths through the pore space will favor containing brine over decane or oil, and the relative brine saturation of the core may be significantly different than that of the injected two-phase bulk fluid. Based on independent empirical observations comparing oil-wet and water-wet formation rocks [22], it has been proposed that stress oscillations are capable of temporarily changing a water-wet rock to become more oil-wet (and vice versa for an oil-wet rock). This mechanism, then, could change the mobile-fluid composition

as oil replaces some of the water in the flowing volume of the rock core. Assuming that the flowing portion of the core's pore volume is constant (no change in absolute intrinsic permeability), a change in bulk-fluid composition will change its effective viscosity and will thus cause pressure drop changes across the core during steady-state two-phase flow.

Other mechanisms that could cause effects such as absolute permeability changes or induced emulsification of the two-phase mixture would also cause pressure drop changes, but these would cause the pressure to change in the same direction regardless of the viscosity of the nonwetting phase. Again, new modeling and experimental efforts will be needed to prove or disprove the altered wettability hypothesis. It is clear, however, that low-frequency stimulation has a profound, repeatable effect on two-phase porous flow behavior that supports the hypothesis that a change in fluid distribution is being induced inside the core.

Mobilization of nonwetting fluids has been proposed to explain some of the field observations of enhanced oil production caused by downhole seismic sources [3]. Water floods are often used to displace trapped oil pockets, but a large percentage of in-place oil is bypassed by these floods. Stimulation may mobilize the trapped oil by changing the formation wettability and allowing it to be more efficiently swept by the water flood. Thus, prior knowledge of a formation's state of wettability may be an important criterion for selecting candidate fields that are likely to respond well to seismic stimulation.

The dynamic mechanical stress levels used in the core experiments (see Fig. 5) are significantly higher than what existing downhole sources produce at distances in excess of 100 m. However, the pore-pressure oscillations induced in the core by the applied mechanical stress were extremely low (see Fig. 6), namely, probably much less than 1 kPa RMS. For these two reasons, it is likely that pore-pressure changes are more important than mechanical strain for inducing enhanced porous flow. Devices that couple energy efficiently to the pore fluids may be preferred over devices that produce primarily elastic strain energy. This remains an open question, however, because mode conversions between various elastic wave types and how these waves couple to the formation pore pressure are strongly influenced by the physical conditions in the fluid-bearing formations.

The one clear target that we can define for effective wavefield parameters is that the source frequency range should be low enough to allow energy to propagate to the target zone, which may be up to several kilometers from the source well, with little loss of amplitude due to attenuation in the medium. The laboratory tests discussed above were all performed with stimulation frequencies of 75 Hz or less and are, thus, scaleable to the field. The stress–strain and pore-pressure measurements can provide input for theoretical and numerical models for stimulated fluid flow.

## CONCLUSIONS

Laboratory experiments on Berea sandstone cores demonstrated that low-frequency (25 to 75 Hz), axial, mechanical stress cycling at RMS amplitudes of 600 kPa and higher can induce significant changes in single-phase and two-phase fluid flow behavior through porous media. During single-phase brine flow, dynamic stress stimulation mobilized *in situ* clay fines that were partially plugging the pores and increased the absolute permeability of the samples by 15 to 20%. Possible physical mechanisms that could explain this observation are (1) viscoelastic phase delays producing relative motion between the pore matrix, fluid, and clay particles and (2) turbulence and particle agitation caused by oscillating fluid-pressure gradients near the clay particles. During two-phase, steady-state flow of immiscible decane–brine and oil–brine mixtures, stimulation changed the bulk-fluid pressure drop across the cores in a manner that suggests that the relative saturations of the nonwetting (decane and oil) fluids was increased. The viscosity of the nonwetting phase relative to the wetting phase (brine) determines whether the pressure drop will increase or decrease during stimulation. Altered matrix wettability is one physical mechanism that could explain these observations. The data presented are largely empirical, and additional experiments and comparisons with theoretical and numerical models will be required to prove or disprove these speculations. Accurate measurements of stress and strain used during the experiments provided estimates of both static and dynamic elastic properties of dry and saturated Berea sandstone. Young's modulus during 10-Hz dynamic stress stimulation is twofold larger than the static value. When the rock is saturated with brine, both the static and dynamic moduli are three- to fourfold lower than for the dry case. The mechanical strain of the pore matrix caused by an applied dynamic stress of 600 kPa RMS was roughly $4 \times 10^{-5}$. The coupled pore-pressure fluctuations induced by this matrix deformation was estimated to be much lower than 2.4 kPa. Existing seismic sources used successfully in the field to enhance oil reservoir production cannot produce stress and strain levels as high as those used in the laboratory but can produce similar small pore-pressure fluctuations. This may indicate that pore pressure is more important than mechanical strain for enhancing porous flow.

## ACKNOWLEDGMENTS

This work was supported in part by the United States Department of Energy (DOE), Office of Fossil Energy; the National Petroleum Technology Office (NPTO), under the Natural Gas and Oil Technology

Partnership (NGOTP); and by the U.S. DOE, Office of Basic Energy Sciences (OBES), Geosciences Division.

## REFERENCES


1. I. A. Beresnev and P. A. Johnson, Geophysics **59**, 1000 (1994).
2. V. N. Nikolaevskiĭ, G. P. Lopukhov, Y. Liao, and M. J. Economides, SPE Prod. Facil., 89 (1996).
3. S. A. Kostrov, W. O. Wooden, and P. M. Roberts, Oil Gas J. **99.36**, 47 (2001).
4. P. M. Roberts, S. A. Kostrov, W. O. Wooden, *et al.*, in *Proceedings of Society Explosion Geophysic Annual Meteengs, San Antonio, 2001* (San Antonio, 2001).
5. P. M. Roberts, I. B. Esipov, and E. L. Majer, Leading Edge **22** (5), 448 (2003).
6. P. M. Roberts, A. Sharma, V. Uddameri, *et al.*, Environ. Eng. Sci. **18** (2), 67 (2001).
7. M. Hilpert, D. Stopper, and G. H. Jirka, EOS Trans. Am. Geophys. Union **77** (46), F204 (1996).
8. L. N. Reddi and S. Challa, J. Environ. Eng. **120** (5), 1170 (1994).
9. O. L. Kouznetsov, E. M. Simkin, G. V. Chilingar, and S. A. Katz, J. Petrol. Sci. Eng. **19**, 191 (1998).
10. M. Hilpert, G. H. Jirka, and E. J. Plate, Geophysics **65**, 874 (2000).
11. D. R. Graham and J. J. L. Higdon, J. Fluid Mech. **425**, 31 (2000).
12. D. R. Graham and J. J. L. Higdon, J. Fluid Mech. **425**, 55 (2000).
13. Y. Pan and R. N. Horne, J. Geophys. Res. **105**, 11021 (2000).
14. D. Tsiklauri and I. A. Beresnev, Phys. Rev. E **63**, 046304 (2001).
15. W.-C. Lo, G. Sposito, and E. Majer, Adv. Water Resour. **25**, 1105 (2002).
16. F. A. L. Dullien, *Porous Media: Fluid Transport and Pore Structure* (Academic, New York, 1979).
17. A. Venkitaraman, P. M. Roberts, and M. M. Sharma, Soc. Petrol. Eng. J. Drilling Complet. **10** (3), 193 (1995).
18. P. M. Roberts, A. Venkitaraman, and M. M. Sharma, Soc. Petrol. Eng. J. Drilling Complet. **15** (1), 19 (2000).
19. P. Poesio, G. Ooms, M. E. H. Van Dongen, and D. M. J. Smeulders, Transp. Porous Media **54**, 239 (2004).
20. D. J. Holcomb, J. Geophys. Res. **86** (B7), 6235 (1981).
21. R. A. Guyer, K. R. McCall, G. N. Boitnott, *et al.*, J. Geophys. Res. **102**, 5281 (1997).
22. R. V. Westermark, J. F. Brett, and D. R. Maloney, SPE J. 67303 (2001).

*Acoustical Physics, Vol. 51, Suppl. 1, 2005, pp. S149–S155. Translated from Akusticheskiĭ Zhurnal, Vol. 51, Suppl., 2005, pp. 169–176.*


# Resonance Properties of Magmatic Structures

**A. L. Sobisevich* and O. V. Rudenko****

** Schmidt Joint Institute of Physics of the Earth, Russian Academy of Sciences, ul. Bol'shaya Gruzinskaya 10, Moscow, 123995 Russia*

*e-mail: alex@ifz.ru*

*** Physical Faculty, Moscow State University, Vorob'evy gory, Moscow, 119992 Russia*

*e-mail: rudenko@acs366.phys.msu.ru*

Received October 7, 2004

**Abstract**—The observation of quasi-harmonic spectral components in the response of volcanic structures to distant seismic events is reported. The resonance frequencies are associated with the presence of a magma center and a magma chamber that contain gas cavities or bubbles. The presence of the region with a reduced density in the vicinity of the Elbrus volcano is confirmed by independent gravimetric measurements and by the results of analyzing the geological data. © *2005 Pleiades Publishing, Inc.*

## RESULTS OF THE GEOLOGICAL-GEOPHYSICAL STUDY OF THE INTERNAL STRUCTURE OF THE ELBRUS VOLCANO

The analysis of the field of tectonic fragmentation [1] shows that the magma chamber of the Elbrus volcano at depths lower than 3 km has the form of a single center. Figure 1 shows the vertical section of this field, which goes through Elbrus and is oriented along the Caucasian ridge. One can distinguish (*4*) the region interpreted as the maternal center, which in the past was a magma source for volcanic chambers and paleoeruptions; (*5*) the region of anomalous fragmentation, which is identified as the Elbrus volcanic chamber; (*2, 3*) one of the possible ways for the cross-flow of the primary magma into the volcanic chamber; and (*1*) the isoline of the field of tectonic fragmentation. The relief along this profile is shown in the plot above the section.

The results of the analysis provide grounds to assume that the magma chamber is located directly under the Elbrus volcanic structure. Its lower boundary lies at a depth of about 8 km. The western boundary of the chamber is almost vertical, and the eastern boundary is inclined at an angle of about 45°. At a depth of approximately 5 km, the chamber width reaches 8 km and gradually decreases in the direction toward the surface. A sharp decrease in the chamber size starts from a depth of about 2 km, and at a depth of 1 km, its characteristic dimensions do not exceed $2 \times 2.5$ km.

The magma chamber of Elbrus lies closer to the western periphery of the maternal center and lies 10–12 km higher than it. It is clear that the supply of the magma material from the center to the chamber must go along some weakened zones. Exactly this zone is determined in the structure of the field of lithosphere tectonic fragmentation, being a mirror image of the weakened (boundary) zone of the western edge of the Trancaucasian transverse elevation. It can be observed from deep levels (depths of 40–45 km) up to a depth of about 12 km (figure).

This pattern agrees well with the data of gravimetric observations. During the period of 1960–2001, it was found that a negative gravitational anomaly occurs in the Elbrus region [2]. A latitude-oriented region of minimum values of the local gravitational field exists. The analysis of the reasons for the formation of this anomaly [2] revealed a relation of gravimetric data to the depth of occurrence and size of inhomogeneities and also their shapes and physical parameters of rocks.

It is natural to assume that, during many thousands of years, the differentiation of materials took place, and the magmatic mass had a variable density (light fractions accumulated at the top and heavy ones went down). It is also possible to assume that, in the upper part of the magma chamber, the volatile fractions were accumulated, which additionally affected the structure of the gravitation anomaly.

The inhomogeneity shape and the density distribution inside it can be manifold. According to [2, 3], the rocks under Elbrus are in a crystalline state. However, they are heated up at least to the melting temperature of diorites $T = 1250$°C. Therefore, the thermal expansion of rocks resulted in a considerable reduction of their density. As for the chamber itself, the rocks in it are in the state of magmatic melt. Therefore, in the process of diorite transition from the crystalline state to the melt, one can expect the next jump in density variation. For example, at $T = 1650$°C, the total decrease in the density of diorite relative to its density at 0°C reaches 490 kg/m$^3$.

If we assume that the temperature of the magmatic chamber is about 1650°C, this geological-geophysical interpretation corresponds to the most recent experimental data obtained from the studies of the modern structure of the gravitational field at the Earth's surface,

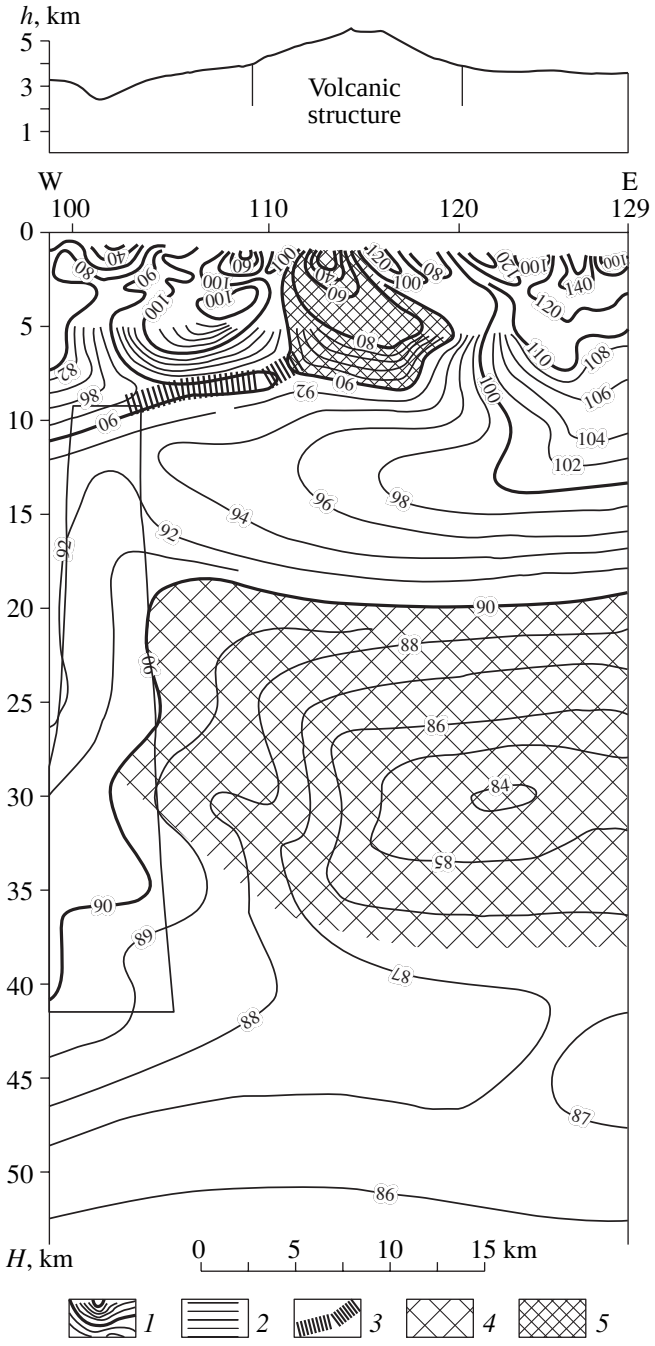


Vertical section of the field of tectonic fragmentation of the crust. The section passes through the Elbrus volcano and is oriented along the Caucasian ridge. (*1*) Isolines of the field of tectonic crust fragmentation (the solid lines correspond to sections at a step of 10 conventional units and the thin lines, at a step of 2 or 1 conventional unit); (*2*) region (zone) of increased fragmentation of the lower part of the crust; (*3*) near-horizon weakened zones (a possible way for primary magma flows into the volcanic chamber); (*4*) region of anomalously low field values at the top of the basalt crust: this region is considered as a potential maternal magmatic center, which was in the past the source of material for filling the volcanic chambers; and (*5*) region of anomalously low field values in the upper part of the crust: this region is identified as the volcanic chamber.

which was studied in detail in 1994–2000 [4]. These results agree well with the conclusions of [2, 3].

Let us turn our attention to the important fact that the Elbrus lava has a porous texture and, consequently, a very low density of 1800–2500 kg/m$^3$. This texture could be formed as a result of the surface flow of magma enriched by volatiles. A sharp decrease of pressure in the process of magma motion to the crater was accompanied by effervescence of gases and boiling of lava, which lead to the formation of cavities in the process of its solidification. Thus, the low density of the Elbrus lava and its porous texture clearly indicate that magma containing a high percentage of gases accumulated in the magmatic chamber of the volcano during a long period of its activity. In the process of their development, the gas formations concentrated at the ceiling of the magmatic chamber and formed a resonant cavity (or several cavities) of considerable dimensions, which was surrounded by melt. Exactly these cavities, where the accumulation of volatiles occurs under high pressure, are associated by many researchers with potential sources of explosion eruptions.

The magma center and the chamber, which are filled with magma and volatiles, can be treated as resonance structures of complex shapes. Under the effect of a broadband seismic perturbation, these structures form secondary geophysical fields in their vicinity, which also contain information on the resonance properties of inhomogeneities.

It is determined that the induced infrasound field in the vicinity of the Elbrus volcano, which reflects the dynamic properties of the magmatic chamber and center, is characterized by the presence of quasi-harmonic components [4, 5]. The presence of magma (its composition, temperature, and viscosity) determines the $Q$ factors of magmatic formations as resonance systems. Moreover, the components connected with the presence of "converted" waves (resulting from multiple reflections at the interfaces of the layered medium) exist in the spectrum of induced infrasound processes. It is necessary to note that, in the frequency range lower than 5–10 Hz, converted waves are almost absent.

While characterizing the processes of formation of the secondary (extremely low-frequency) wave fields in the region of the volcanic structure, it is necessary to take into account the fact that inhomogeneous rupture-block structures are a kind of a filter for transverse waves and weakly affect the longitudinal component. Experimental studies demonstrated that, in the case of an active seismic impact, the resonance structures of the Elbrus volcano are responsible for the appearance of longitudinal waves in the spectrum with the characteristic frequencies in the range of 0.001–0.2 Hz. The observations of induced infrasound fields in the vicinity of the Elbrus volcanic center were conducted for many big seismic events detected by the Baksan laser interferometer [5].

Periods of resonance modes (in seconds) for magmatic formations of the Elbrus volcano according to deformographic observations

| Period of the resonance mode (s) | 70.7 | 68.1 | 66.0 | 64.0 | 61.8 | 59.4 | 56.7 | 52.2 | 49.9 | 45.7 | 44.0 | 42.4 | 40.6 |
|---|---|---|---|---|---|---|---|---|---|---|---|---|---|
| Standard deviation (s) | 0.4 | 0.3 | 0.5 | 0.4 | 0.4 | 0.4 | 0.5 | 0.5 | 0.5 | 0.4 | 0.4 | 0.2 | 0.2 |
| Number of earthquakes | 7 | 19 | 25 | 17 | 16 | 17 | 20 | 10 | 28 | 16 | 17 | 20 | 15 |

## THE BAKSAN LASER INTERFEROMETER-DEFORMOGRAPH AND THE OBSERVATION RESULTS

The geodynamic observatory of Moscow State University is located in the Baksan Valley (Neutrino settlement), 30 km south-east of Tyrnyauz and 20 km away from the Elbrus volcanic structure. A broadband laser interferometer-deformograph is installed at the mark of 650 m along the Main Gallery of the Baksan neutrino observatory of the Nuclear Research Institute. It goes down to 4200 m into the massif (the Andyrchi mountain). The interferometer coordinates are 43°12′ latitude, 42°43′ longitude, and 150°37′ azimuth.

The device is a double-pass unequal-arm Michelson interferometer with a measuring arm 75 m in length. The optical paths of the interferometer are completely evacuated (the pressure $p \approx 5 \times 10^{-5}$ mbar). An electronic detection system provides for the interferometer operation in a wide frequency band, starting from super-low frequencies (restricted only by the length of a series of continuous measurements and the methods used for spectral analysis) up to thousands of hertz. In the normal mode of monitoring lithosphere deformations, the data acquisition is performed through three channels: the low-frequency infrasound channel (from 0.1 Hz and lower), the infrasound channel (at a frequency of 30 Hz within the band of 1 Hz), and the acoustic channel (at a frequency of 1620 Hz within the band of 0.5 Hz; the detection of quadrature components) [6, 7].

In 2000–2001, the results of gravimetric data processing indirectly confirmed the existence of a powerful (up to 15–20 km in diameter) zone of thinning under Elbrus, which is characterized by a reduced elasticity and increased viscosity of the heated substance. The amplitudes of diurnal and semi-diurnal tidal waves turned out to be understated to a certain extent relative to the model values, which is evidence of the presence of a zone with an anomalously low elasticity in the zone crust. In the seismic range (periods of 50–100 s), a series of resonance modes excited only by very close and strong earthquakes were detected. Below, we analyze a series of events detected by the interferometer in 1998–2001.

The earthquakes used as the sources of external excitation for the detection of resonances were conditionally divided into three groups according to seismic manifestations and distance.

The first group included the nine strongest earthquakes with magnitudes from 7.5 to 8.3 MW. Three of them (at the Balleni Islands, March 25, 1998, 8.1 MW; in Salvador, January 13, 2001, 7.7 MW; and in Peru, June 23, 2001, 8.3 MW) belong to high-energy seismic events. In this case, considerable amplitude values are observed for the evaluated modes of induced oscillations in the region of the volcanic structure (one hundred and more in the units of signal-to-noise ratio).

The second and most numerous group (20 events) includes strong earthquakes with magnitudes from 6.8 to 7.6 MW.

Finally, the last group is composed of the earthquakes that happened “not far” from the Baksan Valley. It includes four events: in Afghanistan, May 30, 1998, 6.6 MW; Turkey, August 17, 1999, 7.7 MW; Baku, November 25, 2000, 6.3 MW; and Turkmenistan, December 6, 2000, 7.0 MW. Here, the Turkish earthquake (taking into account its closeness) can also be treated as one of the strongest from the point of view of its effect on the magmatic structures under investigation.

Quantitative estimates for the resonance frequencies excited by the aforementioned earthquakes and not connected with the natural frequencies of the Earth’s oscillations are given in the table. In this range, the lowest-frequency mode with a period of ~71 s is excited only by the strongest earthquakes (a magnitude of ~8 MW). It is detected in the response spectrum for only seven events. Then, a whole series of modes follows, which are steadily detected for the majority of the strongest earthquakes. It is interesting that the structure of the modes excited by “close” earthquakes has some distinctive features: the extremely low-frequency modes are absent while the modes whose periods fall within 40–58 s are well represented [8].

The positions of the central frequencies of spectral lines fluctuate to a certain extent. This is likely to be connected with the complexity of the shapes of the magmatic chamber and center and their different orientations with respect to the foci of different seismic events. This means that the conditions for the interaction of the wave front with the structure differ for different events, which influences the conditions for the excitation of the natural frequencies of resonance structures.

The experimental data on the natural frequencies of the magma center and chamber are the basis for the development of the models for the evaluation of the dimensions and physical properties of inhomogeneous structures. At the same time, these data are clearly insufficient to correctly solve the inverse problems of

an exact reconstruction of the geometrical and physical parameters of scattering objects.

## NONLINEAR AND RESONANCE RESPONSES OF A POROUS MEDIUM NEAR THE MELTING TEMPERATURE

The detected signals resulting from the scattering of elastic waves by inhomogeneous geophysical structures in many cases contain surges at certain frequencies. Lines in the spectrum of a scattered signal are often explained by the resonance phenomena of the origin that is still not quite clear. One may assume that there are inhomogeneities in the media, which either reflect the waves at certain selected frequencies or form resonators with discrete mode spectra in which the energy of natural vibrations can accumulate.

In the experiments described above, in analyzing the seismic signals received near the Elbrus volcano, spectral lines were observed that represented the responses to distant earthquakes. These lines could be associated with the resonances of inhomogeneous structures under Elbrus. However, estimates show that even the presence of the magmatic center containing melted rock does not cause any reflecting boundaries with a sufficient "contrast" in the impedance $\rho c_l$, where $\rho$ is the density of the medium and $c_l$ is the propagation velocity of longitudinal waves. At the same time, a strong contrast arises for transverse waves in the vicinity of the melting point, where the shear modulus $\mu$ and, therefore, the velocity $c_t$ vanish. This feature can noticeably affect the behavior of not only transverse but also longitudinal waves.

An illustrative example of such an effect can be the result known from the dynamic theory of elasticity [9]. If a spherical cavity with radius $R$ vibrates in a medium with a small value of the shear modulus $\mu$, its natural frequency $\omega_0$ and the attenuation coefficient $\delta$ are expressed as

$$\omega_0 = \frac{2c_t}{R}, \quad \delta = \frac{2c_t^2}{c_l R}. \tag{1}$$

It is interesting that the length of the radiated longitudinal wave

$$\lambda_l = \pi\frac{c_l}{c_t}R \gg R \tag{2}$$

is greater than the radius of the vibrating cavity. The relation $\lambda_l/R \gg 1$ is characteristic of concentrated systems or Helmholtz resonators where the vibrating mass is large and the elasticity is small. The attenuation of vibrations during the period is equal to $2\pi\delta/\omega_0 \ll 1$. This means that the cavity vibrations decay slowly loosing their energy for the radiation of longitudinal waves. The $Q$ factor of vibrations that determines the relative width of the spectral line of a frequency response

$$Q = \frac{\omega_0}{\Delta\omega} = \frac{\omega_0}{2\delta} = \frac{c_l}{2c_t} \gg 1 \tag{3}$$

is large. On the one hand, this means that the spectral line of the response is very narrow. On the other hand, the incident signal at the frequency $\omega_0$ is amplified by the cavity by a factor of $Q$, which leads to a noticeable growth of the component $\omega_0$ in the spectrum of the scattered field.

Under actual conditions, it is necessary to take into account the loss for the frequency-dependent friction in the case of a shear deformation of the medium. Moreover, one needs to know how to calculate the response to an incident pulsed or noiselike signal with a broad frequency spectrum. Finally, in the case of strong deformations, it is necessary to solve the problem in a nonlinear formulation.

To develop a dynamic model for a porous medium with the temperature close to the melting point, we consider the basic problem on nonlinear oscillations of a single spherical cavity.

We treat the continuous medium surrounding the cavity as a very viscous isotropic liquid with a shear modulus $\mu$ strongly depending on the prehistory of local loading. The relation between the strain and stress tensors, $u_{ik}$ and $\sigma_{ik}$, in such a medium in the case of shear deformations is given by the expression

$$\begin{aligned}\sigma_{ik} &= 2\mu\int_{-\infty}^{t}\frac{\partial u_{ik}}{\partial t'}\exp\left(-\frac{t-t'}{\tau}\right)dt' \\ &= 2\mu\frac{\partial}{\partial t}\int_0^\infty u_{ik}(t-\xi)\exp\left(-\frac{\xi}{\tau}\right)d\xi.\end{aligned} \tag{4}$$

Here, $\tau$ is the temperature-dependent relaxation time. The higher the temperature, the smaller the relaxation time is in the general case. The process of approaching the equilibrium state occurs according not to an exponential but to a more complex law. In this case, the integral kernel in Eq. (4) must be changed for the function $G(\xi/\tau)$ of a more complex form. If $\omega\tau \gg 1$, where $\omega$ is the frequency of the incident wave, the integral relationship of Eq. (4) can be represented in the form of a series in powers of $1/\tau$:

$$\sigma_{ik} \approx 2\mu u_{ik} - \frac{2\mu}{\tau}\int_0^\infty u_{ik}(t-\xi)d\xi. \tag{5}$$

In the opposite limit of low frequencies or small relaxation times, it is possible to use the expansion in powers of $\tau$:

$$\sigma_{ik} \approx 2\mu\tau\frac{du_{ik}}{dt} - 2\mu\tau^2\frac{d^2u_{ik}}{dt^2}. \tag{6}$$

The first (principal) term in the expansion given by Eq. (6) means that, in the limiting case $\omega\tau \ll 1$, the medium behaves as a liquid with the viscosity being the product of the modulus of shear elasticity by the relaxation time: $\eta = \mu\tau$.

In what follows, we assume that the shear modulus is small in comparison with the bulk modulus, i.e., $\mu \ll K$. In this case, the wave equation for this medium takes the form

$$\frac{\partial^2 \mathbf{U}}{\partial t^2} = c_l^2 \nabla \mathrm{div}\mathbf{U} + c_t^2 \Delta \frac{\partial}{\partial t}\int_0^\infty G\left(\frac{\xi}{\tau}\right)\mathbf{U}(\mathbf{r}, t-\xi)d\xi. \quad (7)$$

Now, let us consider a spherical cavity in this medium and assume that this cavity performs radially symmetric vibrations excited by the pressure of the incident wave. We assume that a compressible gas fills the cavity. We write down the boundary condition at the surface $r = R$ by equating the components of the stress tensor $\sigma_{rr}$ on both sides of the boundary:

$$\frac{P(t)}{\rho_0} = \frac{p(t)}{\rho_0} - c_l^2\left(\frac{\partial U}{\partial r} + U\right) - 2c_t^2 \frac{\partial}{\partial t}\int_0^\infty G\left(\frac{\xi}{\tau}\right)\frac{\partial U(t-\xi)}{\partial r}d\xi. \quad (8)$$

Here, $P(t)$ is the external pressure of the incident wave, $p(t)$ is the gas pressure in the cavity, and $U$ is the radial velocity component. In the process of vibration, the cavity emits a divergent spherical wave with the potential that must satisfy the wave equation and be described by the function

$$\varphi(r, t) = \frac{1}{r}\Phi\left(t - \frac{r-R}{c_l}\right), \quad U = \frac{\partial \varphi}{\partial r}. \quad (9)$$

Substituting Eqs. (9) into Eq. (8) and assuming that $r = R$, we reduce Eq. (8) to the form

$$\frac{d^2\Phi}{dt^2} + 2\frac{c_t^2}{c_l^2}\frac{d}{dt}\int_0^\infty G\left(\frac{\xi}{\tau}\right)\hat{L}\Phi(t-\xi)d\xi - \frac{R}{\rho_0}p(t) = -\frac{R}{\rho_0}P(t). \quad (10)$$

Here, to abridge the expression, we used the following notation for the differential operator:

$$\hat{L} = \frac{d^2}{dt^2} + 2\frac{c_l}{R}\frac{d}{dt} + 2\frac{c_l^2}{R^2}. \quad (11)$$

The internal pressure of the gas varies in the process of vibration of the spherical cavity that is accompanied by a variation of cavity volume. It is also possible to express the pressure through the potential:

$$-p(t) = \frac{3c_g^2\rho_g}{c_l R^2}\left(\frac{d\Phi}{dt} + \frac{c_l}{R}\Phi\right) + (\varepsilon - 1)\frac{c_g^2}{\rho_g}\left[\frac{3\rho_g}{c_l R^2}\left(\frac{d\Phi}{dt} + \frac{c_l}{R}\Phi\right)\right]^2. \quad (12)$$

Here, $c_g$ and $\rho_g$ are the sound velocity in the gas and its density and $\varepsilon$ is the nonlinear parameter [10], which, for the equation of state in the form of an adiabatic, is equal to $(\gamma + 1)/2$. Here, $\gamma = c_p/c_v$ is the ratio of heat capacities at constant pressure $c_p$ and constant volume $c_v$.

Taking into account relation (12), we represent Eq. (10) in the form

$$\frac{d^2\Phi}{dt^2} + \frac{4c_t^2}{c_l R}\left[1 + \frac{R}{2c_l}G'(0) + \frac{3}{4}\frac{c_g^2\rho_g}{c_t^2\rho_0}\right]\frac{d\Phi}{dt} + \frac{4c_t^2}{R^2}\left[1 + \frac{R}{c_l}G'(0) + \frac{R^2}{2c_l^2}G''(0) + \frac{3}{4}\frac{c_g^2\rho_g}{c_t^2\rho_0}\right]\Phi + (\varepsilon - 1)\frac{9}{R^3}\frac{c_g^2\rho_g}{c_l^2\rho_0}\left(\frac{d\Phi}{dt} + \frac{c_l}{R}\Phi\right)^2 + \frac{4c_t^2}{R^2}\int_0^\infty\left[G'\left(\frac{\xi}{\tau}\right) + \frac{R}{c_l}G''\left(\frac{\xi}{\tau}\right) + \frac{R^2}{2c_l^2}G'''\left(\frac{\xi}{\tau}\right)\right]\Phi(t-\xi)d\xi = -\frac{R}{\rho_0}P(t). \quad (13)$$

Ignoring the influence of nonlinearity and lag of internal processes in the medium, i.e., assuming that $\varepsilon = 1$ and $\tau \longrightarrow \infty$, we first consider the simplest particular case. In this case, Eq. (10) takes on the form

$$\frac{d^2\Phi}{dt^2} + \frac{4c_t^2}{c_l R}\left[1 + \frac{3}{4}\frac{c_g^2\rho_g}{c_t^2\rho_0}\right]\frac{d\Phi}{dt} + \frac{4c_t^2}{R^2}\left[1 + \frac{3}{4}\frac{c_g^2\rho_g}{c_t^2\rho_0}\right]\Phi = -\frac{R}{\rho_0}P(t). \quad (14)$$

As it follows from the structure of Eq. (14), the natural frequency of vibrations and their attenuation are given by the expressions

$$\omega_0 = \frac{2c_t}{R}\left[1 + \frac{3}{4}\frac{c_g^2\rho_g}{c_t^2\rho_0}\right]^{1/2}, \quad \delta = \frac{2c_t^2}{c_l R}\left[1 + \frac{3}{4}\frac{c_g^2\rho_g}{c_t^2\rho_0}\right]. \quad (15)$$

The $Q$ factor for the oscillation system described by Eq. (14) is equal to

$$Q = \frac{c_l}{2c_t}\frac{1}{\sqrt{1+\frac{3}{4}\frac{c_g^2\rho_g}{c_t^2\rho_0}}}. \quad (16)$$

Equations (15) were obtained earlier in [11]. It is necessary to note that they differ substantially from the well known Eqs. (4), since, together with the shear viscosity of the medium, they take into account the elasticity of the gas within the spherical cavity. When the medium melts and transforms into a liquid, $c_t \longrightarrow 0$ and the first of Eqs. (15) transforms into the well-known Minnaert formula for the resonance frequency of vibrations of a gas bubble in a liquid [12]. The $Q$ factor given by Eq. (16) does not contain a singularity at $c_t \longrightarrow 0$ in contrast to Eq. (6). The value of $Q$ is large in all cases and reaches its peak value equal to

$$Q = \frac{c_l}{c_g}\sqrt{\frac{\rho_0}{3\rho_g}} \quad (17)$$

when the shear elastic modulus of the medium vanishes.

We could not find any reliable modern data on the temperature dependences of shear elasticity or propagation velocity of transverse waves in the vicinity of the melting temperature for magmatic rocks. As it is demonstrated in the basic work [13], the shear elasticity of polycrystalline materials can drop down noticeably already at the temperatures much lower than the melting temperature. For rough estimations, we take that $c_t \approx c_g = 300$ m/s and $\rho_0/\rho_g = 3000$. In this case, it follows from Eq. (15) that $Rf_0 \approx 100$ m/s; i.e., for frequencies of about 0.1 Hz, the cavity radius must be about 1 km and the $Q$ factor given by Eq. (17) is equal to 7.5. As the shear elasticity decreases (or temperature grows), the cavity size corresponding to the natural frequency of 0.1 Hz decreases and the $Q$ factor increases.

Now, let us consider the important limiting case of low-frequency vibrations, when the characteristic time variation of the cavity volume is large in comparison with the characteristic time of relaxation processes in a very viscous medium, $\omega\tau \ll 1$. In this case, vibration equation (13) takes the form

$$\frac{d^2\Phi}{dt^2} + \frac{4}{\tau}\left(\frac{c_l\tau}{R}\right)\frac{\left(\frac{c_t}{c_l}\right)^2\left(\frac{c_l\tau}{R}\right)+\frac{3}{4}\frac{c_g^2\rho_g}{c_l^2\rho_0}}{1+\left(\frac{c_t}{c_l}\right)^2\left(\frac{c_l\tau}{R}\right)}\frac{d\Phi}{dt} + \frac{3}{\tau^2}\frac{\left(\frac{c_l\tau}{R}\right)^2\frac{c_g^2\rho_g}{c_l^2\rho_0}}{1+\left(\frac{c_t}{c_l}\right)^2\left(\frac{c_l\tau}{R}\right)}\Phi = -\frac{R}{\rho_0}P(t). \quad (18)$$

Note that the term with the third derivative, in which the coefficient $(c_t/c_l)^2\omega\tau$ is very small (in the approximation under consideration), is omitted. The $Q$ factor corresponding to the oscillator described by Eq. (18) is equal to

$$Q = \frac{\sqrt{3}}{4}\frac{\sqrt{\frac{c_g^2\rho_g}{c_l^2\rho_0}}\sqrt{1+\left(\frac{c_t}{c_l}\right)^2\left(\frac{c_l\tau}{R}\right)}}{\left(\frac{c_t}{c_l}\right)^2\left(\frac{c_l\tau}{R}\right)+\frac{3}{4}\frac{c_g^2\rho_g}{c_l^2\rho_0}}. \quad (19)$$

Since the data on the shear elasticity and the relaxation time are insufficient, we use the formula $\eta = \mu\tau$ or $c_t^2 = \eta/\tau\rho_0$. In this case, the natural frequency and the $Q$ factor are written as

$$\omega_0 = \sqrt{3}\frac{c_g}{R}\sqrt{\frac{\rho_g}{\rho_0}}\left(1+\frac{\eta}{\rho_0 c_l R}\right)^{1/2},$$
$$Q = \frac{\sqrt{3}}{4}\frac{\sqrt{\frac{c_g^2\rho_g}{c_l^2\rho_0}}\sqrt{1+\frac{\eta}{\rho_0 c_l R}}}{\frac{3}{4}\frac{c_g^2\rho_g}{c_l^2\rho_0}+\frac{\eta}{\rho_0 c_l R}}. \quad (20)$$

To estimate by Eqs. (20), it is necessary to have numerical values for shear elasticity. As it is demonstrated in [14], the results of recent measurements contradict the common ideas concerning the increase in viscosity with increasing pressure. For basalt lava at a small pressure, an empirical formula [15] is valid:

$$\eta = \eta_0 \exp(b/T), \quad (21)$$

where the constants $\eta_0$ and $b$ vary within the ranges from 1.3 to 6 P and from 2.65 to 2.73 K, respectively. One can readily see that, near the melting temperature, which for basalt is equal to 1150 K, the viscosity is on the order of magnitude of $10^4$–$10^5$ Ps, and we can ignore the viscosity in Eqs. (20) for the cavity radii greater than 1 cm. This cannot be done for more viscous melts.

Estimating the radius of the resonance cavity by Eqs. (20) for a frequency of 0.1 Hz and the parameters of the medium used above in estimates by Eqs. (15) and (16), we obtain a value of about 20 m.

It is possible to imagine a different situation, where not a single cavity but an extended region with increased gas content vibrates in a melted magma. In this case, the density of this region is somewhat smaller than in the absence of volatiles, but the velocity of longitudinal waves may decrease rather strongly. Water with gas bubbles can be an example. The sound velocity in it can decrease down to 30–40 m/s, which is much smaller than the sound velocities in both pure water and pure gas. Assuming that $\rho_g/\rho_0 = 1$ and $c_g = 100$ m/s in Eq. (20), we estimate the radius of a gas-saturated

region with a resonant frequency of 0.1 Hz and a size of about 300 m.

If there is a geological structure containing a strongly viscous liquid with gas-filled cavities (for example, the magmatic chamber of a volcano or the center of a mud geyser), a decrease in two parameters must occur with temperature growth; i.e., the relaxation time $\tau$ and the propagation velocity of shear waves $c_t$ should decrease; at the same time, the size $R$ of the gas-containing cavity must increase. All three trends lead to the growth of the $Q$ factor (Eq. (20)) and, therefore, to an increase in the intensity of the scattered field at low frequencies corresponding to the resonances of the oscillating system described by Eq. (18). In the cases, where an incident wave is strong or the duration of action on a high-quality resonance structure is sufficient for considerable energy accumulation in the cavity, the appearance of a nonlinear response at higher harmonics and combination frequencies, which is described by the nonlinear terms of Eq. (13), is possible. In all the cases, the increase in the structure response, the appearance of the resonance peaks in the spectrum of the scattered signal, and spectrum enrichment with harmonics must be evidence of the temperature rise connected with the growing activity of geological processes.

The linear response of the cavity is calculated by the known formulas. In the particular cases, for the models of Eqs. (14) and (18), the velocity potential of the radiated wave is described by the expression

$$\Phi(t) = -\frac{R}{\rho_0}\int_0^\infty P(t-\xi)\exp(-\delta\xi)\frac{\sin(\xi\sqrt{\omega_0^2-\delta^2})}{\sqrt{\omega_0^2-\delta^2}}d\xi. \quad (22)$$

If the incident wave may be treated as stationary noise, the correlation function for the scattered signal is equal to

$$B(t = t_1 - t_2) = \langle\Phi(t_1)\Phi(t_2)\rangle = \int_{-\infty}^{\infty} S_P(\omega)|K(\omega)|^2\exp(-i\omega t)d\omega, \quad (23)$$

where $S_P(\omega)$ is the intensity spectrum of the incident noise $P(t)$ and $K(\omega)$ is the complex transfer function of the system. In particular, for Eqs. (14) and (18), we have

$$|K(\omega)^2| = \frac{1}{(\omega_0^2-\omega^2)^2+4\delta^2\omega^2}. \quad (24)$$

For a concentrated system, the motion of which is described by linearized Eq. (13), it is simple to obtain generalized expression (24) and calculate the linear spectral response

$$S_\Phi(\omega) = S_P(\omega)|K(\omega)|^2, \quad S_\Phi(\omega) = \left|\frac{1}{2\pi}\int_{-\infty}^{\infty}\Phi(t)\exp(-i\omega t)dt\right|^2. \quad (25)$$

In the presence of a weak nonlinearity, the response also be can calculated analytically. In more complex cases, where the contribution of nonlinear effects is comparable in magnitude with the linear response, it is necessary to use numerical simulation. These data will be published later. Moreover, it seems to be important to perform a generalization of the results presented above to media containing cavities of different size distributed over the volume.

## ACKNOWLEDGMENTS

This work was supported in part by the Russian Foundation for Basic Research (project nos. 02-02-16100 and 03-05-64020-a), Program no. 13 of the Presidium of the Russian Academy of Sciences (project no. 1.4), and the Foundation in Support of Domestic Science.

## REFERENCES

1. Yu. V. Nechaev and A. L. Sobisevich, in *Proceedings of 3rd International Aerospace Congress, Moscow, Russia, 2000* (Moscow, 2000), p. 293.
2. M. V. Avdulov, Sov. Geol., No. 9, 73 (1963).
3. M. V. Avdulov, Izv. Akad. Nauk SSSR, Ser. Geogr. Geofiz., No. 9, 67 (1962).
4. E. A. Rogozhin, L. E. Sobisevich, Yu. V. Nechaev, *et al.*, in *Geodynamics, Seismotectonics and Volcanism of Northern Caucasus*, Ed. by N. P. Laverov (Obl. Inst. Fiz. Zemli Ross. Akad. Nauk, Moscow, 2001) [in Russian].
5. L. E. Sobisevich, Yu. V. Nechaev, A. L. Sobisevich, *et al.*, in *Monitoring of Magmatic Structures of Elbrus Volcano*, Ed. by N. P. Laverov (Obl. Inst. Fiz. Zemli Ross. Akad. Nauk, Moscow, 2001) [in Russian].
6. V. K. Milyukov and V. K. Kravchuk, Vestn. Mosk. Univ., Ser. 3: Fiz., Astron., No. 2, 73 (1996).
7. V. K. Milyukov, V. N. Rudenko, B. S. Klyachko, *et al.*, Izv. Akad. Nauk Ser. Fiz. **63** (6), 1192 (1999).
8. L. E. Sobisevich, V. K. Milyukov, and A. L. Sobisevich, in *Modern Mathematical and Geological Models in the Problems of Applied Geophysics*, Ed. by V. N. Strakhov (Obl. Inst. Fiz. Zemli Ross. Akad. Nauk, Moscow, 2001), pp. 223–248 [in Russian].
9. L. D. Landau and E. M. Lifshitz, *Theory of Elasticity* (Nauka, Moscow, 1986; Pergamon, Oxford, 1986).
10. O. V. Rudenko and S. I. Soluyan, *Theoretical Foundations of Nonlinear Acoustics* (Nauka, Moscow, 1975; Consultants Bureau, New York, 1977).
11. V. N. Alekseev and S. A. Rybak, Akust. Zh. **45**, 603 (1999) [Acoust. Phys. **45**, 535 (1999)].
12. M. A. Isakovich, *General Acoustics* (Nauka, Moscow, 1973) [in Russian].
13. V. N. Zharkov, Trudy Inst. Fiz. Zemli Akad. Nauk SSSR, No. 11, 36 (1960).
14. V. N. Mineev and A. I. Funtikov, Usp. Fiz. Nauk **174** (7), 727 (2004).
15. A. E. Scheidegger, *Physical Aspects of Natural Catastrophes* (Elsevier, Amsterdam, 1975; Nedra, Moscow, 1981).

*Translated by M. Lyamshev*

*Acoustical Physics, Vol. 51, Suppl. 1, 2005, pp. S2–S11. Translated from Akusticheskiĭ Zhurnal, Vol. 51, Suppl., 2005, pp. 6–18.*


# Deformation- and Fracture-Induced Acoustic Emission in Rocks

**A. V. Lavrov and V. L. Shkuratnik**

*Moscow State Mining University, Leninskiĭ pr. 6, Moscow, 117935 Russia*

*e-mail: ftkp@mail.ru*

Received August 17, 2004

**Abstract**—The informative parameters and the behavior of the acoustic emission that accompanies the deformation and fracture of rock samples under various conditions of mechanical loading, thermal action, and humidification are considered. The main directions of the development of models for the acoustic emission in geological materials are analyzed. © *2005 Pleiades Publishing, Inc.*

## INTRODUCTION

Acoustic emission (AE) is the phenomenon of emitting elastic waves as a result of irreversible or partially reversible changes in the structure of a solid under the action of various external and internal physical factors. It is commonly believed that this phenomenon was discovered in the middle of the 19th century in connection with tin deformation, which was accompanied by specific acoustic effects called tin cry.

In 1928, A.F. Ioffe published a paper on the mechanical properties of crystals, which can be considered as the beginning of research into the acoustic emission of rocks [1]. This paper was the first to note that each particular event of stepwise deformation of rock salt is accompanied by a "clock-tick-like noise" and indicated the possibility of using this noise for studying the nature and behavior of the deformation.

Later, from the mid-1950s, it was realized that AE could become one of the most efficient means for real-time monitoring of rock fracture. This was largely due to the successful use of AE signals generated in a stressed rock for predicting hazardous effects in coal mines [2]. At the same time, a systematic study of the AE behavior in rock samples was started [3], which revealed a number of advantages of the AE method. In particular, this method is capable of detecting individual fracture events, which is impossible with such integral rock damage indicators as nonlinear deformation or variation in the propagation velocity and attenuation of elastic waves. Location of AE sources allows one to remotely determine the positions of fracture nuclei in space and decide on their variation in the process of loading. The latter circumstance favorably compares the AE method with microscopy, which only gives the fracture pattern for the moment when the experiment is over and is an essentially destructive testing method, because it uses thin sections.

The sources and mechanisms of AE in rocks are the growth and closure of microcracks and macrocracks, collapse of pores, twinning processes, motion of dislocations and their clusters and their outcrop at grain boundaries, etc. [4–7]. It has been repeatedly noted that AE is more pronounced the more inhomogeneous the material is. The fracture of a perfect crystal occurs abruptly and is not preceded by the AE. In an inhomogeneous material, the defects are activated as the load (temperature) is increased and become capable of producing AE signals long before the macrofracture occurs [8, 9].

Elastic waves produced by defects propagate in the bulk of the rock and undergo certain changes (attenuation and variations in the frequency spectrum). On reaching the surface, the elastic waves are received by a transducer. In some cases (for example, at high temperatures), an intermediate waveguide exists between the rock and the transducer, for example, a steel or quartz rod.

The signal received and converted to an electric pulse is transmitted through a cable to a front-end amplifier, which usually also acts as a preliminary band-pass filter. The noise component of the AE contains both high-frequency and low-frequency components. The low-frequency noise is produced by the test equipment used for loading the samples. The high-frequency noise is generated by electron devices and electromagnetic interference [10].

The output signal of the preamplifier is applied to the main amplifying and filtering unit. Further, the signal is sampled and digitized with the help of an analog-to-digital converter (ADC) and recorded to a computer's hard disk. The sampling rate determines the upper boundary of the frequency spectrum of the recorded signal in accordance with the Nyquist theorem. The waveform of a recorded AE signal is schematically shown in Fig. 1.

## INFORMATIVE PARAMETERS OF ACOUSTIC EMISSION

Acoustic emission produced in the process of deformation and fracture of rock may conventionally be cat-

egorized into two types: discrete and continuous. The term discrete AE refers to the acoustic emission consisting of individually distinguishable pulses; the term continuous AE refers to the acoustic emission that has the form of a continuous wave field or is recorded as a single continuous noiselike signal.

The prevailing source of practically observed AE in rocks is the stepwise development of cracks. The AE produced in this process is discrete; therefore, it is the discrete AE's informative parameters that are predominantly used in geological monitoring. Among these parameters, the main ones are as follows [4, 11]:

(i) the total acoustic emission count (total AE), i.e., the total number of AE pulses with an amplitude above a given threshold ($U_t$ in Fig. 1) observed during the analysis time;

(ii) the acoustic emission count rate, i.e., the number of AE pulses above a given threshold in unit time;

(iii) the number of acoustic emission pulses, i.e., the total number of pulses in discrete AE during the analysis time (for example, from the beginning of loading of the sample until a specified stress is achieved);

(iv) the acoustic emission activity, i.e., the number of AE pulses in a unit time;

(v) the amplitude of the acoustic emission signal, i.e., the maximum value of the AE signal;

(vi) the acoustic emission energy, i.e., the acoustic energy released by the AE source and carried by the waves produced in the material;

(vii) the beginning of recording of the acoustic emission signal, i.e., the time when the processor of the AE receiver starts processing the AE signal after it exceeds the threshold; and

(viii) the difference in arrival times of the AE signal, i.e., the time interval between the arrival times of the AE waves at the *i*th and *j*th receiving transducers.

The first four of the above parameters, to a certain degree of time resolution, characterize the number of elementary events of defect initiation and propagation in the material. Their common disadvantage is their certain ambiguity due to the dependence on the resolution of the AE receiving equipment.

The total count and number of AE pulses are time integrals of, respectively, the count rate and the AE activity and are the most widely used acoustic emission monitoring parameters, which positively correlate with the inelastic strain rate [12].

If the amplitude of the AE signal is known, the energy of elementary fracture events can approximately be evaluated.

The beginning of recording of the AE signal, which indicates the time when the signal arrives at the reception point, allows us to compare the emission monitoring data with conventionally studied rock parameters (strain, stress, elastic wave velocity, etc.).

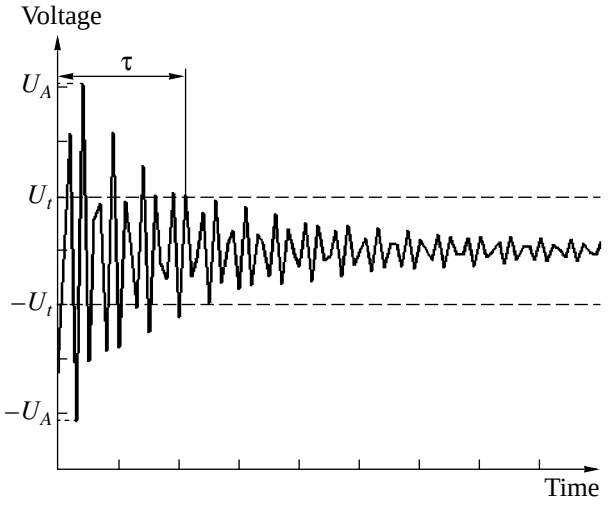


**Fig. 1.** Schematic view of the AE signal: $U_t$ is the threshold level for recording, $U_A$ is the amplitude of the signal, and $\tau$ is its duration.

If information on the velocities of elastic waves produced by a source and on the difference in their arrival times at different AE receivers is available, coordinates of the source can be retrieved. The minimum number of receivers necessary to locate (determine the coordinates) of a source in space is four; on a plane, three; on a line (a rod sample), two. Since rocks exhibit velocity anisotropy, it is commonly accepted that the minimum number of receivers required to reliably locate a source in space is six.

Location of AE sources plays the key role in studying the redistribution of microcracks in the fracture process. Location of the AE sources not only gives qualitative information on the positions and shapes of the fracture regions but also allows us to quantitatively characterize the process of fracture localization in space in terms of the point-to-point correlation integral $C(R)$ defined as

$$C(R) = \frac{2N_R(r < R)}{N(N-1)}, \quad (1)$$

where $N_R(r < R)$ is the number of source pairs separated by a distance $r$ (shorter than the given $R$) and $N$ is the total number of events analyzed [12, 13].

If the source distribution is self-similar, $C(R)$ is proportional to $R^D$, where $D$ is the fractal dimension of the distribution ($0.0 \le D \le 3.0$). The fractal dimension $D$ is defined as the slope of the plot $C = f(R)$ on logarithmic coordinates. Low values of $D$ indicate the presence of clustering, i.e., grouping of the sources, whereas $D = 3.0$ is characteristic of a uniform source distribution in space without a pronounced clustering. At the same time, $D$ carries no information about the geometric shape of the spatial distribution. In particular, $D = 2.0$ can refer to a uniform source distribution on a plane, as well as to a clustered distribution in space. Similarly,

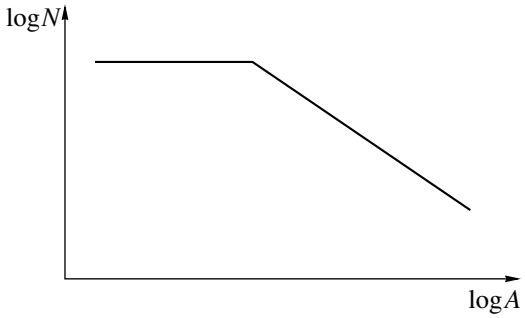


**Fig. 2.** Cumulative amplitude distribution of received AE signals: $A$ is the signal amplitude and $N$ is the number of signals whose amplitude is lower than the given value.

$D$ = 1.0 can refer to a distribution of sources on a line, as well as to their strongly clustered distribution in space [13]. Therefore, to best characterize the spatial source distribution, the fractal dimension $D$ must be considered together with the general spatial source pattern.

In experiments with hydraulic fracture of cubic samples, the fractal dimension of the spatial source distribution was found to depend on the lateral pressure applied to sample's faces and on the type of rock. The value the fractal dimension was found to be within 1.7 to 2.4 [14].

The measurements of signal arrival times allow us to determine the distribution of time intervals between consecutive AE events. This distribution is in a number of cases exponential, which indicates that the AE flow is characterized by the Poisson distribution law [15]. The AE events occur independently, and the AE history exerts no effect on the current and future events.

In recent years, the understanding of the flow of AE events as a Poisson process has undergone significant changes. In particular, it was found that the distribution is not exponential and the AE is not a Poisson process [16]. As a possible alternative, it was proposed to describe the AE process by the Polya distribution, which allows for the correlation between events [17].

The non-Poisson nature of the flow of AE events is taken into account in the so-called self-excitation model [13]. In the framework of this model, which relies on observations of AE emission in rocks under different loading conditions, the probability that an event occurs in a short time interval is

$$\lambda(t) = \mu_0 + p_1 t + \sum_{t_i < t} g(t - t_i), \qquad (2)$$

where the constant $\mu_0$ characterizes a stationary Poisson process, $p_1 t$ is the linear time trend component, $t_i$ is the time when the $i$th event is recorded, the function $g(t - t_i)$ characterizes the influence of previous events on the event at time $t$ (self-excitation), $g(t) = a_0 \exp(-\beta t)$, and $a_0$ and $\beta$ are the constants. The integral $s = \int_0^{+\infty} g(t)dt = a_0/\beta$ characterizes the degree of self-excitation, i.e., the effect of AE history on future events. This quantity can be evaluated from the measured arrival times of the AE signals.

A number of independent experimental works are known to give evidence characterizing the distribution of time intervals between consecutive AE events in rocks and inhomogeneous materials as the power-law scaling:

$$N(\tau) \sim \tau^{-\gamma}, \qquad (3)$$

where $N(\tau)$ is the distribution of time intervals $\tau$ between consecutive AE events and $\gamma$ is the dimensionless exponent. A power-law distribution similar to Eq. (1) was obtained, in particular, in field measurements of AE activity near the active volcano Stromboli [18]. The critical exponent was found to be $\gamma = 1.2 \pm 0.1$, which is in good agreement with numerical simulations of self-organizing criticality [19, 20]. At the same time, when the AE threshold recording level was changed, the $N(\tau)$ distribution deviated from the power-law scaling.

The amplitude distribution of received AE signals and its variation in the process of loading characterizes the evolution of the fracture process in time. For example, amplitude analysis reveals typical rock fracture stages, in particular, transition of the fracture from one hierarchy level to another [21].

The amplitude distribution of AE signals is usually represented in logarithmic coordinates, in which the abscissa axis represents the logarithm of the amplitude or the amplitude in decibels; the ordinate axis, the logarithm of the number of events whose amplitude is greater than that plotted on the abscissa axis (Fig. 2). The plot constructed in this manner can be approximated by a straight line:

$$\log N = a - b \log U_A, \qquad (4)$$

where $U_A$ is the amplitude of the AE signal, $N$ is the number of signals whose amplitude is greater than $U_A$, and $a$ and $b$ are constants. The $b$ value, which enters into Eq. (2), characterizes the slope of the amplitude distribution.

Experiments show that the $b$ value depends on the type of rock and on experimental conditions. The $b$ value of a rock sample is often observed to decrease in the process of loading the sample as it approaches macrofracture. For example, in the process of loading a dolerite sample, its $b$ value decreased from 0.3–0.9 at the beginning of the experiment to 0.0–0.3 as the sample approached the ultimate strength [22]. A similar decrease in the $b$ value before macrocracking was observed in the hydraulic fracture of cubic tuff and granite samples 100 mm on a side [14]. The increase in the contribution of higher-amplitude events with approaching the mechanical instability was observed in a composite sample subjected to a static loading and excited by elastic pulses [23].

The decrease in the $b$ value when approaching the ultimate strength is usually considered as a possible precursor of macrofracture. Indeed, a decrease in the $b$ value means that the share of high-amplitude events in the total AE flow increases. High-amplitude AE signals are produced by large cracks; therefore, an increase in the $b$ value may be regarded as a result of crack coalescence, formation of higher rank cracks, and transition of the fracture process to a higher hierarchy level with the following macrofracture.

It was theoretically shown that attenuation of elastic waves, as they propagate from the source (defect) to the AE receiver, exerts a significant effect on the amplitude distribution of the recorded AE signals [24, 25].

The numerical simulation of the amplitude distribution of received signals [26] has shown that a spatial localization of sources (for example, their redistribution from a uniform distribution over the bulk of the sample into a uniform distribution over a plane) reduces the $b$ value, as observed in experiments. The decrease is observed in spite of the fact that all the sources continue emitting with the same amplitude. It has been demonstrated that calculations of the amplitude distribution of sources must use true amplitudes of the emitted rather than received signals [24–26]. It is also necessary to allow for the attenuation of the AE signals in the process of propagation from the source to the receiver. Therefore, it is necessary to use multichannel AE measurement systems to provide for the location of the sources.

The most comprehensive idea of the AE process and sources can be obtained from a detailed analysis and interpretation of the received signal waveform. It is also necessary to take into account that the waveform is determined by not only the source but also by transformation of the signal as it travels from the source to the receiver. Reflections of the signal are also of importance in testing the rock samples. Due to reflections, after one or two periods of vibration, the signal mainly characterizes the reflections rather than the source. The conditions at the contact boundary between the transducer and rock and characteristics of the receiving channel (receive transducer, filters, amplifiers, etc.) also affect the recorded signal.

One of the most commonly used methods for processing AE signals is Fourier analysis, which yields frequency spectra of the signals and their variation in the course of fracture evolution. A widely used version is the windowed Fourier transform, which divides the signal into portions (time intervals) and performs the Fourier transforms over each interval. Narrowing the time window improves the time resolution, but this is achieved at the expense of less adequate representation of low frequencies [10].

Using power spectra of autocorrelation and cross-correlation functions of two signals allows one to estimate their similarity through calculating the coherence function $C_{xy}(f)$ [10]:

$$C_{xy}(f) = \frac{|\Gamma_{xy}(f)|^2}{\Gamma_{xx}(f)\Gamma_{yy}(f)}, \quad (5)$$

where $f$ is the frequency; $\Gamma_{xx}(f)$ and $\Gamma_{yy}(f)$ are autospectral densities of signals $x$ and $y$, respectively; and $\Gamma_{xy}(f)$ is their cross-correlation density. High values of the coherence function indicate that waveforms of the signals are similar. If the signals are identical, their coherence function is constant and equals unity.

In recent years, wavelet analysis, which was developed earlier in seismology, has been increasingly used in AE studies. The wavelet analysis allows one, in particular, to increase the signal-to-noise ratio by creating appropriate digital filters. The wavelet spectrum clearly shows in what region and at what frequencies the signal carries the local energy maximum. This feature may be used, for example, to extract and filter out the reflected waves [27]. The wavelet analysis was used to filter out high-frequency and low-frequency noise and to identify waves of different types that arrive after the longitudinal wave [10]. At the same time, we should note that, for the wavelet filter to be used in the automated mode of operation, a physically justified model of noise for the particular experiment must be available. Otherwise, the wavelet analysis may produce unwanted artefacts.

The analysis of the moment tensor, similar to the seismic moment tensor in earthquake mechanics, provides information on the source type and orientation. The moment tensor $M_{pq}(\tau)$ is defined so that the displacement $u_n$ in the direction of coordinate $x_n$ at a given spatial point $\vec{x}$ is written as follows:

$$u_n(\vec{x}, t) = \int_{-\infty}^{+\infty} M_{pq}(\tau)\frac{\partial}{\partial \xi_q} G_{np}(\vec{x}, t-\tau; \vec{\xi}, 0)d\tau, \quad (6)$$

where $G_{np}$ is the Green's tensor and $\vec{\xi}$ is the position vector. Summation is implied in indices that enter into the expression twice.

At present, several moment tensor analysis methods have been developed, which can be categorized into two groups: absolute methods and relative methods. The absolute methods yield absolute values of the moment tensor, but they require calculation of the Green's function. The methods use the amplitude and sign of the first arrival at several AE receivers or the full waveform. In the latter case, the solution is sought for by the method of successive approximations [28].

The relative methods apply to groups (clusters) of sources whose size should not be greater than the predominant wavelength of the AE signals or the distance between the cluster and the receivers. An advantage of the relative methods is that they do not calculate the Green's function. The moment tensor is calculated relative to that of one of the sources of this cluster (refer-

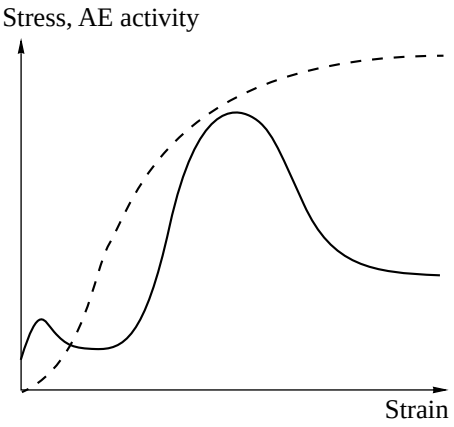


**Fig. 3.** Schematic generalized plots of the stress (dashed line) and AE activity (solid line) versus the longitudinal strain in the process of uniaxial loading of a rock salt sample [32].

ence source). The moment tensor of the reference source can be calculated by the absolute methods. The accuracy of the relative method is determined by the error within which the moment tensor of the reference source is known [28].

## THE MAIN FEATURES OF AE IN ROCK SAMPLES

### *Staged Charater of the AE*

One of the main distinctive features of AE in the process of mechanical fracture is its staged character, i.e., the dependence of the AE characteristics on the sample fracture stage. Changes in the AE parameters are often used to diagnose these stages. A regular sequence of AE stages in the process of fracture evolution creates conditions for predicting catastrophic macrofractures in inhomogeneous rocks.

The sequence of the AE stages with evolution of the rock damage in the process of mechanical loading was indicated in early experimental works [29]. For example, the process preceding the macrofracture of samples of low-strength coal subjected to uniaxial stress was clearly divided into three stages: relatively low activity (isolated groups of relatively weak pulses), high activity (a considerable amplitude of AE pulses), and reduced AE activity (pulses of a relatively high amplitude alternate with relatively weak signals). The third stage terminates in the macrofracture of the sample. Transitions between the AE stages are clear and stepwise.

This staged character was absent in medium-strength and high-strength coal, in which intermittent AE activity was observed over the entire loading process: the pulses followed in groups, the pulse rate and amplitude in a group monotonically increasing with approaching the macrofracture. In high-strength and medium-strength coal, the AE appeared much later than in low-strength coal. The groups of pulses were separated by quiescence intervals. In each group except for the last one, which ends up with the macrofracture, the AE activity and amplitude first grow and then gradually fall off [29].

The intermittent activity in medium-strength and high-strength coal occurs because individual parts of the sample sequentially lose their bearing strength. The high AE activity in low-strength coal is observed almost from the very beginning of loading due to the high initial concentration of cracks. An increase in the load continuously creates fracture zones and releases energy, which reduces the intensity of the final shock [29].

The alternation of high and low AE intensity intervals in the process of deformation of coal samples was also observed in [30]. Three stages of AE evolution were distinguished. The initial stage, which approximately corresponds to elastic deformation of the sample, is characterized by insignificant AE activity. The next stage, from the point where the sample reaches its elastic limit to the point of ultimate strength (maximum of the stress–strain curve), is characterized by a high AE intensity. Beyond the ultimate strength, the AE is characterized by a low intensity, similar to that at the first stage. The beginning and end of each stage was clearly seen as an inflection in the plot of the total AE versus time.

The staged character of AE clearly manifests itself in loading rock salt and salt rock samples. The number of distinguishable stages for loading at a constant stress rate (four stages) and at a constant strain rate (six stages) is different [31]. The behavior of the AE activity versus stress under these two conditions is also essentially different. In particular, at a constant strain rate, the maximum activity occurs beyond the ultimate strength, on the falling part of the stress–strain curve, whereas at a constant stress rate, the maximum activity occurs at the maximum consolidation of the sample (Fig. 3) [32].

A similar behavior was observed in stepwise loading tests of salt with keeping the load constant at each step until AE activity stabilizes [33]. The experiments have shown that the stepwise increase in the AE activity in response to a step in the loading is maximal when consolidation of the sample is maximal. Also, beginning with this moment, the AE activity falls off, as the load is kept constant, not to the background level but to a certain higher value. This circumstance was used as a basis for a fundamentally new fast method to determine the long-term strength of salt. On the whole, results reported in [31, 33] have shown that each condition and each stage of salt rock deformation refers to a particular behavior of AE, informative parameters of which experience specific anomalous changes at the boundaries between the stages. These changes can be used to identify each of the deformation stages; to determine the limits of elasticity, the strength, and the long-term strength; and to detect decelerating, steady-state, or evolving creep.

Note that the decay in the AE activity $A$ at each stage of the stepwise loading of rocks (i.e., at a constant loading) usually obeys the Omori law (Fig. 4) [34]:

$$A = \frac{N_0}{(t+c)^p}, \quad (7)$$

where $N_0$, $c$, and $p$ are constant values. As the rock approaches the macrofracture, $N_0$ increases and the exponent $p$ decreases [12, 35]. The decrease in $p$ can be regarded as a precursor of the forthcoming catastrophic failure.

If the acoustic activity of rocks is low, for example under triaxial loading, the recognition of acoustic emission stages is possible through the analysis of the signal's fine structure, one of the informative parameters being, in particular, the amplitude ratio of adjacent half-periods of the AE pulse [36].

The staged character of AE and its relation to the staged character of deformation and fracture of crystalline rocks (granite) was studied in detail in [37, 38]. In addition to AE activity, the study used such parameters as amplitude, duration, and rise time of the signal, along with the number of its intersections of the threshold level. At early loading stages, an insignificant AE activity due to closure of existing pores and cracks was observed. The beginning of microfracture, at which a positive nonlinear component of cubic strain appears, was accompanied by a peak in the AE activity. Also, local maximums of the signal duration and number of intersections of the threshold level were observed [38].

Concluding the review of data on the staged character of AE, we should mention the phenomenon of stillness observed immediately before the macrofracture or, in the case of loading on a rigid test facility, immediately after the peak stress [38]. The presence and duration of this stillness and its position relative to the peak stress (before or after) is determined by the loading conditions and the type of rock. This phenomenon is observed in samples, as well as on a greater scale: before shock bumps in mines and before earthquakes. The stillness phenomenon seems to be a universal feature of the fracture process and is typical of not only the AE but also of electromagnetic radiation that accompanies the deformation and fracture of rocks [40].

### *Relation between the AE Characteristics and the Rock Structure*

Along with loading conditions, the AE behavior is determined by the structure and properties of rock. In particular, the more brittle the rock, the longer the duration of the acoustic stillness mentioned above. If the rock is sufficiently plastic, the stillness may be absent [39]. Plastic rocks (for example, rock salt) are characterized by a more uniform energy release than that in brittle rocks (for example, granite) during the entire loading process. In brittle rocks, the most intense fracture is observed at later deformation stages, closer to the macrofractur. At this stage, the signal amplitude and the AE activity of brittle rock sharply increase [41].

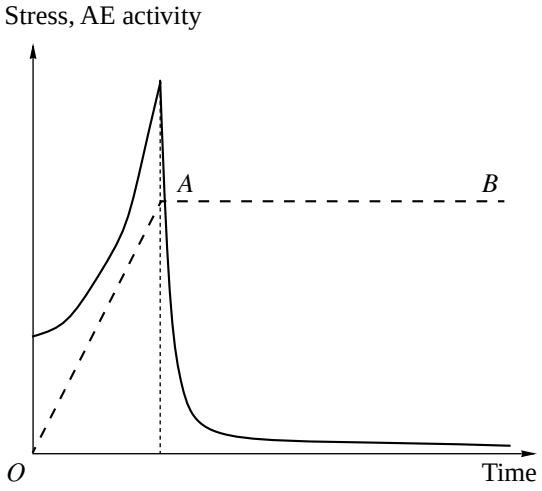


**Fig. 4.** Schematic generalized plots of the stress (dashed line) and smoothed AE activity (solid line) versus time in the process of (*OA*) monotonic loading and (*AB*) further strain in the creep mode.

The degree of initial homogeneity exerts a strong influence on the AE behavior. In more homogeneous rocks, the AE begins later and the greatest part of acoustic signals are observed immediately before the complete failure of the sample, which hampers the prediction of the macrofracture from AE data [42].

The homogeneity of rock is closely related to the characteristic size $\bar{d}$ of grains that constitute the rock. The influence of the grain size on AE was particularly studied in [43, 44]. The experiments were conducted with rocks of approximately the same composition but different grain size and its variance: relatively evenly graded granodiorite with $\bar{d}$ = 1 mm, evenly graded gray granite with $\bar{d}$ = 3 mm, and unevenly graded pegmatite with $\bar{d}$ = 20 mm and grain size scattered within 10 to 40 mm. The samples were tested under uniaxial loading. The total number of AE signals recorded from the onset of loading to the instant of fracture was the greater, the coarser the rock was. The total number of AE pulses recorded when loading granodiorite was 90% less than that in pegmatite and 60% less than that in gray granite [42]. Coarser grained rocks are characterized by higher AE energies [43, 44].

### *The AE under Cyclic Loading of Rock Samples and Its Use for Estimating Past Mechanical Stresses*

A cyclic uniaxial loading of rock samples is accompanied by the Kaiser effect: when the stress is smaller than the maximum value achieved previously, the AE activity is close to the background level and it abruptly increases when the stress achieves this value [45–47].

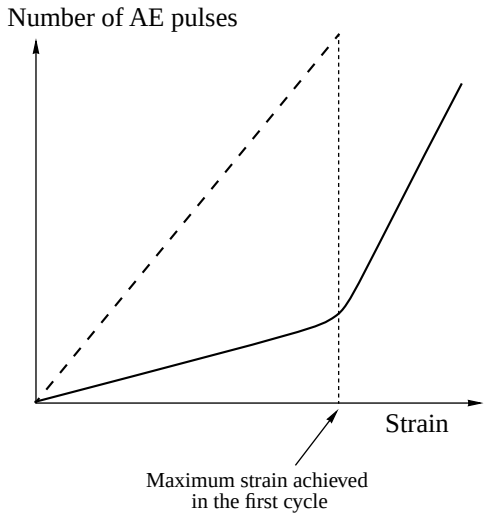


**Fig. 5.** Schematic generalized plots of the number of AE pulses versus strain in the first (dashed line) and second (solid line) loading cycles.

A consequence of the abrupt increase in the AE activity is an inflection (change in the slope) of the curve representing the total number of AE pulses versus stress and schematically depicted in Fig. 5. The Kaiser effect is an indication of the memory of rocks; i.e., their ability to accumulate, store, and reproduce information about thermodynamic actions they have experienced [48–50]. The Kaiser effect is observed in rocks of vastly different origin and composition. In brittle crystalline rocks, as the loading approaches the ultimate strength, the effect manifests itself less clearly: the AE appears before the memorized stress and strain level is achieved. The memory degrades with increasing time interval between the loading cycles and under the action of such impairing factors as humidification and heating between the mechanical and loading cycles or in the process of loading [46, 48, 49]. In plastic rock salt, the Kaiser effect is clearly observed at all stages, including the deformation beyond the ultimate strength [52].

Since the Kaiser effect was discovered in the early 1950s, it attracts the attention of researchers due to its possible use for estimating the stress experienced by rock in the Earth's crust. However, the main difficulty is that rock in the Earth's crust is in a complex stressed state, directions and proportions between the main stress components being unknown in advance. Dedicated laboratory experiments have shown that uniaxial compression of samples of different orientations does not allow one to determine the stress that affected the rock in the massif. One of these experiments [53] subjected a cubic sample to two cycles of uniaxial stress. In the second cycle, the stress direction was perpendicular to that in the first cycle. In the second cycle, the Kaiser effect was absent. When the loading direction in the second cycle was the same as that in the first cycle, the Kaiser effect was clearly observed. High sensitivity of the Kaiser effect to the difference in directions of the strain tensor's principal axes in sequential loading cycles was corroborated experimentally [54, 55] and by numerical simulations of fracture under cyclic loading [51, 55].

This sensitivity, on the one hand, is an obstacle for the application of the Kaiser effect in stress measurements (direction of the principal axes in the Earth's crust is usually known only approximately). On the other hand, it seems possible to use the sensitivity to accurately find the directions of these axes by testing a series of samples oriented in different directions. The Kaiser effect must be most clearly observed in the sample whose axis coincides with the direction of the maximum compression stress in the massif.

When the direction of uniaxial loading coincides with that of the maximum principal compression stress in the previous cycle of triaxial axisymmetric compression, the Kaiser effect is observed. However, it manifests itself in a more complex fashion than under the uniaxial compression. Specifically, the AE activity increases gradually and the Kaiser effect is observed when the amount of uniaxial loading reaches the value equal to a linear combination of principal stresses of the previous triaxial cycle, $\sigma_1 - (k + 1)\sigma_3$, where $\sigma_1$ and $\sigma_3$ are the principal stresses of the previous triaxial cycle and $k$ is the dimensionless coefficient characteristic of the particular rock.

Thus, in the simplest version, uniaxial loading allows us to obtain information about the combination of principal stresses but not about each of them separately. More sophisticated methods exist, which use a series of triaxial tests with different lateral pressures to scan the entire damage surface (the analogue of the loading surface in the theory of plasticity) and thereby retrieve the value of each of the principal stresses individually [56].

### *The AE under Actions Other Than Mechanical Loading*

The AE behavior considered above refers to various conditions of mechanical loading of rocks. However, being a consequence of continuity violation, AE in rocks takes place under actions of other types, in particular, under humidification (or drying) or heating.

Humidification (drying) of rocks containing clay minerals is accompanied by their swelling (shrinkage), fracture, and acoustic emission. Experiments with siltstone have shown that the AE activity in the process of swelling is much (several times) higher than that in the process of shrinkage. At the beginning of swelling (shrinkage), the AE activity increases, reaches its maximum, and then gradually falls off. A stabilization of the swelling (shrinkage) deformation reduces the AE to its background level [57].

Heating of rocks is accompanied by AE. The reasons for the heating to cause fracture and AE may be vastly different: temperature gradient in the sample due

to its nonuniform heating, difference in elastic properties and in coefficients of thermal expansion of the rock's component minerals, evaporation of moisture and explosion of gaseous or liquid inclusions, and microfracture [58, 59]. Rocks of similar composition and different grain size demonstrate the same behavior as under the mechanical loading: coarser-grained rocks exhibit higher AE activity and energy. Also, the AE activity and energy of quartz-containing rocks are higher due to the thermal expansion anisotropy of the grains of this mineral [59].

Rocks subjected to cyclic heating with the temperature amplitude growing every cycle exhibit the so-called AE memory effect: the AE is absent until the temperature reahces the maximum value observed in the previous cycle and, after that, it abruptly increases [58]

## SIMULATION OF AE

The development of AE models is conducted in several directions. First of all, we should mention the class of models that simulate the emission of elastic waves by developing defects, such as dislocations [5, 6] and cracks [60, 61]. The crack shape is often idealized; for example, disk-like cracks are considered [62]. Models of this type can be used to calculate the waveform of AE pulses.

Along with models of emitting cracks, analytical models of rock damage are created that model the evolution of AE activity in time disregarding the real emission mechanism. Such models rely on the results of the fracture mechanics and relate the AE activity to the total number of developing cracks or to the number of jumps in the process of their propagation [63].

In recent years, a class of models has appeared, such as power-law distributions of the AE source energy and the time intervals between sequential signals [64], which aim to give a mesoscopic description of the general statistical properties of the process. An example of work in this direction is the model that employs an analogy between mechanical fracture and fusion of fuse links [65]. A characteristic feature of this model is that, when the control parameter $I$ (current, which is an analog of mechanical stress) exceeds its critical value $I_c$, elements of the model (fuse links) change their properties (are activated) rather than fail completely. This feature allows this model to simulate the AE at stages that are far from macrofracture. The change in properties of a particular element at $I > I_c$ is accompanied by a redistribution of the properties of the adjacent elements. Combined with the redistribution of mechanical stress caused by activation of the elements, this effect may produce avalanche series of AE signals separated by periods of relative quiescence.

At early fracture stages, only short series of AE events are observed. After accumulating a certain damage, AE activity grows and finally achieves a steady state, in which the increase in the control parameter is balanced by an increase in the damage. Simulations have shown that, in the steady-state mode, the AE activity experiences significant fluctuations, and the amplitudes and intervals between sequential signals are distributed by the power law [65].

Unlike the static model [65], the dynamic model [66] is capable of modeling not only the AE activity, but also the overall signal waveform. This is achieved by solving the equations of motion for the two-dimensional lattice subjected to antiplanar deformation. Model [66] can also be used to obtain the power-law distribution of the signal energy.

Along with analytical models, a significant role in modern AE studies belongs to dedicated software packages. In [68], the displacement discontinuity method (a version of the method of boundary elements) was used to simulate brittle fracture of rock under various loading conditions. It was assumed that the AE activity is proportional to the number of microcracks activated at the current loading stage. The simulation results have shown good qualitative agreement with the experiment, including the case of cyclic loading.

The discrete element method implemented in the PFC software package is capable of simulating not only AE kinetics but also a detailed signal waveform. This is achieved through calculating the energy released in the process of breaking the bonds between disk-shaped (or spherical) particles that constitute the model rock [68].

## CONCLUSIONS

The investigation of the mechanisms and behavior of deformation and fracture of rocks under various loading conditions is one of the foreground tasks in geomechanics. The main method used in this area is based on mechanical tests of samples supplemented by various measurements. Until relatively recently, these measurements determined only the longitudinal and transverse deformations and the dynamics of acoustic and electrical properties in the course of loading. As follows from this review, acoustic emission is presently becoming the most effective tool for solving research problems in the physics of strength, plasticity, and fracture of geological materials. This transition is facilitated by the progress in both the study of the AE phenomenon in geological media and the development of the equipment and techniques used for the acoustic emission measurements.

Concluding this concise review, we emphasize that it considered the AE behavior only in rock samples. This is, on the one hand, due to space considerations and, on the other hand, because the parameters and space–time dynamics of geological material structure in samples are different from those in the massif. Also, one should keep in mind that laboratory methods of experimental geoacoustics (including the AE methods) significantly differ from the methods that study rocks as they occur in nature (*in situ*). These differences prima-

rily manifest themselves in the spectrum and propagation conditions of AE signals and in the intensity and nature of interferences from which the signals must be separated.

## ACKNOWLEDGMENTS

This work was supported in part by the Russian Foundation for Basic Research (project no. 04-05-64885) and the Council on Support Grants for Leading Scientific Schools (project no. NSh-1467.2003.5).

## REFERENCES

1. A. D. Ioffe, Usp. Fiz. Nauk **8** (4), 466 (1928).
2. S. D. Vinogradov, *Acoustic Observations of Rock Failure Processes* (Nauka, Moscow, 1964) [in Russian].
3. O. G. Shamina, Izv. Akad. Nauk SSSR, No. 5, 513 (1956).
4. V. A. Greshnikov and Yu. V. Drobot, *Acoustic Emission. Application for Testing Materials and Products* (Izd. Standartov, Moscow, 1976) [in Russian].
5. V. D. Natsik and K. A. Chishko, Akust. Zh. **28**, 381 (1982) [Sov. Phys. Acoust. **28**, 225 (1982)].
6. V. S. Boĭko and V. D. Natsik, in *Elementary Processes of the Plastic Deformation of Crystals* (Naukova Dumka, Kiev, 1978), pp. 159–188 [in Russian].
7. N. S. Kuznetsov, Tekhn. Diagnost. Nerazrush. Kontrol', No. 3, 65 (1990).
8. A. G. Konstantinova, in *Acoustic Emission of Materials and Structures* (Izd. Rostov. Univ., Rostov-on-Don, 1989), Chap. 2, pp. 137–141.
9. V. I. Yukalov, A. Moura, and H. Nechad, J. Mech. Phys. Solids **52** (2), 453 (2004).
10. C. U. Grosse, F. Finck, J. H. Kurz, and H. W. Reinhardt, Constr. Build. Mater. **18**, 203 (2004).
11. *System of Nondestructive Testing. Types and Technology of Nondestructive Testing. Terms and Definitions: A Handbook* (Gos. Unitarn. Predpr. Nauch. Tekh. Tsentr Bezopasnosti Promyshl. Gosgortekhnadzora Rossii, Moscow, 2003), Ser. 28, Issue 4 [in Russian].
12. D. Lockner, Int. J. Rock Mech. Min. Sci. Geomech. Abstr. **30** (7), 883 (1993).
13. X. Lei, K. Masuda, O. Nishizawa, *et al.*, J. Struct. Geol. **26** (2), 247 (2004).
14. K. Itakura and K. Sato, in *Proceedings of 6th Conference on Acoustic Emission and Microseismic Activity in Geologic Structures and Materials, Clausthal-Zellerfeld, 1998* (Trans Tech. Publ., Clausthal-Zellerfeld, 1998), p. 29.
15. S. I. Buĭlo, Defektoskopiya, No. 4, 54 (2000).
16. T. E. Unander, Doctoral Dissertation (Norwegian Univ. Sci. Technol., Trondheim, 2002).
17. M. Armeite, M. I. Lopez Pumarega, L. V. Perez, and J. E. Ruzzante, http://www.ndt.net/article/wcndt00/papers/idn433.htm.
18. P. Diodati, F. Marchesoni, and S. Piazza, Phys. Rev. Lett. **67** (17), 2239 (1991).
19. A. Sornette and D. Sornette, Europhys. Lett. **9** (3), 197 (1989).
20. K. Chen, P. Bak, and S. P. Obukhov, Phys. Rev. A **43** (2), 625 (1991).
21. N. G. Tomilin and V. S. Kuksenko, in *Earth Science: Physics and Mechanics of Geomaterials* (Vuzovskaya Kniga, Moscow, 2002), pp. 116–135 [in Russian].
22. G. M. Fonseka, S. A. F. Murrell, and P. Barnes, Int. J. Rock Mech. Min. Sci. Geomech. Abstr. **22** (5), 273 (1985).
23. G. A. Sobolev, A. V. Ponomarev, A. V. Kol'tsov, *et al.*, Fiz. Zemli, No. 1, 79 (2001).
24. T. E. Unander, Int. J. Rock Mech. Min. Sci. Geomech. Abstr. **30** (7), 947 (1993).
25. J. Weiss, Bull. Seismol. Soc. Am. **87** (5), 1362 (1997).
26. A. V. Lavrov, Akust. Zh. **51** (3), 383 (2005) [Acoust. Phys. **51** (3), 321 (2005)].
27. A. Lavrov, M. Wevers, and A. Vervoort, J. Acoust. Emiss. **20**, 292 (2002).
28. G. Manthei, J. Eisenblatter, and T. Dahm, Constr. Build. Mater. **15** (5–6), 297 (2001).
29. A. G. Konstantinova, in *Mine Aerogasdynamics and Safety of Mining* (Nauka, Moscow, 1964), pp. 155–162 [in Russian].
30. V. A. Fatkhi and L. V. Bugaenko, in *Forecast of Mining and Geological Conditions of Coal Mining by the Mine Geology and Geophysics Methods* (Vsesoyuzn. Nauch. Issled. Inst. Gorn. Geomekh. Markcheĭderskogo Dela (VNIMI), Leningrad, 1985), pp. 13–15 [in Russian].
31. V. L. Shkuratnik and Yu. L. Filimonov, in *Proceedings of International Conference on Geodynamics and Stressed State of the Earth's Interior, Novosibirsk, 2004* (Novosibirsk, 2004), p. 35.
32. Y. Filimonov, A. Lavrov, and V. Shkuratnik, J. Strain Anal. **38**, 157 (2002).
33. V. L. Shkuratnik and V. S. Yamshchikov, in *Mechanics of Jointed and Faulted Rock*, Ed. by H. P. Rossmanith (Balkema, Rotterdam, 1995), pp. 469–471.
34. A. Saichev and D. Sornette, cond-mat/0311493.
35. V. Rudajev, J. Vilhelm, J. Kozak, and T. Lokajicek, Int. J. Rock Mech. Min. Sci. Geomech. Abstr. **33** (7), 743 (1996).
36. A. S. Voznesenskiĭ, Yu. V. Demchishin, E. M. Shafarenko, *et al.*, in *Proceedings of the X Session of the Russian Acoustical Society, Moscow, 2000* (Izd. GEOS, Moscow, 2000), p. 190 [in Russian].
37. E. Eberhardt, D. Stead, and B. Stimpson, Int. J. Rock Mech. Min. Sci. **34** (3–4), 633 (1997).
38. E. Eberhardt, D. Stead, B. Stimpson, and R. S. Read, Can. Geotech. J. **35** (2), 222 (1998).
39. L. Zh. Gorobets, S. B. Dubrova, V. N. Bovenko, and O. F. Panchenko, Fiz. Tekh. Vys. Davlenii, No. 2, 65 (1995).
40. P. G. Kapiris, K. A. Eftaxias, and T. L. Chelidze, Phys. Rev. Lett. **92** (6), 065702 (2004).
41. I. T. Aĭtmatov and V. A. Mansurov, in *Acoustic Emission of Materials and Structures* (Izd. Rostovskogo Univ., Rostov-on-Don, 1989), Part 2, pp. 111–116.
42. A. G. Konstantinova, *Seismoacoustic Studies of Preejection Fracture of Coal Beds* (Nauka, Moscow, 1977) [in Russian].

43. E. Eberhardt, B. Stimpson, and D. Stead, Rock Mech. Rock Eng. **32** (2), 81 (1999).
44. R. Přikryl, T. Lokajíček, C. Li, and V. Rudajev, Rock Mech. Rock Eng. **36** (4), 255 (2003).
45. J. Kaiser, Arch. Eisenhuettenwes. **24** (1–2), 43 (1953).
46. K. Kurita and N. Fujii, Geophys. Res. Lett. **6** (1), 9 (1979).
47. C. Li and E. Nordlund, Rock Mech. Rock Eng. **26** (4), 333 (1993).
48. V. V. Rzhevskiĭ, V. S. Yamshchikov, V. L. Shkuratnik, *et al.*, Dokl. Akad. Nauk SSSR **273** (5), 1094 (1983).
49. V. L. Shkuratnik and A. V. Lavrov, *Memory Effects in Rock. Physical Laws and Theoretical Models* (Izd. Akad. Gorn. Nauk, Moscow, 1997) [in Russian].
50. R. A. Guyer and P. A. Johnson, Phys. Today **52** (4), 30 (1999).
51. A. V. Lavrov, V. L. Shkuratnik, and Yu. L. Filimonov, *Acoustic Emission Memory Effect in Rock* (Izd. Mosk. Gos. Gorn. Univ., Moscow, 2004) [in Russian].
52. Y. Filimonov, A. Lavrov, Y. Shafarenko, and V. Shkuratnik, Pure Appl. Geophys. **159** (6), 1321 (2002).
53. C. E. Stuart, P. G. Meredith, S. A. F. Murrell, and J. G. Van Munster, Int. J. Rock Mech. Min. Sci. Geomech. Abstr. **30** (7), 937 (1993).
54. D. J. Holcomb, Int. J. Rock Mech. Min. Sci. Geomech. Abstr. **30** (7), 929 (1993).
55. A. Lavrov, A. Vervoort, M. Wevers, and J. A. L. Napier, Int. J. Rock Mech. Min. Sci. **39** (7), 287 (2002).
56. B. J. Pestman and J. G. Van Munster, Int. J. Rock Mech. Min. Sci. Geomech. Abstr. **33** (6), 585 (1996).
57. V. G. Ruiz de Argandoña, L. Galleja, and L. M. Suárez del Rio, Eng. Geology **39** (3–4), 147 (1995).
58. V. V. Rzhevskiĭ, V. S. Yamshchikov, V. L. Shkuratnik, *et al.*, Dokl. Akad. Nauk SSSR **283** (4), 843 (1985).
59. C. Jones, G. Keaney, P. G. Meredith, and S. A. F. Murrell, Phys. Chem. Earth **22** (1/2), 13 (1997).
60. M. V. Lysak, Eng. Fract. Mech. **47** (6), 873 (1994).
61. M. V. Lysak, Eng. Fract. Mech. **55** (3), 443 (1996).
62. S. Hirose and J. D. Achenbach, Eng. Fract. Mech. **39** (1), 21 (1991).
63. V. L. Shkuratnik and A. V. Lavrov, Fiz. Tekh. Probl. Razrabotki Polezn. Iskopaemykh, No. 1, 25 (1995).
64. S. Ciliberto, A. Guarino, and R. Scorretti, Physica D (Amsterdam) **158** (1/4), 83 (2001).
65. S. Zapperi, A. Vespignani, and H. E. Stanley, Mat. Res. Soc. Proc. **409**, 355 (1996).
66. M. Minozzi, G. Caldarelli, L. Pietronero, and S. Zapperi, Eur. Phys. J. B **36** (2), 203 (2003).
67. A. V. Lavrov, A. Vervoort, and J. A. L. Napier, in *Proceedings of the 2nd Biot Conference on Poromechanics, Poromechanics II, Lisse, 2002*, Ed. by J.-L. Auriault, C. Geindreau, P. Royer, *et al.* (Swets & Zeitlinger, Lisse 2002), p. 991.
68. J. F. Hazzard and R. P. Young, Int. J. Rock Mech. Min. Sci. **37** (5), 867 (2000).

*Translated by A. Khzmalyan*

*Acoustical Physics, Vol. 51, Suppl. 1, 2005, pp. S23–S36. Translated from Akusticheskiĭ Zhurnal, Vol. 51, Suppl., 2005, pp. 31–45.*


# A High-Power Intrawell Radiator of Shear Waves for Coherent Seismoacoustics

**V. S. Averbakh, V. V. Artel'nyĭ, B. N. Bogolyubov, A. L. Virovlyansky, A. I. Malekhanov, A. P. Maryshev, and V. I. Talanov**

*Institute of Applied Physics, Russian Academy of Sciences, ul. Ul'yanova 46, Nizhni Novgorod, 603950 Russia*

*e-mail: viro@hydro.appl.sci-nnov.ru*

Received August 16, 2004

**Abstract**—A brief review of investigations in the field of coherent seismoacoustics is presented, and the general requirements for seismoacoustic wave radiators intended for solving problems of remote sounding are formulated. The principle of operation of a novel high-power radiator created at the Institute of Applied Physics, Russian Academy of Sciences, for generating low-frequency seismic waves is described, and the results of the analytical and numerical modeling of this radiator are presented. The main element of the radiator is a piezoelectric cylinder executing bending vibrations in a well filled with water. The concept of sectioning the radiating cylinder for increasing the efficiency of excitation of various radiator modes and improving the matching the radiator with the medium is formulated. The results of the field measurements of the space–time structure of the seismic field generated by the sectioned radiator are presented. On the basis of these measurements, estimates of the power, efficiency, and quality factor of the radiator are obtained. © *2005 Pleiades Publishing, Inc.*

## INTRODUCTION

The possibilities of using acoustic signals for affecting the state of rock and diagnosing its structure have been studied intensively over the last decades. The results of these studies allow one to consider seismoacoustics as an independent and promising field of geophysics. The solution of some of its most urgent problems requires the use of intense acoustic signals in the range of relatively low frequencies from ~10 to ~1000 Hz. Such signals are considered to be an effective tool for the remote acoustic action on oil pools that is aimed at increasing oil recovery and for crosswell sounding used for monitoring oil fields during exploitation. The signals are also needed for solving problems of engineering seismic prospecting of mineral resources (including the prospecting on the sea shelf) and for the visualization of subsurface inhomogeneities in the construction of important structures. It is expected that the methods of low-frequency seismoacoustics may be very efficient in solving the problem of monitoring the condition of the Earth's interior in earthquake zones.

In recent years, a promising tendency appeared in seismoacoustics, which is connected with the use of controlled coherent radiators and related fundamental possibility of using the coherent properties of received signals for solving inverse problems. The high and long-term stability of these radiators makes it possible to realize coherent methods of forming and detecting the signal field, which are nontypical for seismic investigations. This, in turn, allows one to increase the resolution of sounding in space and (or) time coordinates. Another important feature is that the long-term accumulation and application of special procedures of the correlation analysis of coherent signals makes it possible to considerably increase the depth (range) of sounding at relatively low radiation levels.

From the mid-1990s, field experiments have been carried out at the Institute of Applied Physics of the Russian Academy of Sciences, which have clearly demonstrated the prospects of coherent methods of seismoacoustic sounding [1]. These experiments used previously designed high-power coherent hydroacoustic radiators (with various methods of matching them with rock) and specially developed compact surface vibration radiators. In these experiments, various approaches to the solution of problems of coherent sounding of the inhomogeneous medium were modified, which, in particular, were based on the employment of the signals modulated in a special way [2] and on coherent methods of formation of an extended receiving aperture (the aperture synthesis method combined with the matched space–time filtering) [3]. For instance, in one of the experiments in the Nizhni Novgorod region, a geological relief was reconstructed to a depth of about 2 km with a spatial resolution of the layered structure of ~10 m (at an operating frequency of 227 Hz) [2].

The results obtained show that the development of high-power controlled coherent radiators of seismic signals in the low-frequency range (up to ~1 kHz) and the investigation of their radiating characteristics in field experiments are of considerable interest for realizing the potential advantages of coherent seismoacous-

tics. Along with the adaptation of high-power hydroacoustic radiators for seismoacoustic investigations and the development of surface vibration radiators of the required frequency band [1], the problem of creating special intrawell radiators is quite urgent. Their most important field of application is the intensification of oil production and the crosswell sounding of oil pools.

The known intrawell radiators that are used in practice do not meet the above-mentioned requirements. For example, high-frequency (~10–30 kHz) piezoelectric radiators of longitudinal waves, whose radiation is localized in the so-called bottom-hole zone, serve strictly for recovering its permeability (their typical radiating power is ~1 kW and the radius of action is not greater than ~1 m from the well axis) [4, 5]. Some information is available about the employment of magnetostriction radiators [6], which also operate at rather high frequencies (and have lower radiating power). A considerable reduction in the operating frequency to the values of about 1 kHz and lower is possible by using the parametric generation of waves of difference frequency inside the medium by employing the biharmonic operating mode of high-frequency piezoelectric radiators, which undoubtedly is of interest from the point of view of realization of the multifrequency action on the producing layer, as well as from the point of view of crosswell sounding [7]. A grave disadvantage of this approach lies in the relatively low efficiency of the parametric conversion, which is a "free parameter" in theoretical estimates of the level of secondary radiation (because it cannot be calculated with sufficient definiteness owing to the uncertainty in the values of the nonlinearity parameter of rock). Rather powerful impact radiators (spark sources [8] or gas exploders [9]) are, in principle, broadband and, therefore, lack the necessary coherence and the possibility of choosing (controlling) the radiated signals. It should be noted that Vibroseis surface low-frequency (~10 Hz) radiators [10], being an alternative to the intrawell radiators, also have considerable drawbacks from the point of view of realization of coherent approaches to problems of seismoacoustic sounding. In addition to the low value of the transfer coefficient characterizing the radiating power transfer into bulk P waves, they offer very limited possibilities for controlling the regimes of radiation and formation of prolonged coherent packages (this is caused in part by the unpredictable changes in the properties of subsurface soil under the action of intense vibrations).

The obvious difficulty of developing high-power low-frequency intrawell radiators consists in their limited transverse dimension, which cannot exceed the inner diameter of the well (as a rule, 10–20 cm). This means that the traditional approach based on the radiation of cylindrically symmetric radial waves is not efficient because of the decrease in power with the decrease in frequency (probably, with the exception of a parametric converter), and an alternative design should be found. One of the solutions is the integration of sectioned piezoelectric rings in a working volume (a cylindrical column) in such a way that the radiator as a whole executes bending vibration. The transmission of vibration through the liquid filling the well to the walls of the pipe casing results in the radiation of mainly transverse S waves into the outer space. The most essential point in this scheme is the generation of bending vibration free of the frequency-dependent restriction of the power of radial vibration of the working surface. The effective frequency range of radiation can be reduced to hundreds and tens of hertz, which suggests good prospects for this radiator for acoustic action and crosswell sounding at distances above 1 km.

The first prototype of a powerful bending low-frequency intrawell radiator created at the Institute of Applied Physics to the order of OAO SibINKor (Tyumen) was successfully tested in the autumn of 1999 at Samotlor deposit of Nizhnevartovsk basin [11–13]. On the basis of this prototype, the institute developed and manufactured a modified variant of a bending radiator [14] to the order of Shell International Company (Netherlands). In this paper, we describe the principle of operation of this radiator and present the results of its field tests. Some results of the analytical and numerical modeling of the operating characteristics of this radiator are also discussed.

## THE PRINCIPLE OF OPERATION AND THE ANALYTICAL MODEL OF THE RADIATOR

The radiator is designed for the operation in a well filled with liquid. It is assumed that the thickness of the liquid layer $\Delta R$ between the radiating cylinder and the steel pipe casing, which is the outer boundary of the well, is considerably smaller than the cylinder radius $R$. The cylinder vibration is transmitted through the water to the pipe casing, whose motions eventually lead to the radiation of seismic waves beyond the pipe, as is schematically shown in Fig. 1.

The main element of the radiator is a cylindrical column consisting of washer-shaped piezoelectric plates. A separate plate is shown in Fig. 2. One side of the plate (side A) carries two electrodes divided by an insulating strip, and the other side (side B) is covered with one electrode. The plates are combined in pairs in such a way that their sides A coincide. To all the sides B, the ground potential is applied, and to sides A of different electrodes, the potentials $+V$ and $-V$ are applied. As a result, one half of the ceramic column contracts and the other half expands. Periodic changes in the voltage $V$ excite bending vibration of the cylinder as a whole.

Some important characteristics of the radiator can be estimated using the simplest analytical model. In this model, we take into account that the length of the radiating cylinder $l$ is much greater than its radius $R$. This condition allows us to use the thin rod approach [15], in the framework of which the frequencies of nat-

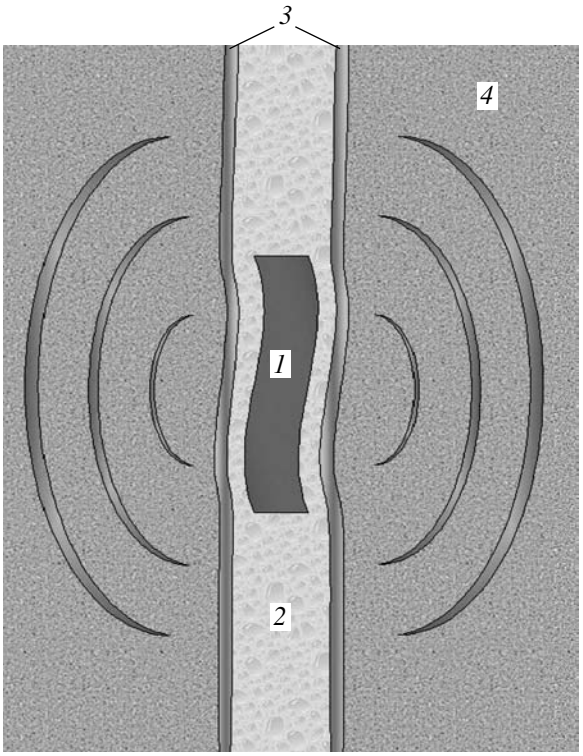


**Fig. 1.** Schematic representation of the principle of operation of the radiator. Bending vibration of (*1*) the piezoelectric cylinder acting through (*2*) water excite the vibration of (*3*) the pipe casing. The latter vibration generates seismoacoustic waves in (*4*) the soil.

ural vibrations of a cylinder in air are expressed by the formula

$$f = \frac{\gamma}{2\pi l^2}\sqrt{\frac{q}{m}}, \quad (1)$$

where $m$ is the mass per unit length of the cylinder and $q$ is the moment of inertia of the cylinder cross section. The quantity $\gamma$ is a numerical coefficient, the values of which for the natural frequencies corresponding to the first four modes of bending vibration of the cylinder are given in Table 1.

The design of the radiating cylinder is described in detail in [14]. As indicated above, its main part is a cylinder consisting of the piezoelectric plates shown in Fig. 2. There is also a cylindrical compound layer and an exterior steel tube, which also represents a cylindrical layer. The moment of inertia of the cross section of the cylindrical layer is expressed by the formula [15]

$$q_s = E(R_2^4 - R_1^4)/4, \quad (2)$$

where $R_1$ and $R_2$ are the inner and outer radii of the layer and $E$ is the Young's modulus of the layer material. The coefficient $q$ in Eq. (1) is the sum of the coefficients $q_s$ of all layers of the radiating cylinder.

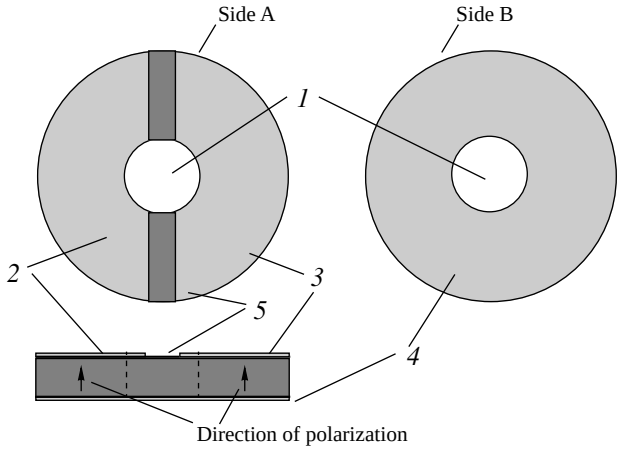


**Fig. 2.** Piezoelectric plate: (*1*) hole at the center of the piezoelectric plate, (*2*) the first sectioned electrode, (*3*) the second sectioned electrode, (*4*) continuous electrode, and (*5*) insulating strip.

Now we consider the operation of the radiator in a well filled with water. First, we consider the simplest case when we can neglect the vibration of the pipe casing (and, consequently, the surrounding soil). In this approximation, the cylinder vibration leads only to the flow of water in a narrow layer between the cylinder's and the pipe casing. A relatively simple analysis shows that the dynamics of the radiating cylinder is described in this case by the formulas determining the cylinder's vibration in air. The allowance for the influence of water and presence of the well boundaries is achieved by adding the added mass of liquid to the proper mass of the radiator. The value of the added mass per unit of the cylinder length for $\Delta R \ll R$ is given by the expression

$$\mu = \pi\rho_w\frac{R^3}{\Delta R}, \quad (3)$$

where $\rho_w$ is the water density. The resonance frequencies of the radiating cylinder in this model is given as before, by Eq. (1), with the replacement of $m$ by $m + \mu$.

The radiating cylinder, being the main component of the radiator, whose tests are discussed in this paper, had the length $l = 2.04$ m and radius $R = 0.073$ m. The cylinder's mass per unit length was $m = 99.8$ kg/m, and the width of the water layer between the cylinder and the pipe casing was $\Delta R = 4$ mm. The estimate of the added mass calculated by Eq. (3) gives $\mu = 314.2$ kg. Thus, the inclusion of the added mass increases the effective mass of the cylinder by a factor of four. According to

**Table 1**

| Mode | 1 | 2 | 3 | 4 |
|---|---|---|---|---|
| $\gamma$ | 22.37 | 61.67 | 120.9 | 199.86 |

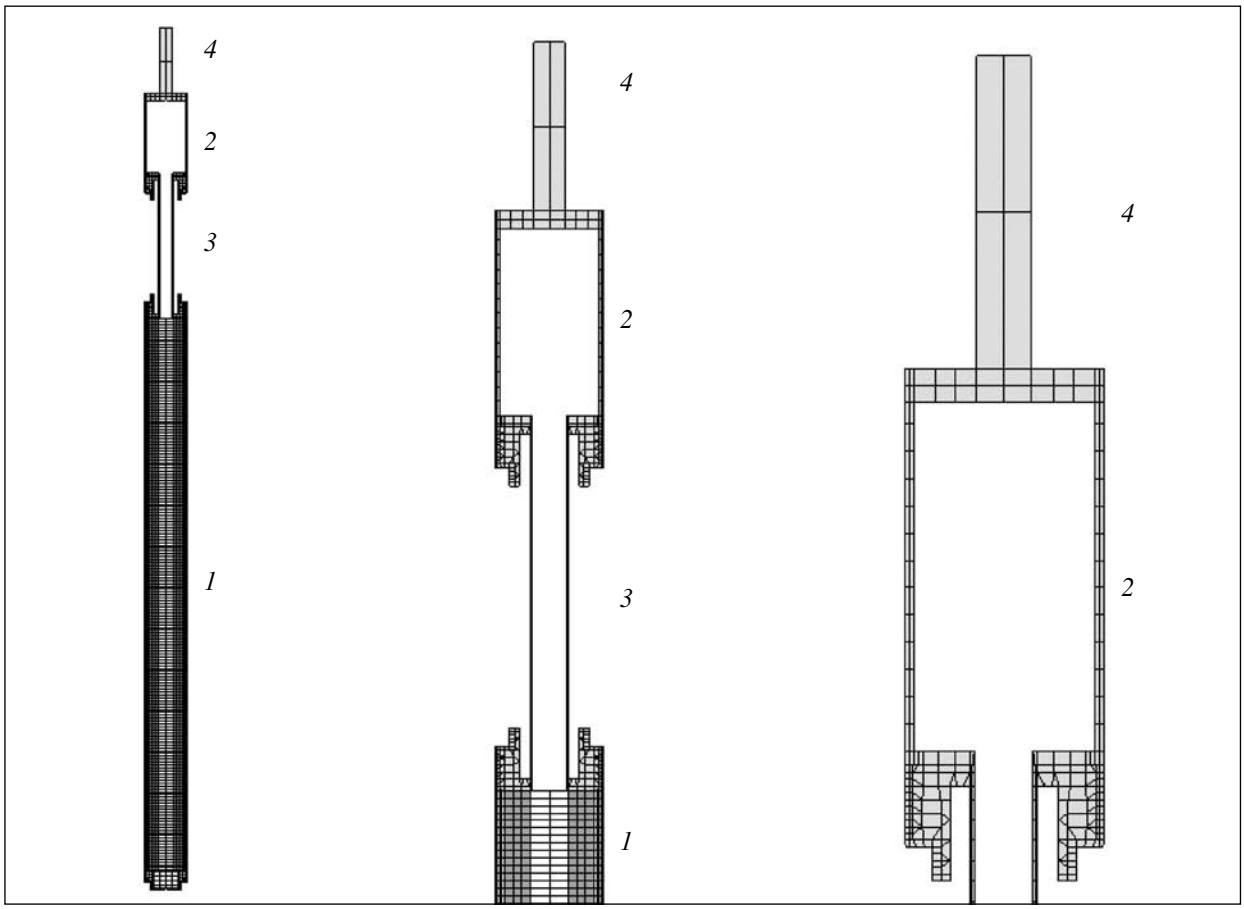


**Fig. 3.** Finite-element model of the radiator (three views with different magnification): (*1*) radiating cylinder, (*2*) equipment container, (*3*) shock-absorber, and (*4*) hanger.

Eq. (1), this means that, after the radiator is placed in the well, its resonance frequencies decrease by half.

Obviously, in reality, the pipe casing and the soil do not remain stationary. Moreover, numerical calculation shows that, under the conditions of soft unconsolidated soil at the testing area of the Institute of Applied Physics, the vibration amplitude of the pipe casing at the resonance frequencies may be of the same order of magnitude as the vibration amplitude of the radiating cylinder. Nevertheless, we will see that, even under these conditions, Eq. (1) (with the addition of the added mass given by Eq. (3) to $m$) adequately predicts the values of the resonance frequencies. In a firmer soil, which is typical of the large depths where oil pools are usually deposited, the accuracy of the discussed analytical description can only be higher.

## THE RADIATOR MODES AND THE CONCEPT OF SECTIONING

The numerical modeling of the operation of our radiator was performed by the finite-element method using the ANSYS multi-purpose program package [16]. The finite-element model of the radiator in air is shown in Fig. 3. In addition to radiating cylinder *1*, it includes container for equipment *2*, shock-absorber *3*, and hanger *4*, by which the radiator is fastened to the string of piping for lowering into the well.

For the analysis of the radiator operation in a well filled with water, a more complex model was used. The radiator shown in Fig. 3 was placed in a pipe casing filled with water. The pipe casing was placed inside a cylindrical volume of homogeneous soil 36 m high and 18 m in radius. The parameters of the soil were chosen on the basis of information obtained during well drilling at the testing area (see below). The absorption was introduced into the elements modeling the soil. Near the radiator, the absorption was very weak, but it grew sharply as the boundary of the volume occupied by soil was approached. This was done for the maximal attenuation of the waves reflected from the boundary. The introduction of such an attenuation is a standard procedure and makes it possible to model the radiator operation in an unbounded space.

One of the main goals of the modeling was to study the modes of bending vibration of the radiator. The first three modes are shown in Fig. 4 (for clarity, the vibration amplitudes are magnified compared to the real

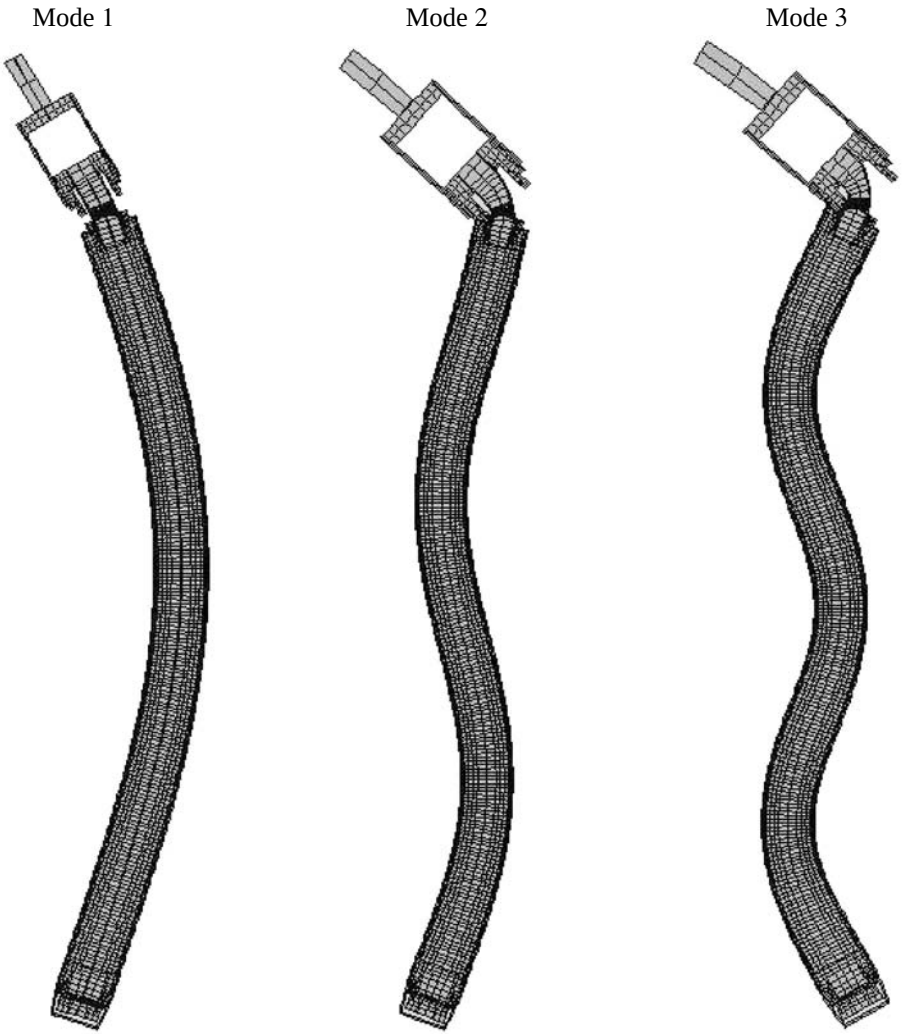


**Fig. 4.** The first three bending modes of the radiator.

ones). The forms of the modes in air and in a well with water differ little. However, this cannot be said about the resonance frequencies. The latter are given below in Tables 2 and 3. Numerical modeling with the ANSYS program package shows that the addition of the equipment unit, shock-absorber, and hanger leads not only to some change in the resonance frequencies of the modes of the radiating cylinder predicted by our analytical model. With these elements, the second mode of the cylinder splits into two modes with similar forms of vibration but noticeably different resonance frequencies. To emphasize the closeness of eigenfunctions of these modes determining the form of the rod vibration, both modes will be called the second ones. For this reason, in Tables 2 and 3, two resonance frequencies are given for the second mode (certainly, with the exception of the rows corresponding to the analytical model).

Note the very good agreement between the measured values of the resonance frequencies and the values obtained with modeling by the finite-element method. The analytical model overestimates the values of the resonance frequencies in air. The reason is that it does not take into account the influence of the equipment unit, shock absorber, and hanger. These elements increase the effective length of the radiator, which leads to a decrease in the resonance frequencies compared to the frequencies of the radiating cylinder (see Eq. (1)). In a well filled with water, the analytical model works better, since, in this case, the added mass of the water layer, which is correctly taken into account by this model, begins to play an essential part. Thus, using simple formulas (1)–(3), it is possible to estimate the reso-

**Table 2.** Resonance frequencies of the radiator modes in air

| Mode number | 1 | 2 | 3 |
|---|---|---|---|
| Eq. (1), $f$ (Hz) | 123 | 339 | 664 |
| ANSYS, $f$ (Hz) | 78 | 169; 282 | 588 |
| Measurements, $f$ (Hz) | 79 | 169; 284 | 597 |

**Table 3.** Resonance frequencies of the radiator modes in a well filled with water ($\Delta R$ = 4 mm)

| Mode number | 1 | 2 | 3 |
|---|---|---|---|
| Eq. (1), $f$ (Hz) | 60 | 166 | 326 |
| ANSYS, $f$ (Hz) | 49 | 110; 186 | 300 |
| Measurements, $f$ (Hz) | 49 | 112; 185 | 285 |

nance frequencies and judge the changes that will be caused by the variation of one or another of the parameters of the radiating cylinder. The obvious restriction of the analytical model is the fact that it does not predict the splitting of the second mode.

Of even greater importance is the fact indicated at the end of the previous section: the resonance frequencies and forms of modes weakly depend on the soil properties. This allows us to work out some universal recommendations for the optimal excitation of individual modes. Note that the form of every mode is characterized by a sequence of portions with curvature of different sign. The change of sign takes place at the points of zero curvature, which are located near the mode nodes. Within the part of the cylinder with the curvature of the same sign, all the halves of the piezoelectric plates (see above) lying to one side of the symmetry plane of the radiating cylinder behave in the same way: they simultaneously contract or expand. It is this consideration that lies at the basis of the concept of sectioning the radiator, that is, dividing it into sections, as shown in Fig. 5. The boundaries of the sections are chosen to be located near the nodes of the second and third modes. For optimal excitation of a required mode, the signs of the voltages should be selected in such a way that, under the action of piezoelectric forces, the cylinder would bend reproducing the mode form. The field tests described below confirmed that such sectioning results in a considerable increase in the efficiency of the radiator operation.

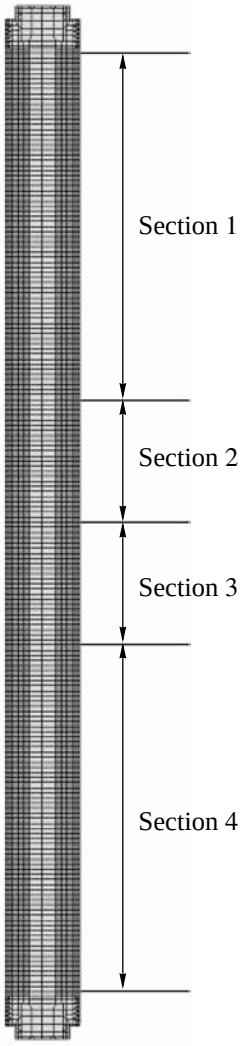


**Fig. 5.** Scheme of radiator sectioning.

## EXPERIMENTAL STUDY OF THE RADIATOR

### *Description of the Experiment*

The experimental study of the radiator was carried out at the testing area of the Institute of Applied Physics, 35 km away from Nizhni Novgorod. Beforehand, three identical wells 20 m in depth were drilled and equipped. Every well was cased with a steel pipe 168 mm in diameter. The space between the pipe casing and the well walls was filled with concrete. The layout of the wells and the orientation of coordinate axes are shown in Fig. 6. During the tests, the radiator was positioned in well *1*, and the receiving equipment was in one of the two other wells at distances of 3 and 50 m from the radiator. All three wells were filled with water. In describing the results, we use the Cartesian coordinate system with the $z$ axis directed vertically upward and the $x$ axis directed along the line passing through the three wells. The $y$ axis lies in the horizontal plane perpendicular to the $x$ axis (see Fig. 6).

From the analysis of the soil sample obtained from the well drilling, rough estimates of the mean density of

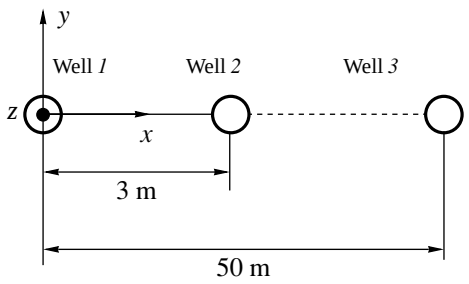


**Fig. 6.** Layout of wells at the testing area and the orientation of coordinate axes.

soil at the testing area ($\rho_g$ = 1730 kg/m$^3$), the mean velocity of longitudinal seismic waves ($c_p$ = 550 m/s), and the mean velocity of transverse waves ($c_s$ = 280 m/s) were obtained.

The seismic waves were recorded by using an intrawell geophone designed and tested at the Institute of Applied Physics. This instrument consists of a spherical geophone intended for measuring the acoustic pressure inside a well filled with water and of three orthogonally oriented piezoelectric accelerometers for measuring the *x*, *y*, and *z* components of vibration displacements of the well walls.

During all the measurements, the radiator was located at a constant depth (its center was at a distance of 11 m from the surface). The radiation occurred in three regimes differing in the sets of signs of the voltages applied to various sections of the radiator.

*Regime 1*. All the sections are fed in-phase. The voltages applied to all halves of piezoelectric plates located to one side of the symmetry plane of the radiator are the same. Obviously, in this regime, the first mode is excited most efficiently.

*Regime 2*. The voltage *V* is applied to sections 1 and 2, and the voltage –*V* is applied to sections 3 and 4. In this case, the vibration, in which the curvatures of the upper and lower halves of the radiator have opposite signs, is excited best of all. In this regime, the second mode is excited efficiently.

*Regime 3*. The voltage *V* is applied to sections 1 and 4, and the voltage –*V* is applied to sections 2 and 3. This regime is optimal for exciting the third mode.

In the investigations the results of which are discussed below, the rms value of the voltage *V* was varied in the range from 200 to 270 V.

For studying the frequency dependence of the characteristics of seismic waves, signals with a rather slow linear change of frequency (linear frequency modulated (LFM) pulses) were radiated. The duration of every pulse was 25.6 s. The frequency deviation within these pulses was usually equal to two or three hundreds of hertz. The operation of the radiator in the frequency range from 20 to 500 Hz was investigated.

In every regime of radiation, two sets of measurements were performed. In one set, the radiator vibrated in the *yz* plane, and in the other set, in the *xz* plane. The change of orientation was carried out by turning the radiator about its axis through 90°.

For studying the spatial structure of the radiator field, the vertical distributions of the field were measured by using the geophone placed in measuring wells *2* or *3* shown in Fig. 6. The geophone was successively fixed at various depths at a step of 0.5 m (in well *2*) or 1 m (in well *3*). In well *2*, the measurements were performed in the depth range from 0 to 13.5 m, and in well *3*, in the range from 3 to 15 m. For every geophone position, the voltage at the radiator was measured along with the signals at the outputs of the four geophone channels: three components (*x*, *y*, and *z*) of acceleration and the pressure. Some data obtained from these measurements are presented in the next section.

### *Results of Measuring the Field Distribution in the Vertical Plane*

The measured dependences of the acceleration components on time were converted (dividing by $\omega^2$, where $\omega$ is the angular frequency) into the components of particle displacement in the medium. The displacements in the directions *x*, *y*, and *z* will be designated below as $s_x$, $s_y$, and $s_z$, respectively. Figure 7 shows, as an example, the displacements $s_x$ and $s_y$ measured by the geophone in well 2 at a depth of 12 m. At the radiation of an LFM pulse, every point in time is characterized by a corresponding value of frequency. Therefore, in the diagrams of the dependences of displacement on time shown in Fig. 7, the abscissa axis represents not the time but the corresponding frequency.

The radiation was carried out in regime 2, and the radiator oscillated in the *yz* plane. As could be expected, under these conditions, the displacement amplitude in the *y* direction exceeds the displacement amplitude in the *x* direction. As was mentioned, regime 2 is optimal for the excitation of the second mode. This agrees well with the presence of maxima at frequencies of 180 and 110 Hz, i.e., the resonance frequencies of the two second modes into which the second mode of the radiating cylinder splits in the presence of the equipment unit, shock-absorber, and hanger. We also note the broad maximum at the resonance frequency of the third mode 280 Hz. This mode is excited, although not efficiently, in regime 2 as well. The results of the tests in regime 1 (which are not presented here) confirm that, in this regime, the first mode is excited best of all.

A more detailed pattern of the radiation field in regime 2 is shown in Figs. 8–10. In Figs. 8 and 9, showing the distributions of the components $s_x$ and $s_y$ at a distance of 3 m from the radiator (well 2), the maxima near the frequencies of 110 and 180 Hz, which were present in Fig. 7, are observed. Figures 8 and 9 also show the dependence of the field amplitude on the depth. We discuss this dependence below, in the consideration of the Fourier transform of the vertical distributions of the field in well 2. Since the radiator oscillates along the *y* axis, the displacement vector component $s_y$ predominates. In similar measurements, when the radiator oscillates along the *x* axis, the diagrams of distribution of the $s_x$ and $s_y$ components (which are not presented here) are similar in appearance, with the only difference that the $s_x$ component becomes dominant.

From Fig. 10 we see that, on the way from well 2 to well 3, that is, at a distance of 47 m, the signal ampli-

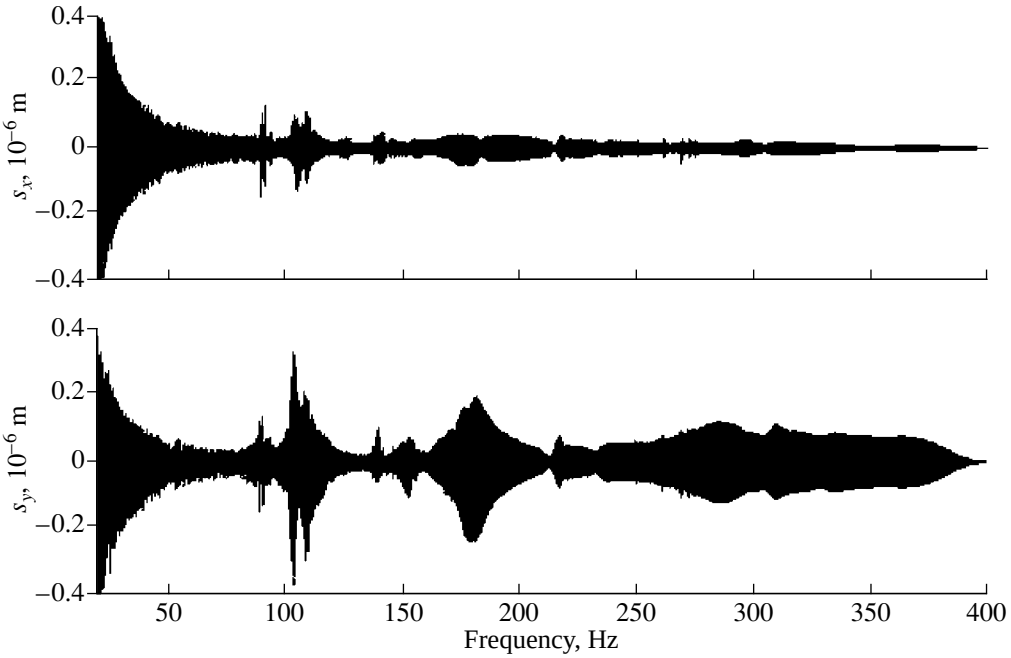


**Fig. 7.** Components of the displacement vector along the *x* axis (top) and *y* axis (bottom) as functions of radiation frequency. Radiation regime 2. The radiator vibrates in the *yz* plane.

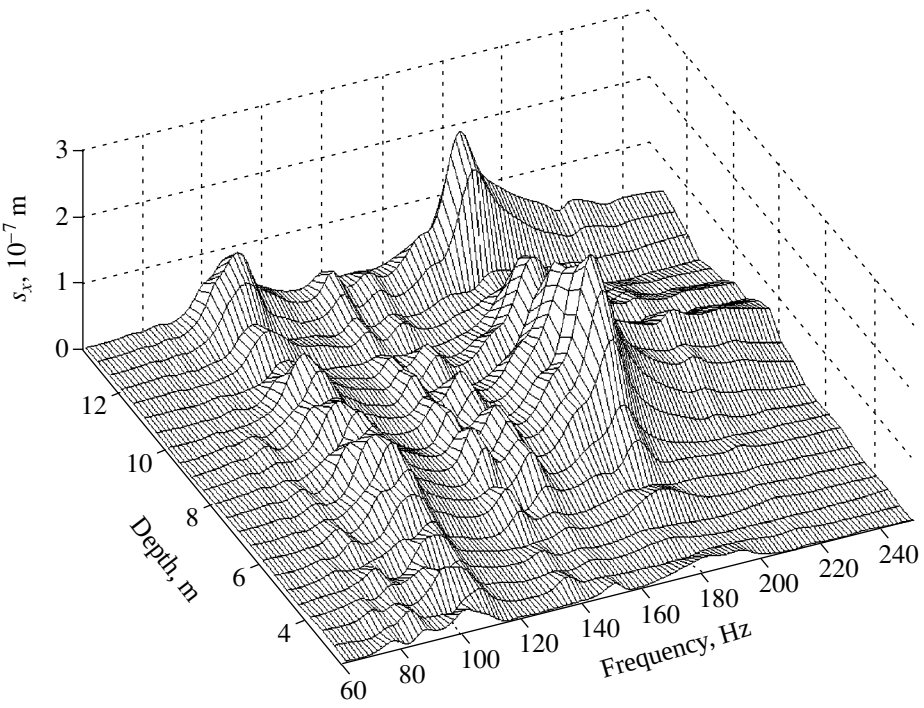


**Fig. 8.** Dependence of the displacement vector component along the *x* axis in well 2 (3 m from the radiator) on the depth and frequency. Radiation regime 2. The radiator vibrates in the *yz* plane.

tude attenuates by two orders of magnitude. A substantial dependence of attenuation on frequency manifests itself in the shift of the maximum in the frequency dependence of the $s_y$ component from 180 Hz at a distance of 3 m to about 170 Hz at 50 m. The measurements show that, at a distance of 50 m, the $s_y$ component predominates regardless of the orientation of the symmetry plane of the radiator (i.e., regardless of the

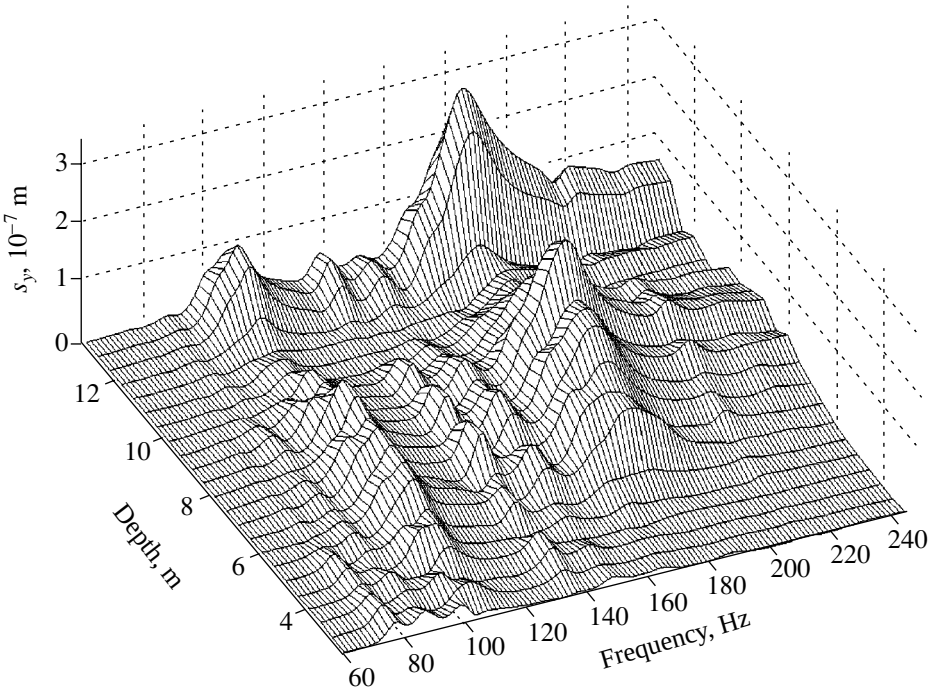


**Fig. 9.** The same as in Fig. 8 for the displacement vector component along the *y* axis.

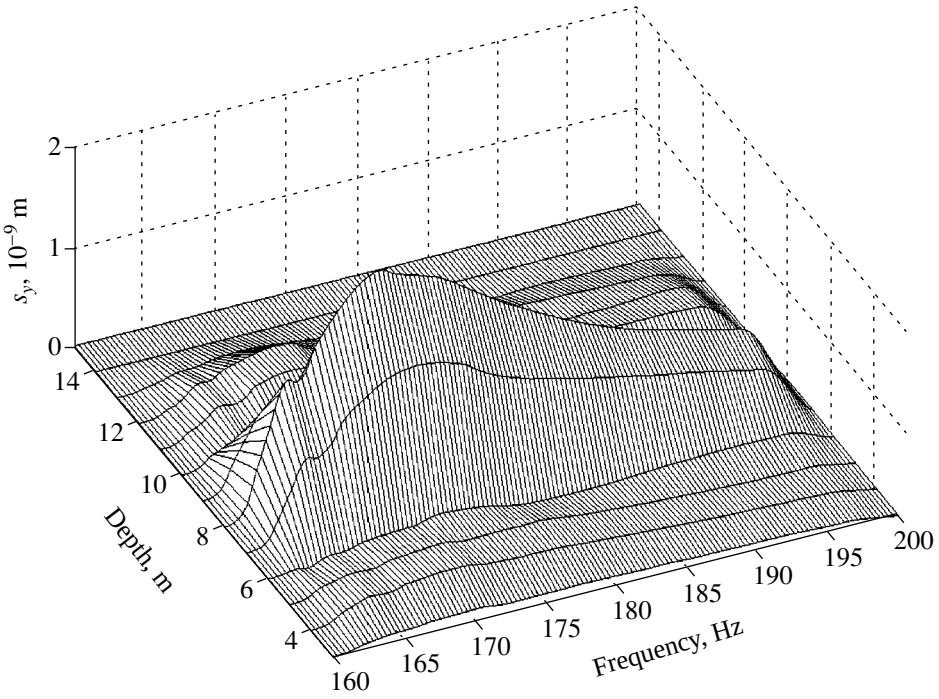


**Fig. 10.** The same as in Fig. 9 for measuring the seismic waves in well 3 (50 m from the radiator).

direction in which it vibrates). The explanation of this rather unexpected effect requires a more detailed knowledge of the soil structure at the testing area and a modeling of the seismic field with consideration for this information. Such investigations have not yet been conducted.

Figures 11 and 12 show the distributions of the $s_x$ and $s_y$ components in well 2 at the radiator operation in

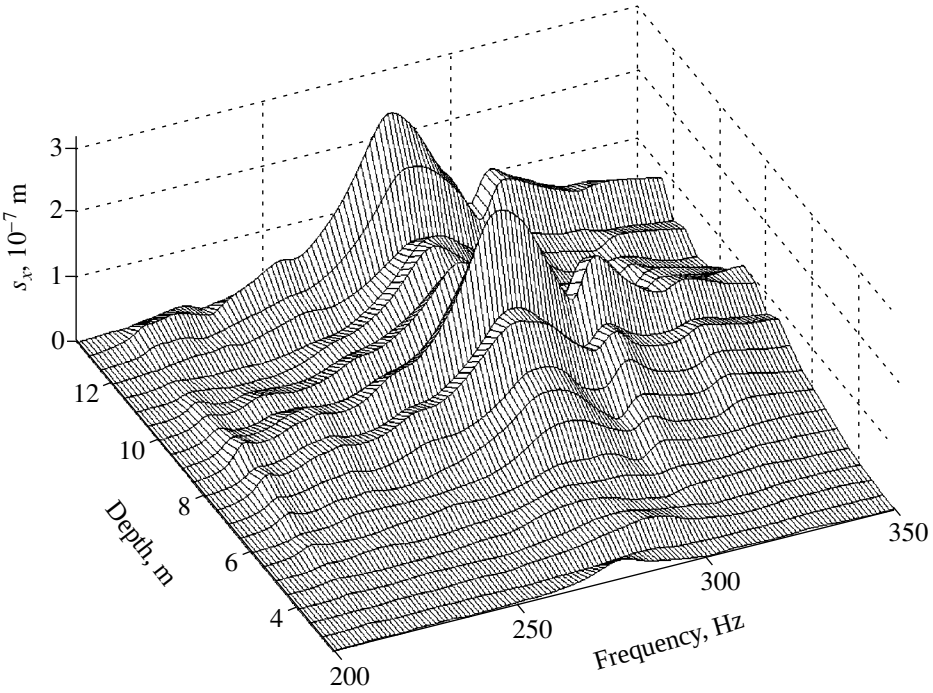


**Fig. 11.** The same as in Fig. 8 for radiation regime 3.

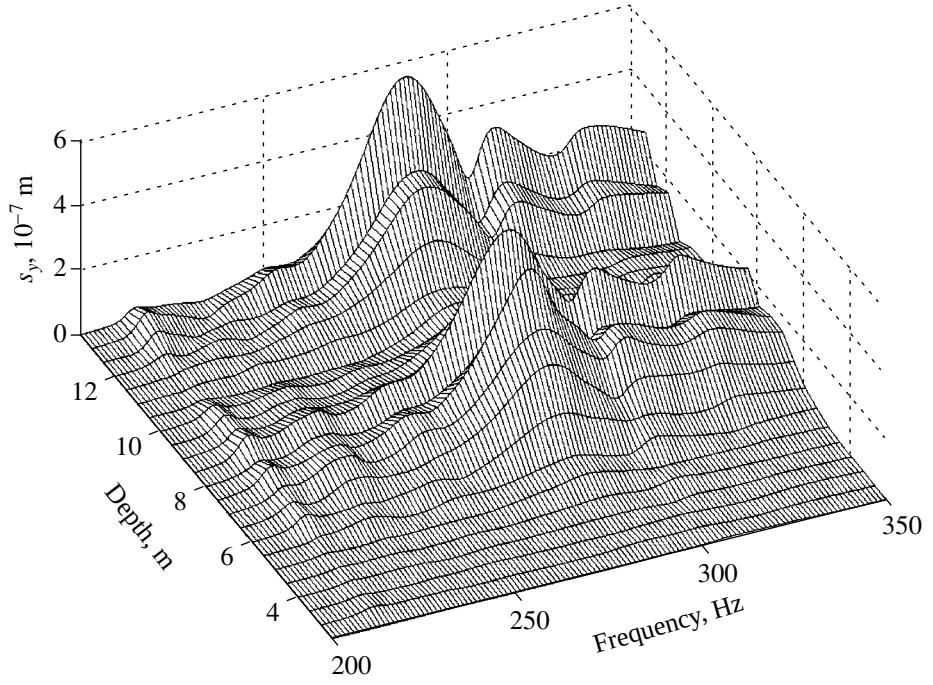


**Fig. 12.** The same as in Fig. 11 for the displacement vector component along the *y* axis.

regime 3, that is, when the third mode is efficiently excited. As is expected, the radiation is maximal at the resonance frequency of this mode, 285 Hz. As in the previous example, when the radiator oscillates along the *y* axis, the $s_y$ component predominates. After rotation of the radiator symmetry plane through 90° (in this case, it oscillates along the *x* axis), the contribution of the $s_x$ component, as might be expected, increases. In the farther well, as in regime 2, the $s_y$ component predominates at any orientation of the radiator vibration

plane. The dependences of the amplitude of $s_y$ on frequency and depth resemble the analogous dependences for regime 2 shown in Fig. 10. Because of the frequency dependence of attenuation, the maximum of $s_y$ at a distance of 50 m shifts to lower frequencies. In regime 3, the magnitude of the shift is about 15 Hz.

On the basis of the results of mathematical simulation, it is expected that the bending vibration of the radiator primarily results in the generation of shear seismic waves. The value of the phase velocity of shear waves near the radiator is taken to be equal to $c_s$ = 280 m/s. Then, the wavelengths at the resonance frequencies of the first, second, and third modes (as a resonance frequency of the second mode, we take 180 Hz) are equal to $\lambda_1$ = 5.6 m, $\lambda_2$ = 1.5 m, and $\lambda_3$ = 1 m, respectively. Since the length of the radiating cylinder is 2.04 m, it is obvious that, at the first-mode operation, the reactive component of the seismic field predominates near the radiator. At the operation at the second and third modes, in contrast, a substantial contribution of the active component can be expected. In the finite-element numerical modeling, the travelling waves clearly manifest themselves even at a distance of 3 m from the radiator. Hence, it follows that, using the Fourier analysis of the vertical field distributions in well 2 shown in Figs. 8, 9, 11, and 12, it is possible to make conclusions regarding the angular structure (radiation pattern) of the radiator.

In both radiation regimes, in the vertical field distribution at a distance of 3 m from the radiator, we can see the minima at the horizon of the radiator center (a depth of 11 m). At a depth of about 8 m, we see maxima, which can be interpreted as the manifestation of the contribution of the waves travelling at the grazing angles close to 45°. Symmetric (with respect to the depth of the radiator center) maxima are observed at depths of about 13 m. Here, it should be remembered that the measurements of the field in well 2 were performed only to this depth. So, one cannot state with confidence that, beginning from the depth of 13 m, the field amplitude steadily decreases.

For determining the radiation pattern of the radiator, we calculated the spatial Fourier transform of the complex field amplitude measured in well 2. For every frequency (of the range corresponding to the radiated LFM pulse), the spectrum was calculated by the formula

$$S_y(\kappa) = \int_0^L H(z)s_y(z)e^{i\kappa z}dz, \quad (4)$$

where $L$ = 13.5 m is the maximal depth to which the field was measured, $H(z)$ is the Hanning weighting window, and $\kappa$ is the spatial frequency. Every harmonic corresponding to $|\kappa| < k_s = \omega/c_s$ can be interpreted as the amplitude of a plane wave travelling at the grazing angle $\chi$ determined by the relation $\kappa = k_s\sin\chi$. The results are displayed in Figs. 13 and 14. The abscissa axis, instead of the spatial frequency, represents the corresponding grazing angle.

The field measurements were conducted in a depth range in which the received signals were mainly formed by the waves propagating in the direction toward the surface. The contributions of only these waves—in our designations they have positive grazing angles—are shown in Figs. 13 and 14. As one would expect, in regime 2, the maximal radiation was observed at frequencies close to 180 Hz, and in regime 3, at frequencies close to 285 Hz. The waves with maximal intensity propagate in regime 2 at the angle $\chi \approx 40°$, and in regime 3, at the angle $\chi \approx 35°$.

Note that, with an increase in frequency, in both regimes, the grazing angles on the average decrease. This is a reasonable and expected result. Indeed, with the increase in frequency, the wave number $k_s = \omega/c_s$ grows. However, the characteristic scales of the radiator oscillation modes determining the scales of the transverse structure of the seismic field (at least, near the radiator) change to a much smaller degree. Roughly, it may be thought that the spatial frequency $\kappa$ corresponding to the spectrum maximum is independent of $\omega$. Then, the grazing angle $\chi = \arcsin(\kappa/k_s)$ decreases with the growth of $\omega$. This is what we see in Figs. 13 and 14.

## THE POWER, EFFICIENCY, AND QUALITY FACTOR OF THE RADIATOR

The data of the measurements of the vertical field distributions in receiving wells 2 and 3 make it possible to roughly evaluate the radiation power. For this purpose, we will use the following formula for the energy-flux density in a seismic wave. We consider a plane shear wave travelling along the $x$ axis. The particles of the medium are considered as oscillating along the $y$ axis. Then, the projection of the energy flux density vector on the $x$ axis is

$$G_x = \frac{\omega^2\rho c_s}{2}|u_y|^2, \quad (5)$$

where $\omega$ is the angular carrier frequency, $\rho$ is the density of the medium, $c_s$ is the velocity of shear waves, and $u_y$ is the complex amplitude of the particle displacement. If waves travelling at an angle to the $x$ axis are considered, formula (6) is modified in an evident way. A similar formula exists for longitudinal waves (with the replacement of $c_s$ and $u_y$ by the corresponding characteristics of longitudinal waves, $c_p$ and $u_x$), but it will not be needed, because, in our case, the contribution of shear waves to the total field is dominant.

In estimating the radiation power, we considered waves measured by the geophone to be quasi-plane and

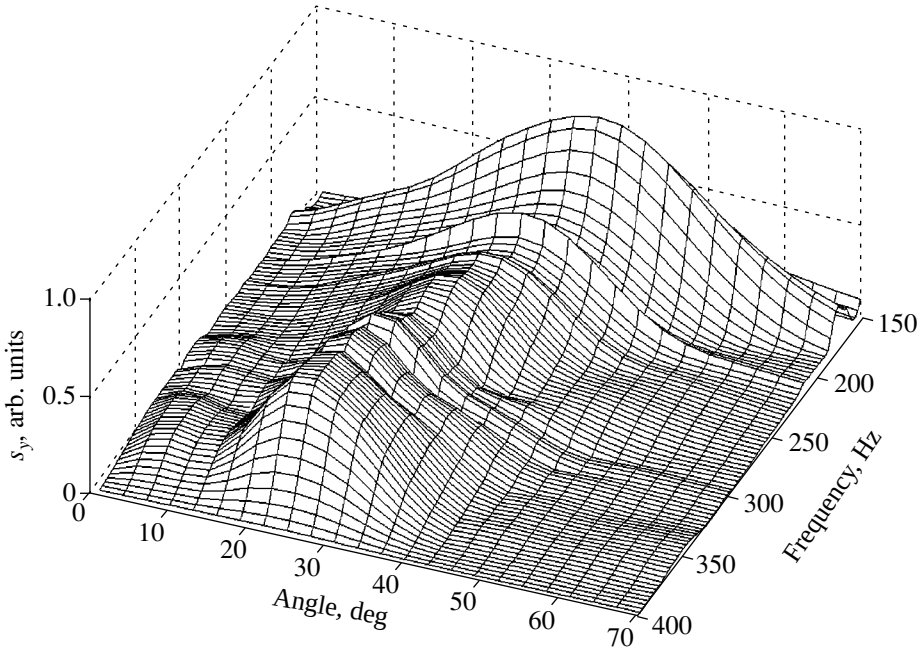


**Fig. 13.** Radiation pattern in the vertical plane at a distance of 3 m from the radiator in the angle–frequency coordinates. Radiation regime 2.

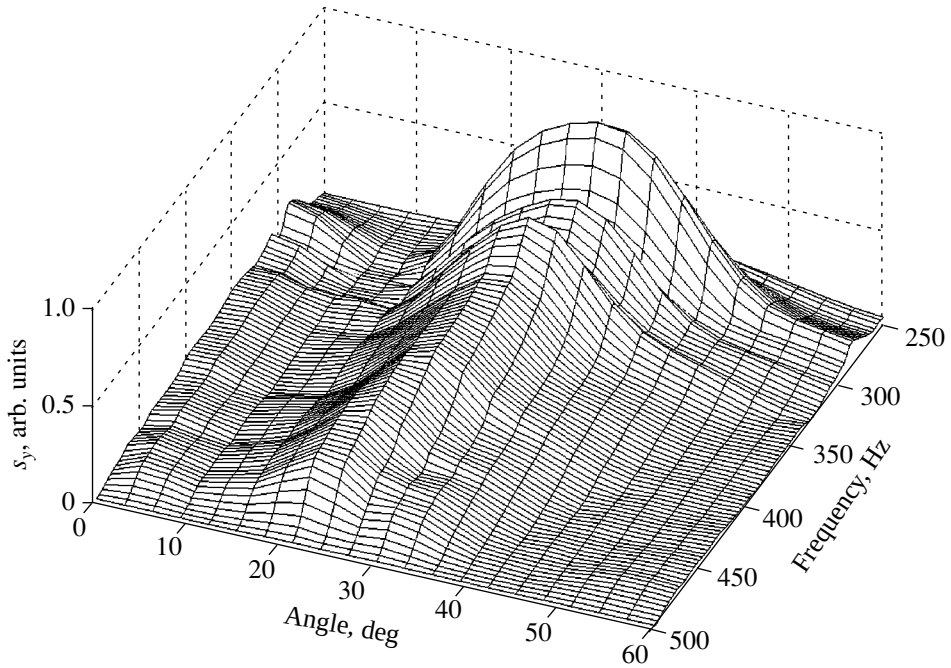


**Fig. 14.** The same as in Fig. 13 for radiation regime 3.

used the above formula. In addition, we assumed that the dependence of the displacement amplitude in the horizontal plane on the azimuth angle $\theta$ is expressed by the coefficient $\cos\theta$. In reality, the azimuth dependence is, certainly, more complex. For example, from Figs. 9–12, it is seen that, after the radiator rotation through 90°, no radical changes occur in the amplitudes of the displacement components. Therefore, the available data make it possible only to evaluate the order of magnitude of the radiation power.

Using Eq. (6) and the experimental data, we integrated the energy flux density vector over the cylindri-

cal surfaces of radii 3 and 50 m surrounding the radiator. In this way, we evaluated the energy fluxes through these surfaces. Comparing the values of the fluxes through these surfaces, we estimated the attenuation in the medium. Then, knowing the energy flux through the surface with the 3-m radius and the attenuation coefficient of seismic waves, we can evaluate the total radiation power. And, finally, taking into account that the increase in the applied voltage by a factor of $n$ leads to an increase in the radiation power by a factor of $n^2$, we predicted the radiation power for the case when a voltage of 1 kV is applied to the radiator.

It turned out that, with such a voltage applied in regime 2, the value of the radiation power at the resonance frequency of the second mode $f = 180$ Hz is equal to 207 W. The attenuation coefficient at this frequency is about 0.73 dB/m or 1.2 dB/$\lambda$ ($\lambda$ is the wavelength). At the operation in regime 3, for the resonance frequency of the third mode $f = 280$ Hz, the radiation power is 1250 W and the attenuation coefficient is 1.3 dB/m or 1.3 dB/$\lambda$.

These values of the power are, presumably, underestimated, because the measurement of the vertical field distribution was performed only to a depth of 14 m. In the integration over the cylindrical surfaces, we did not consider the contributions of the waves propagating below this depth. The formal application of the above procedure for calculating the power radiated in regime 1 (with the voltage of 1 kV applied to the radiator) at the resonance frequency of the first mode 48.5 Hz gives a value of 14 W.

To estimate the efficiency of our radiator, in the experiments with the radiation of the third mode, accurate measurements of amplitudes and phases of the current and voltage delivered to the radiator were carried out. It was found that, at a frequency of 280 Hz, the radiator efficiency was 60%, that is, 60% of the consumed power was converted into the radiation energy.

In the analysis of the forms of maxima of LFM signals measured in well 2, the estimates of the $q$ factor of radiator oscillations at the resonance frequencies of the three bending modes were obtained. The results are presented below (the symbol $\Delta f$ denotes the radiation bandwidth by the 3-dB level):

regime 1: $f = 48.5$ Hz, $\Delta f = 1.2$ Hz, $q = f/\Delta f = 40$;

regime 2: $f = 180$ Hz, $\Delta f = 9$ Hz, $q = f/\Delta f = 20$;

regime 3: $f = 280$ Hz, $\Delta f = 25$ Hz, $q = f/\Delta f = 11$.

## CONCLUSIONS

The field tests of the prototype of the sectioned intrawell radiator at the testing area of the Institute of Applied Physics confirmed the feasibility and efficiency of the proposed design. The experiment showed that this radiator is capable of radiating high-power low-frequency shear seismic waves in the frequency range from 40 to 400 Hz, both at the resonance frequencies and in relatively broad frequency bands in the upper part of this range. The radiation power of the manufactured prototype can reach ~1 kW with an efficiency of 60%. The $Q$ factor of the resonances of the radiator varies from 11 to 40 for different modes.

An important result is the confirmation of the adequacy of the finite-element and analytical models of the radiator. The analytical model is intended for a preliminary rapid evaluation of the main characteristics of the radiator (resonance frequencies, amplitudes of forced vibrations, etc.). It allows one to study their dependences on the characteristic parameters of the radiating cylinder (length, diameter, case thickness, etc.). The final design of the radiator and the analysis of its main operating and strength characteristics were performed using the numerical finite-element model constructed on the basis of the ANSYS program package. The use of this modern powerful technology of engineering analysis makes it possible to predict with a high accuracy the operating parameters of the radiator and to optimize its structure for obtaining the required performance.

The efficiency of the concept of sectioning the radiator is demonstrated. The separation of the radiating cylinder into sections, which are fed independently, enables one to excite various modes of the radiator in the optimal way. This offers additional possibilities for matching the radiator parameters with the environment and controlling the spatial characteristics of radiation.

## ACKNOWLEDGMENTS

This work was supported by the Shell International Company (the Interdepartmental Science and Technology Center project no. 2067) and the Russian Foundation for Basic Research (project nos. 02-02-17089, 03-02-31006-k, and 04-02-31009-k).

## REFERENCES

1. A. V. Lebedev and A. I. Malekhanov, Izv. Vyssh. Uchebn. Zaved., Radiofiz. **7**, 579 (2003).
2. V. S. Averbakh, B. N. Bogolyubov, Yu. M. Zaslavskiĭ, *et al.*, Akust. Zh. **45**, 5 (1999) [Acoust. Phys. **45**, 1 (1999)].
3. V. S. Averbakh, V. V. Artel'nyĭ, B. N. Bogolyubov, *et al.*, Akust. Zh. **47**, 437 (2001) [Acoust. Phys. **47**, 371 (2001)].
4. O. L. Kuznetsov and S. F. Efimova, *Ultrasound Application in Oil Industry* (Nedra, Moscow, 1983) [in Russian].
5. V. A. Aleksandrov, V. B. Zheleznyĭ, Yu. V. Kazakov, and D. B. Ostrovskiĭ, Karotazhnik, No. 107, 23 (2003).
6. V. P. Mitrofanov, A. I. Dzyubenko, B. V. Terent'ev, *et al.*, Karotazhnik, No. 45, 25 (1998).
7. V. A. Aleksandrov, V. B. Zheleznyĭ, V. B. Zhukov, *et al.*, Geofizika, No. 5, 30 (1999).

8. V. V. Kalinin, M. L. Vladov, S. F. Aptikaev, *et al.*, Geofizika, No. 5, 29 (2003).
9. G. G. Kocharyan, V. N. Kostyuchenko, A. M. Budkov, and I. S. Svintsov, Geofizika, No. 6, 17 (2003).
10. *Theory and Practice of Nonexplosive Surface Seismic Prospecting*, Ed. by M. B. Shneerson (Nedra, Moscow, 1998) [in Russian].
11. L. S. Brilliant, B. N. Bogolyubov, I. V. Tsykin, *et al.*, Neft. Khoz., No. 9, 86 (2000).
12. G. A. Potapov and V. M. Pravdukhin, Neft. Khoz., No. 9, 82 (2000).
13. B. N. Bogolyubov, V. N. Lobanov, V. I. Rylov, *et al.*, Preprint No. 550, IPF RAN (Institute of Applied Physics, Nizhni Novgorod, 2000) [in Russian].
14. V. S. Averbakh, V. V. Artel'nyĭ, B. N. Bogolyubov, *et al.*, Preprint No. 643, IPF RAN (Institute of Applied Physics, Nizhni Novgorod, 2003) [in Russian].
15. L. D. Landau and E. M. Lifshitz, *Theory of Elasticity* (Nauka, Moscow, 1986; Pergamon, Oxford, 1986).
16. K. A. Basov, *ANSYS in Examples and Problems* (Komp'yuter Press, Moscow, 2002) [in Russian].

*Translated by A. Svechnikov*

*Acoustical Physics, Vol. 51, Suppl. 1, 2005, pp. S37–S42. Translated from Akusticheskiĭ Zhurnal, Vol. 51, Suppl., 2005, pp. 46–52.*


# Fluctuations of Acoustic Field in a Granular Medium

**E. D. Bazhenova, A. N. Vil'man, and I. B. Esipov**

*Andreev Acoustics Institute, Russian Academy of Sciences,*
*ul. Shvernika 4, Moscow, 117036 Russia*
*e-mail: ibesipov@akin.ru*

Received August 17, 2004

**Abstract**—Results of an experimental study of sound propagation in a granular medium are presented. It is found that, in the case of excitation of a harmonic signal with a constant amplitude, the acoustic response of a single grain strongly varies in time. The dependence of the harmonic component amplitudes in the response spectrum on the level of signal excitation proves to be nonmonotonic and also strongly varies in time. The most intense fluctuations are observed in the subharmonic component of the propagating signal. The intensity fluctuation spectra of the harmonic components of the response are obtained for the frequency range of $10^{-4}$–$10^{-1}$ Hz. A possible mechanism that may be responsible for the slow fluctuations of an acoustic field in a granular medium is discussed. 

## INTRODUCTION

It is known that the character of propagation of acoustic vibrations in granular media noticeably differs from analogous propagation in continuous media. The mechanical properties of granular media are determined to a great extent by the contacts between the grains. The concentration of elastic deformation energy in the regions of the contacts leads to anomalously high values of the nonlinear acoustic characteristics of granular media, which is typical of many rocks, for example [1–3]. This property of granular media allows us to associate it with a wide class of media with the nonlinear elasticity of structural type. While the nonlinear acoustic properties of classical continuous media, such as single crystals or homogeneous fluids, are determined by the special properties of deformation at the molecular level, the corresponding characteristics of granular media depend on their structure. In this sense, the characteristics of granular media manifest themselves at a small-scale level, i.e., on the scales determined by the grain sizes [4]. This fact leads to essential qualitative and quantitative differences, for example, in the equations of state for the media. While the relative strain of a continuous medium $\Delta$ in the first approximation is proportional to the applied stress $\Delta \approx P$, in the case of spherical grains this relationship is more complex: $\Delta \approx P^{2/3}$ [5]. Therefore, the propagation velocity of acoustic waves in a granular medium $c^2 = \partial P/\partial\rho \approx P^{1/3}$ is a nonlinear function of the applied stress $P$. Correspondingly, the nonlinearity parameter of the medium $\varepsilon = \rho_0 \partial c^2/\partial P \approx P^{-5/6}$ also strongly depends on the applied stress. Here, $\rho$ is the density of the medium and $\rho_0$ is its equilibrium value. It turns out that the nonlinear properties of granular media noticeably manifest themselves even in the case of relatively deformations. For example, nonlinear distortions in rocks are already noticeable at deformations of about $\Delta \approx 10^{-9}$ [6]. This is evidence of the fact that the typical values of the nonlinearity parameter of granular media are 3–4 orders of magnitude higher than the corresponding values of the nonlinearity parameter in homogeneous continuous media.

Lately, attention was given to the investigation of the behavior of granular media on the single grain scale [7–14]. It is noted that, under small stresses, noticeable deviations from regular stress–strain relations are observed [9, 14]. These relations are usually valid only asymptotically for sufficiently large stresses, when a granular medium can be considered to be well compacted. In this case, the response to a cyclic loading in such media is, as a rule, of a hysteretic character in the stress–strain relation. This property of granular media manifests itself in the peculiarity of nonlinear distortions of acoustic waves, when the third harmonic of a propagating acoustic signal grows proportionally to the square of the signal amplitude and its level may dominate over the level of the second harmonic [15]. It was found that vibrations of a single grain in the acoustic field of constant amplitude is subjected to slow fluctuations [7]. In the present paper, we discuss the results of an experimental study of slow fluctuations in the nonlinear vibrations of grains in a medium under the effect of a propagating acoustic field and propose a possible mechanism of these fluctuations in a granular medium.

## EXPERIMENT

In our investigations, as a granular medium, we used granite chips 1–2 cm in size. This medium filled a round plastic container with a flat bottom (Fig. 1). The diameter of the container was 20 cm, and the height was 25 cm. A circular piezoceramic plate with a thickness of 12 mm and a diameter of 100 mm was placed on the

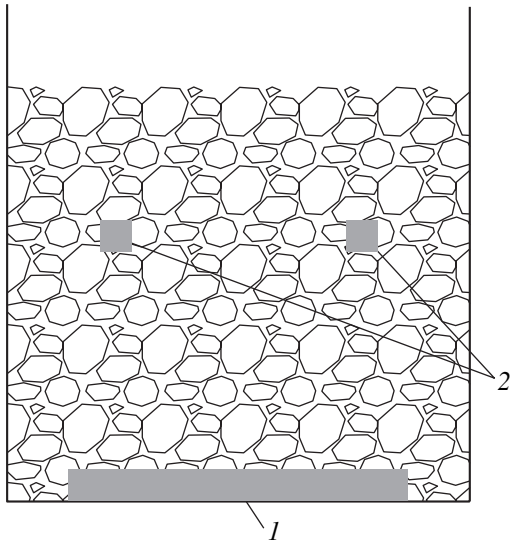


**Fig. 1.** Schematic diagram of the experimental setup: (*1*) a piezoceramic plate and (*2*) the AR-18 receivers.

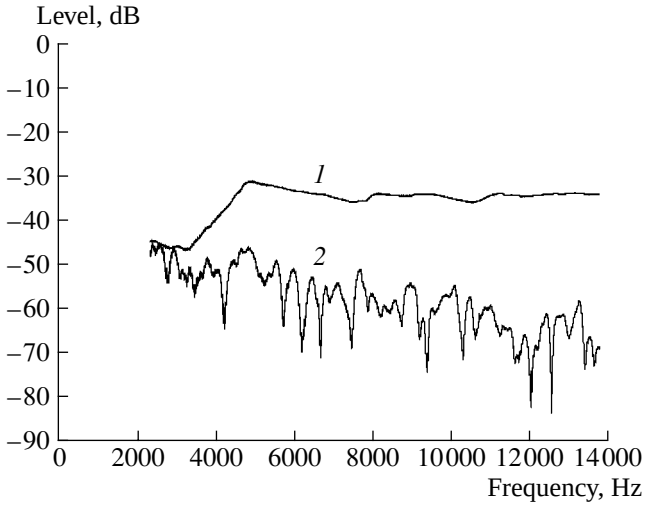


**Fig. 2.** Frequency response of a receiver in a granular medium at a distance of 7 cm from the source. (*1*) The frequency characteristic of the radiated signal and (*2*) the characteristic of the detected signal.

container's bottom. This plate was the source of acoustic signals. The plate radiation was monitored by an accelerometer fixed directly at the plate. The acoustic signals were received by two accelerometers of the AR-18 type, which were positioned within the granular medium at a distance of 7 cm from the source. A layer of the granular medium with a thickness of about 10 cm was lying over the receivers. The weight of the receivers was 1.2 g. The receivers were shaped as cylinders with a length of 10 mm and a diameter of 6 mm. The sensitivity of the receivers was 2.38 pC/*g*, and the electrical capacitance of the receivers was equal to 830 pF. Here, *g* is the acceleration of gravity. Thus, the dimensions of the receivers were close to the size of the grains surrounding them, and these receivers could be considered as elements of the medium itself. The receivers were installed in the medium symmetrically with respect to the source axis and oriented parallel to these axis. The distance between them was also 7 cm. Therefore, the receivers detected vertical accelerations. The frequency characteristic of the receivers provided an opportunity to efficiently detect the vibrations in the frequency range up to 20 kHz.

Figure 2 shows the transient characteristic of the medium in the range from 2 to 14 kHz. The choice of the frequency range for investigation was substantiated by the fact that the signals of lower frequencies were poorly excited by this piezoceramic plate and the detection of higher frequency signals needed other kinds of receivers with lower sensitivity. One can see that this characteristic strongly varies with the signal frequency. At the same time, the acoustic signal on the average attenuates effectively (by 20 dB) in this frequency range. This fact allows us to consider these changes in the transient characteristic to be independent of the container resonance, and, in the case of acoustic measurements, there is no need to prevent signal reflections from the container walls and the free surface of the medium. In [7], this form of the transient characteristic is associated with the interference of the signals arriving at the receiver by different paths. The fact that, under the conditions of this experiment, we could transmit the signal effectively from the source to a receiver only in a relatively narrow frequency band did not permit us to measure with an acceptable accuracy the velocity of sound propagation by the determination of the delay time in the process of propagation of a broadband acoustic signal. The width of the cross-correlation function of the signal radiated by the piezoceramic plate and the signal detected by one of the receivers turned out to be close to the delay time of the maximum of the measured function, which is evidence of the instability of the process of signal propagation.

The variation of the received signal level as a function of the radiation level is shown in Fig. 3. This and subsequent experiments were conducted with the radiation of a tonal signal at a frequency of 5.6 kHz. One can see that, on the whole, the behavior of the measured dependence is the same for the signals detected by the two receivers. However, the linear relation between these two characteristics is valid only on the average and on a large interval of measurement of the signal amplitude. The specific features of this dependence for different receivers are different, which is the evidence of the independent character of signal propagation from the source to each of the receivers. The maximum level of the received signal corresponds to the piezoceramic plate vibrations with an acceleration of 0.6 m/s$^2$. In this case, the amplitude of plate vibrations was as small as 5 Å. These parameters of plate vibrations correspond to a radiation level of –10 dB. The level of grain vibrations detected by the receivers was approximately 10 dB

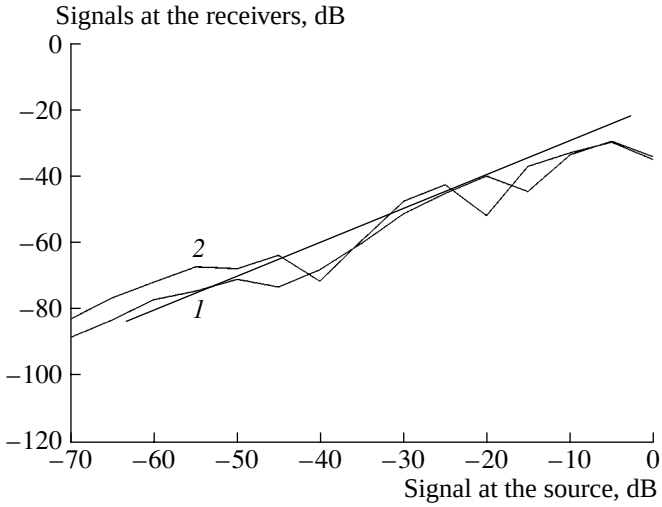


**Fig. 3.** Signal level at the receivers in a granular medium as a function of radiation level. The straight line corresponds to the direct proportionality. Curves (*1*) and (*2*) correspond to different receivers.

smaller. It is necessary to note that accelerometers were sufficiently massive and responded to the acceleration of the medium's grains that were in contact with them. The nonmonotonic character of the dependence of the detected response level for a single grain on the load of the medium was associated in [16] with the percolation development of the bonds between the grains that transmit the elastic signal between the source and a receiver. This percolation chain of contacts between grains is very sensitive to the load parameters. An increase in the load leads to a chain rearrangement, which leads, in turn, to variations in its effective elasticity. The fact that this rearrangement occurs discretely is apparently caused by the discrete number of contacts that transmit the signal.

Below, we present the results of measuring the acoustic field in the medium as a function of time. Figure 4 shows the time dependences of signal levels at one of the receivers. The corresponding behavior of the levels of harmonic components in the spectrum of detected signals is also shown in this figure. Primarily, we note that a subharmonic component appeared in the

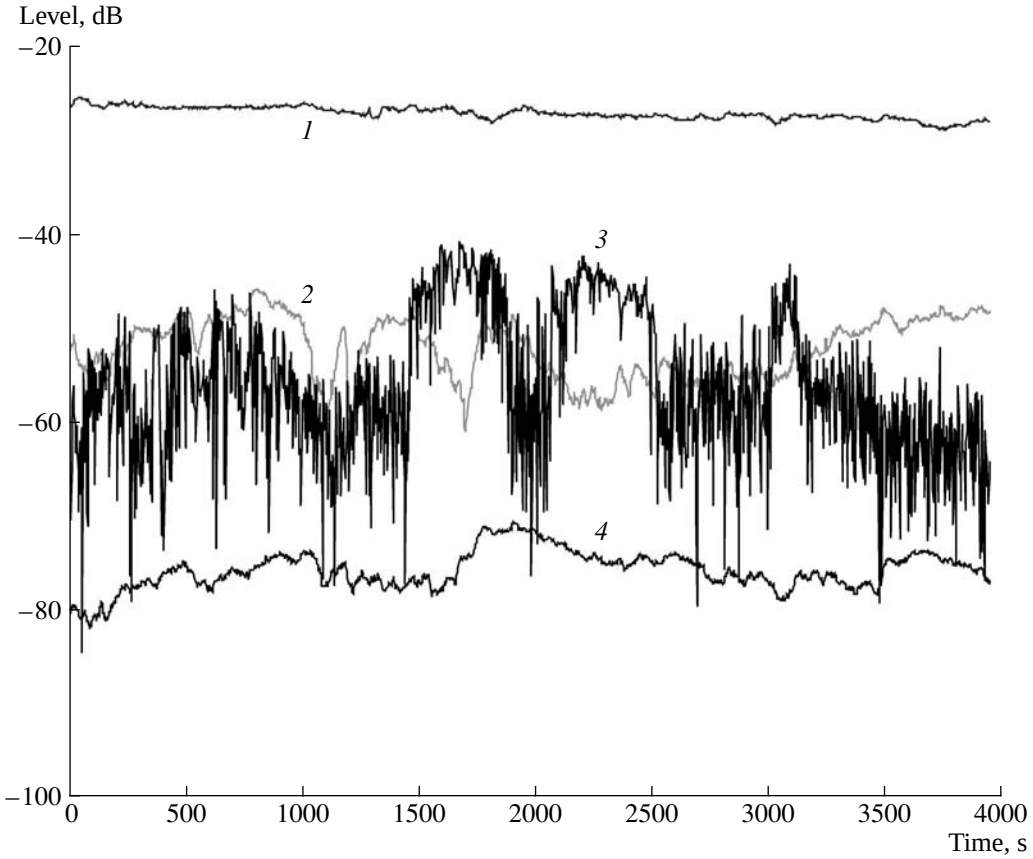


**Fig. 4.** Time dependence of harmonic signal components. (*1*) Signal level at the receiver in the granular medium at a frequency of 5.6 kHz, (*2*) second harmonic level at the receiver in the granular medium at a frequency of 11.2 kHz, (*3*) subharmonic level at the receiver in the granular medium at a frequency of 2.8 kHz, and (*4*) third harmonic level at the receiver in the granular medium at a frequency of 16.8 kHz.

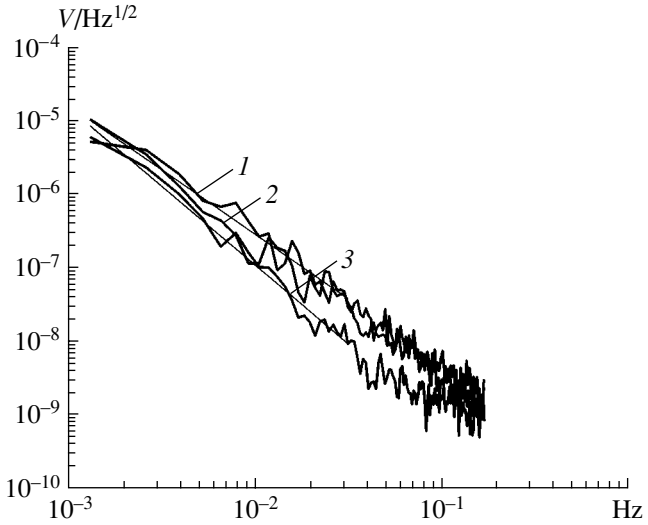


**Fig. 5.** Fluctuation spectrum for a signal in the granular medium at a frequency of 5.6 kHz. Radiation levels of (*1*) –10, (*2*) –15, and (*3*) –20 dB.

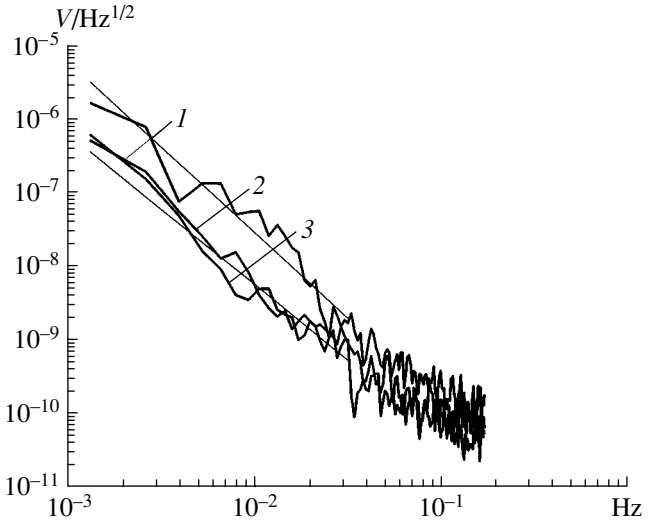


**Fig. 6.** Fluctuation spectrum for the second harmonic of the signal in a granular medium at a frequency of 11.2 kHz. Radiation levels of (*1*) –10, (*2*) –15, and (*3*) –20 dB.

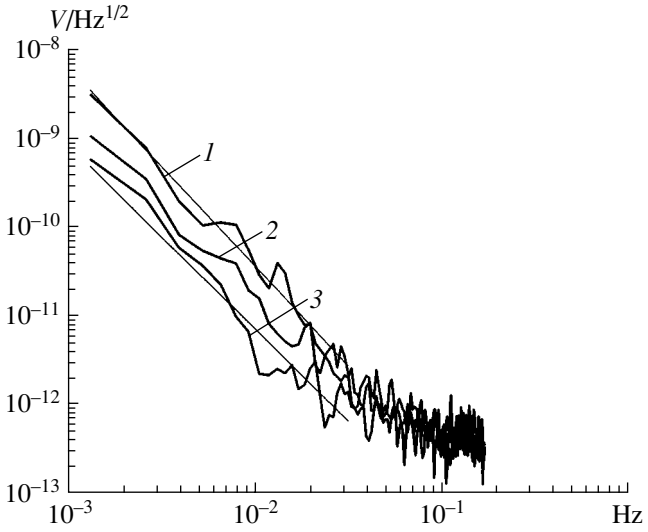


**Fig. 7.** Fluctuation spectrum for the third harmonic of the signal in a granular medium at a frequency of 16.8 kHz. Radiation level of (*1*) –10, (*2*) –15, and (*3*) –20 dB.

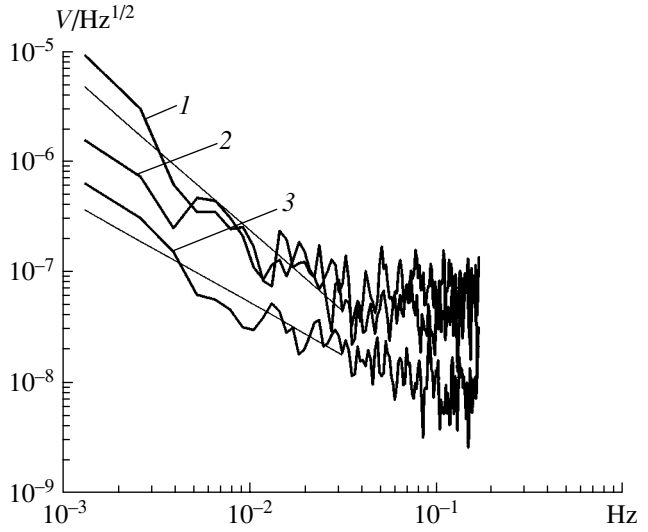


**Fig. 8.** Fluctuation spectrum for the subharmonic of the signal in a granular medium at a frequency of 2.8 kHz. Radiation level of (*1*) –10, (*2*) –15, and (*3*) –20 dB.

detected signal spectrum. The characters of signal fluctuations at both receivers for the corresponding harmonic components are similar. The signal level at the fundamental frequency of 5.6 kHz changes randomly by 5–6 dB. The fluctuation levels of harmonic components are much higher. The most intense fluctuations are those of the subharmonic component of the signal. In this case, the level changes by orders of magnitude in a jump. This fact is evidence of the forced excitation of subharmonic components, when the conditions for their excitation are of a threshold character [17].

## SPECTRA OF ACOUSTIC FIELD FLUCTUATIONS

Figures 5–8 present the spectra averaged over 30 realizations for the fluctuations of the harmonic components of a signal at a receiver for different radiation levels. Spectral processing demonstrates that the spectrum of signal fluctuations can be conditionally divided into two characteristic parts: a low-frequency component and high-frequency noise. The major part of fluctuation energy is contained in low-frequency random oscillations. The spectrum of these fluctuations lies within the range of $f = 10^{-3}$–$10^{-1}$ Hz and drops monotonically

towards high frequencies according to the power law $S(f) \approx Af^{-n}$, where the power index $n$ changes depending on the level of signal radiation and occupies the range $n = 1.7–2$. In any case, $n$ is always greater than unity for the low-frequency part of the fluctuation spectrum. The power index in the frequency dependence of the fluctuation spectrum tends to grow as the signal level decreases. This is a consequence of the faster decrease in the spectral density of fluctuations in the high-frequency range $f > 10^{-2}$ Hz in comparison with the low-frequency part of the spectrum, which almost does not change. It is interesting to note that the power index in the frequency dependence for the low-frequency part of the fluctuation spectrum of the acoustic signal is close to the values $n = 1.7–2.2$ measured in experiments with acoustic signal propagation through a medium of identical glass balls [7]. This fact indicates the generality of the mechanism of the low-frequency intensity modulation of sound propagating through a medium consisting of grains of different materials and shapes.

The fluctuation spectrum of the signal at the second harmonic that is given in Fig. 6 demonstrates that the change in the signal level leads first of all to a decrease in the low-frequency part of the spectrum $f < 3 \times 10^{-2}$ Hz. In this case, the power index in the frequency dependence of the fluctuation spectrum slightly decreases with a decrease in the signal level and acquires values within the range $n = 2.3–2.0$. The fluctuation spectrum of the third harmonic, which is given in Fig. 7, behaves in a similar way. Here, the power index $n$ lies within the range $n = 2.3–2.1$ as the signal level varies by 10 dB. The high-frequency noise in this case is caused by the electronic noise of the measuring circuit.

The fluctuation spectrum of the subharmonic component of the signal (Fig. 8) looks differently. Here, at high signal levels, one can separate two characteristic ranges, namely, the low- and high-frequency ones. In this case, the high-frequency part of the spectrum at high signal levels has a portion with a spectral density independent of frequency, which is typical of uncorrelated noise. While the spectral density of subharmonic fluctuations in the low-frequency range $f < 5 \times 10^{-3}$ Hz decreases monotonically with the decrease in the signal level, this dependence in the high-frequency range $f > 5 \times 10^{-3}$ Hz is of a threshold character. As the signal level changes by 5 dB, the spectrum in this frequency range changes insignificantly. However, if the signal decreases by 5 dB more, the spectral density of fluctuations drops to become ten times smaller. This leads to the fact that the frequency dependence of the fluctuation spectrum for the subharmonic of the signal is on the average flatter and the corresponding power index of this dependence varies within the range $n = 1.5–1.0$ as the signal level decreases.

Apparently, the fluctuation spectrum of the detected signal in the low-frequency range, where $n > 1$, must reach a maximum or, at least, saturation. This is necessary because the intensity of fluctuations must remain finite. In our experiments, it was impossible to obtain reliable data to confirm this statement. To get complete information on the character of the fluctuation spectrum, it is necessary to process much longer signal records than those obtained in our experiments.

## CONCLUSIONS

The conducted experimental investigations of acoustic wave propagation in a granular medium with the detection of the acoustic field by receivers whose the dimensions are close to the grain size indicate the statistical character of the propagation process. Under these conditions, a receiver has a limited number of contacts with neighboring grains and can be considered as one of the elements of the medium. In the case of excitation of a harmonic signal with constant amplitude, the acoustic field in the medium strongly fluctuates. Harmonic and subharmonic components are excited in the medium even at small values of the excited signal amplitude. The nonmonotonic character of the dependence of the field level in the medium on the amplitude of the excited signal indicates a considerable role of contacts between grains in the formation of the acoustic field in a granular medium. In this case, the acoustic perturbations are transmitted from one grain to another only through the contacts, which occupy a very small part of a grain and, therefore, cannot provide the stability of the medium. Thus, one can state that a granular medium is in a metastable state and that an acoustic field even with a relatively small amplitude can change the structure of contacts. The structure of the contacts forms chains transmitting signals from the source to a receiver. The spatial density of these elastic chains is determined by the dimensions of grains and the number of contacts between them. A small displacement of contacts between grains occurs under the effect of acoustic vibrations, which can radically change the structure of an elastic chain and, therefore, the elastic properties of the medium. In this case, the acoustic impedance of the medium changes. When a granular medium is compacted, the number of contacts between grains grows, which leads to the growth of the spatial density of the elastic chains transmitting acoustic perturbations. In this case, the elastic properties of a medium tend to saturation.

The process of thermal deformation arising at the points of grain contacts, where the acoustic energy is concentrated in the medium, is discussed as a possible mechanism governing the slow changes in the contact structure [7]. The stability of the frequency dependence of the spectrum in a rather wide frequency range ($10^{-3}$–$10^{-1}$ Hz) may be a consequence of the fractal character of the elastic structure of the chains transmitting the signals from the source to a receiver.

The noise-like spectrum of fluctuations in the high-frequency range (over $10^{-1}$ Hz) can be related to the fast hopping of contact points or their destruction under the

load applied to the medium. In any case, this process is similar to the acoustic emission that arises in granular media under the effect of perturbations [18].

The excitation of the subharmonic component in the spectrum of an acoustic signal is a threshold phenomenon. It requires very intense acoustic fields for realization. As a rule, this phenomenon is observed at phase transformations. In the case of a granular medium, where the elasticity is determined by the contacts between grains, this threshold amplitude of vibrations is the gravitational acceleration $g$. The fact that, at even moderate signal amplitudes (0.5 m/s$^2$), intense subharmonic components are present in the spectrum testifies that the propagation of acoustic signals in a granular medium is accompanied by the localization of the elastic energy of acoustic vibrations at single grains.

Thus, the results obtained indicate a complex character of acoustic signal propagation in a granular medium. The analysis of the acoustic field on the single grain scale revealed the statistical character and the strong nonlinearity of the propagation process, which are realized even when the signal amplitude is relatively small. The results of the experimental study provide an opportunity to develop a model of slow fluctuations of acoustic field in a granular medium.

## ACKNOWLEDGMENTS

This work was supported by the Russian Foundation for Basic Research, project no. 05-02-1750.

## REFERENCES

1. *Problems of Nonlinear Seismics* (Nauka, Moscow, 1987) [in Russian].
2. I. A. Beresnev, A. V. Nikolaev, V. S. Solov'ev, and G. M. Shalashov, Izv. Akad. Nauk SSSR, Fiz. Zemli, No. 10, 32 (1986).
3. L. A. Ostrovsky and P. A. Johnson, Riv. Nuovo Cimento **24** (7), 1 (2001).
4. I. Yu. Belyaeva, V. Yu. Zaĭtsev, and L. A. Ostrovskiĭ, Akust. Zh. **39**, 25 (1993) [Acoust. Phys. **39**, 11 (1993)].
5. L. D. Landau and E. M. Lifshitz, *Theory of Elasticity* (Nauka, Moscow, 1986; Pergamon, Oxford, 1986).
6. K. E.-A. Van Den Abeele, P. A. Johnson, R. A. Guyer, and K. R. McCall, J. Acoust. Soc. Am. **101**, 1885 (1997).
7. C.-H. Liu and S. R. Nagel, Phys. Rev. Lett. **68**, 2301 (1992).
8. C.-H. Liu, S. R. Nagel, D. A. Schecter, *et al.*, Science **269** (5223), 513 (1995).
9. T. Travers, D. Bideau, A. Gervois, *et al.*, J. Phys. A **19**, L1033 (1986).
10. B. Miller, C. O'Hern, and R. P. Behringer, Phys. Rev. Lett. **77**, 3110 (1996).
11. H. J. Herrmann, D. Stauffer, and S. Roux, Europhys. Lett. **3**, 265 (1987).
12. F. Radjai, M. Jean, J.-J. Moreau, and S. Roux, Phys. Rev. Lett. **77**, 274 (1996).
13. M. D. Rintoul and S. Torquato, Phys. Rev. Lett. **77**, 4198 (1996).
14. H. A. Makse, D. L. Johnson, and L. M. Schwartz, Phys. Rev. Lett. **84**, 4160 (2000).
15. V. E. Nazarov and A. M. Sutin, Akust. Zh. **34**, 491 (1988) [Sov. Phys. Acoust. **34**, 285 (1988)].
16. R. C. Hidalgo, Ch. U. Grosse, F. Kun, *et al.*, Phys. Rev. Lett. **89**, 205501 (2002).
17. K. A. Naugol'nykh and L. A. Ostrovsky, *Nonlinear Wave Processes in Acoustics* (Cambridge Univ. Press, Cambridge, 1988; Nauka, Moscow, 1990).
18. A. V. Lavrov, Akust. Zh. **51**, 383 (2005) [Acoust. Phys. **51**, 321 (2005)].

*Translated by M. Lyamshev*

*Acoustical Physics, Vol. 51, Suppl. 1, 2005, pp. S43–S53. Translated from Akusticheskiĭ Zhurnal, Vol. 51, Suppl., 2005, pp. 53–65.*


# Magnetoelastic Sensors and Geophones for Vector Measurements in Geoacoustics

**A. S. Belyakov**

*Schmidt Joint Institute of Physics of the Earth, Russian Academy of Sciences, Bol'shaya Gruzinskaya ul. 10, Moscow, 123995 Russia*

*e-mail: askbel@ifz.ru*

Received February 3, 2004

**Abstract**—The process of earthquake origination is associated with the action of intrinsic forces of both natural and artificial origin, which substantially change the stress fields in the Earth's crust. These slow movements are accompanied by acoustic noise (acoustic emission). Broadband measurements of acoustic emission from naturally deposited rocks is an effective tool for an instrumental monitoring of the Earth's crust that is aimed at earthquake forecasting. Considerable advances in this direction have become possible with the development of a new type of acoustic sensors with a velaccelerometric characteristic, for which the sensitivity increases by three orders of magnitude when the frequency increases tenfold. In geoacoustic observation systems, this makes it possible to considerably expand the amplitude–frequency range of investigation and creates new opportunities for a detailed analysis of the earthquake origination process. The results of observations of high-frequency underground acoustic noise, which were carried out in various regions of the Earth, in wells and edits, with the use of hardware/software systems containing new broadband magnetoelastic acoustic geophones, have confirmed experimentally its relation to slow deformations in the Earth's crust. It turns out that underground hum in the frequency range from 16 to 2000 Hz contains new independent information on changes in the stressed state and is a sensitive indicator of tectonic and tidal movements. Practical investigations performed by researchers from the Institute of Volcanology, Far East Division of the Russian Academy of Sciences, in Petropavlovsk-Kamchatski have convincingly proved that acoustic noise variation may serve as a reliable seismic alert. The present publication is devoted to the history of the development and application of magnetoelastic geophones. 

## INTRODUCTION

The results of research and design work forming the basis of vector geoacoustics—a new promising branch of geophysical instrumentation that uses the method of magnetoelastic conversion of mechanical stresses into electrical voltage—are considered. This method, which has been recently recognized in measurement technology, proved to be quite promising and was used to solve many technical problems, where it successfully competed with conventional methods for measuring forces and vibrations. However, its application was confined for a long time to measuring large static forces for internal mechanical stresses up to $10^8$ Pa in a magnetoeleastic transducer.

The research and design work performed by the author of this paper confirmed the applicability and efficiency of the magnetoelastic method for mechanical stresses below $10^{-3}$ Pa. This indicated that the range of mechanical stresses being converted was at least 220 dB and formed the basis for the development of a new trend in the force measurements and vibrometry. In particular, magnetoelastic conversion was used for designing, fabricating, and testing acoustic sensors and geophones, which reliably detect vibrating displacements in the frequency range from 16 to 2000 Hz for an electromechanic coupling coefficient of $10^{-3}$ V $s^3$/m.

Geophones with magnetoelastic acoustic sensors [1] can measure the parameters of motion in solid, liquid, and mixed media in an amplitude range exceeding 260 dB. This is ensured by the shape of their amplitude–frequency characteristic, for which the sensitivity increases in proportion to the cube of frequency. Acoustic vibrations with displacement amplitudes greater than $10^{-4}$ m in the low-frequency region of the frequency range and smaller than $10^{-15}$ m in its high-frequency region can be measured simultaneously. The need for such measurements is dictated by the very low values of the background hum amplitudes in actual geological media at frequencies up to 2000 Hz. Fine variations of these amplitudes carry new independent information on the changes in the stressed state of the Earth's crust and can be used for on-line control over a local seismic hazard.

The first geoacoustic measurements were made by the well-known Italian seismologist Professor Michel Stefano de Rossi at the end of the 19th century [1]. He obtained interesting data concerning the possibility of short-term forecast of local earthquakes. Rossi used a carbon seismic microphone invented by himself [2] and

the Bell telephone invented in 1876; however, the outstanding achievements of the Italian seismologist were undeservedly forgotten for a long time. Until recently, seimologists all over the world have been using electrodynamic seimometers whose sensitivity increases in proportion to the frequency of vibrations being measured. Such instruments cannot be used for measuring the background vibrations in the acoustic frequency range, since their amplitudes decrease by approximately three orders of magnitude as the frequency increases only tenfold. High-frequency measurements are also complicated by the fact that microseismic vibrations with frequencies up to 10 Hz and amplitudes of about $10^{-6}$ m are always present in the Earth's crust. For this reason, the limited dynamic range of analog channels used for measuring the velocities of displacements does not allow one to increase the amplification coefficient. A small gain comes from the instruments measuring the acceleration, which have a sensitivity increasing in proportion to the squared frequency (i.e., increases by two orders of magnitude upon a tenfold increase in frequency); however, their actual sensitivity is insufficient for detecting the underground hum.

## FUNDAMENTALS OF MAGNETOACOUSTIC CONVERSION

Instruments based on magnetostriction have been used in hydroacoustics since 1920. The direct magnetostriction effect discovered by Joule in 1847 is used in hydroacoustic emitters, while the inverse effect discovered by Villari in 1868 is used in receivers. These effects have been studied comprehensively. Some researchers believe that the magnetoelastic and magnetostriction effects are identical; however, no convincing proof of this fact has yet been obtained. On the contrary, there is obvious evidence that these effects often accompany each other but have noticeable differences. For example, nickel is known to exhibit magnetostriction, whereas the magnetoelastic effect is not observed in it. In contrast, electric steel with a high concentration of silicon does not show any noticeable magnetostriction after special mechanical, chemical, and thermal treatment, while the magnetoelastic effect clearly manifests itself in this material. In addition, the frequency doubling effect observed in magnetostrictive transducers is not typical of magnetoelastic transducers.

Magnetoelastic conversion was first described in [3], where a deformable element made of a ferromagnetic material placed into a measuring coil was proposed for measuring the mechanical stress. Subsequent publications on magnetoelastic conversion appeared only after 1953 [4]. However, magnetoelastic force and moment meters appeared on the measuring instruments market as early as 1954 under the commercial names PRESSDUKTOR and TORDUCTOR, respectively; these instruments were manufactured by ASEA (Vasteros, Sweden).

Magnetoelastic (magnetoanisotropic) conversion is associated with intrinsic processes of interaction between magnetic and mechanical fields, which occur at the boundaries of ferromagnetic crystal structures. A rigorous theoretical description of these processes has not been obtained as yet, and experimental studies involve considerable technical difficulties. Among the theoretical studies devoted to the interaction of electromagnetic and force fields in ferromagnets, the works by E.I. Kondorskiĭ are of most interest [5]. In these works, the conditions for the displacement of boundaries between adjacent domains $k$ and $l$ are considered. Such a displacement may take place if the free energy density $W_e$ of external forces has different values on different sides of the wall separating the domains. The magnetic domains forming a polycrystal structure of a ferromagnet have a size of about $10^{-5}$ m and a uniform saturation magnetization $M_s$; the average magnetization of the entire volume of the ferromagnet may be zero for an appropriate orientation of magnetic domains. The magnetic moment of each domain is determined by its volume $V$ and by the magnitude and direction of magnetization $M_s$, which can be noticeably changed only by varying the temperature in the vicinity of the Curie point. However, the free energy $W$ of a domain in an external magnetic field $H$ changes due to the appearance of a new term $W_h$ representing the energy of the magnetic moments of domains in the4 external field:

$$W_h = -\mu_0 \int M_s H \delta V,$$

where $\mu_0$ is the magnetic constant ($4\pi \times 10^{-7}$ H/m). As a result, the domains acquire an equilibrium state with their arrangement other than in zero magnetic field. The specific work done on the displacement of domain walls is given by the expression

$$\delta[(W_e)_l - (W_e)_k] = \mu_0 M_s(\cos\Theta_k - \cos\Theta_l)\delta H,$$

where $\Theta_k$ and $\Theta_l$ are the angles between vectors $M_s$ in domains $k$ and $l$ and the direction of magnetic field variation $\delta H$, which may differ from the direction of $H$ in the general case. If the displacement of the walls between magnetic domains is caused by a change in the uniform mechanical stress $\delta\sigma$, the work done on the displacement of domain walls is given as

$$\delta[(W_e)_l - (W_e)_k] = 3/2\lambda_s(\cos^2\varphi_k - \cos^2\varphi_l)\delta\sigma,$$

where $\varphi_k$ and $\varphi_l$ are the angles between the directions of magnetization of domains $k$ and $l$ and the direction of mechanical stress variation $\delta\sigma$, and $\lambda_s$ is the magnetostriction corresponding to the easy magnetization axis. The reversible change in the volume of the $k$th domain under the simultaneous action of magnetic field and

mechanical stresses is described by the Kondorskiĭ formula

$$\delta_{nkl} = \sum_{l \neq k} \int_{lsk} [\mu_0 M_s(\cos\Theta_k - \cos\Theta_l)\delta H + 3/2\lambda_s(\cos^2\varphi_k - \cos^2\varphi_l)\delta\sigma]dS_{kl}/C_{kl},$$

where $C_{kl} = d/dn[(W_i)_k - (W_i)_l + d\sigma_{kl}(1/R_1 + 1/R_2)]$ is the gradient of internal forces and $R_1$ and $R_2$ are the curvature radii of the walls.

The Kondorskiĭ formula yields a fundamental solution to the problem of reversible displacements of domain walls in homogeneous ferromagnetic materials when the magnetic stray fields can be ignored. The main difficulty in the practical application of this formula for specific materials is associated with the determination of the gradients of internal forces, which are complex functions of the structural state of the sample and the energy density $W_i$ of internal forces. At the same time, this formula explains the general regularities, which are independent of random properties of individual samples. It can be seen, in particular, that mechanical stresses play the same role as the external magnetic field in the displacement of walls and in the change of magnetization. This is confirmed experimentally by the fact that an emf emerges in the measuring coil connected with the sample upon a change in mechanical stresses (in accordance with the law of electromagnetic induction), as well as upon a change in the magnetic field. Changing the conditions at the boundaries between magnetic domains, the mechanical stresses induce and/or facilitate the rotation of spontaneous magnetization vectors $M_s$, which gives rise to electromagnetic induction. In all probability, this is the mechanism of magnetoelastic conversion of a force (mechanical stress) into an electric voltage; in this case, many parameters determining the state and the behavior of the ferromagnet in electromagnetic and mechanical force fields change. It has been established experimentally that the relation between mechanical stresses and their electrophysical properties is quite stable in some ferromagnets. This property is successfully employed in a large group of magnetoelastic measuring transducers.

## MAGNETOELASTIC CONVERSION OF FORCE

During the three decades following the publication of the results on magnetoelastic meters in 1954, the main trends in research and design were formed and the prospects of the development of the method for the magnetoelastic conversion of force into an electric signal were determined. The unique potentialities of transducers developed by this time determined the main fields of their application: the measurement of strong forces (up to several millions of newtons) in rolling mills and presses, the measurement of large moments at propulsion shafts of large sea vessels, and the measurement of weight and force for heavy-duty metallurgical, mining, and chemical plants. The operation principle and the design of widely used force transducers are described in detail in technical literature. Therefore, below, we will consider only those fundamental and structural results that can be used in some way in the development of geoacoustic instruments.

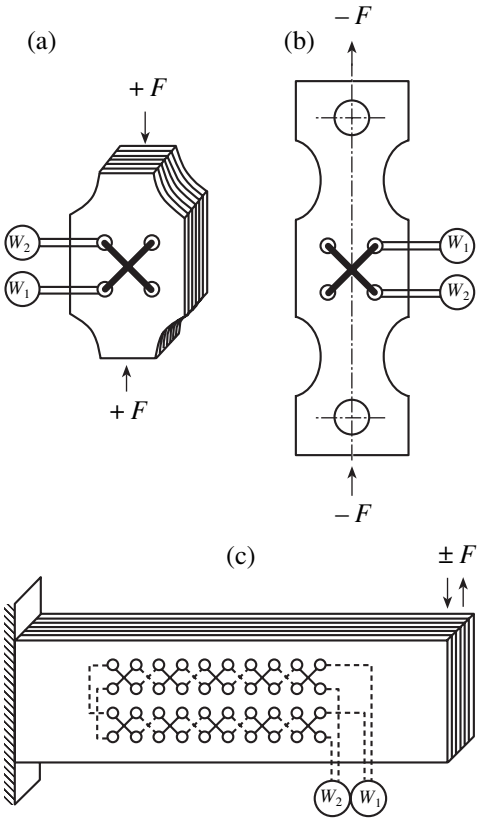


**Fig. 1.** Schematic diagrams of magnetoelastic force transducers.

From the variety of designs of magnetoelastic transformer force transducers (transducers with ac magnetization, as well as those with magnetizing and measuring coils), the following three groups with basically different designs can be singled out.

A representative of the first group of magnetoelastic transformer force transducers is known as PRESSDUCTOR (Fig. 1a). This device was developed for measuring very large compressive forces (from several tens to several millions of newtons) [6]. The main advantage of this transducer is its large rigidity and durability. Its drawbacks include its inability to measure small and alternating forces, nonuniformity of the mechanical stress field in the magnetic core, instability of contact stresses at the surfaces of force application, and nonlinearity of conversion due to the strong effect of magnetostriction.

The second group (Fig. 1b) found its application in transducers employed for measuring moderate tensile

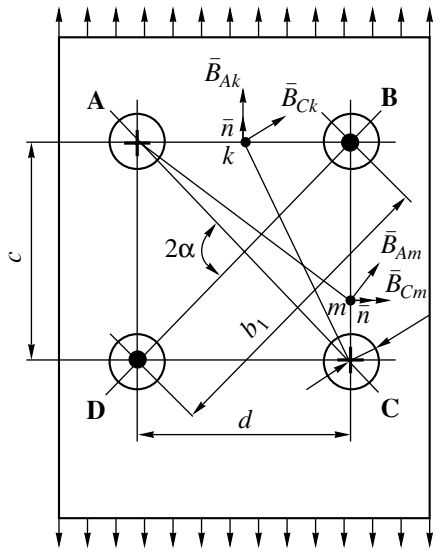


**Fig. 2.** Elementary cell of a magnetoelastic transducer.

forces [7]. The main advantage of this group of transducers lies in the possibility of a multiple increase in their sensitivity by connecting several elementary cells of the transducer in series. Such a connection does not increase the cross-sectional area of the active zone of the magnetic core, which makes it possible to reduce the lower boundary of the measuring range to 300 N. A further lowering of the boundary of the measuring range in this group is hindered by the influence of the uncompensated magnetostriction, which excites internal mechanical stresses in the active zone of the core. These stresses vary at double the frequency of the magnetization current, reach values of 2.5 Pa, and bend the initial segment of the static characteristic of conversion. To ensure the linearity of such transducers, they must be artificially loaded with a constant force reaching 25% of the measurement limit. This sharply reduces the dynamic range and makes the measurement of alternating forces impossible.

In the third group (Fig. 1c), the force being measured is replaced by the moment. This immediately made it possible to eliminate most of the above-mentioned drawbacks and opened new possibilities. The most significant of these features are the conversion of alternating forces, the reduction of the lower boundary of the force measurement range to a few thousandths of a Newton, the high linearity of conversion, the differential measuring technique, the invariance to ambient temperature and electromagnetic fields, and the compensation of the effect of internal magnetostriction. All the three design groups belong to transducers of the transformer type [8], in which the coupling between the windings varies depending on the magnitude, direction, and sign of mechanical stresses in the active zone of the core. In the differential method of measurements, two groups of windings are used. Some windings are located in the compression zone, while others are in the extension zone. The force being measured changes the coupling between the primary and secondary windings of the transducer. This coupling increases in the extension zone and decreases in the compression zone, which makes it possible to implement the differential method of measurement in the simplest way at the very initial stage of conversion.

To obtain an analytical description of the operation of a magnetoelastic force transducer, we can use its electric model in the form of a transformer with varying coupling between the primary winding $W_1$ fed by alternating current and the measuring secondary winding $W_2$ (see Fig. 1). The coupling between the windings varies and depends on the force being measured, which can be conveniently represented in the form of an averaged mechanical stress $\sigma$ in the zone of the windings; this makes it possible to compare various designs of transducers. In the case of a cantilever transducer, a transition from the measured force $F$ or bending moment $M_\mathrm{b}$ to mechanical stresses $\sigma$ is carried out using the familiar formulas

$$\sigma = F/S_m \text{ or } \sigma = M_\mathrm{b}y/J_x,$$

where $S_m$ is the area of the active cross section of the core, $J_x$ is the moment of resistance of the cross section to bending, and $y$ is the distance from the neutral axis of the core to the point of cross section under investigation.

We assume that mechanical stresses in the region of the windings are uniformly distributed over the core cross section, the magnetic permeability is independent of magnetic induction $B$, and magnetostriction is absent. The static characteristic of the transducer is determined by the dependence of the output voltage $U_2$ across the secondary winding on the mechanical stress $\sigma$ being measured:

$$U_2 = w_2 d\Phi_2/dt = f(\sigma), \quad (1)$$

where $\Phi_2$ is the magnetic flux through the plane of the measuring winding $W_2$ placed in holes B and D (Fig. 2) and $w_2$ is the number of turns in winding $W_2$. The magnetic flux $\Phi_2$ is defined as

$$\Phi_2 = \int_s BdS\cos(B, n),$$

where $S$ is the area of the diagonal plane bounded by holes B and D with the measuring winding, $B$ is the magnetic induction in the diagonal plane, and $n$ is the normal to this plane. The magnetic induction arising in the plane bounded by holes B and D due to current $i_1$ in the magnetizing winding $W_1$ placed in holes A and C cannot be determined, since the function describing the variation of magnetic permeability from the longitudinal to the transverse direction is unknown. For this reason, the longitudinal ($\Phi_l$) and transverse ($\Phi_t$) magnetic fluxes are determined through the plane bounded by holes A and B (or D and C) and through the plane bounded by holes A and D (or B and C), respectively.

The magnetic fluxes $\Phi_b$ and $\Phi_n$ can be determined assuming that they are excited by equal and opposite currents in two conductors, $i_1 w_1$, passing through the holes at corners A and C of rectangle ABCD:

$$\Phi_n = \int_s B_c dS \cos(B, n) + \int_s B_a dS \cos(B, n),$$
$$\Phi_b = \int_s B_a dS \cos(B, n) + \int_s B_c dS \cos(B, n). \quad (2)$$

In the absence of stray fields, in accordance with the first Kirchhoff rule for a branched magnetic flux, we can write

$$\Phi_2 = \Phi_l + \Phi_t. \quad (3)$$

Solving Eqs. (2) and (3) together and performing some simplifying transformations, we obtain the expression for the flux through the plane of the secondary winding of the elementary transducer:

$$\Phi_2 = \mu_0 i_1 w_1 h/2\pi\{\mu_l \ln(2b_1 \cot\alpha/d) - \mu_t \ln(2b_1 \tan\alpha/d)\},$$

where $\mu_l$ and $\mu_t$ are the permeabilities along and across the direction of the mechanical stress and $h$ is the core thickness.

For a multielement single-row transducer, allowance should be made for the effect of the magnetizing current in the nearest hole of the neighboring cell, which doubles the first term in expression (2) for the longitudinal flux $\Phi_l$. In this case, the flux through the plane of the secondary winding is

$$\Phi_2 = \mu_0 i_1 w_1 h/2\pi\{\mu_l \ln(2b_1 \cos\alpha/d\sin^2\alpha) - \mu_t \ln(2b_1 \tan\alpha/d)\}.$$

The static characteristic of the $n$-element single-row force transducer with a series arrangement of the cells is defined, in accordance with Eq. (1), as

$$U_{2n} = \mu_0 w_1 w_2 hn/2\pi di/dt \times \{\mu_l \ln(2b_1 \cos\alpha/d\sin^2\alpha) - \mu_t \ln(2b_1 \tan\alpha/d)\},$$

or

$$U_{2n} = k_n di/dt(\mu_l k_l - \mu_t k_t),$$

where $k_n = \mu_0 w_1 w_2 hn/2\pi$, $k_l = \ln(2b_1 \cos\alpha/d\sin^2\alpha)$, and $k_t = \ln(2b_1 \tan\alpha/d)$ are constant structural coefficients.

For the linear segment of the transducer, we can write

$$K_l - k_t = \mu_{l0} k_{l0} - \mu_{t0} k_{t0} + k\sigma,$$

where $k$ is the sensitivity factor depending on the electrophysical properties and the state of the core material; $\mu_{l0}$ and $\mu_{t0}$ are the initial values of the longitudinal and transverse permeabilities in the absence of mechanical stresses due to external forces, or

$$U_2 = U_0 + k_f F, \quad (4)$$

where $U_2$ is the output voltage of the transducer, $U_0$ is the initial output voltage, and $k_f$ is the proportionality factor between the force $F$ being measured and the output voltage $U_2$. The initial output voltage $U_2$ is determined to a greater extent by the anisotropy in the properties of the core; the proportionality factor $k_f$ depends on the magnetoelastic sensitivity of the ferromagnetic material. The design of the core affects the values of both coefficients.

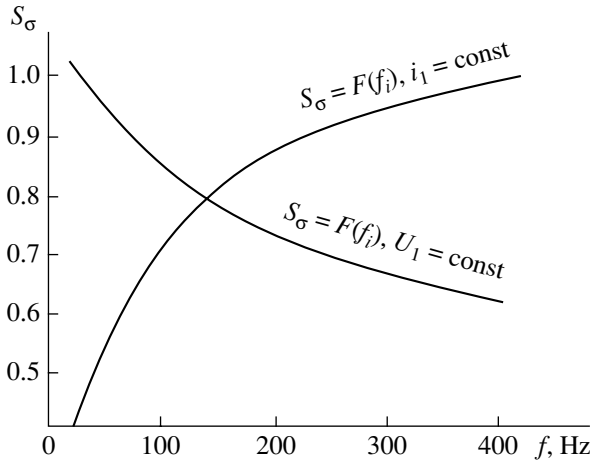


**Fig. 3.** Sensitivity of a magnetoelastic transducer as a function of the magnetization current frequency.

In the simplest case, the bending moment transducer (Fig. 1c) has the form of a cantilever beam whose bending moment is produced by a force $F$ applied to the free end. The proportionality factor $k_f$ in Eq. (4) linearly increases with the distance between the point of application of the force on the core axis and the locus of the holes with the windings, while the initial stress $U_0$ remains unchanged. An increase in the distance between the holes with the windings and the neutral axis of the core also linearly increases the proportionality factor $k_f$ without affecting the value of $U_0$. An increase in the number of turns $w_2$ in the secondary winding linearly changes the values of $U_0$ and $k_f$. The total current $i_1 w_1$ of the primary winding and its frequency $f$ also affect the value of $U_0$. Figure 3 illustrates this dependence.

## MAGNETOELASTIC CONVERSION OF ACOUSTIC SIGNALS

A magnetoelastic transformer-type transducer (see Fig. 1c) developed as a small alternating force meter and supplied with an inertial mass can be used in geophysics as a one-component accelerometer. In this case, the upper frequency of the inertial force variation is limited by the frequency of the magnetizing current,

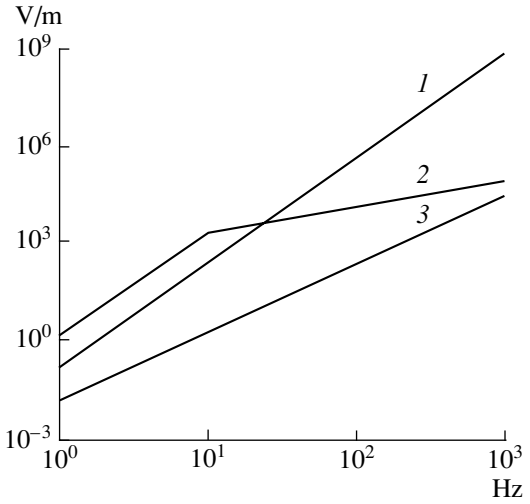


**Fig. 4.** Comparative characteristics of sensitivity of (*1*) a velaccelerometer, (*2*) a velocimeter, and (*3*) an accelerometer.

and the accuracy of conversion is determined by the instability of this current. Such a transducer has no advantages over conventional piezoelectric crystal accelerometers. It can be used in seismometry for conversion of strong vibrations with frequencies up to 10 Hz. For higher frequencies, better results can be obtained when magnetization by a direct current or permanent magnets is used [9, 10]. In this regime, the conversion parameters are satisfactory at frequencies from 1 to 30 Hz and unique at frequencies exceeding 30 Hz. This is due to the fact that, for magnetization by a constant magnetic field, an increase in sensitivity upon an increase in the frequency of vibrations to the principal mechanical resonance is 60 dB per decade of frequency growth.

By way of example, we can compare the efficiencies of operation of a magnetoelastic transducer intended for measuring the inertial force $F$ emerging in inertial mass $m$ at a magnetizing current frequency of 250 Hz (the maximal frequency of effective magnetization) and at magnetization by a static field (velocity-acceleration measuring mode) for inertial force $F$ varying at a frequency of 1 Hz ($\omega = 2\pi$).

If the base of the transducer is displaced in accordance with the law

$$X = X_0 \sin \omega t, \text{ we have } F = m^2 X_0 \sin \omega t.$$

This force, which varies with frequency $\omega = 2\pi$, modulates the constant magnetic flux $\Phi = \Phi_0 kF$, where $k$ is a constant coefficient characterizing the generalized parameters of the transducer. For a constant magnetic flux, the output voltage of the transducer is given by the expression

$$U_{\text{out}0} = dF/dt = k\Phi_0 m\omega^3 X_0 \cos \omega t.$$

For a varying magnetic flux due to magnetizing current of frequency 250 Hz ($\omega_n = 2\pi\ 250$), the output voltage is

$$U_{\text{out}250} = k\Phi_0 m\omega^2 X_0 (\sin \omega_n t \cos \omega + \omega_n t \cos \omega_n t \sin \omega t).$$

Since $\omega_n \gg \omega$, we can write

$$U_{\text{out}250} = k\Phi_0 m\omega^2 X_0 \omega_n \cos \omega_n t \sin \omega t.$$

Comparing the amplitude values of the output voltage for various regimes of magnetization, we can easily verify that

$$U_{\text{out}250}/U_{\text{out}0} \approx \omega_n/\omega = 250.$$

In other words, the magnetization at a frequency of 1 Hz by an alternating current of frequency 250 Hz leads to a gain, which is numerically equal to the frequency of the magnetization current. However, such a regime creates additional difficulties and noise, since it requires a stable ac source of comparatively high power and gives rise to intrinsic noise from the magnetostriction and Barkhausen effects.

Transducers with a wide frequency band require the regime of a constant magnetic flux. Although such a regime sets a limit of approximately 10 Hz on the lower frequency of effective conversion, it has indisputable advantages at high frequencies. In particular, Fig. 4 shows the characteristic of a velaccelerometer (*1*), which shows a sensitivity growth rate of 60 dB per decade of the frequency increase in the force being measured to the resonance frequency of 2500 Hz and makes it possible to compensate for an analogous decrease in the level of the underground hum in actual geological media. The sensitivity characteristics of the accelerometer (*3*) and velocimeter (*2*) are also shown for comparison.

The complete independence of the transducer with a magnetic flux produced by a high-energy permanent magnet paved the way for designing multipurpose acoustic detectors operating in the low-frequency region of the acoustic frequency range, in which the range of displacements being measured may exceed 260 dB. This is ensured by the sharp (as $\omega^3$) ascent of the amplitude–frequency characteristic of the transducer with frequency, the high frequency of the mechanical resonance, the low level of intrinsic noise, the absence of power consumption, the thermal endurance, strength, stability, and unlimited service life.

## MAGNETOELASTIC SENSORS

Among the various possible designs of magnetoelastic sensors, we consider the structural schemes forming the basis of magnetoelastic acoustic seismometers (geophones) of various purpose. The first and simplest design of a sensor (Fig. 5a) is formed by a cylindrical magnetoelastic element *1* (other shapes of the cross section are also possible) with a length-to-equivalent diameter ratio of about 10 [11]. The magnetoelastic element is magnetized in the axial direction by a magnetic field produced by permanent magnet(s) *2*

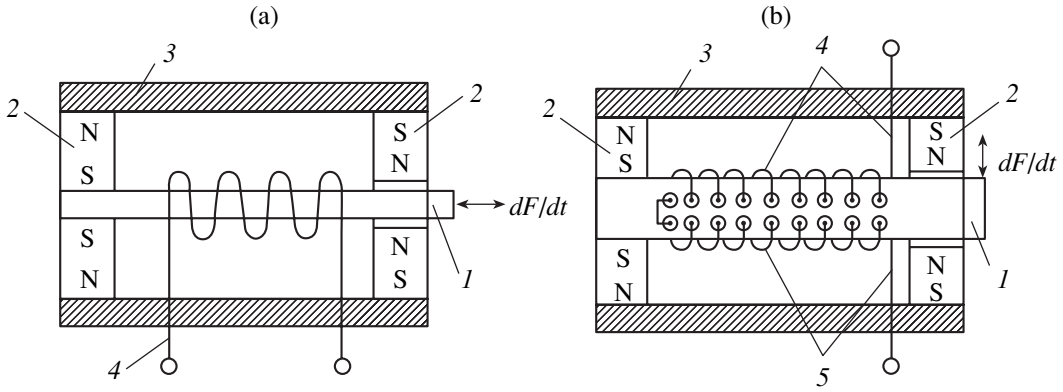


**Fig. 5.** Magnetoelastic sensor with (a) an axial sensitivity and (b) a transverse sensitivity.

embedded in casing *3*. Measuring coil *4* is wound on this element. Upon a change in the axial force applied to the end of magnetic element *1*, the magnetic flux in it changes, and an emf induced in measuring coil *4* serves as the output signal. The output signal is proportional to the rate of variation of the applied force. Along with the obvious advantages of the design of this simplest axial sensor, it has a serious drawback, namely, the sensitivity to an applied varying magnetic field whose effect is difficult to get rid of (especially at frequencies below 10 Hz). Another design of a sensor (Fig. 5b) is distinguished by the fact that two symmetric measuring coils *4* and *5* are coupled with magnetoelastic element *1* that has a rectangular or other cross section. Each coil embraces the same cross-sectional area of magnetoelastic element *1* magnetized by permanent magnet(s) *2*. Coils *4* and *5* are connected in series, which virtually eliminates the effect of external magnetic fields and axial force. In this design, the input quantity is the transverse and not axial force. Although we obtain a gain in noise immunity, the design of the sensor with a transverse transducer is inferior to the design with an axial transducer in simplicity and rigidity of the magnetoelastic element, which lowers the mechanical resonance frequency and the upper limit of the conversion frequency. Both schemes of sensors are used for designing geophones.

Magnetoelastic conversion forms the basis of acoustic geophones determining the displacement vector components in a solid medium in a rectangular or other coordinate system. The use of the same type of transducers makes it possible to obtain practically identical transfer characteristics in all components. However, a combination of two types of transducers (axial and transverse) should be used in some cases associated with a limited space (wells) [1]. Without dwelling on design features, let us consider the possibility of designing multicomponent sensors, proceeding from the fact that the sensitive magnetoelastic element is magnetized by a permanent magnet. This will be denoted conditionally by poles N and S.

The problem of determining the displacement vector projection onto a horizontal plane for particles of the medium in a wave field can be solved by using any of the two above-mentioned sensors. Figure 6 shows the diagrams of decomposition of the horizontal component of an acoustic signal in orthogonal directions of the longitudinal axes of axial-sensitivity transducers. The scheme of decomposition into two *X* and *Y* components can be implemented either using two transducers (Fig. 6a) or four pairwise coaxial transducers (Fig. 6b). In the latter case, the main disadvantage of axial transducers is compensated for, since the emfs induced by the longitudinal component of the external magnetic field in coaxial coils $Ux_1$ and $Ux_2$ or $Uy_1$ and $Uy_2$, connected in series or against each other, are mutually compensated, while the desired signals are added. When a narrow directional pattern is necessary, the number of coaxial pairs can be increased. Supplementing any of the schemes shown in Fig. 6 with one or two vertical coaxial transducers, it is possible to record three projections of a space vector.

The sensitive element of the magnetoelastic transducer for an intrawell sensor shown in Fig. 7 has the form of a beam with a cross section in the form of a rectangular cross. If its longitudinal axis coincides with

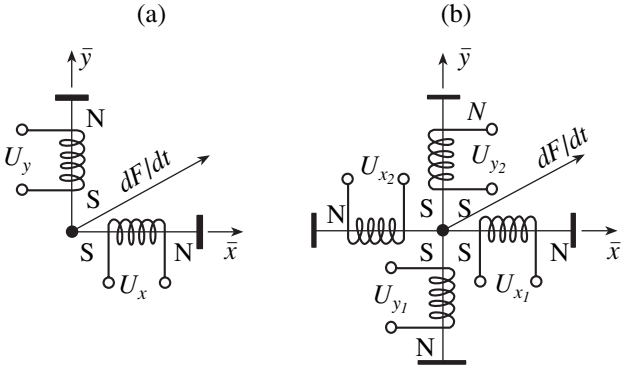


**Fig. 6.** Connection of axial-sensitivity sensors.

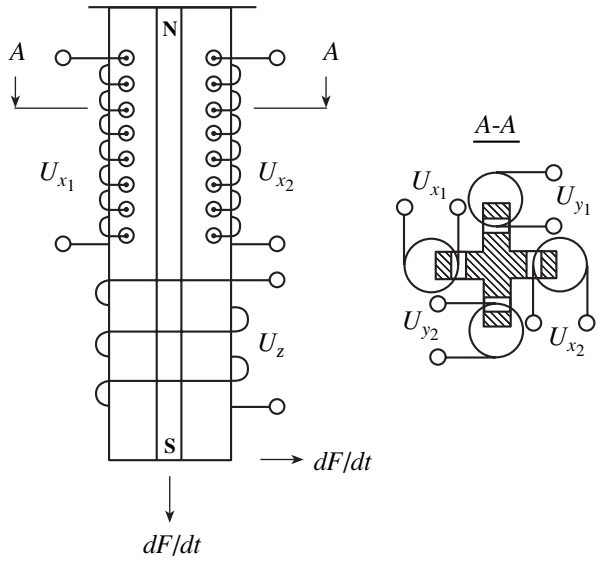


**Fig. 7.** Combined magnetoelastic sensor with a transverse sensitivity and an axial sensitivity.

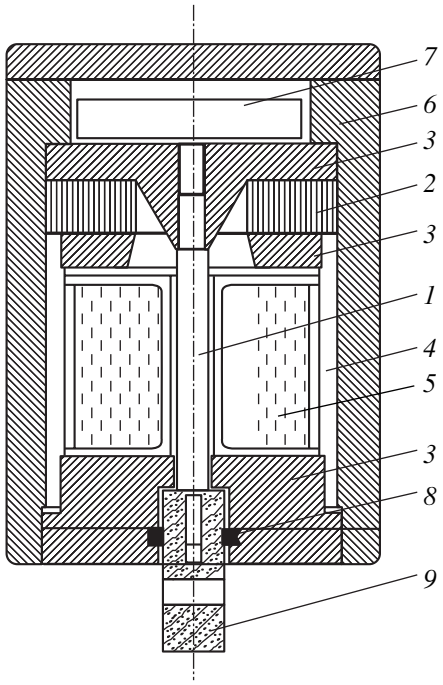


**Fig. 8.** Schematic diagram of a surface magnetoelastic geophone.

the vertical, the difference in the emfs induced in coils $Ux_1$ and $Ux_2$ is proportional to the component corresponding to horizontal direction H1, while the difference in the emfs induced in coils $Uy_1$ and $Uy_2$ is proportional to the component corresponding to horizontal direction H2. The emf of the winding embracing the entire cross section of the sensitive element is proportional to the vertical component *V* of the space vector. The combined sensor has drawbacks typical of axial and transverse transducers. The axis (vertical) component *V* in it has a broader frequency band but is not protected against the external magnetic field. The two horizontal components H1 and H2 are well protected from external magnetic fields but are frequency-limited to a certain extent. In spite of this, such a compromise proved to be quite effective for seismic measurements in wells, since electromagnetic noise in wells is insignificant while the frequencies of the signals under study are practically within the frequency range of magnetoelastic combined sensors.

## MAGNETOELASTIC GEOPHONES

Geoacoustic instruments are used for seismic prospecting of minerals, in engineering seismometry, and in seismology. In seismic prospecting, seismometers (geophones) are used in large groups on the surface. The working conditions determine the main requirements for surface instruments. Above all, this is a small mass, reliability, and low cost. In connection with the development of high-resolution seismic prospecting in recent years, elevation of the upper frequency (up to 250 Hz) of the detectable reflected signal has become a vital problem. This increases the resolution of seismic prospecting by the method of reflected waves and increases the elaboration depth of well logs being studied.

Figure 8 shows the block diagram of a one-component magnetoelastic geophone intended for surface detection of reflected waves in the frequency range up to 2500 Hz with a displacement amplitude range exceeding 240 dB. The geophone consists of magnetoelastic element *1*, permanent magnet *2*, pole pieces *3*, external core *4*, measuring coil *5*, casing *6*, preamplifier *7*, and gasket *8*. The geophone is connected to the ground via rod *9*. It should be noted that, instead of the casing of the geophone, its sensitive element is directly connected to the object under investigation (ground). This makes it possible to increase the actual frequency range to the maximal possible extent and to considerably suppress the effect of atmospheric acoustic noise during surface measurements. Preamplifier *7* ensures the matching of the signal from the measuring coil of the geophone with an extended transmission line.

For three-component measurements of acoustic emission and for reflection seismic prospecting with vertical seismic profiling, the combined magnetoelastic sensor shown in Fig. 7 is supplied with an inertial mass and is fixed in a high-strength sealed casing. The schematic diagram of an intrawell three-component magnetoelastic acoustic geophone of the MAG-3S type is shown in Fig. 9. The geophone consists of sensitive element *1*, heavy-duty permanent magnet *2*, lower pole pieces *3*, a high-strength casing and external core *4*, inertial mass *5*, vertical component measurement coils *6*, preamplifier unit *7*, upper pole piece *8*, and sealed con-

nector 9. The amplitude–frequency characteristic of the MAG-3S geophone makes it possible to detect acoustic signals in the range from 16 to 1250 Hz, as well as seismic-prospecting signals of any frequency, which can be excited by a seismic vibrator. Axial-sensitivity one-component transducers (see Fig. 5a) can also be used for constructing multicomponent geophones and acoustic antennas, in which the displacement vector of the net mass can be decomposed into the required number of components along preset directions. The magnetoelastic transducer makes it possible to design geophones in which the sensitive element is in direct contact with the medium being controlled and ensures a rigid connection of several sensitive elements to the same inert mass. Such a connection is possible in view of the large linear conversion range ensuring independent measurement of weak high-frequency signals against the background of large and slowly varying static loads (e.g., from thermal deformations in structural elements) and high-intensity low-frequency vibrations. Multielement antenna systems for passive and active location of noisy and moving objects in the frequency range from 30 to 3000 Hz in liquid media can be constructed on the basis of a magnetoelastic transducer with direct action of a force on the sensitive element. Such systems can be used for determining not only the azimuth of propagation of vibrations but also the direction to the source.

It was noted above that magnetoelastic geophones can be successfully used for detecting reflected waves in vertical seismic profiling. Three-dimensional measurements of the displacement vector by one-component magnetoelastic sensors in an intrawell geophone have no fundamental limitations. However, the available materials and technologies ensure the required conversion parameters only for a comparatively large inertial mass and for a large size of the sensing element. In this connection, a slight difference in the amplitude–frequency characteristics of the vertical and horizontal channels was accepted in designing a three-component magnetoelastic geophone for intrawell application [12]. The mechanical resonance has a frequency of about 1.2 kHz for the vertical component and about 350 Hz for the horizontal component. The mechanical resonance frequency of horizontal components can be increased by raising the structural rigidity of a modified sensor [13]. The features of intrawell magnetoelastic geophones make it possible to use these instruments not only for solving prospecting and engineering problems but also for solving fundamental problems related to monitoring the variations of the stressed state of the medium for forecasting purposes [14]. In addition, a high-strength magnetoelastic sensor with a very large linear conversion range makes it possible to use a large inertial mass (up to several tons) for performing unique experiments (e.g., the detection of dynamic gravitation).

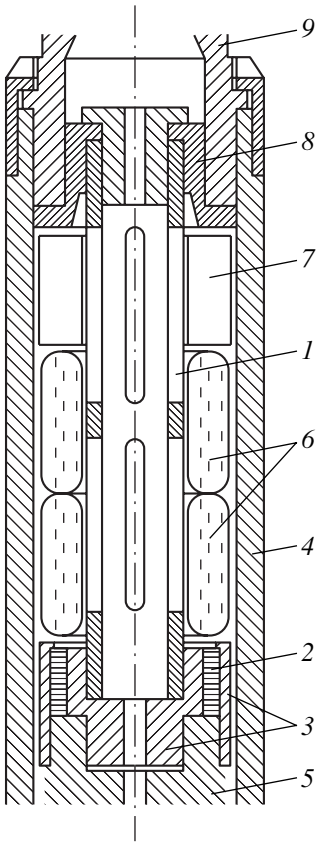


**Fig. 9.** Schematic diagram of an intrawell magnetoelastic geophone.

## AMPLIFICATION AND FORMATION OF OUTPUT SIGNALS

The source of the output voltage in a magnetoelastic acoustic sensor is an inductive–resistive element (copper coil wound on a ferromagnetic core), whose resistance varies from 100 to 5000 Ω depending on the design. Like any resistive element, it is characterized by a certain level of thermal noise voltage. According to the Nyquist–Johnson, the mean square of thermal noise voltage $U$ across the terminals of the electric coil of resistance $R$ in thermal equilibrium at absolute temperature $T$ is $U^2 = 4kTR\delta f$, where $k = 1.38 \times 10^{-23}$ J/K is the Boltzmann constant; $\delta f$ is the frequency band in hertzs, in which the thermal noise voltage is measured. At room temperature $T$ = 293 K, we have $4kT = 1.62 \times 10^{-20}$ V$^2$/Hz Ω. A 5000-Ω conductor at room temperature has an rms thermal noise of about 0.7 μV in a frequency band up to 10000 Hz and 7 nV in a band of 100 Hz. According to its spectral composition, thermal noise belongs to the Gaussian white noise type. It is associated only with physical phenomena and cannot be reduced. Schottky noise emerging due to fluctuations of the current passing through a conductor and flicker noise emerging due to fluctuations of the resistance of the sensor coil are also of this type. Their total amplitude is much smaller than that of thermal noise.

The total intrinsic noise of a magnetoelastic transducer in the frequency range from 16 to 2000 Hz with a measuring coil whose resistance is up to 5 kΩ does not exceed 0.2 μV under normal conditions; this noise is of the white noise type and depends on the frequency band being measured. Consequently, in designing the analog part of the amplification channel, one must ensure an input noise from the preamplifier (PA) at the same level and the required amplification. In addition to signal amplification, the PA must ensure optimal matching of the output resistance with the extended cable transmission line, which may be 5000 m long. The coasting cable has a resistivity of 25.5 Ω/km of the conducting core and large distributed capacitance and inductance. The amplification coefficient of the PA may reach 60 dB; its transmission band ranges from 10 to 5000 Hz and the output resistance does not exceed 10 Ω. In the PA circuit developed by us, two operational dc amplifiers are used. The first amplifier (153UD5A) is connected as a noninverting amplifier with a coefficient of 40 dB, while the second amplifier (544UD1A) is connected as an inverting amplifier with a coefficient of 20 dB and is supplemented with high-power transistors. After preamplification, the broadband geophone signal is additionally amplified by a matching amplifier with coefficients of 6, 12, 26, 32, or 38 dB. The matching amplifier has a band from 10 to 5000 Hz and intrinsic input noise below 5 μV. Its output resistance is also designed for operation with a cable transmission line up to 5 km long.

In the simplest monitoring system, amplified signals are fed to the input of a three-channel four-band analog amplifier, in which the signals are additionally amplified by 34 dB in 1/3 octave bands with central frequencies of 30, 160, 500, and 1000 Hz. Then, these signals are detected and slightly filtered to ensure the suppression of the carrier frequency but preserve the dynamics of its amplitude fluctuations. The resulting low-frequency dc signals are converted into a digital form and recorded by a PC according to the program developed for continuous and prolonged monitoring. This program also provides the computation and recording of the minute average signal amplitude in each of the 12 channels.

## CONCLUSIONS

Magnetoelastic geophones had been successfully tested under field conditions for 15 years in various regions of the Northern Hemisphere in wells, edits, and mounds. Occasional monitoring was carried out in continental regions of central Russia, Belarus, and Northern Caucasus, as well as on the Pacific coast of California (USA), Honshu island (Japan), and Petropavlovsk-Kamchatskii. Currently, continuous monitoring of underground sound is carried out in central Russia (Obninsk), the northern Caucasus (Kislovodsk), and Kamchatka (Petropavlovsk-Kamchatskii). Each study of broadband underground sound confirms in some way or another its natural origin. The relation between this sound and the tidal variation of gravity always manifests itself in a certain way. However, the nature of this relation remains enigmatic. In particular, a daily peak in underground noise is observed in almost all cases. Many researchers attribute this peak to anthropogenic noise. However, after continuous monitoring in summer and in winter, it was found that the daily peak in winter is observed at midnight rather than during the daytime. The variation of the daily peak phase in underground sound was found to occur during vernal and autumnal equinoxes. These data suggested an energy model of the variation of underground hum on the basis on the variation of the strain rate magnitude associated with the solar component of tide [15–17]. All this has made it possible for the researchers from the Institute of Volcanology, Far East Division of the Russian Academy of Sciences, Petropavlovsk-Kamchatskii, on the basis of the data of a continuous geoacoustic monitoring carried out by a magnetoelastic geophone in a deep well since the end of 2001, to regularly submit conclusions concerning possible seismic hazards to the local commission on earthquake forecast. With rare exception, all submitted conclusions (exceeding 40 in number) were confirmed by subsequent events.

Destructive earthquakes occurring in 2003 in California (United States) and Iran proved that earthquake forecasting remains an urgent problem. Its solution requires that all available means, including geoacoustic monitoring by magnetoelastic geophones, be used. Geoacoustics is the most effective instrument for studying the earthquake origination processes. This method has become practicable after the development of magnetoacoustic geophones, which ensure reliable measurements of displacements with amplitudes smaller than $10^{-12}$ m in a solid medium. Magnetoelastic geophones made it possible to automatically determine the amplitudes of low-intensity underground sound and the direction to its source; this, in turn, opens up new prospects for estimating the anisotropy of the stressed state of minerals at the measurement site. This can be done using a magnetic geophone recording three components of the acoustic signal vector. Three components are mechanically formed in the total inertial mass and are singled out by three individual coils, each of which is connected with the orthogonal axes of the directional pattern. The signal detection scheme is determined by the specific measurement problem. The simplest monitoring can be carried out using the scheme of analog separation of several frequency bands and digital recording of the signal amplitude averaged over a certain period in each band. The position of the geophone and the frequency bands for monitoring can be chosen using an information system with a digital amplitude–frequency analyzer in real time. The time of averaging can be operatively varied in accordance with the scale and task of monitoring.

The technique and strategy proposed for earthquake forecasting are rather simple. The extent of seismic risk

for a specific territory (a large city or an atomic power plant) is determined by the methods of classical seismology, for which a seismic hazard control system is developed. Magnetoelastic geophones are installed in three deep wells on this territory. Each geophone is connected with the monitoring center via a mobile communication system ensuring high-quality transmission of three signals in frequency bands from 16 to 2000 Hz. At the monitoring center, acoustic signals can be authentically reproduced and recorded on a digital medium and then placed on local computer networks and Internet using modern computer processing equipment. A real-time visual observation system can be developed on the basis of conventional multimedia computers.

Analysis of underground hum variations in the chosen frequency bands at all points of observation (Institute of Volcanology, Far East Division of the Russian Academy of Sciences, Petropavlovsk-Kamchatskii) is the first statistically verified stage of earthquake forecast. The analysis was carried out in comparison with a model series on a time interval of 30 days, which was renewed every day. At this stage, an indication of a possible earthquake is the gradual disappearance of the pronounced daily variation of the underground sound amplitude in individual frequency bands (over months or weeks). A stable observation of this feature is a premise of transition to the next stage of forecasting. The models of prediction features of the second and third stages of the forecast can be substantiated after carrying out a statistical analysis of the actual origination and evolution of earthquakes recorded by magnetoelastic geophones at a special test site (e.g., the USGS test site in Parkfield, California). A feature of the second stage may be a sharp and substantial increase in the underground hum amplitude level in most of the frequency bands (this stage lasts for 12 h according to the data from Nagano prefecture, Japan, 1996). The observation at the second stage should be performed in real time on a monitor screen during a time interval of about five days with renewal every 6 min. The second feature is, in turn, a premise of transition to the third (final) stage and consists in an avalanche-like increase in seismoacoustic emission in high-frequency bands immediately before an earthquake (the duration of this stage is on the order of tens of minutes or minutes according to the data of underground observations). The final stage is accompanied by a sound specific for each observation point. This feature must be observed on the screen of a monitor within an approximately two-hour time window with a 10-s renewal interval.

## REFERENCES


1. A. S. Belyakov and A. V. Nikolaev, Izv. Ross. Akad. Nauk, Fiz. Zemli, No. 7, 74 (1993).
2. M. S. Rossi, *Dell'osservatorio ed archivio geodinamico* (Dalla Tipogr. Della Pace, Roma, 1883).
3. F. V. Maĭorov, Tr. Tsentr. Aerogidrodin. Inst., No. 445 (1939).
4. O. Dahle and B. Dahle, SE Patent No. 151267 (12 May 1953).
5. E. S. Kukharkin, *Fundamentals of Engineering Electrophysics* (Nauka, Moscow, 1969) [in Russian].
6. O. Dahle, ASEA J. **32** (9), 115 (1959).
7. A. S. Belyakov, SU Patent No. 155014 (1963).
8. A. S. Belyakov and T. D. Belyakova, Available from VINITI, No. 5 (1983), p. 128.
9. A. S. Belyakov *et al.*, SU Patent No. 1376763 (1986).
10. A. S. Belyakov and T. D. Belyakova, in *Devices and Methods for Earthquake Registration* (Nauka, Moscow, 1987), pp. 52–55 [in Russian].
11. A. S. Belyakov, in *Instrumental and Experimental Methodical Investigations in Seismometry* (Nauka, Moscow, 1993), pp. 18–20 [in Russian].
12. I. P. Bashilov and A. S. Belyakov, RF Patent No. 1721564 (1993).
13. A. S. Belyakov, RF Patent No. 1 833 501 (1992).
14. A. S. Belyakov and A. V. Nikolaev, Izv. Ross. Akad. Nauk, Fiz. Zemli, No. 8, 79 (1995).
15. A. S. Belyakov, V. S. Lavrov, A. V. Nikolaev, and L. L. Khudzinskiĭ, in *Seismic Devices* (Obshch. Inst. Fiz. Zemli Ross. Akad. Nauk, Moscow, 1998), pp. 83–86 [in Russian].
16. A. S. Belyakov, V. S. Lavrov, A. V. Nikolaev, and L. L. Khudzinskiĭ, Izv. Ross. Akad. Nauk, Fiz. Zemli, No. 12, 39 (1999).
17. A. S. Belyakov, V. S. Lavrov, A. V. Nikolaev, and L. L. Khudzinskiĭ, Dokl. Akad. Nauk **375** (4), 531 (2000).


*Translated by N. Wadhwa*

*Acoustical Physics, Vol. 51, Suppl. 1, 2005, pp. S54–S60. Translated from Akusticheskiĭ Zhurnal, Vol. 51, Suppl., 2005, pp. 66–73.*


# Search for Hydrocarbons by the Method of Induced Seismoacoustic Emission in Wells

**V. V. Dryagin*, O. L. Kuznetsov**, A. A. Starodubtsev*, and V. E. Rok****

** ZAO Intensonik & Co., ul. Amundsena 100, Yekaterinburg, 620016 Russia*

*e-mail: dryagin@sky.ru*

*** All-Russia Geosystems Research Institute, Varshavskoe sh. 8, Moscow, 113105 Russia*

Received November 1, 2004

**Abstract**—Regular specific features have been observed for the first time in the response of a fluid-saturated porous medium to a high-intensity seismoacoustic field. Experimental investigations show that the observed behavior can serve as a basis for a new effective complex technology capable of detecting hydrocarbons and water in the near-well zone and selectively restoring the fluid conductivity in oil pools. *© 2005 Pleiades Publishing, Inc.*

The transfer and conversion of energy in a multicomponent and heterophase porous geological medium are accompanied by the emission of seismoacoustic and electromagnetic waves, which can provide important information about the mechanical, geochemical, and electromagnetic processes in this medium and about its nonlinear properties [1]. In recent years, much attention has been devoted to theoretical and experimental investigations of changes in the seismoacoustic activity of geological media in response to various artificial external actions.

The acoustic emission in a complex heterogeneous medium can be induced by an elastic impulse capable of initiating stepwise slippage at the contacts between blocks, which is accompanied by elastic vibrations whose spectrum is enriched with high-frequency components. An increase in the amplitude and frequency of vibrations usually takes place at the final stage of rock fracture and in the course of crack growth. For example, it was demonstrated [2, 3] that the amplitudes of elastic vibrations of active blocks in a mountain mass at characteristic quasi-resonance frequencies can be two to three times greater than the amplitude of external action, which is explained by the release of energy stored in the geological medium.

A vibroseismic action from the Earth's surface upon oil fields, which is used in the technology of increasing the producing oil pool recovery, is also based on the radiation and reradiation of elastic energy in a broad frequency range.

There are various descriptions of the mechanisms of elastic energy transformation in a mountain mass, which are based on the interaction of static stresses in this mass with elastic vibrations in local foci exhibiting maximum stress concentrations or containing hydrocarbon fields. Such foci are characterized by altered local conditions of the interaction between solid elements of the medium at the contact zones. According to the concept of the transformation of seismic energy radiated from an on-ground vibrator toward a producing oil pool, which is presented in [4], the vibrations of geological blocks at their resonance frequencies are sequentially excited in the characteristic interval from 10 to 30 Hz. In turn, the resonance vibrations of these geological blocks occurring in the stressed state lead to their decomposition, which is accompanied by the acoustic emission in the high-frequency range (10–30 kHz). The volume density of the acoustic energy at each stage of transformation significantly increases at the expense of the energy gained from the stressed state of rocks, which leads to breakage of various filtration barriers hindering the flow of fluids through capillaries of the porous medium. It was suggested that the approach proposed in [4] can be used not only to solve the problem of increasing the oil pool discharge by seismic methods but also to search for zones of increased oil saturation and to monitor such zones in the course of the field development. All these tasks can be accomplished by a complex method based on the analysis of seismoacoustic emission (SAE) in a broad range from extremely low (seismic) to ultrasonic frequencies.

The excitation of acoustic emission in a geological medium under the action of low-frequency elastic waves was also attributed [5] to the process of pore opening in the course of rock microfracture caused by pressure variations. The transformation of the energy of an elastic wave propagating deep in the Earth is also accompanied by the excitation of vibrations in a wide range from infrasonic to hypersonic frequencies. According to the concept developed in [6], the SAE represents the high-frequency noise response of a deformed cracked medium and the frequency range of such response extends from seismic (15–300 Hz) to high (>1 kHz) acoustic frequencies. It was shown that anomalous SAE variations can be related, in addition to

purely technical factors, to a change in the dynamic conditions for fluids occurring in cracked media.

The mechanisms of the enhancement of ultrasonic vibrations in the course of vibrational action from the Earth's surface upon hydrocarbon collectors possessing a block structure were theoretically studied in [7]. This interaction was subdivided into three stages, including (i) the transfer of weak harmonic vibrations to the collector blocks, (ii) the excitation of microscopic vibrations in these blocks in the fluid flows, and (iii) the onset of elastic resonance vibrations accompanied by the emission of ultrasonic waves into the surrounding fluid. These waves are capable of breaking dense oil films in interblock contacts of the collector, which favors the restoration of the fluid conductivity and improves the oil filtration in the oil pool. Thus, the energy pumping from low to high frequencies via the induced vibrations of blocks leads to the generation of acoustic waves in the interblock fluid with an intensity on the order of $10^{-1}$ W/cm$^2$, which is sufficient for breaking dense films and restoring the oil filtration. The frequency range of these vibrations extends up to several hundred or a few thousand hertz.

The patented "Anchar" technology [8] intended for the direct exploration of hydrocarbon fields is also based on their response to the vibrational action from the Earth's surface. According to this method, the probing vibrations in a geological medium are produced by a seismic vibrator operating for 3 min. The comparison of the signals detected by acoustic receivers before and after this action provides information sufficient to judge on the presence of a hydrocarbon field. The idea of the proposed technical solution consists in that, in response to the probing vibrational action, a geological medium containing hydrocarbons produces a secondary emission that begins immediately after the onset and continues for some time after the termination of this action. An interesting feature is that the vibrator and the response detector operate in the same infrasonic frequency range (1–4 Hz). This approach was inspired by the ideas of M.A. Sadovskii and A.V. Nikolaev formulated as long ago as in 1982, according to which any geological medium produces seismic emission and external actions stimulate the sources of microseismic noise. These acoustic sources exhibit maximum intensity in the regions of gas and oil fields.

Another method based on the detection of natural and induced SAE signals under seismic vibrations excited for oil and gas prospecting was patented in [9]. This method also uses the analysis of the dynamics of the induced SAE to judge on the presence of hydrocarbons.

The results of our investigations of the acoustic emission in wells showed that the response signal can be induced by a high-intensity (8–10 W/cm$^2$) acoustic action used for the restoration of the fluid conductivity in the near-well zone of a producing oil pool [10, 11]. The proposed method of acoustic action was intended to improve this characteristic both in the near-well zone and in more distant regions of the oil pool. Indeed, the hydrodynamic data obtained upon the acoustic action throughout the producing oil pool with interlayers on one of the oil fields in the Perm region revealed an increase in fluid conductivity by 80–130% in the near-well zone and by 40–160% in the far zone. These results confirm that the acoustic action at a given intensity leads to profound changes in the properties of a saturated porous medium.

In our experiments, the SAE signals were detected and recorded with the aid of a device placed in a well, comprising a transducer, an acoustic sensor, and the corresponding control and data acquisition systems. The device was programmed for cyclic operation, each cycle including a record of the initial SAE signal, an acoustic action, and repeated signal recording at preselected points over a preset interval of depths. In terms of geophysics, this method may be called seismoacoustic emission logging (SAEL) in the course of logging–acoustic action–logging cycles. The combination of two functions—high-power acoustic action and high-sensitivity SAE detection—in the same device allows the SAE signal profile over the well depth to be obtained both within and outside the producing oil pool. The SAE signal is monitored before, during, and after the acoustic action.

It was established that an acoustic action upon the near-well space leads to a change in the SAE signal. The maximum contribution to this change was due to variations in the properties of fluids occurring in the pore space of the collector, which was confirmed by other methods of geophysical investigations of the wells in the course of a complex (influx–composition) study of the field development. In a collector saturated with oil and/or gas, the acoustic action led to an increase in the SAE intensity, whereas water-saturated collectors exhibited a decrease in this intensity.

As is known [12, 13], an acoustic action upon a fluid-saturated collector leads to changes in some properties and in the state of the fluid. The possible manifestation include oil outgassing, an increase in fluidity and a decrease in viscosity of oil, a change in the phase state of hydrocarbons, etc. The observed effects are correlated with the total energy and spectrum of SAE and with the character of collector saturation. The SAEL approach to investigations of the current state of the collector saturation consisted in the measurement and analysis of changes in the SAE signal and in establishing relations between these changes and the character of the fluid saturating the near-well space of the producing oil pool, as monitored by independent (geophysical) methods.

The SAEL procedure was as follows. The initial SAE signal spectrum in the acoustic and ultrasonic frequency range was measured at a preset well depth with the aid of an AAV-400 programmed instrumentation set [14, 15]. Then, a controlled high-power acoustic action

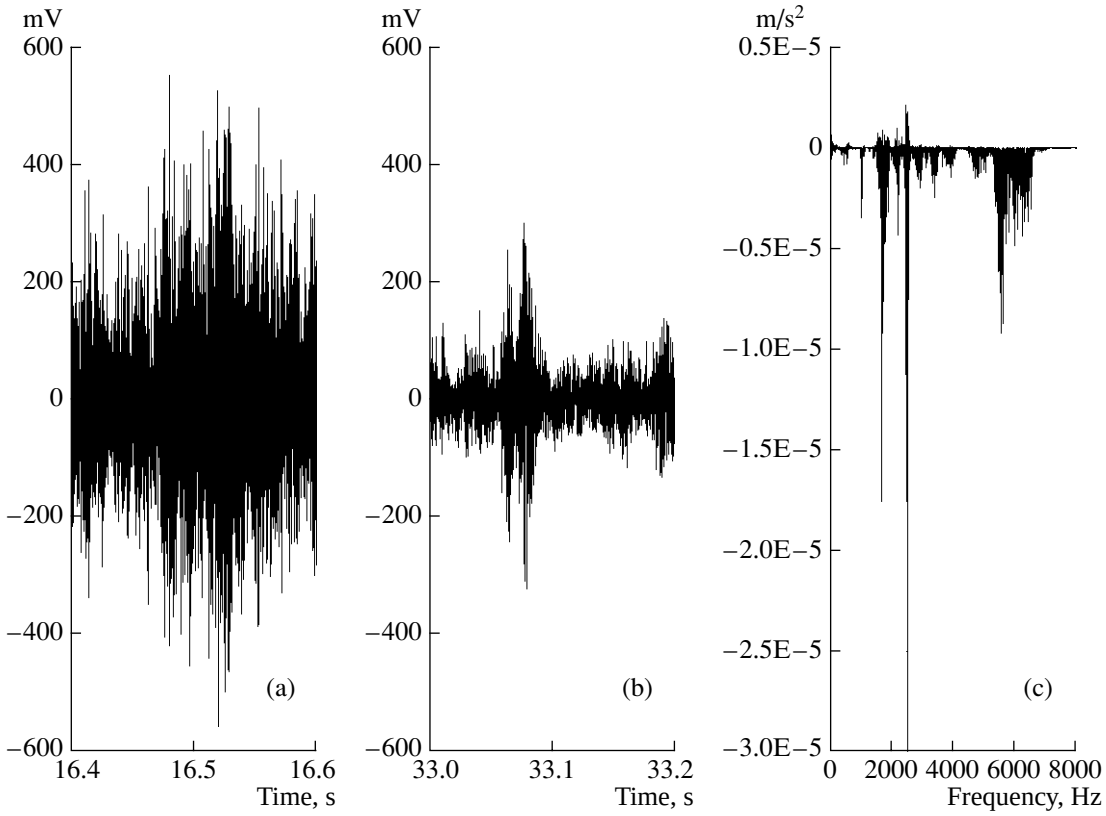


**Fig. 1.** Seismoacoustic emission of well no. 1125 (Bystrinskoe field) with a water-saturated collector (2049.5 m): SAE signals (a) before and (b) after acoustic action; (c) the difference in the SAE frequency spectra measured before and after the acoustic action.

upon the near-well zone was produced with the aid of acoustic radiators at preset points of the well. Immediately after the termination of the acoustic action, the SAE signal was measured again and the absolute and differential SAE characteristics were determined.

Although the oil and gas fields are characterized by anomalously high seismoacoustic noise levels, the dynamics of the observed secondary emission can be clearly distinguished on this background. This dynamics exhibits opposite trends, depending on the character of collector saturation. In the case of an oil-saturated collector, the secondary emission increases, while in a water-saturated collector it decreases. This behavior of the secondary acoustic emission underlies the proposed technology of selective restoration of the fluid conductivity of producing oil pools, which combines the acoustic monitoring of the character of collector saturation and the selective action upon the oil pool by an intense acoustic field.

The potential of the proposed method of restoration of the fluid conductivity in producing wells can be illustrated by the results obtained at the Bystrinskoe oil field in Western Siberia. We have studied two regions of one producing oil pool in this field, which were spaced approximately by 10 km. Both wells were characterized by conventional geophysical methods in the course of regular schedule production maintenance.

Prior to the acoustic action, the well was characterized by the background SAE signal profile measured throughout the perforation zone and the adjacent top and bottom regions of the pool. The measured signals were processed online using a fast Fourier transform (FFT) program, and the corresponding waveforms and frequency spectra were obtained in the range from 10 Hz to 22 kHz with various degrees of averaging. The SAE signal monitoring and processing was performed at all preselected points used for constructing a logging spectrogram and the corresponding logging integral SAE energy profiles in preset spectral intervals.

The subsequent acoustic action consisted of the cycles of short-term probing and immediate SAE response monitoring at each point of a selected interval of well depths, followed by an analysis of the signal dynamics. The first well (no. 1125) was characterized by geophysical methods as providing a water flow. Figure 1 shows a typical SAE time series measured in the middle of the producing oil pool (at a depth of 2049.5 m) before and after the acoustic action and also shows the corresponding difference spectrum obtained upon FFT processing with complete averaging over a total recording time of 15–30 s. The signal amplitudes were mea-

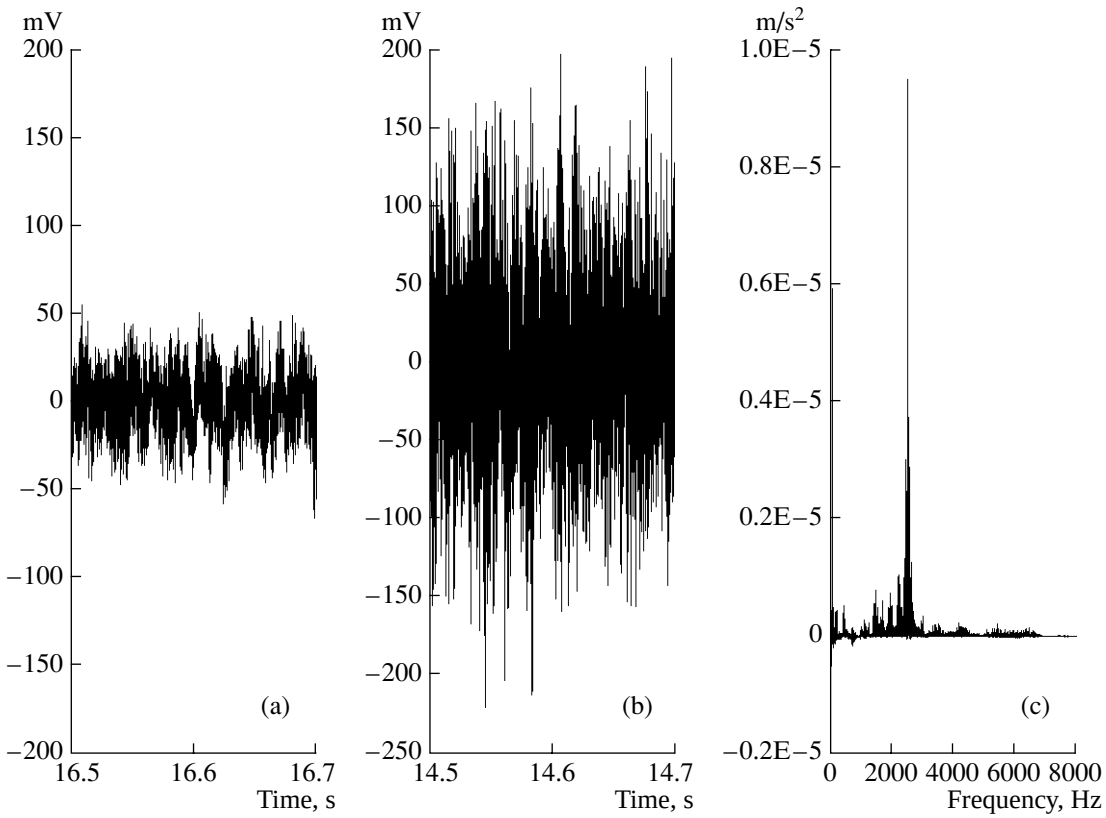


**Fig. 2.** Seismoacoustic emission of well no. 1964 (Bystrinskoe field) with an oil-saturated collector (2064.5 m): SAE signals (a) before and (b) after acoustic action; (c) the difference in the SAE frequency spectra measured before and after the acoustic action.

sured at the output of the intrawell device. The spectral harmonics are expressed in the acceleration units with allowance for the device sensitivity and the transmission function of the data recording system.

Similar measurements were performed in another well (no. 1964) of the same oil pool, which were also preliminarily characterized by geophysical methods and classified as oil-producing. As can be seen from the data for this well measured in the middle of the producing oil pool (at a depth of 2064.5 m) and presented in Fig. 2, there is an increase in the SAE signal intensity upon the acoustic action. This increase was observed over the entire producing oil pool thickness. The main contribution to the total signal energy and to the increment for both wells was provided by the high-frequency components (1–7 kHz).

The initial SAE spectra measured in the two wells of the same pool are much alike and reflect the characteristic features of the given pool. In contrast, changes observed upon the acoustic action in the two cases exhibit opposite trends in their dynamics and significant differences in magnitude. For well no. 1125 with a water-saturated collector, the integral SAE energy decreases by a factor of 4.4, whereas this energy in the well No. 1964 with an oil-saturated collector increases by a factor of 1.96 (for the indicated depths).

It should be noted that the SAEL investigations in the two wells described above were performed under conditions of a short-term depression, which favored the influx of the fluid from the pool to the well. For this reason, it was not excluded that the SAE signals contained components related to the fluid filtration in the pore space and in the perforations. An analysis of such signals was performed in [16] based on the spectra of acoustic and electromagnetic noise caused by fluid filtration in the pools.

However, the results of a series of experiments performed in various (pressure observation, monitor, killed, and unperforated) wells, where the process of filtration in the pore space was eliminated, gave essentially the same results. For example, the unperforated monitor well no. 20020 (Bavly, Tatarstan) was checked for the collector saturation character by SAEL in comparison with geophysical methods. In an oil pool preliminarily characterized by low oil production, the induced SAE signal upon the acoustic action exhibited a strongly anomalous character (Fig. 3.). The anomalous time series displayed separate pulses with high-frequency filling and a repetition rate of about 3–7 Hz. This pattern is analogous to that observed on the daytime surface by means of the “Anchar” technique.

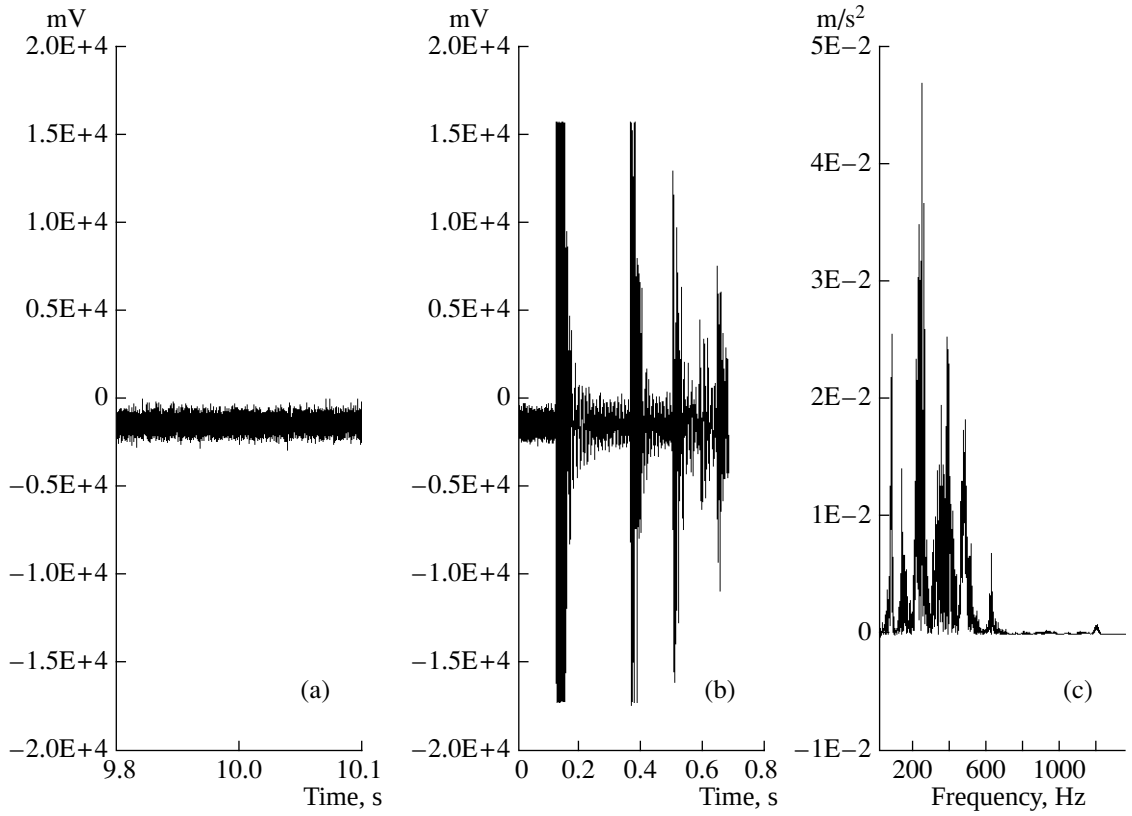


**Fig. 3.** Seismoacoustic emission of well no. 20020 (Bavly field) with an oil-saturated collector (1754 m): SAE signals (a) before and (b) after acoustic action; (c) the difference in the SAE frequency spectra measured before and after the acoustic action.

The results of subsequent monitoring in a different well of the same pool upon the seismoacoustic perforation showed evidence of an increase in the oil yield. Analogous results were obtained in various oil fields of Western Siberia, Kazakhstan, and Komi Republic.

In the course of SAEL, it was possible to calculate the SAE energy in a certain frequency interval (selected by experts upon preliminary online analysis of the signal). This energy was assigned to the given point and recorded in the logging diagram synchronized with the device propagating in depth of the well. Using the resulting logging diagrams obtained by conventional geophysical methods, it was possible to perform a comparative analysis with allowance for the preceding investigations. As can be seen from such a comparative logging diagram presented in Fig. 4, the SAE signals measured before and after the acoustic action outside the layer corresponding to the collector are virtually the same. At the same time, a strong anomaly in the signal measured upon the acoustic action closely coincides with the oil-saturated collector layer identified using the conventional logging techniques.

The general algorithm of the collector saturation characterization by means of the SAEL can be illustrated by an example of identification of the oil- and water-saturated collector layers in the same well (Fig. 5). This is essentially a kind of water–oil contact profiling, which is important in solving the geological problems encountered in the field development.

According to the proposed algorithm, the SAE signals are measured before and after the acoustic action, and then the absolute and relative SAE energy differences are calculated with allowance for the statistical spread of the background. The background spread depends on the general tectonic situation and exhibits an individual character for each field, typically ranging from a fraction of percent to about ten percents. Only the SAE signals exceeding the background spread are accepted as reliable (see “Oil” and “Water” curves in Fig. 5). The oil saturation coefficient was calculated using the “Oil” profile and normalized to the peak in this curve, which was considered corresponding to the absolute oil saturation coefficient determined by geophysical or other standard methods.

The data presented in Fig. 5 were obtained in well no. 141 at the Mamontovskoe oil field in Western Siberia and compared to the results of geophysical investigation using the well radiation data according to the terminal and electrical casing logging. The logging was performed over new (unperforated) intervals, so as to provide for an objective comparison of various methods of evaluation of the collector saturation. The results fully confirmed the validity of the saturation assessment based on the SAEL algorithm.

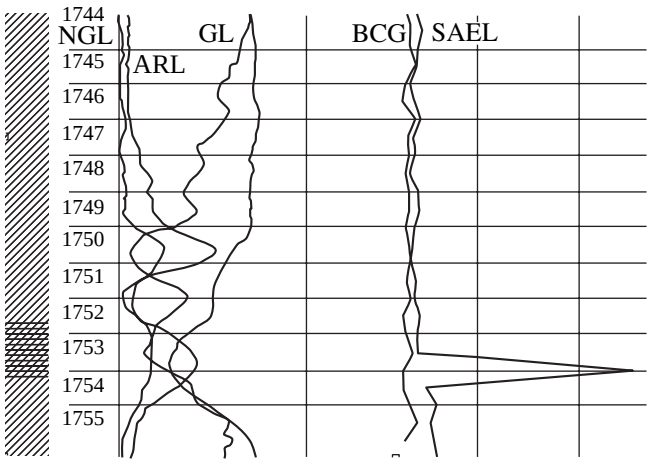


**Fig. 4.** Logging profiles of well no. 20020 (Bavly field): NGL, neutron gamma logging; ARL, apparent resistance logging; GL, gamma logging; BCG, background SAE signal before acoustic action; SAEL, seismoacoustic emission logging upon acoustic action; the left-hand column shows the geological column with a depth scale (m) and indicates the oil-saturated collector.

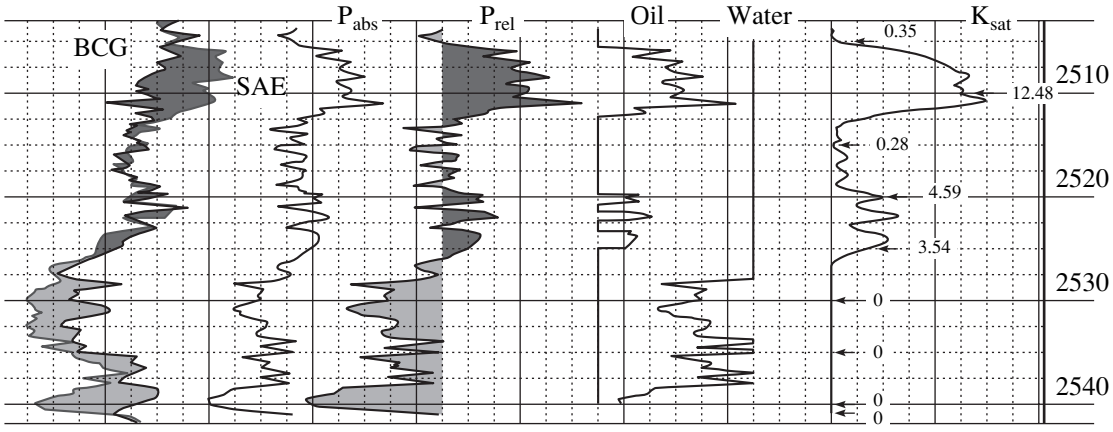


**Fig. 5.** Seismoacoustic emission logging algorithm: BCG, background SAE signal before acoustic action; SAE, seismoacoustic emission signal upon acoustic action; $P_{abs}$, absolute SAE energy difference before and after acoustic action; $P_{rel}$, SAE energy difference relative to background; Oil, positive energy difference minus statistical spread of background; Water, negative difference minus statistical spread of background; $K_{sat}$, oil saturation coefficient calculated using the "Oil" curve and normalized to the maximum oil saturation according to independent geophysical data; the right-hand scale indicates the depth (m).

Taking into account that the effects described above were observed in all wells where the SAEL measurements were performed and the results could be checked by independent methods, we can conclude that the proposed method is applicable to evaluation of the character of the collector saturation. According to this method, a reliable criterion for the assessment of the collector saturation is offered by the difference between the integral SAE energies determined before and after the acoustic action upon the near-well zone.

## REFERENCES

1. *Problems of Geophysics of the XXI Century*, Ed. by A. V. Nikolaev (Nauka, Moscow, 2003) [in Russian].
2. G. A. Sobolev, A. V. Ponomarev, and A. V. Kol'tsov, Fiz. Zemli, No. 12, 72 (1995).
3. V. M. Sboev, Izv. Akad. Nauk SSSR, Fiz. Zemli, No. 10, 57 (1982).
4. B. F. Simonov, V. N. Oparin, N. A. Kaniskin, *et al.*, Neft. Khoz., No. 5, 41 (2000).
5. V. N. Belonenko, M. V. Pavlov, A. D. Makurov, *et al.*, Neft. Prom-st., Ser. Neftepromysl. Delo, Nos. 8–9, 18 (2000).
6. O. B. Khavroshkin, V. V. Tsyplakov, and N. A. Vidmont, Vestn. Otdel. Geolog. Geofiz. Geokhim. Gorn. Nauk Ross. Akad. Nauk (OGGGGN RAN) **1**, No. 2(12) (2000).
7. A. S. Alekseev, V. A. Tsetsokho, A. V. Belonosova, *et al.*, Fiz. Tekh. Probl. Razrabotki Poleznykh Iskopaemykh, Geomekh., No. 6, 3 (2001).
8. S. L. Arutyunov, G. L. Loshkarev, B. M. Grafov, *et al.*, RF Patent No. 2045079 (4 January 1992).

9. G. A. Butenko, V. A. Mikhaĭlov, and V. V. Tikshaev, RF Patent No. 2 105 324, Mezhdunarodn. Patent. Klassifik. (MPK): G01V1/00 (1998).
10. V. V. Dryagin, Nauchn. Tekh. Vestn. Karotazhnik, No. 98 (2002).
11. V. P. Mitrofanov, A. I. Dzyubenko, N. Yu. Nechaeva, and V. V. Dryagin, Geolog. Geofiz. Razrabotka Neftyanykh Mestorozhdeniĭ, No. 10, 36 (1998).
12. O. L. Kuznetsov and S. A. Efimova, *Application of Ultrasound in Petroleum Industry* (Nedra, Moscow, 1983) [in Russian].
13. O. L. Kuznetsov, É. M. Simkin, and G. V. Chilingar, *Physical Grounds of Acoustic Effects on Oil and Gas Deposits* (Mir, Moscow, 2001) [in Russian].
14. V. V. Dryagin and O. L. Kuznetsov, Nauch. Tekh. Zh. Tekhnologii TÉK, No. 5 (12) (2003).
15. *Produktsiya ZAO Intensonik & K*, in Nauch. Tekh. Vestn. Karotazhnik, Nos. 45, 46, 55, 64, 98, 107 (1998–2003).
16. A. I. Ipatov, A. V. Gorodnov, L. P. Petrov, *et al.*, Nauch. Tekh. Vestn. Karotazhnik, No. 9 (122), 51 (2004).

*Translated by P. Pozdeev*

*Acoustical Physics, Vol. 51, Suppl. 1, 2005, pp. S54–S60. Translated from Akusticheskiĭ Zhurnal, Vol. 51, Suppl., 2005, pp. 66–73.*


# Search for Hydrocarbons by the Method of Induced Seismoacoustic Emission in Wells

**V. V. Dryagin*, O. L. Kuznetsov**, A. A. Starodubtsev*, and V. E. Rok****

** ZAO Intensonik & Co., ul. Amundsena 100, Yekaterinburg, 620016 Russia*

*e-mail: dryagin@sky.ru*

*** All-Russia Geosystems Research Institute, Varshavskoe sh. 8, Moscow, 113105 Russia*

Received November 1, 2004

**Abstract**—Regular specific features have been observed for the first time in the response of a fluid-saturated porous medium to a high-intensity seismoacoustic field. Experimental investigations show that the observed behavior can serve as a basis for a new effective complex technology capable of detecting hydrocarbons and water in the near-well zone and selectively restoring the fluid conductivity in oil pools. *© 2005 Pleiades Publishing, Inc.*

The transfer and conversion of energy in a multicomponent and heterophase porous geological medium are accompanied by the emission of seismoacoustic and electromagnetic waves, which can provide important information about the mechanical, geochemical, and electromagnetic processes in this medium and about its nonlinear properties [1]. In recent years, much attention has been devoted to theoretical and experimental investigations of changes in the seismoacoustic activity of geological media in response to various artificial external actions.

The acoustic emission in a complex heterogeneous medium can be induced by an elastic impulse capable of initiating stepwise slippage at the contacts between blocks, which is accompanied by elastic vibrations whose spectrum is enriched with high-frequency components. An increase in the amplitude and frequency of vibrations usually takes place at the final stage of rock fracture and in the course of crack growth. For example, it was demonstrated [2, 3] that the amplitudes of elastic vibrations of active blocks in a mountain mass at characteristic quasi-resonance frequencies can be two to three times greater than the amplitude of external action, which is explained by the release of energy stored in the geological medium.

A vibroseismic action from the Earth's surface upon oil fields, which is used in the technology of increasing the producing oil pool recovery, is also based on the radiation and reradiation of elastic energy in a broad frequency range.

There are various descriptions of the mechanisms of elastic energy transformation in a mountain mass, which are based on the interaction of static stresses in this mass with elastic vibrations in local foci exhibiting maximum stress concentrations or containing hydrocarbon fields. Such foci are characterized by altered local conditions of the interaction between solid elements of the medium at the contact zones. According to the concept of the transformation of seismic energy radiated from an on-ground vibrator toward a producing oil pool, which is presented in [4], the vibrations of geological blocks at their resonance frequencies are sequentially excited in the characteristic interval from 10 to 30 Hz. In turn, the resonance vibrations of these geological blocks occurring in the stressed state lead to their decomposition, which is accompanied by the acoustic emission in the high-frequency range (10–30 kHz). The volume density of the acoustic energy at each stage of transformation significantly increases at the expense of the energy gained from the stressed state of rocks, which leads to breakage of various filtration barriers hindering the flow of fluids through capillaries of the porous medium. It was suggested that the approach proposed in [4] can be used not only to solve the problem of increasing the oil pool discharge by seismic methods but also to search for zones of increased oil saturation and to monitor such zones in the course of the field development. All these tasks can be accomplished by a complex method based on the analysis of seismoacoustic emission (SAE) in a broad range from extremely low (seismic) to ultrasonic frequencies.

The excitation of acoustic emission in a geological medium under the action of low-frequency elastic waves was also attributed [5] to the process of pore opening in the course of rock microfracture caused by pressure variations. The transformation of the energy of an elastic wave propagating deep in the Earth is also accompanied by the excitation of vibrations in a wide range from infrasonic to hypersonic frequencies. According to the concept developed in [6], the SAE represents the high-frequency noise response of a deformed cracked medium and the frequency range of such response extends from seismic (15–300 Hz) to high (>1 kHz) acoustic frequencies. It was shown that anomalous SAE variations can be related, in addition to

purely technical factors, to a change in the dynamic conditions for fluids occurring in cracked media.

The mechanisms of the enhancement of ultrasonic vibrations in the course of vibrational action from the Earth's surface upon hydrocarbon collectors possessing a block structure were theoretically studied in [7]. This interaction was subdivided into three stages, including (i) the transfer of weak harmonic vibrations to the collector blocks, (ii) the excitation of microscopic vibrations in these blocks in the fluid flows, and (iii) the onset of elastic resonance vibrations accompanied by the emission of ultrasonic waves into the surrounding fluid. These waves are capable of breaking dense oil films in interblock contacts of the collector, which favors the restoration of the fluid conductivity and improves the oil filtration in the oil pool. Thus, the energy pumping from low to high frequencies via the induced vibrations of blocks leads to the generation of acoustic waves in the interblock fluid with an intensity on the order of $10^{-1}$ W/cm$^2$, which is sufficient for breaking dense films and restoring the oil filtration. The frequency range of these vibrations extends up to several hundred or a few thousand hertz.

The patented "Anchar" technology [8] intended for the direct exploration of hydrocarbon fields is also based on their response to the vibrational action from the Earth's surface. According to this method, the probing vibrations in a geological medium are produced by a seismic vibrator operating for 3 min. The comparison of the signals detected by acoustic receivers before and after this action provides information sufficient to judge on the presence of a hydrocarbon field. The idea of the proposed technical solution consists in that, in response to the probing vibrational action, a geological medium containing hydrocarbons produces a secondary emission that begins immediately after the onset and continues for some time after the termination of this action. An interesting feature is that the vibrator and the response detector operate in the same infrasonic frequency range (1–4 Hz). This approach was inspired by the ideas of M.A. Sadovskii and A.V. Nikolaev formulated as long ago as in 1982, according to which any geological medium produces seismic emission and external actions stimulate the sources of microseismic noise. These acoustic sources exhibit maximum intensity in the regions of gas and oil fields.

Another method based on the detection of natural and induced SAE signals under seismic vibrations excited for oil and gas prospecting was patented in [9]. This method also uses the analysis of the dynamics of the induced SAE to judge on the presence of hydrocarbons.

The results of our investigations of the acoustic emission in wells showed that the response signal can be induced by a high-intensity (8–10 W/cm$^2$) acoustic action used for the restoration of the fluid conductivity in the near-well zone of a producing oil pool [10, 11]. The proposed method of acoustic action was intended to improve this characteristic both in the near-well zone and in more distant regions of the oil pool. Indeed, the hydrodynamic data obtained upon the acoustic action throughout the producing oil pool with interlayers on one of the oil fields in the Perm region revealed an increase in fluid conductivity by 80–130% in the near-well zone and by 40–160% in the far zone. These results confirm that the acoustic action at a given intensity leads to profound changes in the properties of a saturated porous medium.

In our experiments, the SAE signals were detected and recorded with the aid of a device placed in a well, comprising a transducer, an acoustic sensor, and the corresponding control and data acquisition systems. The device was programmed for cyclic operation, each cycle including a record of the initial SAE signal, an acoustic action, and repeated signal recording at preselected points over a preset interval of depths. In terms of geophysics, this method may be called seismoacoustic emission logging (SAEL) in the course of logging–acoustic action–logging cycles. The combination of two functions—high-power acoustic action and high-sensitivity SAE detection—in the same device allows the SAE signal profile over the well depth to be obtained both within and outside the producing oil pool. The SAE signal is monitored before, during, and after the acoustic action.

It was established that an acoustic action upon the near-well space leads to a change in the SAE signal. The maximum contribution to this change was due to variations in the properties of fluids occurring in the pore space of the collector, which was confirmed by other methods of geophysical investigations of the wells in the course of a complex (influx–composition) study of the field development. In a collector saturated with oil and/or gas, the acoustic action led to an increase in the SAE intensity, whereas water-saturated collectors exhibited a decrease in this intensity.

As is known [12, 13], an acoustic action upon a fluid-saturated collector leads to changes in some properties and in the state of the fluid. The possible manifestation include oil outgassing, an increase in fluidity and a decrease in viscosity of oil, a change in the phase state of hydrocarbons, etc. The observed effects are correlated with the total energy and spectrum of SAE and with the character of collector saturation. The SAEL approach to investigations of the current state of the collector saturation consisted in the measurement and analysis of changes in the SAE signal and in establishing relations between these changes and the character of the fluid saturating the near-well space of the producing oil pool, as monitored by independent (geophysical) methods.

The SAEL procedure was as follows. The initial SAE signal spectrum in the acoustic and ultrasonic frequency range was measured at a preset well depth with the aid of an AAV-400 programmed instrumentation set [14, 15]. Then, a controlled high-power acoustic action

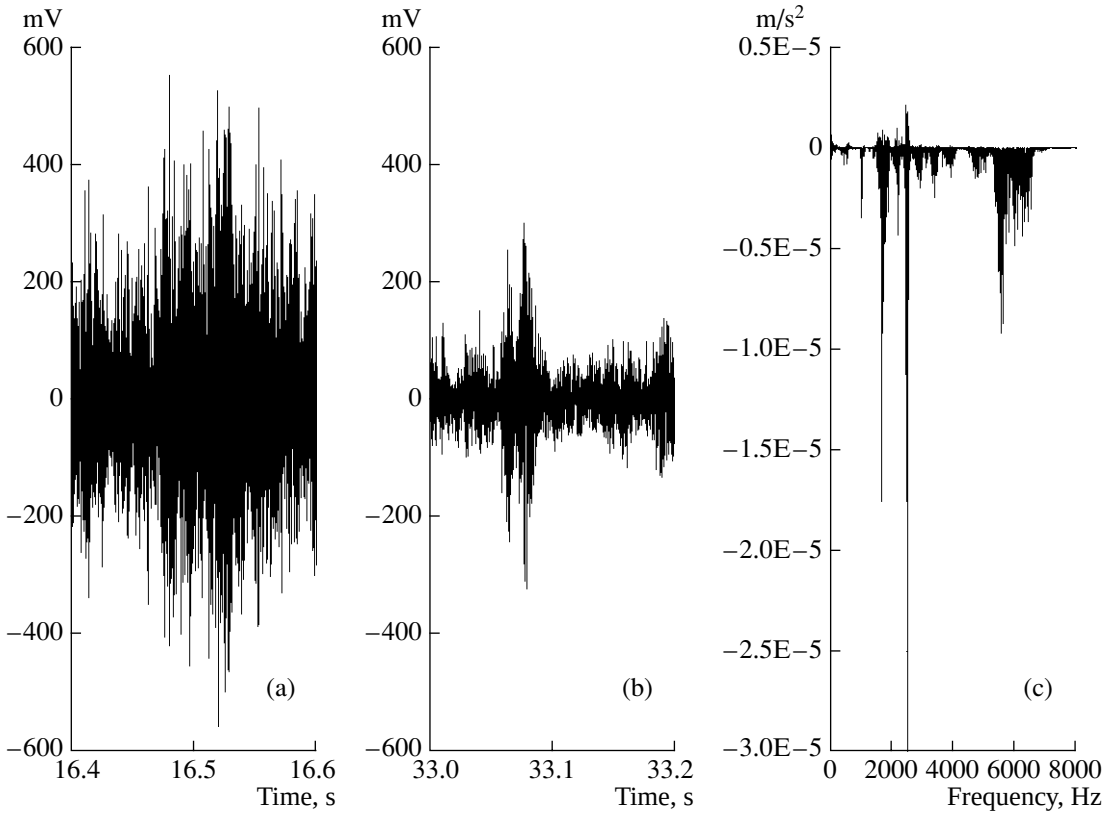


**Fig. 1.** Seismoacoustic emission of well no. 1125 (Bystrinskoe field) with a water-saturated collector (2049.5 m): SAE signals (a) before and (b) after acoustic action; (c) the difference in the SAE frequency spectra measured before and after the acoustic action.

upon the near-well zone was produced with the aid of acoustic radiators at preset points of the well. Immediately after the termination of the acoustic action, the SAE signal was measured again and the absolute and differential SAE characteristics were determined.

Although the oil and gas fields are characterized by anomalously high seismoacoustic noise levels, the dynamics of the observed secondary emission can be clearly distinguished on this background. This dynamics exhibits opposite trends, depending on the character of collector saturation. In the case of an oil-saturated collector, the secondary emission increases, while in a water-saturated collector it decreases. This behavior of the secondary acoustic emission underlies the proposed technology of selective restoration of the fluid conductivity of producing oil pools, which combines the acoustic monitoring of the character of collector saturation and the selective action upon the oil pool by an intense acoustic field.

The potential of the proposed method of restoration of the fluid conductivity in producing wells can be illustrated by the results obtained at the Bystrinskoe oil field in Western Siberia. We have studied two regions of one producing oil pool in this field, which were spaced approximately by 10 km. Both wells were characterized by conventional geophysical methods in the course of regular schedule production maintenance.

Prior to the acoustic action, the well was characterized by the background SAE signal profile measured throughout the perforation zone and the adjacent top and bottom regions of the pool. The measured signals were processed online using a fast Fourier transform (FFT) program, and the corresponding waveforms and frequency spectra were obtained in the range from 10 Hz to 22 kHz with various degrees of averaging. The SAE signal monitoring and processing was performed at all preselected points used for constructing a logging spectrogram and the corresponding logging integral SAE energy profiles in preset spectral intervals.

The subsequent acoustic action consisted of the cycles of short-term probing and immediate SAE response monitoring at each point of a selected interval of well depths, followed by an analysis of the signal dynamics. The first well (no. 1125) was characterized by geophysical methods as providing a water flow. Figure 1 shows a typical SAE time series measured in the middle of the producing oil pool (at a depth of 2049.5 m) before and after the acoustic action and also shows the corresponding difference spectrum obtained upon FFT processing with complete averaging over a total recording time of 15–30 s. The signal amplitudes were mea-

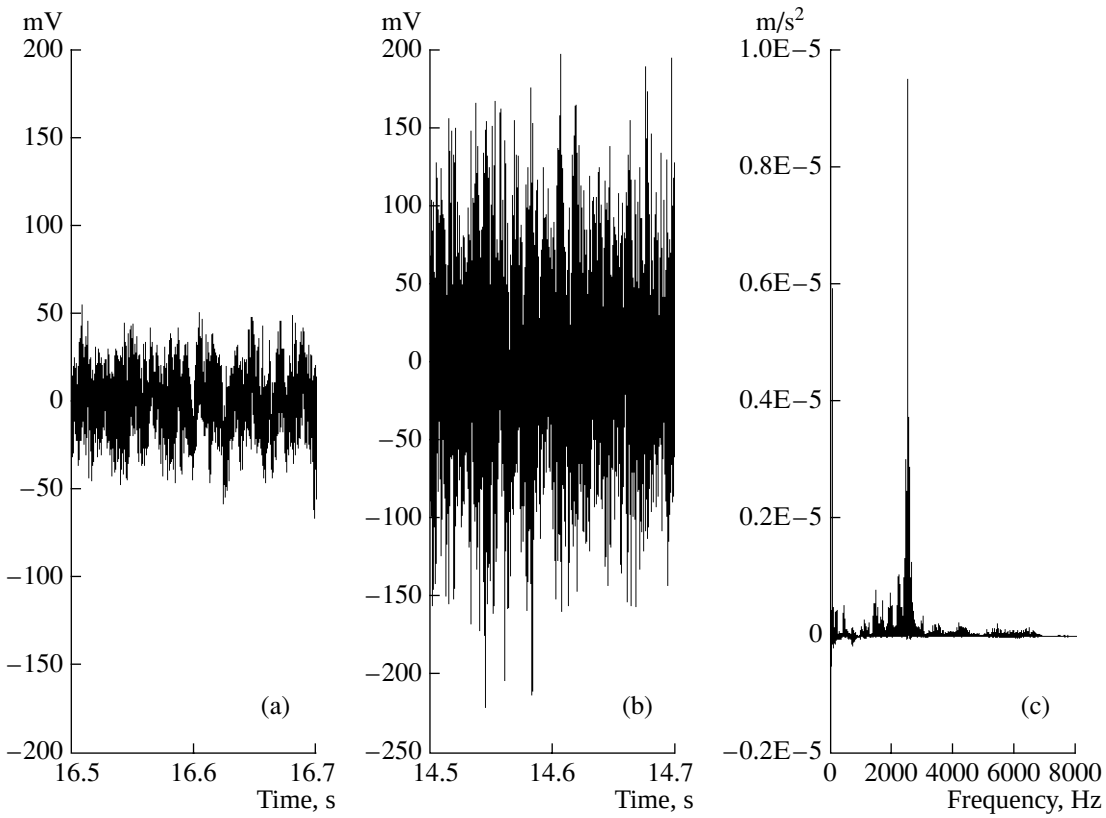


**Fig. 2.** Seismoacoustic emission of well no. 1964 (Bystrinskoe field) with an oil-saturated collector (2064.5 m): SAE signals (a) before and (b) after acoustic action; (c) the difference in the SAE frequency spectra measured before and after the acoustic action.

sured at the output of the intrawell device. The spectral harmonics are expressed in the acceleration units with allowance for the device sensitivity and the transmission function of the data recording system.

Similar measurements were performed in another well (no. 1964) of the same oil pool, which were also preliminarily characterized by geophysical methods and classified as oil-producing. As can be seen from the data for this well measured in the middle of the producing oil pool (at a depth of 2064.5 m) and presented in Fig. 2, there is an increase in the SAE signal intensity upon the acoustic action. This increase was observed over the entire producing oil pool thickness. The main contribution to the total signal energy and to the increment for both wells was provided by the high-frequency components (1–7 kHz).

The initial SAE spectra measured in the two wells of the same pool are much alike and reflect the characteristic features of the given pool. In contrast, changes observed upon the acoustic action in the two cases exhibit opposite trends in their dynamics and significant differences in magnitude. For well no. 1125 with a water-saturated collector, the integral SAE energy decreases by a factor of 4.4, whereas this energy in the well No. 1964 with an oil-saturated collector increases by a factor of 1.96 (for the indicated depths).

It should be noted that the SAEL investigations in the two wells described above were performed under conditions of a short-term depression, which favored the influx of the fluid from the pool to the well. For this reason, it was not excluded that the SAE signals contained components related to the fluid filtration in the pore space and in the perforations. An analysis of such signals was performed in [16] based on the spectra of acoustic and electromagnetic noise caused by fluid filtration in the pools.

However, the results of a series of experiments performed in various (pressure observation, monitor, killed, and unperforated) wells, where the process of filtration in the pore space was eliminated, gave essentially the same results. For example, the unperforated monitor well no. 20020 (Bavly, Tatarstan) was checked for the collector saturation character by SAEL in comparison with geophysical methods. In an oil pool preliminarily characterized by low oil production, the induced SAE signal upon the acoustic action exhibited a strongly anomalous character (Fig. 3.). The anomalous time series displayed separate pulses with high-frequency filling and a repetition rate of about 3–7 Hz. This pattern is analogous to that observed on the daytime surface by means of the “Anchar” technique.

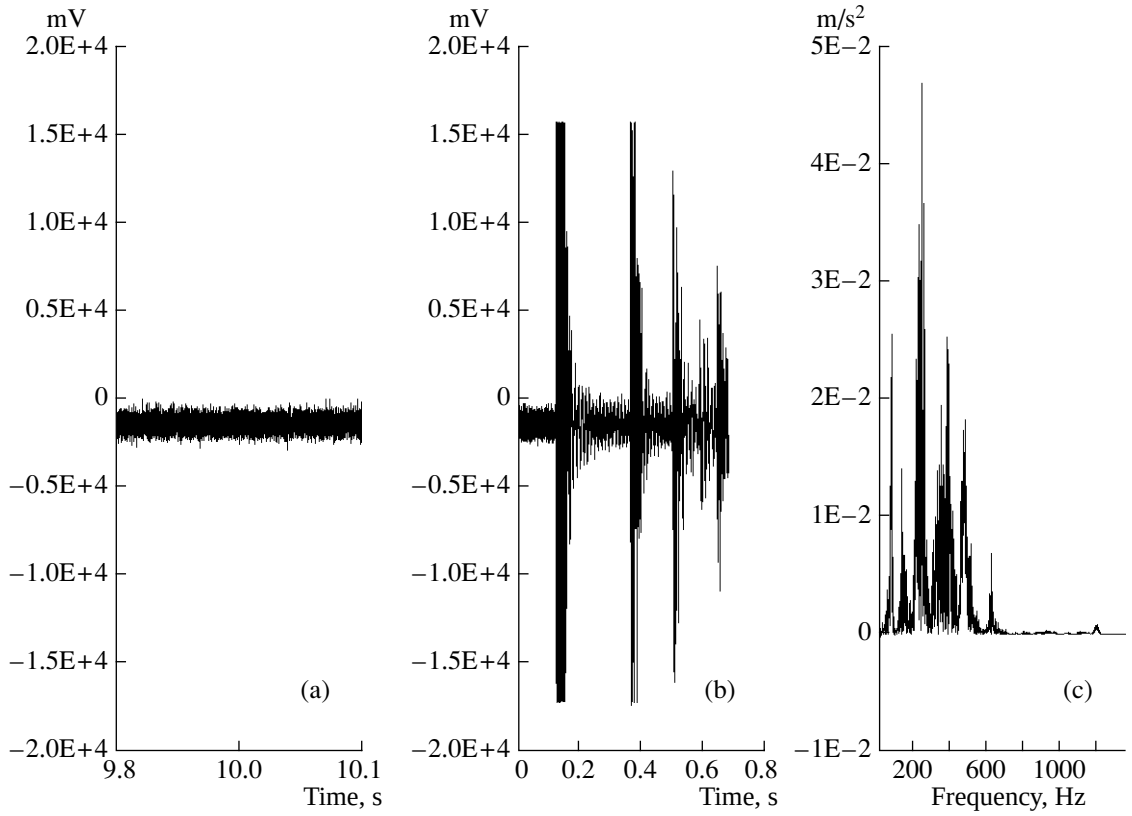


**Fig. 3.** Seismoacoustic emission of well no. 20020 (Bavly field) with an oil-saturated collector (1754 m): SAE signals (a) before and (b) after acoustic action; (c) the difference in the SAE frequency spectra measured before and after the acoustic action.

The results of subsequent monitoring in a different well of the same pool upon the seismoacoustic perforation showed evidence of an increase in the oil yield. Analogous results were obtained in various oil fields of Western Siberia, Kazakhstan, and Komi Republic.

In the course of SAEL, it was possible to calculate the SAE energy in a certain frequency interval (selected by experts upon preliminary online analysis of the signal). This energy was assigned to the given point and recorded in the logging diagram synchronized with the device propagating in depth of the well. Using the resulting logging diagrams obtained by conventional geophysical methods, it was possible to perform a comparative analysis with allowance for the preceding investigations. As can be seen from such a comparative logging diagram presented in Fig. 4, the SAE signals measured before and after the acoustic action outside the layer corresponding to the collector are virtually the same. At the same time, a strong anomaly in the signal measured upon the acoustic action closely coincides with the oil-saturated collector layer identified using the conventional logging techniques.

The general algorithm of the collector saturation characterization by means of the SAEL can be illustrated by an example of identification of the oil- and water-saturated collector layers in the same well (Fig. 5). This is essentially a kind of water–oil contact profiling, which is important in solving the geological problems encountered in the field development.

According to the proposed algorithm, the SAE signals are measured before and after the acoustic action, and then the absolute and relative SAE energy differences are calculated with allowance for the statistical spread of the background. The background spread depends on the general tectonic situation and exhibits an individual character for each field, typically ranging from a fraction of percent to about ten percents. Only the SAE signals exceeding the background spread are accepted as reliable (see “Oil” and “Water” curves in Fig. 5). The oil saturation coefficient was calculated using the “Oil” profile and normalized to the peak in this curve, which was considered corresponding to the absolute oil saturation coefficient determined by geophysical or other standard methods.

The data presented in Fig. 5 were obtained in well no. 141 at the Mamontovskoe oil field in Western Siberia and compared to the results of geophysical investigation using the well radiation data according to the terminal and electrical casing logging. The logging was performed over new (unperforated) intervals, so as to provide for an objective comparison of various methods of evaluation of the collector saturation. The results fully confirmed the validity of the saturation assessment based on the SAEL algorithm.

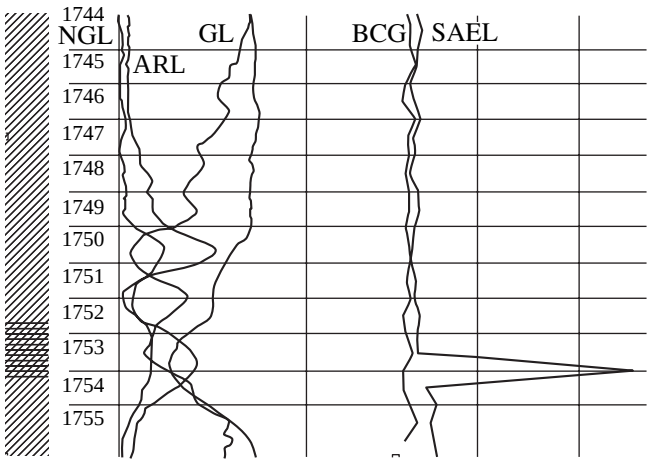


**Fig. 4.** Logging profiles of well no. 20020 (Bavly field): NGL, neutron gamma logging; ARL, apparent resistance logging; GL, gamma logging; BCG, background SAE signal before acoustic action; SAEL, seismoacoustic emission logging upon acoustic action; the left-hand column shows the geological column with a depth scale (m) and indicates the oil-saturated collector.

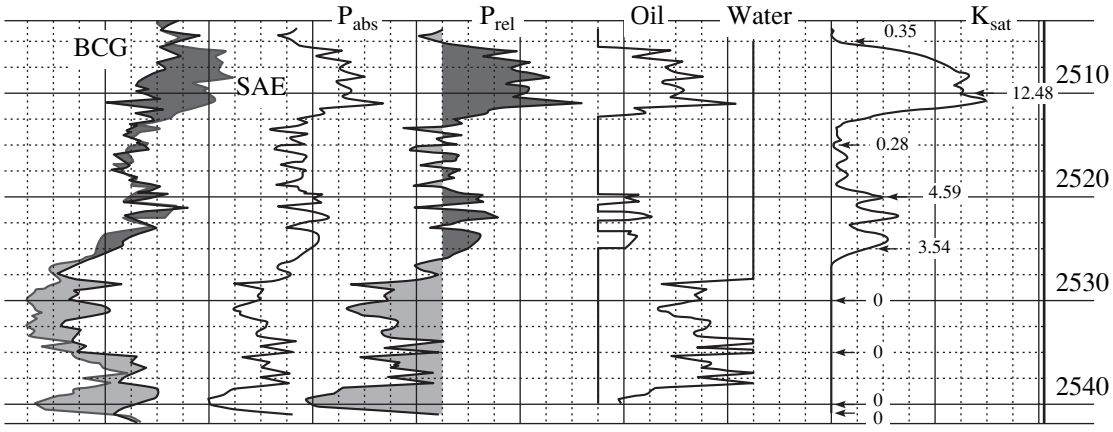


**Fig. 5.** Seismoacoustic emission logging algorithm: BCG, background SAE signal before acoustic action; SAE, seismoacoustic emission signal upon acoustic action; $P_{abs}$, absolute SAE energy difference before and after acoustic action; $P_{rel}$, SAE energy difference relative to background; Oil, positive energy difference minus statistical spread of background; Water, negative difference minus statistical spread of background; $K_{sat}$, oil saturation coefficient calculated using the "Oil" curve and normalized to the maximum oil saturation according to independent geophysical data; the right-hand scale indicates the depth (m).

Taking into account that the effects described above were observed in all wells where the SAEL measurements were performed and the results could be checked by independent methods, we can conclude that the proposed method is applicable to evaluation of the character of the collector saturation. According to this method, a reliable criterion for the assessment of the collector saturation is offered by the difference between the integral SAE energies determined before and after the acoustic action upon the near-well zone.

## REFERENCES

1. *Problems of Geophysics of the XXI Century*, Ed. by A. V. Nikolaev (Nauka, Moscow, 2003) [in Russian].
2. G. A. Sobolev, A. V. Ponomarev, and A. V. Kol'tsov, Fiz. Zemli, No. 12, 72 (1995).
3. V. M. Sboev, Izv. Akad. Nauk SSSR, Fiz. Zemli, No. 10, 57 (1982).
4. B. F. Simonov, V. N. Oparin, N. A. Kaniskin, *et al.*, Neft. Khoz., No. 5, 41 (2000).
5. V. N. Belonenko, M. V. Pavlov, A. D. Makurov, *et al.*, Neft. Prom-st., Ser. Neftepromysl. Delo, Nos. 8–9, 18 (2000).
6. O. B. Khavroshkin, V. V. Tsyplakov, and N. A. Vidmont, Vestn. Otdel. Geolog. Geofiz. Geokhim. Gorn. Nauk Ross. Akad. Nauk (OGGGGN RAN) **1**, No. 2(12) (2000).
7. A. S. Alekseev, V. A. Tsetsokho, A. V. Belonosova, *et al.*, Fiz. Tekh. Probl. Razrabotki Poleznykh Iskopaemykh, Geomekh., No. 6, 3 (2001).
8. S. L. Arutyunov, G. L. Loshkarev, B. M. Grafov, *et al.*, RF Patent No. 2045079 (4 January 1992).

9. G. A. Butenko, V. A. Mikhaĭlov, and V. V. Tikshaev, RF Patent No. 2 105 324, Mezhdunarodn. Patent. Klassifik. (MPK): G01V1/00 (1998).
10. V. V. Dryagin, Nauchn. Tekh. Vestn. Karotazhnik, No. 98 (2002).
11. V. P. Mitrofanov, A. I. Dzyubenko, N. Yu. Nechaeva, and V. V. Dryagin, Geolog. Geofiz. Razrabotka Neftyanykh Mestorozhdeniĭ, No. 10, 36 (1998).
12. O. L. Kuznetsov and S. A. Efimova, *Application of Ultrasound in Petroleum Industry* (Nedra, Moscow, 1983) [in Russian].
13. O. L. Kuznetsov, É. M. Simkin, and G. V. Chilingar, *Physical Grounds of Acoustic Effects on Oil and Gas Deposits* (Mir, Moscow, 2001) [in Russian].
14. V. V. Dryagin and O. L. Kuznetsov, Nauch. Tekh. Zh. Tekhnologii TÉK, No. 5 (12) (2003).
15. *Produktsiya ZAO Intensonik & K*, in Nauch. Tekh. Vestn. Karotazhnik, Nos. 45, 46, 55, 64, 98, 107 (1998–2003).
16. A. I. Ipatov, A. V. Gorodnov, L. P. Petrov, *et al.*, Nauch. Tekh. Vestn. Karotazhnik, No. 9 (122), 51 (2004).

*Translated by P. Pozdeev*

*Acoustical Physics, Vol. 51, Suppl. 1, 2005, pp. S61–S66. Translated from Akusticheskiĭ Zhurnal, Vol. 51, Suppl., 2005, pp. 74–79.*


# Nonlinear Waves in Porous Media Saturated with Live Oil

**S. Z. Dunin and V. N. Nikolaevskiĭ**

*Shmidt United Institute of Physics of the Earth, Russian Academy of Sciences, Bol'shaya Gruzinskaya ul. 10, Moscow, 123995 Russia*

*e-mail: victor@ifz.ru*

Received June 2, 2004

**Abstract**—A nonlinear equation is obtained for waves propagating in porous media of arbitrary consolidation (relative rigidity) saturated with live (i.e., air-bearing) oil. The equation describes the evolution of fast and slow Biot–Frenkel longitudinal acoustic waves propagating in both directions and allows one to analyze the reflected waves and their interaction. For a wave of the second kind, the diffusion coefficient is determined. The dependences of the dispersion and dissipation parameters on the rigidity of the oil pool structure and on the depth of the oil pool occurrence are analyzed. © *2005 Pleiades Publishing, Inc.*

The presence of gas bubbles (even in small proportion) in the fluid of an oil deposit leads to a radical change in the acoustical characteristics of the saturated porous medium.[1] Experiments [1] show that the presence of gas bubbles is the factor responsible for changes in the reflection properties of saturated porous media and in the sound absorption and wave velocity in them.

The efficiency of the action of elastic vibrations on oil pools is determined by the choice of the optimum frequency [2] and by the intensity of the acoustic signal. In the experiments on the intensification of oil production, the intensity of the elastic vibrations acting on oil pools was on the order of $I \sim$ 1–100 kW/m$^2$ [3], which corresponds to the pressure drop in an acoustic wave $\delta P = (2I\rho_{10}c)^{1/2} \approx$ 1–10 atm. Here, $\rho_{10}$ and $c$ are the density of the skeleton of the porous medium and the velocity of sound propagation in it, respectively.

The influence of gas bubbles on the acoustic properties of the medium was analyzed in [4–7] in the framework of the linear theory. In [5], the higher derivative with respect to time was taken into account in the relation between pressure and density of a gas-bearing medium and nonlinear waves propagating in such media were analyzed. In this analysis, pores were assumed to be isolated and the effect of interphase interaction caused by liquid flows was ignored. In [4], nonlinear waves propagating in a fluid-saturated soft ground were considered. Experimental data for pressure waves in a porous medium saturated with a gas-bearing fluid were reported in [8].

[1] For oil with gas bubbles, we use the term "live oil," as is customary in both Russian and English-language literature (in contrast to still, i.e., degassed oil).

In this paper, we analyze nonlinear equations that describe the waves propagating in saturated porous media in terms of the generalization [4] of the Biot–Frenkel theory with allowance for the Biot apparent mass and the Rayleigh equation for individual bubbles. The gas bubbles determine to a great extent the compressibility of the fluid itself.

To take into account the effect of gas bubbles, we use the cell model approximation. In this model, the gas content is determined from the relation

$$\varphi = \frac{R^3}{R^3 - b^3} = \frac{4\pi R^3}{3} n = \frac{4\pi R^3}{3}\rho_2 N = \frac{\rho_L - \rho_2}{\rho_L - \rho_g}. \quad (1)$$

Here, $R$ is the current size of a gas bubble; $b$ is the current size of the cell containing this bubble; $n$ and $N$ are the numbers of bubbles in a unit volume and in a unit mass of the fluid, respectively; and $\rho_2$ is the density of the mixture,

$$\rho_2 = (1 - \varphi)\rho_L + \varphi\rho_g, \quad (2)$$

where $\rho_L$ and $\rho_g$ are the densities of the liquid and gaseous phases of the fluid, respectively.

The relation between the current $R$ and equilibrium $R_0$ radii of a bubble and the pressure in the bubble is determined by the formula

$$\left(\frac{P_{g0}}{P_g}\right)^{1/\gamma} = \left(\frac{R}{R_0}\right)^3 = \frac{\rho_{20}}{\varphi_0\rho_2}\frac{1 - (\rho_2/\rho_L)}{1 - (\rho_g/\rho_L)}, \quad (3)$$

where the subscript 0 refers to the equilibrium state and $\gamma$ is the adiabatic index of the gaseous phase.

From Eq. (3), we derive the nonlinear dependence of the pressure in the gaseous phase on the fluid density variation:

$$P_g = P_{g0} + c_0^2 \delta\rho_2 \left(1 + \frac{\gamma+1}{2\varphi_0}\frac{\delta\rho_2}{\rho_{20}}\right), \tag{4}$$

$$\delta\rho_2 = \rho_2 - \rho_{20},$$
$$c_0^{-2} = \frac{d\rho_2}{dP} = \varphi_0(1-\varphi_0)\frac{\rho_{L0}}{\gamma P_{g0}} \tag{5}$$
$$+ \varphi_0(1-\varphi_0)\frac{\rho_{g0}}{\gamma P_{g0}} + (1-\varphi_0)^2 c_{L0}^2.$$

Here, $c_0$ and $c_{L0}$ are the velocities of sound in the fluid-with-bubbles mixture and in the liquid phase of the fluid.

The parameters of the medium that vary in the course of wave propagation can be taken into account in the framework of the Rayleigh approximation, which describes the dynamics of the bubble behavior in a cell [8]:

$$\left(\frac{\partial}{\partial t} + v\frac{\partial}{\partial r}\right)v = -\frac{1}{\rho_{L0}}\frac{\partial P}{\partial r} - m_0\frac{\nu}{k_0}v; \quad v = \dot{R}\frac{R^2}{r^2}. \tag{6}$$

Here, $\dot{R}$ is the velocity of the bubble surface and $P$ is the pressure in the liquid part of the fluid inside a cell; in addition, $\langle P\rangle = P_2$ is the pressure in the liquid–gas mixture, which is determined as the average pressure in the cell:

$$P_2 = \frac{4\pi}{3(b^3 - R^3)}\int_R^b P(r)dr. \tag{7}$$

Integrating over the cell volume and using Eqs. (1) and (6), we obtain

$$P_2 = P(R) - \frac{\rho_{L0}R_0}{3\varphi_0\rho_{20}}$$
$$\times\left[\left(1 - \frac{3}{2}\varphi_0^{1/3}\right)\left(1 + \frac{\delta\rho_2}{\rho_{20}}\right)\ddot{\rho} + \frac{1}{6\varphi_0\rho_{20}}(\dot{\rho})^2\right],$$
$$P(R) = P_g + \frac{4\mu^*}{3\varphi_0\rho_{20}}\dot{\rho}\left(1 + \frac{\delta\rho_2}{\rho_{20}}\right), \tag{8}$$
$$\mu^* = \mu\left(1 + \frac{m_0R_0^2}{4k_0}\right).$$

Note that, in the framework of the cell model, we have $\varphi_0 < 8/27$. For greater $\varphi_0$, it is necessary to take into account the interaction between bubbles.

The system of equations that determines the kinematic and dynamic properties of the saturated porous medium depending on the velocities $v_1$ and $v_2$ and densities $\rho_1$ and $\rho_2$ of the phases and on the pressure in the mixture $\delta P_2$ can be written in the form

$$\rho_{20}m_0\frac{v_2}{v_f} + \rho_{10}(1-m_0)\frac{v_1}{v_f}$$
$$= [1 - \varepsilon(1-m_0)]\frac{\delta P_2}{v_f^2} + \varepsilon\frac{\rho_{10}c_{10}^2}{v_f^2}\frac{v_1}{v_f},$$
$$\alpha^*\rho_{20}m_0\frac{v_1}{v_f} - (\alpha^* - 1)\rho_{20}m_0\frac{v_2}{v_f} = m_0\frac{\delta P_2}{v_f^2}, \tag{9}$$
$$m_0\delta\rho_{20} + (1-\varepsilon)(1-m_0)\beta_1\delta P$$
$$= [(1-\varepsilon)(1-m_0)]\frac{v_1}{v_f} + m_0\frac{v_2}{v_f},$$

where $c_{10}$ is the longitudinal velocity in the matrix,

$$\alpha^* = \alpha - i\frac{\omega_c}{\omega}; \quad \omega_c = \frac{\nu m_0}{k}; \quad \varepsilon = \beta_1 K_b; \quad v_f = \frac{\omega}{k}.$$

Here, $\alpha$, $\omega_c$, $\nu$, $k_0$, $K_b$, and $\beta_1$ are the factor of apparent mass of the liquid, the Biot frequency, the kinematic viscosity of the liquid, the permeability of the medium, and the bulk modulus and compressibility of the matrix, respectively; $\varepsilon$ is the arbitrary relative rigidity of the matrix.

Equations (9) are derived without considering the hydrodynamic nonlinearity. The operators of differentiation with respect to time, $\partial/\partial t$, and coordinate, $\partial/\partial x$, are replaced by the frequency and wave number operators, $\omega = i\partial/\partial t$ and $k = -i\partial/\partial x$. In the linear case, this corresponds to harmonic changes in the wave: $\exp(i\omega t - ikx)$.

We write the rheological equations for the variations of the matrix density and the effective stress:

$$\delta\sigma^f = (1-m_0)\varepsilon\delta P_2 + e_{xx}\rho_{m0}c_{m0}^2, \tag{10}$$

$$\frac{\delta\rho_1}{\rho_{10}} = (1-\varepsilon)\beta_1\delta P_2 + \varepsilon\frac{v_1}{v_f}, \tag{11}$$

where $c_{m0} = c_{10}(1-m_0)$ is the longitudinal wave velocity in the matrix and $e_{xx}$ is the strain of the porous medium in the wave. We note that, in the case under consideration, $\varepsilon$ is not a small parameter.

We solve system of equations (9) in combination with Eq. (8), which retains the nonlinear terms involved in $\delta P_g$ (see Eq. (4)). In the low-frequency limit, when

$\omega_c \gg \omega$ and $\alpha^* = i\omega_c/\omega$, we obtain a nonlinear equation in $\omega$, $k$, and $\delta P_2$:

$$\left[k^4 + i\frac{\omega_c\omega\rho_{20}^2\beta^{(2)}}{\rho_{10}m_0\varepsilon}k^2 + i\frac{\omega_c\omega^3\rho_{20}^2\beta^{(1)}\rho_0}{\rho_{10}m_0\varepsilon c_{10}^2}\right]\frac{\delta P_2}{\rho_{20}c_0^2} \tag{12}$$
$$= -i\omega_c\omega^3\left[\rho_0 - \varepsilon\frac{\rho_{10}c_{10}^2}{\rho_{20}v_f^2}\right]\frac{\gamma+1}{2m_0\varphi_0\rho_{10}\varepsilon c_0^2c_{10}^2}\left(\frac{\delta P_2}{\rho_{20}c_0^2}\right)^2,$$

$$\rho_0 = m_0\rho_{20} + (1-m_0)\rho_{10}$$

$$\beta^{(1)} = (1-m_0)(1-\varepsilon)\beta_1 + m_0\rho_{20}c_0^{-2}(\omega)$$

$$c_0^{-2}(\omega) = c_{L0}^{-2} + c_0^{-2}\left(1 - \frac{\omega^2}{\omega_r^2} + i\frac{\omega\omega_c\delta}{\omega_r^2}\right)^{-1}$$

$$\beta^{(2)} = \rho_{20}^{-1}\{\beta^{(1)}\varepsilon\rho_{10} \tag{13}$$
$$+ c_{10}^{-2}[1-\varepsilon(1-m_0)][m_0 + (1-\varepsilon)(1-m_0)]$$

$$\omega_r^2 = \frac{R_0^2}{3\varphi_0c_0^2\left(1 - \frac{3}{2}\varphi_0^{1/3}\right)};$$

$$c_0^2 = \frac{\gamma P_{g0}}{\varphi_0(1-\varphi_0)\rho_{L0}}; \quad \delta = 1 + \frac{4k_0}{m_0R_0^2}.$$

In the linear approximation in $\delta P_2/\rho_{20}c_0^2$, when the right-hand side of Eq. (12) can be ignored, the expression enclosed in the square brackets becomes equal to zero. The solution of the biquadratic equation in the wave number $k$ determines the spectrum of Biot waves propagating in the porous medium saturated with a gas-bearing fluid:

$$K_+^2 = \frac{\beta^{(1)}\rho_0}{\beta^{(2)}\rho_{20}c_{10}^2}\omega^2 = \frac{\omega^2}{c_1^2(\omega)} \tag{14}$$
$$K_-^2 = -i\frac{\beta^{(2)}\rho_{20}^2}{\varepsilon\rho_{20}m_0}\omega_c\omega.$$

Here, $c_1(\omega)$ is the velocity of the fast wave (wave of the first kind, according to Biot), whose frequency dispersion is determined by the dependence of $\beta^{(1)}$ and $\beta^{(2)}$ on $c_0(\omega)$. The solution $K_-$ determines the diffusion wave, which is a wave of the second kind (according to Biot), whereas $K_+$ is the wave of the first kind that is observed in experiments at low frequencies.

The wave equation can be obtained as follows: we factorize the left-hand side of Eq. (12) by replacing the expression in square brackets with the expression $(k^2 - K_+^2)(k^2 - K_-^2)$ and by applying the substitution $k = -i\partial/\partial x$, $\omega = i\partial/\partial t$. Then, we obtain

$$\left[\frac{\partial^2}{\partial x^2} - \frac{\partial^2}{c_1^2(\omega)\partial t^2}\right]\left[\frac{\partial^2}{\partial x^2} - D\frac{\partial}{\partial t}\right]\frac{\delta P_2}{\rho_{20}c_0^2} \tag{15}$$
$$= -N\frac{\partial^3}{\partial t^3}\left(\frac{\delta P_2}{\rho_{20}c_0^2}\right)^2.$$

Here,

$$D = \frac{\beta^{(2)}\rho_{20}^2}{\varepsilon\rho_{20}m_0}\omega_c$$

is the low-frequency diffusion coefficient for the wave of the second kind and

$$N = (\gamma+1)\frac{\omega_c}{2\varphi_0\varepsilon\rho_{10}c_0^2c_{10}^2}\left(\rho_0 - \rho_{10}\varepsilon\frac{c_{10}^2}{c_1^2}\right)$$

is the nonlinear factor.

Multiplying Eq. (15) by $c_1^2(\omega)$ and replacing $\omega$ with the operator of differentiation with respect to time, we arrive at a sixth-order equation. This equation describes the waves propagating in both directions, which is important for considering the reflection and refraction of waves.

Equation (15) is nonlinear for waves of both the first and the second kinds. The nonlinear term corresponds to the interference interaction of the waves of the first and second kinds. When the right-hand side of Eq. (15) is ignored, the solution to the equation is a superposition of solutions describing the waves of both kinds.

The equation can be simplified if we consider a wave propagating in only one direction. We pass to this case by using the following representations:

$$k^2 - K_+^2 = (k-K_+)(k+K_+) \approx 2\delta kK_+;$$

$$K^2 - K_-^2 = K_+^2 - K_-^2 \approx -K_-^2 \quad (K_+^2 \gg K_-^2).$$

Then, Eq. (12) takes the form

$$(k-K_+)\frac{\delta P_2}{\rho_{20}c_0^2} \tag{16}$$
$$= i\frac{\omega\omega_c^3}{2K_+K_-^2}\frac{(\gamma+1)[\rho_0 - \varepsilon\rho_{10}(c_{10}^2/c_1^2)]}{2\varphi_0c_0^2\rho_{10}\varepsilon c_{10}^2}\left(\frac{\delta P_2}{\rho_{20}c_0^2}\right)^2.$$

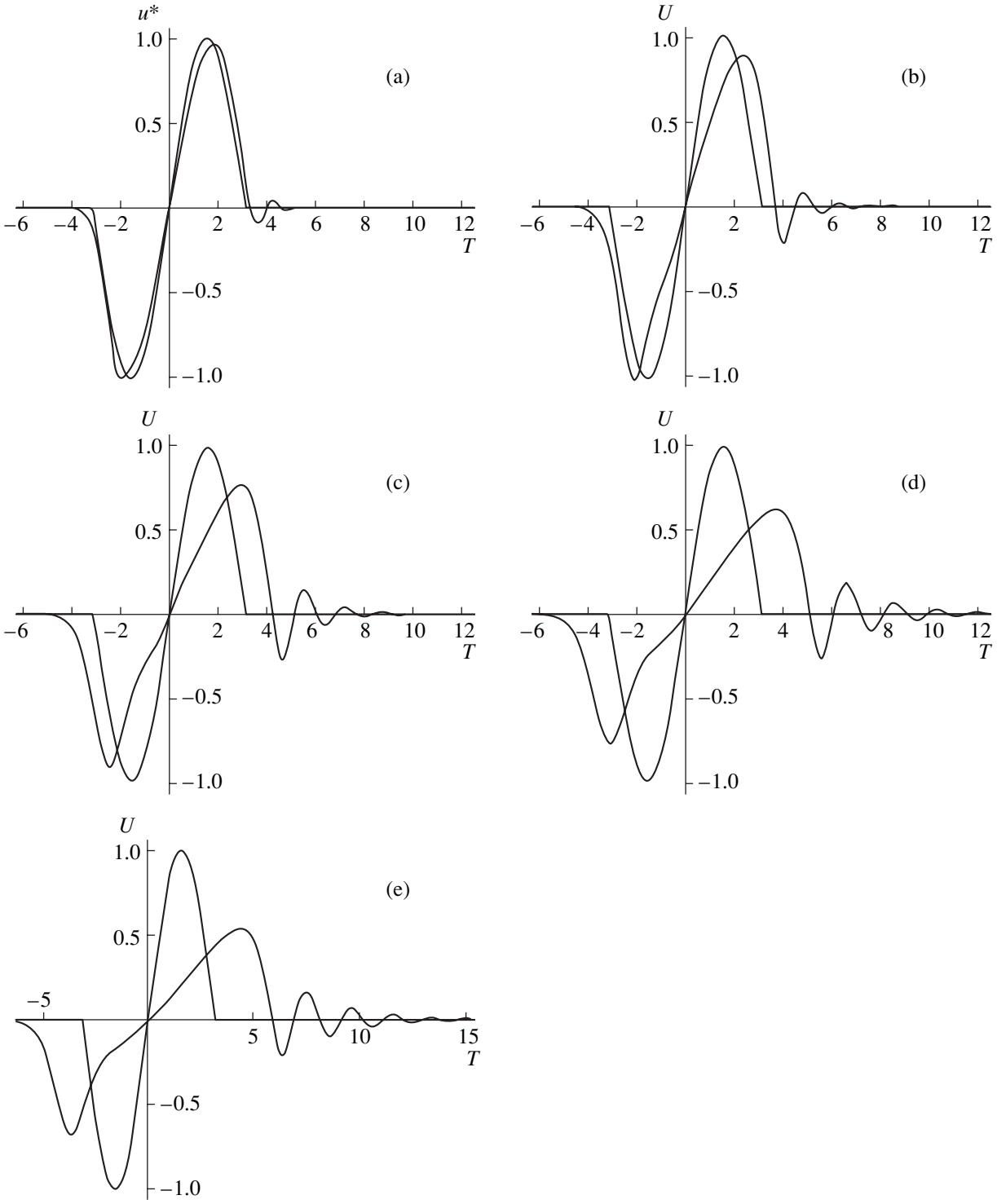


**Fig. 1.** Structure of the wave at different distances $Z$ = (a) 0.25, (b) 1, (c) 2, (d) 4, and (e) 6; Re = 25 and $\sigma = 4.48$.

Expanding $K_+$ in powers of $\omega$, we obtain

$$k - K_+ \cong \delta k + \omega\rho_{20}c_0^2\rho_{10}^{-1}c_{+0}^{-2}\omega_r^2[\omega^2 - i\omega\omega_c\delta].$$

Changing to the low space $\delta k = -i\partial/\partial x$ and time $\omega = i\partial/\partial t$ coordinates, we obtain a nonlinear differential equation for the wave of the first kind that propagates in one direction:

$$\left[\frac{\partial}{\partial t} + \frac{R_0^2 c_{+0}\rho_{20}}{6\varphi_0 m_0}\frac{\partial^3}{\partial x^3} - \frac{R_0^2\rho_{20}\omega_c}{6m_0\varphi_0}\frac{\partial^2}{\partial x^2}\right]\delta P_2$$

$$+\frac{(\gamma+1)\rho_{20}}{2\rho_0\varphi_0}\frac{\delta P_2}{\rho_{20}c_0^2}\frac{\partial}{\partial x}\delta P_2 = 0 \qquad (17)$$

$$(c_{+0}/c_0)^2 = \varepsilon c_{10}^2 c_0^{-2}\rho_{10}\rho_{10}^{-1} + \rho_{20}\rho_{10}^{-1}m_0^{-1}.$$

Introducing the variable

$$u = \frac{\gamma+1}{2\varphi_0}\frac{c_{0+}}{\rho_{10}}\frac{\delta P}{c_0^2}$$

and changing to dimensionless variables $u/u_0 = u^*$, where $u_0 = \frac{\gamma+1}{2\varphi_0}\frac{c_{0+}}{\rho_{10}}\frac{\delta P_0}{c_0^2}$ is the scale of velocity and $\delta P_0$ is the amplitude of the initial disturbance, we represent Eq. (17) in the standard dimensionless form:

$$\left[\frac{\partial}{\partial t^*} + \frac{\partial^3}{\sigma^2\partial x^{*3}} - \frac{\partial^2}{\mathrm{Re}\,\partial x^{*2}} + u^*\frac{\partial}{\partial x^*}\right]u^* = 0,$$

where $t^* = tc_+l_0^{-1}$, $x^* = (x - tc_+)/l_0$, $l_0$ is the length scale of the initial disturbance and $\sigma$ and Re are the parameters that determine the dispersive and dissipative properties of the medium in the presence of a travelling acoustic wave. For a liquid with bubbles, the corresponding parameters $\sigma_L$ and $\mathrm{Re}_L$ are determined by the expressions

$$\sigma_L^2 = 3(\gamma+1)\delta P_0 l_0^2 P_0^{-1}R_0^{-2};$$

$$\mathrm{Re}_L = (\gamma+1)\delta P_0 l_0 P_0^{-1}(2\varphi_0\nu^*)^{-1}c_0;$$

$$c_0^2 = \gamma P_0\rho_{L0}^{-1}\varphi_0^{-1}; \quad \nu^* = 4\nu/3\varphi_0;$$

$$(\sigma/\sigma_L)^2 = m_0(c_0/c_+)^2$$

$$= \sigma_L^2\rho_{10}m_0^2\rho_{20}^{-1}(1 + \varepsilon c_{10}^2\rho_{10}^{-2}c_0^{-2}\rho_0^{-1}\rho_{20}^{-1});$$

$$\mathrm{Re}/\mathrm{Re}_L = 4k_0(c_0/c_+)R_0^{-2}\delta^1.$$

This form of expressions is convenient for analyzing the influence of the porous skeleton on the character of wave propagation in a saturated porous medium. First if all, one can see that $(\sigma/\sigma_L) \ll 1$ and $\mathrm{Re}/\mathrm{Re}_L \ll 1$; i.e., the presence of the porous skeleton deteriorates the dispersive–dissipative properties of the medium.

Let us make some estimates for a situation close to field experiments. We take the intensity of the acoustic action to be equal to $I \approx 1$–$100$ kW/m$^2$ [2], which yields $\delta P_0 \approx 1$–$10$ atm; for the depth of the oil pool occurrence $H \approx 10^2$–$3\times10^3$ m, we have $P_0 \approx \rho_{10}gH = 0.25$ atm. Let the bubble radius be $R_0 \approx 10^{-4}$ m and the signal have the characteristic frequency $\nu = 1/\tau \approx 10^2$–$10^3$ Hz (its duration is $\tau$). Then, $l_0 \approx c_1\tau \approx (1$–$10)$ m. We also accept that $\gamma = 1$, $\varphi_0 \approx 10^{-2}$–$10^{-3}$, and $\nu^* \approx 10^{-(4-3)}$ m$^2$/s. Then, $\sigma_L \approx (7$–$5)\times10^{(4-5)}H^{-1/2}$ and $\sigma_L/\mathrm{Re} \approx (1$–$1.7)\times10^{-4}H^{-1/2}$. Let us assume that $\rho_{10}/\rho_{20} = 2.5$, $m_0 = 0.25$ $c_{10} = 3\times10^3$ m/s, and $k_0 \approx 10^{-(10-12)}$ m$^2$. In this case, for the dispersion, we obtain $\sigma \approx \sigma_{L0}0.4[1 + 7.5\times10^3\varepsilon c_0^{-2}]^{-1} = (2.8$–$2)\times10^{(4-5)}H^{-1/2}[1 + 7.5\varepsilon/H]^{-1}$; $\sigma/\mathrm{Re} \approx \sigma_L/\mathrm{Re}_L = 2\times10^8\,k_0 = 2\times10^{-(2-4)}$ m$^2$.

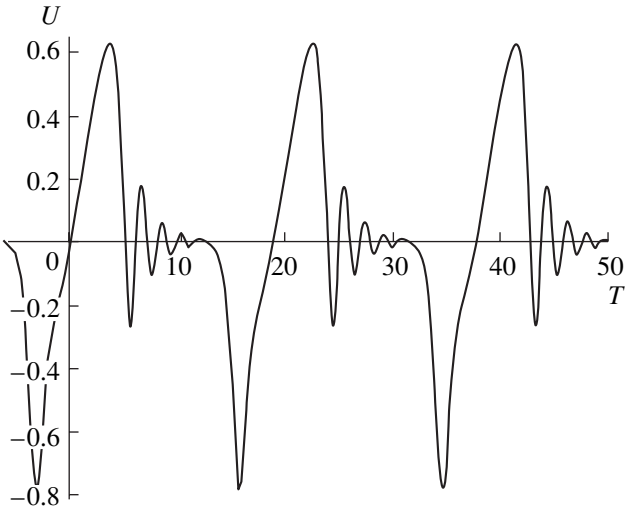


**Fig. 2.** Structure of the sequence of signals with oscillations; $Z = 4$, $\mathrm{Re} = 25$, and $\sigma = 4.48$.

The values of these parameters determine the conditions of signal propagation. In the region where $\sigma/\mathrm{Re} = 1$ or smaller, the wave propagates in the oscillating wave packet mode (when $\sigma < 14$). We performed calculations for the signal at $\sigma = 4.48$ and $\mathrm{Re} = 25$ for different dimensionless distances $Z = (\gamma+1)u_0(x/2\tau c_{+0}^2)$ in the dimensionless time $T = t/\tau$ ($x$ is the distance from the source and $t$ is the arrival time of the wave front). In Fig. 1, the black lines represent the wave profile at excitation. Figure 2 shows the results of calculations for a sequence of pulses separated by such time intervals that, at distances corresponding to the formation of the oscillatory mode, the wave causes continuous vibrations of the oil pool and stimulates intense changes in the parameters of the medium so as to enhance the oil production.

When $\sigma > 14$, the initial signal breaks into solitons (see, e.g., [9]), whose effect on the pool may be of a shaking character. The number of shakes $N_S$ per cycle can be approximately determined as $N_S \approx \sigma/10$. The duration of the signal in each of the solitons $\tau_s$ can be approximately estimated as the duration of the initial signal $\tau$ divided by the number of solitons $N_S$: $\tau_s = 10\tau/\sigma = (4$–$5)\times10^{-(3-4)}H^{1/2}[1 + 7.5\varepsilon/H]$. One can see that the duration of a soliton increases with the depth $H$.

## ACKNOWLEDGMENTS

We are grateful to D.N. Mikhaĭlov for performing the calculations.

## REFERENCES


1. A. L. Anderson and L. D. Hampton, J. Acoust. Soc. Am. **67**, 1865 (1980).
2. *Seismic Action on an Oil Pool*, Ed. by M. A. Sadovskiĭ and V. A. Nikolaev (IFZ RAN, Moscow, 1993).
3. V. P. Dyblenko, R. N. Kamalov, R. Ya. Shariffulin, and I. A. Tufanov, *Production Increase and Revival of Wells by Vibrowave Action* (Nedra, Moscow, 2000) [in Russian].
4. V. N. Nikolaevskiĭ, *Mechanics of Porous and Cracked Media* (Nedra, Moscow, 1984) [in Russian].
5. S. Z. Dunin and V. V. Surkov, Akust. Zh. **26**, 700 (1980) [Sov. Phys. Acoust. **26**, 396 (1980)].
6. S. L. Lopatnikov and P. Yu. Gorbachev, Fiz. Zemli, No. 8 (1987).
7. S. Z. Dunin and O. V. Nagornov, Mekh. Zhidk. Gaza, No. 6, 142 (1984).
8. V. E. Dontsov, V. V. Kuznetsov, and V. E. Nakoryakov, Mekh. Zhidk. Gaza, No. 4, 85 (1984).
9. V. E. Nakoryakov, B. G. Pokusaev, and I. R. Shreĭber, *Wave Propagation in Gas–Vapor–Liquid Media* (Inst. Teplofiz., Novosibirsk, 1984) [in Russian].


*Translated by E. Golyamina*

*Acoustical Physics, Vol. 51, Suppl. 1, 2005, pp. S67–S77. Translated from Akusticheskiĭ Zhurnal, Vol. 51, Suppl., 2005, pp. 80–91.*


# Interaction of Acoustic Waves with Cracks: Elastic and Inelastic Nonlinearity Mechanisms on Different Time Scales

**V. Yu. Zaĭtsev*, V. É. Gusev**, V. E. Nazarov*, and B. Castagnéde****

** Institute of Applied Physics, Russian Academy of Sciences,*
*ul. Ul'yanova 46, Nizhni Novgorod, 603950 Russia*
*e-mail: vyuzai@hydro.appl.sci-nnov.ru*
*** Université du Maine, Av. O. Messiaen, 72 085 Le Mans, France*
Received May 24, 2004

**Abstract**—The interrelated elastic and inelastic fast and slow effects of acoustic wave interaction with cracks are discussed from a unified point of view. Special attention is given to the dissipative manifestations of the presence of cracks and to the effects of the symmetrically time-reversible slow dynamics observed for acoustically activated cracks. These effects can be more pronounced than the conventionally discussed nonlinear elastic effects (such as higher harmonic generation). Taking into account the main geometric features of cracks, a thermoelastic mechanism is proposed to consistently interpret the experimental data. Consequences of the results of these studies for seismics are discussed, and the possibilities of using the observed effects for nonlinear acoustic diagnostics of cracks are discussed. © *2005 Pleiades Publishing, Inc.*

## INTRODUCTION

Today, it is generally recognized that the presence of cracks causes considerable changes in the linear and nonlinear acoustic properties of solids (as compared to perfect crystals and homogeneous amorphous materials). In particular, one should note the high level of acoustic nonlinearity and its nonclassical character (e.g., nonmonotonic and fractional-power amplitude dependences for the harmonics of the signal), an enhanced absorption of elastic waves, the dependence of dissipation on the wave amplitude and on the static pressure on the sample, and pronounced effects of slow dynamics (the memory for the preliminary acoustic activation and the logarithmic behavior in time). When the concentration of cracks is relatively high, the linear elastic moduli of the material may also be noticeably reduced, but, in the case of a low defect concentration, the elasticity of the material remains almost the same while the absorption and the nonlinear properties may already be noticeably changed.

Evidently, all these manifestations are associated with the relative "softness" of cracks, although some of the conventional reasoning leaves a number of significant questions open to discussion. The popular radio engineering analogy is based on the statement that cracks can be considered as diode-like elements: under tensile stress, they are easily opened, and under compression stress, they are closed, so that, under compression, the material behaves as an intact solid. For sufficiently large strains, this interpretation of the nonlinearity of cracks may be useful, but the question of how the cracks can considerably change their state under moderate strains on the order of $10^{-6}$ or less remains open, because, at such strains, the acoustic nonlinearity of the material usually becomes noticeable. Many of the defect models predict [1] that a crack can be almost completely closed when the mean compression strain in the material is approximately equal to the crack's aspect ratio $d/L$, where $d$ and $L$ are the characteristic values of the opening (thickness) and the diameter of the crack, respectively. Typical values of this ratio for cracks, e.g., in rock, are within $10^{-4}$–$10^{-3}$. For the acoustic parameters (such as absorption or elastic moduli) of cracked media, this leads to their pronounced dependence on the applied pressure until the mean strain of the material reaches $10^{-4}$–$10^{-3}$. Then, the pressure-dependent parameters flatten out approaching the values typical of the homogeneous material, which testifies that the cracks are completely closed (see, e.g., [2]). An acoustic action on the material with moderate mean strains $\varepsilon \sim 10^{-6}$–$10^{-5}$ also leads to noticeable changes in the time-average elasticity and dissipation (which can be observed by the changes in the parameters of the resonance peaks of a weaker probing wave, as described in, e.g., [3]). If we assume that the change in the properties of the material in the presence of such small strains is associated with the closure of the narrowest cracks with the aspect ratio $d/L \sim 10^{-6}$ or smaller, we obtain that, for the millimeter or submillimeter cracks, which are typical of rock, their average opening $d$ is about the atomic size or smaller. This conclusion is physically meaningless and points to the necessity to improve the aforementioned radio engineering analogy.

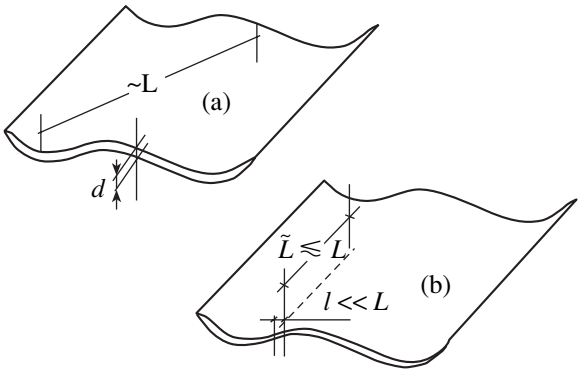


**Fig. 1.** Crack with wavy surfaces (a) without an internal contact and (b) with an internal contact with the dimensions $\tilde{L} \times l$. When $\tilde{L} \longrightarrow l$, the line contact transforms to a point contact.

We note that, in view of the enhanced dissipation of elastic waves in cracked media, models that ascribe this loss to the friction and/or adhesion hysteresis at the crack surfaces were developed within the last 40 years (see, e.g., [4, 5]). Such models give reasonable estimates of losses for waves of sufficiently large amplitudes, including the prediction of an almost constant $Q$ factor of a material in a wide frequency range. However, in the framework of these models, no explanation can be found for the low-amplitude (linear) absorption. The following citation from [4] clarifies the problem: "…For the range of strains used in our experiments, an upper limit of interface displacement [at a crack surface] ranges from $10^{-12}$ cm in the low strain amplitude experiments… The displacements are so small [3–4 orders of magnitude smaller than the atomic size] that the friction characteristics of the interfaces should be quite different from what would be observed in a macroscopic friction experiment…" The atomic-force microscopy data obtained in recent years demonstrate the threshold character of the friction-hysteresis loss, whose manifestation requires that the absolute displacement at the contacting surfaces exceeds the atomic size (see, e.g., [6]). On the other hand, the loss observed in the experiment is much greater than that in homogeneous materials even for ultimately small wave amplitudes, which points to the presence of a nonthreshold mechanism of elastic energy dissipation by the cracks.

One version of such a nonthreshold thermoelastic mechanism of loss in solid bodies with cracks was proposed by Savage [7]. Unlike the insignificant role of such a loss in a homogeneous solid, the presence of cracks strongly increases the loss owing to the introduction of the additional scale characterizing the inhomogeneity of thermoelastic fields and being much smaller than the elastic wavelength. The frequency dependence of this loss has a maximum which corresponds to the coincidence of the thermal wavelength with the characteristic diameter of a crack. The analysis performed in [7] shows that such a mechanism predicts reasonable values for the elastic wave dissipation in the seismic frequency range. Assuming a wide distribution of cracks in size, in this model it is also possible to obtain an almost constant value of the $Q$ factor in a broad frequency range. However, since, in the framework of this mechanism, the maximum energy loss rapidly decreases with decreasing diameter of the crack (as the inverse cube of the diameter), the approximately constant $Q$ factor of rock observed in the frequency range from hertz to megahertz can be explained only by assuming the presence of unreasonably high concentrations of extremely small cracks. In addition, to explain the pronounced amplitude dependence of absorption in cracked media for moderate strain amplitudes $\varepsilon \sim 10^{-6}$, the thermoelastic mechanism [7] requires the assumption that high concentrations of cracks with unlikely small aspect ratio $d/L$ are present.

In this paper, we discuss the mechanism of acoustic nonlinearity of cracks that eliminates the aforementioned discrepancies and allows us from a unified point of view not only to consider the linear (small-amplitude) absorption and its fast amplitude-dependent variations but also to take into account the effects of slow dynamics. In addition, we present the results of experiments on the nonlinear interaction of acoustic waves with cracks in rods and plates. These results agree well with the proposed interpretation.

## BASIC GEOMETRIC FEATURES OF CRACKS AND THEIR PHYSICAL CONSEQUENCES

As was noted above, a crack is a planar defect of a solid with a small aspect ratio $d/L \ll 1$ (its typical values are $d/L \sim 10^{-4}$–$10^{-3}$). Hence, for a complete closure of a crack, it is necessary to produce a mean strain in the material on the order of $d/L$. This estimate weakly depends on the details of the crack model [1] and proves to be much greater than the typical acoustic wave amplitudes $\varepsilon \sim 10^{-6}$–$10^{-5}$ at which the aforementioned nonlinear elastic and dissipative effects become noticeable. Another important feature of cracks, which follows from their images obtained with optical, electron, and atomic-force microscopies and agrees well with the known models of crack formation, is that the contacting surfaces of cracks are usually wavy rather than flat (i.e., their shape resembles a series of ridges and valleys rather than a set of local peaks and dips). When the crack is formed, these initially matched wavy surfaces not only move in different directions along the normal but also are shifted in the tangential direction forming internal contacts. Because of the wavy curvature of the crack surfaces, the resulting contacts are not of a point character but are extended in one direction, as shown in Fig. 1 [8]. It is essential that, in the vicinity of a contact, the local distance between the crack surfaces (or their mutual penetration) $\tilde{d}$ is much smaller than the

average distance $d$ of the crack opening. Owing to this geometry, the vicinity of the contact is more sensitive to external stress (by a factor of about $d/\tilde{d} \gg 1$) than the crack as a whole. Therefore, the state of the contacts in a crack may considerably change in the presence of a relatively weak mean strain in the medium: $\varepsilon \sim 10^{-6}$–$10^{-5}$ (which is much smaller than the strain $\varepsilon \sim d/L \sim 10^{-4}\ldots10^{-5}$ necessary for a complete closure of the crack).

In connection with this, a question arises as to whether these contacts, which are very small compared to the whole crack, are capable of absorbing a considerable amount of acoustic energy. For the manifestation of the commonly discussed friction and adhesion losses at the contacts, it is necessary (as was noted above) that the displacements of the surfaces in the contact region be greater than the atomic size $a$. For a crack with a characteristic diameter $L$, the mean strain $\varepsilon$ (be it compression or tension) produced in the medium may cause a maximum displacement of the contacting surfaces of the crack (in either the tangential or the normal direction) on the order of $\Delta \sim \varepsilon L$ [8–10]. As noted in [9], this estimate does not depend on the details of the crack model and agrees well with the above statement that an mean compression strain of about the aspect ratio of the crack, $\Delta \sim d/L$, causes the displacement of contacting surfaces $\Delta \approx d$, which results in a complete closure of the crack. On the other hand, the condition that $\Delta$ exceeds the atomic size $a$ ($\Delta > a$) determines the threshold mean strain $\varepsilon_{th} > a/L$, below which the displacement of the surfaces occurs on a subatomic scale. For the typical value $a \sim 3 \times 10^{-10}$ m and crack size $L \sim 10^{-3}$ m, the threshold mean strain is $\varepsilon_{th} \sim 3 \times 10^{-7}$ (which agrees well with the threshold of the amplitude-dependent loss observed experimentally). Below this value, the adhesion and friction losses on the crack surface cannot be activated.

At the same time, even for a much smaller strain, a channel for a rather effective dissipation of the acoustic wave energy is formed owing to the locally enhanced thermoelastic loss. This possibility was demonstrated in [7] with the use of the exact solution obtained for an elliptic crack. Indeed, in the presence of stress and strain inhomogeneities (due to the microstructure of the material), the gradients of temperature variations induced by an elastic disturbance are determined not by the elastic wavelength but by the much smaller inhomogeneity scale $L$ or by the thermal wavelength $\delta$ itself [11]. When the crack size $L$ and $\delta$ coincide, the elastic energy loss at the crack as a whole is maximum [7]. A similar result can be obtained without specifying the crack model in detail, by estimating the temperature gradients and the corresponding losses in the vicinity of the crack on the basis of the approach used in [11] in application to losses in polycrystals. When applied to a crack, this approach yields the following approximate expressions for the elastic energy loss $W$ per period for the low-frequency limit ($L \ll \delta$), the high-frequency limit ($L \gg \delta$), and the vicinity of the relaxation maximum ($L \sim \delta$) [8]:

$$W_{LF} \approx 2\pi\omega T(\alpha^2K^2/\kappa)L^5\varepsilon^2, \quad \omega \ll \omega_L \approx \kappa/(\rho CL^2), \quad (1)$$

$$W_{HF} \approx 2\pi T(\alpha^2K^2/\rho C)[\kappa/(\rho C\omega)]^{1/2}L^2\varepsilon^2, \quad \omega \gg \omega_L, \quad (2)$$

$$W_{\text{crack}}^{\max} \approx 2\pi T(\alpha^2K^2/\rho C)L^3\varepsilon^2, \quad \omega \approx \omega_L, \quad (3)$$

where $\omega$ is the circular frequency, $T$ is the temperature, $\alpha$ is the coefficient of volumetric thermal expansion, $K$ is the bulk modulus, $\rho$ is the density, $C$ is the specific heat, $\varepsilon$ is the mean strain in the medium, $\kappa$ is the thermal conductivity coefficient, and $\omega_L$ is the characteristic thermal relaxation frequency corresponding to the size $L$ of the crack. For example, for $L \sim 1$ mm, the relaxation frequency $\omega_L$ falls within ($10^{-1}$–1) rad/s for most types of rock and metals. In determining the low-frequency loss (1), by analogy with [11], we took into account that the crack size $L$ is the characteristic scale within which the elastic stress changes from the mean value $\sigma$ to zero at the free boundaries of the crack. In deriving the high-frequency asymptotics (2), we used the fact that different crack models identically predict a tip stress concentration of the form $\sigma_{\text{tip}} \sim \sigma/\sqrt{r/L}$ [12] (where the distance $r$ is measured with respect to the crack tip). Precisely this region gives the main contribution to the high-frequency dissipation. Expression (3) for estimating the maximum loss is obtained from the condition of equality of the low- and high-frequency asymptotics, which is achieved when the characteristic thermal wavelength coincides with the size of the defect. Solutions (1)–(3), being independent of the details of the crack model, agree well with the exact solution [7] obtained for elliptic cracks.

To obtain similar estimates of the thermoelastic loss at the internal contact, it is necessary to take into account the stress distribution between the contact itself and the arc stiffness of the crack as a whole. For the contacts, which are soft compared to the crack rigidity, this leads to the situation where the stress $\sigma_c$ at the contact exceeds the mean stress $\sigma$ by a factor of about $L/l \gg 1$; i.e., $\sigma_c \sim \sigma(L/l)$ (but not proportional to $(L/l)^2$, as assumed in, e.g., [5]). The region of the near-contact stress localization penetrates into the material to a depth of about the contact width $l \ll L$ [13]. (We note that the aforementioned features of the stress distribution do not depend on the details of the crack and contact models.) Then, the application of the approach used in [11] leads to the following expressions for the

thermoelastic energy loss per period at a contact of length $\tilde{L}$ and width $l$:

$$W_{LF} \approx 2\pi\omega T(\alpha^2 K^2/\kappa) l^2 \tilde{L} L^2 \varepsilon^2, \quad \omega \ll \omega_l \approx \kappa/(\rho C l^2), \tag{4}$$

$$W_{HF} \approx (2\pi/\omega)\kappa T(\alpha K/C\rho)^2 \tilde{L}(L/l)^2 \varepsilon^2, \ \omega \gg \omega_l, \tag{5}$$

$$W_{\text{cont}}^{\max} \approx 2\pi T(\alpha^2 K^2/\rho C)\tilde{L} L^2 \varepsilon^2, \quad \omega \approx \omega_l. \tag{6}$$

Structurally, these expressions resemble Eqs. (1)–(3), although the high-frequency asymptotics of the contact loss is $\sim\omega^{-1}$, which differs from $\omega^{-1/2}$ obtained for narrow cracks. This is caused by the difference in the characters of stress concentration at the contact and at the crack perimeter, near which the high-frequency loss at the crack as a whole is localized: the latter is described by Eq. (2) obtained under the condition $\delta \ll L$. The comparison of Eqs. (3) and (6) for the loss in the vicinity of the relaxation maximum leads to a result that is unexpected at a first glance: for contacts with the length $\tilde{L} \sim L$, the maximum loss at the crack as a hole and at a narrow contact with a much smaller area prove to be on the same order of magnitude, although the relaxation maximum for the narrow contact $l \ll L$ may lie at a point whose coordinate on the frequency axis is 4–6 orders of magnitude greater and fall in the kilohertz or even megahertz frequency range. Expressions (1)–(6) for losses per period at a single crack or at a contact make it possible, for a given defect concentration, to estimate the damping decrement in the medium by the known relation $\theta = W/(2W_{\text{elast}})$, where $W_{\text{elast}}$ is the elastic energy in the wave per unit volume of the material and $W$ is the energy loss per period in the same volume.

### *Consequences for the Small-Amplitude Absorption*

The expressions presented above point to the necessity to reconsider the popular assumption that the thermoelastic loss is insignificant for, e.g., seismic waves. For small-amplitude waves ($\varepsilon \le 10^{-7}$–$10^{-9}$), the aforementioned thermoelastic loss mechanism may even predominate. From Eqs. (1)–(6), it follows that cracks with several soft contacts may cause a noticeable thermoelastic absorption in a frequency range extending over several orders of magnitude (from the relaxation frequency of the crack to the relaxation frequencies of the contacts). Consider a crack of size $L$ containing a single contact of width $l \ll L$ and length $\tilde{L} \sim L$. This contact, in the vicinity of its relaxation frequency $\omega_l$, causes a dissipation that is approximately equal to the dissipation caused by $N = (L/l)^3 \gg 1$ microcracks of size $l$ with the same relaxation frequency [7]. The equivalent number of microcracks $N$ may be great: for the typical ratio $L/l \sim 10^2$ observed for real cracks, this number is $N \sim 10^6$. In view of the wide distribution in size of cracks in real rocks, for realistic crack concentrations, the aforementioned mechanism predicts a weakly varying damping decrement in a wide frequency range, from fractions of hertz to ultrasonic frequencies. This result agrees with [7], but it was obtained without assuming unreasonably high concentrations of microcracks to account for the high-frequency loss.

### *The Possibility of Observing Nonlinear Effects at Moderate Amplitudes*

Another important consequence of the above consideration is the conclusion that moderate mean strains $\varepsilon \sim 10^{-6}$–$10^{-5}$, which often are too small to cause any noticeable changes in the state of the crack as a whole, can considerably change the dimensions $l$ and $\tilde{L}$ of individual contacts between the crack surfaces. According to Eqs. (4)–(6), these changes may noticeably affect the dissipation of a weak probing wave (even if the adhesion-hysteresis and friction losses remain insignificant for this wave). Specifically, this mechanism (possibly, along with other mechanisms of amplitude-dependent dissipation) predicts that, in cracked media, favorable conditions may be formed for the acoustic analog of the Luxembourg–Gorki effect, which was one of the first manifestations of the nonlinear interaction of waves observed experimentally [14]. The effect consists in the amplitude modulation transfer from one intense radio wave to another harmonic wave as a result of their interaction in the ionospheric plasma (this effect was first detected in 1933 for the radiation of high-power radio stations in Luxembourg and in Gorki). In this effect, the presence of components with frequencies $\omega_1 \pm \Omega$ in the spectrum of the modulated intense wave leads to the appearance of modulation components with frequencies $\omega_2 \pm n\Omega$ ($n = 1, 2, \ldots$) in the initially harmonic wave of frequency $\omega_2$. Such a cross-modulation is caused by the changes induced at low frequencies $n\Omega$ in the absorption of the probing wave (because of the nonlinearity of the plasma). Small variations in the propagation velocity were insignificant for this effect [15]. (A similar effect of sound-by-sound amplitude modulation was observed in a field experiment for the interaction of seismoacoustic waves in a sandy ground with a dissipative acoustic nonlinearity [16].) Below, we present the results of observation of the elastic wave interaction in samples with single cracks, including the cross-modulation of the Luxembourg–Gorki type and the effects of the "slow dynamics" of acoustically activated cracks, for which the aforementioned features of cracks and contacts play an important role.

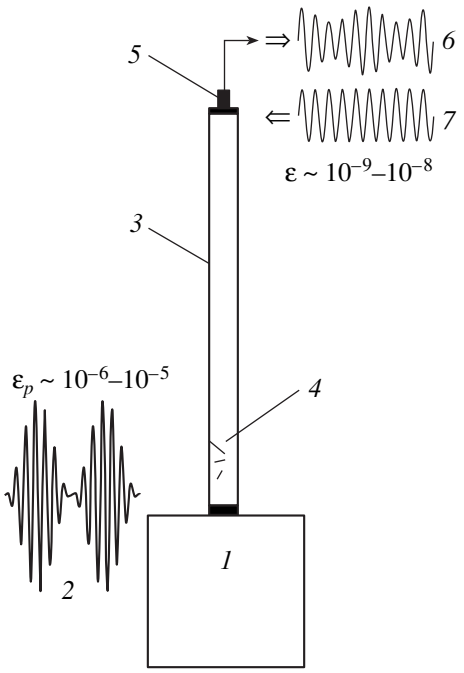


**Fig. 2.** Schematic diagram of the experiment: (*1*) loading mass with a piezoelectric transducer, (*2*) modulated pumping with $\varepsilon_p \sim 10^{-6}$–$10^{-5}$, (*3*) a glass rod 8 mm in diameter and 30 cm in length, (*4*) cracks made by a thermal shock, (*5*) accelerometer and the source of the probing wave with $\varepsilon \sim 10^{-9}$–$10^{-8}$, (*6*) the shape of the nonmodulated transmitted probing signal, and (*7*) the shape of the modulated received probing signal.

## EXPERIMENTAL RESULTS AND THEIR INTERPRETATION

### *Observation of the Analog of the Luxembourg–Gorki Cross-Modulation for Elastic Waves at Cracks*

The experiments (including the acoustic analogue of the Luxembourg–Gorki effect [8, 17]) were performed with the interaction of longitudinal resonance modes in glass rods (8 mm in diameter and 25–30 cm in length) containing one to three thermally initiated curved cracks with a size $L$ of about 2–4 mm. The schematic diagram of an experiment is shown in Fig. 2. In these experiments, the amplitudes and frequencies of acoustic waves were measured with accuracies of ±0.01 dB and ±0.5 Hz, respectively. Figure 3a shows an induced modulation spectrum observed for the probing wave with the amplitude $\varepsilon \sim 10^{-8}$ under the effect of an intense pumping wave that was amplitude-modulated with a frequency of several hertz. In the reference sample without cracks, the level of the modulation components (because of the background nonlinearity of the material and the equipment) was 25–40 dB lower than that in the sample with cracks. The resonance curves obtained for the probing wave with different levels of intense sinusoidal pumping at another mode (Fig. 3b) clearly demonstrate that the pumping primarily affects

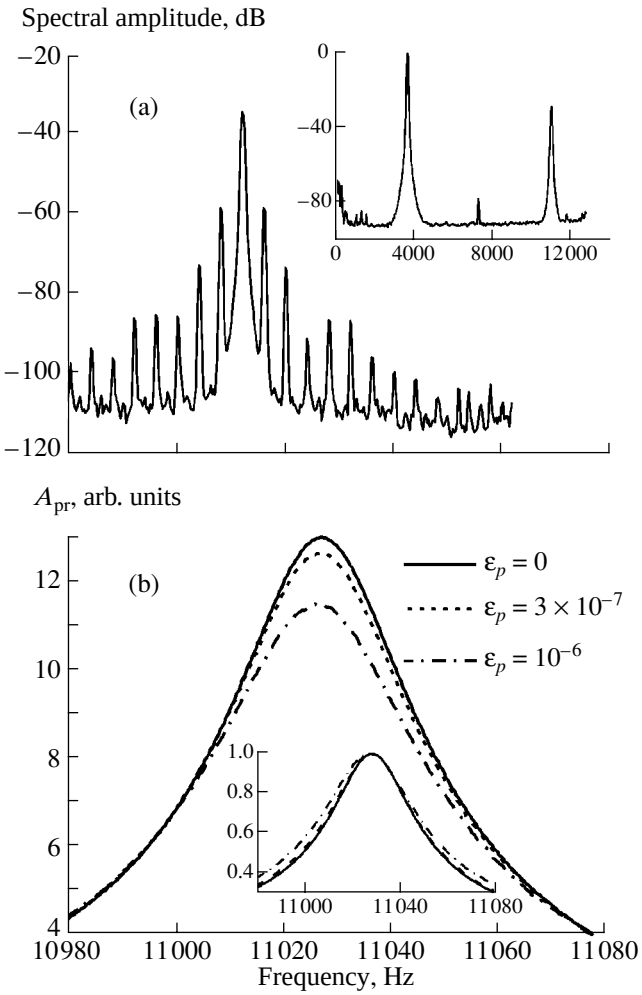


**Fig. 3.** Experimental observation of the Luxembourg–Gorki effect for acoustic waves. (a) Modulation spectrum of the probing wave at the second mode of the resonator ($F$ = 11 kHz) with the amplitude $\varepsilon \sim 10^{-8}$ under the effect of the 3-Hz-modulated intense ($\varepsilon_p \sim 10^{-6}$) pumping at the first mode ($F$ = 3.6 kHz); the inset shows the relative levels of the pumping and probing waves. (b) Resonance curves of the probing wave for different levels of the pumping wave; the curves demonstrate more than 10% variations of the $Q$ factor for the probing mode in contrast to the virtually invariable resonance frequency; the inset shows the same curves in the normalized form.

the $Q$ factor of the resonance while the change in its position plays a secondary role. The damping decrement of the probing wave and the levels of the modulation components depend (nonmonotonically in many cases [17]) on the pumping amplitude, but, with respect to the amplitude of the weak probing wave, these levels are linear. Quantitative estimates by Eqs. (4)–(6) for two or three cracks of millimeter size with internal line contacts show that, for the probing wave, this mechanism may cause a change of about 10% in the $Q$ factor of the sample under study (with the initial value $Q \sim$ 300–350) as a result of "turning on and off" the contacts

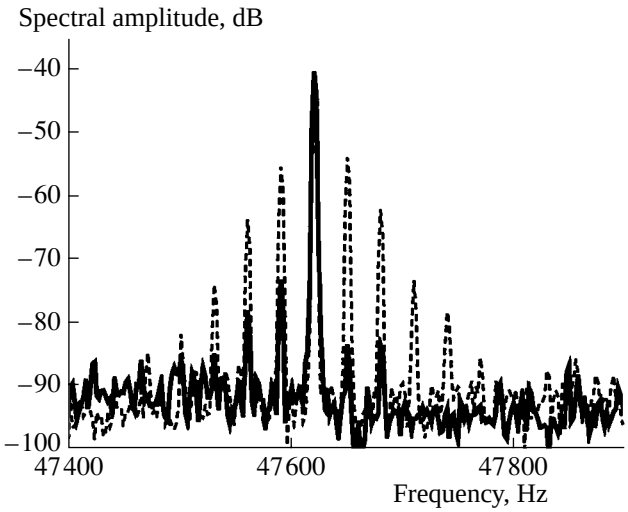


**Fig. 4.** Example of the Luxembourg–Gorki cross-modulation in a glass plate with an artificial cracklike defect in the form of a cut with an inserted plate (the dashed line refers to the cut with the inserted plate, and the solid line, to the cut without the plate).

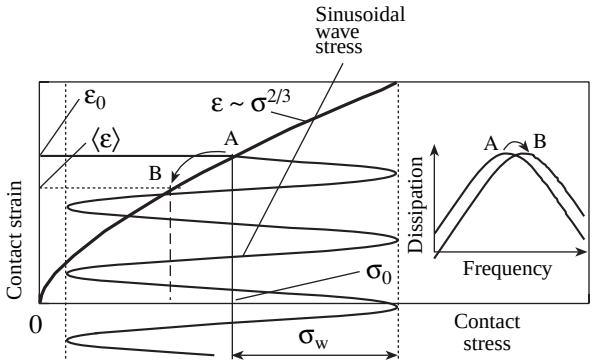


**Fig. 5.** Schematic representation of the softening of a Hertzian contact by an oscillating action because of the asymmetric dependence of its compression on the applied elastic stress. The unperturbed static equilibrium position $A = (\sigma_0, \varepsilon_0)$ and the shifted position $B = (\langle\sigma\rangle, \langle\varepsilon\rangle)$. In the case of the contact between the surface reliefs in the form of hemispheres of radius $R$ that move a distance of $2\Delta$ closer to each other under the action of a force $F$, the compression strain is $\varepsilon_0 = \Delta/R$ and $\sigma_0 = F/R^2$, where these quantities are much smaller than the local strain and stress at the point of contact.

by the pumping wave. The decisive role of the crack for this effect was demonstrated by independent experiments with a glass plate that had a cut into which a metal plate could be inserted (and then eliminated) to form an artificial cracklike defect (Fig. 4). The results of this reference experiment correlate with the results of other experiments with real cracks, because they show that, for the effects under investigation, the contribution of the possible manifestations of nonlinearity at the points where radiators and receivers are attached to the sample (as well as the nonlinearity of the transducers themselves) is insignificant. Indeed, in the comparison of samples with real cracks and without them, the attachment areas inevitably were different and, in principle, they could be responsible for the difference in the results. In the experiment with the artificial defect (controlled by the plate inserted into the cut), the sample under study, together with the radiators and the receiver, was the same and, hence, the observed nonlinear effects were definitely associated with the manifestation of the nonlinearity of the cracklike defect.

### *Induced Transparency and Induced Dissipation*

To understand the following experimental results [18] obtained for resonators of the aforementioned type, it is necessary to remember that the frequency corresponding to the maximum thermoelastic absorption, $\omega = \omega_l \approx D/l^2$ ($D = \kappa/\rho c$ is the thermal diffusivity), at the internal contact of the crack is determined by the contact width $l$, and that, when $l$ is on the order of one or several microns, this frequency estimated for glass falls into the kilohertz frequency range. As was noted above, a moderate mean strain $\varepsilon \sim 10^{-6}$–$10^{-5}$ can considerably change the width of the contact in the crack, which is also true when the action is of an oscillating character. For example, for a contact with the equilibrium compression strain $\varepsilon_0$ under the effect of the stress $\sigma_0$, where these quantities are related by the Hertz law $\varepsilon_0 \sim \sigma_0^{2/3}$ [11], an oscillating stress $\sigma_w$ comparable to $\sigma_0$ may considerably reduce the mean compression of the contact $\langle\varepsilon\rangle$, as schematically illustrated in Fig. 5. It should be noted that such a demodulation (rectification of oscillations) had been observed for both the macroscopic contact nonlinearity of contacting surfaces [19] and the so-called ultrasonic mode of atomic-force microscopy [20]. A consequence of such an average decrease in the contact width should be a shift of the relaxation maximum $\omega_l$ of thermoelastic loss toward higher frequencies (see the inset in Fig. 4). As a result of this upward shift of $\omega_l$, the $Q$ factor of the resonator for oscillations with frequencies below $\omega_l$ should increase while, for higher frequency modes, to which the relaxation maximum has become closer, the $Q$ factor may decrease. Among several samples with cracks (the parameters of contacts in the cracks were for the most part random), we succeeded in finding a sample that clearly demonstrated the aforementioned behavior. From Fig. 6, one can see that, in this sample, at the first longitudinal resonance lying below 4 kHz, the $Q$ factor increased (from $98 \pm 1$ to $117 \pm 1$) under the effect of the pumping field whose frequency was an order of magnitude higher, whereas at the next resonance observed at about 10 kHz (as well as at other higher frequency resonances), the $Q$ factor simultaneously

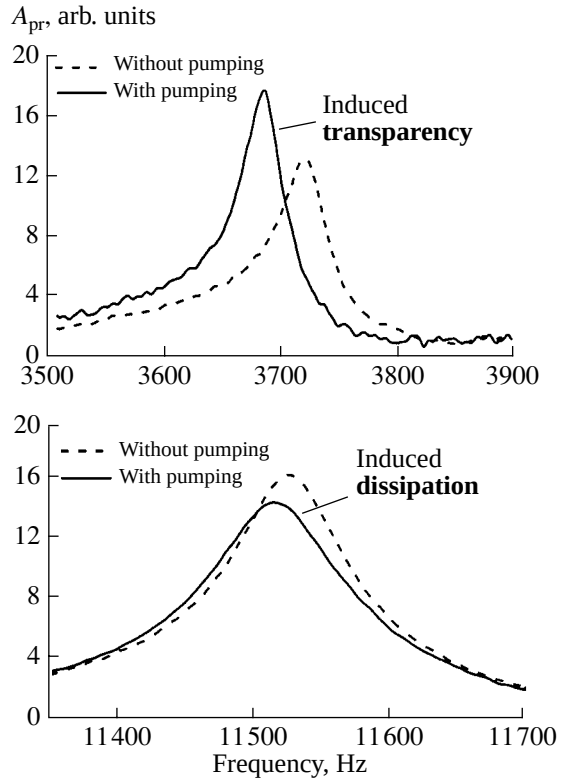


**Fig. 6.** Resonance curves of the probing wave simultaneously measured at different modes under the effect of pumping. The mode at the frequency $F$ = 3.7 kHz exhibits a dissipation decrease, whereas, for the mode with $F$ = 11.5 kHz, the loss increases. Unlike the opposite changes in losses, the frequencies of both modes are shifted downward. The pumping level (at $F$ = 40–50 kHz) is $\varepsilon \sim 10^{-6}$.

decreased (from 154 ± 1 to 115 ± 1). In contrast to the aforementioned opposite changes in the $Q$ factors, the resonance frequencies of all observed peaks were simultaneously shifted downward, as one would expect because of the "softening" of the contact with an average decrease in its width.

A further increase in the wave amplitude $\sigma_w > \sigma_0$ should switch the contact to the clapping regime. For this case, the Hertz law predicts that the average rigidity, as well as the contact width, should again increase. Then, one should expect a nonmonotonic behavior of the parameters of the probing resonance with increasing pumping amplitude: a tendency for an increase in the resonance frequency and an increase in the $Q$ factor of the resonance after its decrease at smaller pumping amplitudes. All these features were also observed in the experiment, which can be seen in Fig. 7. The inset in Fig. 7 represents the calculated (by the Hertz model) variation of the period-average compression of the contact $\langle\varepsilon\rangle$ as a function of the oscillating stress amplitude $\sigma_w$ normalized to the static stress $\sigma_0$.

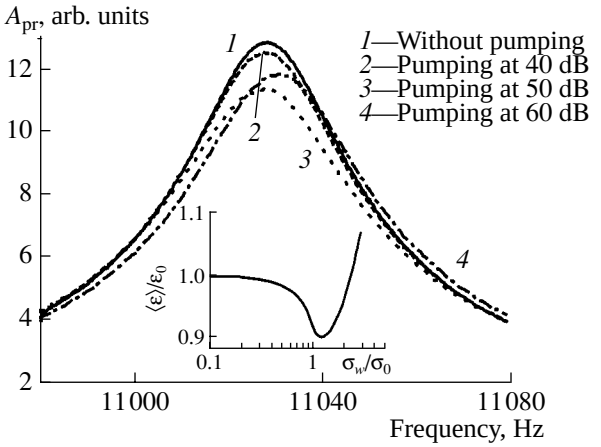


**Fig. 7.** Nonmonotonic dependences of the induced loss and the resonance frequency shift of the probing wave on the pumping amplitude. The inset shows the result of numerical simulation of the mean compression of the Hertzian contact (first a decrease and then an increase) versus the increasing amplitude of the oscillating load.

### *The Slow Dynamics of Dissipative and Elastic Properties with a Logarithmic Time Dependence*

The effects of the slow, logarithmic in time, dynamics are characterized by the remarkable similarity for a wide variety of materials with imperfect (defect) structures (a logarithmic creep, ageing, magnetic relaxation, etc.). Recently, a relaxation characterized by a logarithmic time dependence was observed in acoustically activated rock [21]. As a rule, such a behavior is ascribed to the complex relaxation dynamics of systems with a wide distribution of certain energy barriers characterizing the microstructural bonds in the material. The activation breaks these bonds, which later gradually recover under the effect of temperature fluctuations. The logarithmic-type relaxation is formed for a certain broad spectrum of these energy barriers, whose nature and relation to the microstructure of the material remain open to question [21]. Such a mechanism evidently implies a considerable asymmetry of the activation and relaxation processes (i.e., a fast breaking of bonds and a slow recovery). Note that, in addition to rocks with multiple defects [21], a slow relaxation and memory effects were observed for an ultrasound-activated single crack [22], for which the threshold of parametric generation of subharmonics and higher harmonics of the "reading wave" retained for several minutes a memory for the action of the other intense pumping wave.

In our experiments with samples containing single cracks, a slow drift of acoustic parameters was also observed. To reveal the features of these effects, the shape of the resonance peaks of the weak probing wave $\varepsilon < 10^{-8}$ was recorded. Its behavior was studied for the first time both in the course of the activation of the sample by the pumping wave at another frequency (with

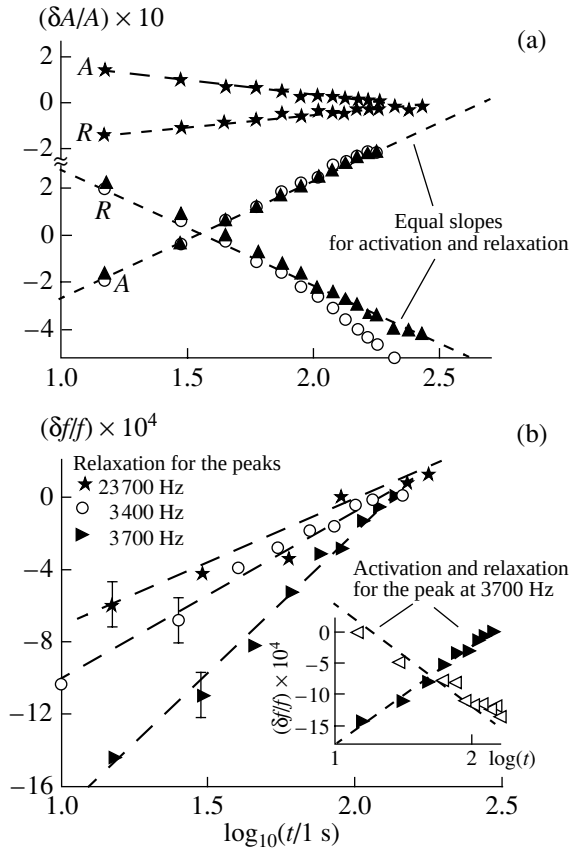


**Fig. 8.** Logarithmic dynamics of the probing wave in a glass rod with a crack. (a) Dynamics of the amplitude ($Q$ factor) of the probing resonances with identical slopes of the dependences at the acoustic activation (indicated with $A$) and at the subsequent relaxation (indicated with $R$). (b) Analogous behavior of the resonance frequency shift at relaxation for several peaks and (inset) at both activation and relaxation for the peak at the frequency $F$ = 3700 Hz.

typical strains $\varepsilon \sim 10^{-6}$–$10^{-5}$) and after the pumping was switched off. The experiments revealed a slow dynamics for both dissipation (the $Q$ factor of the probing resonance) and elastic properties (the position of the resonance peak). Figure 8 presents the corresponding dependences of the variations of the probing resonance maximum (proportional to the variations of the $Q$ factor) and the shift of its position on the frequency axis, $\delta f/f_0$, as functions of the logarithm of the time interval, which was measured beginning from the instant of switching on or off the pumping wave. The logarithmic behavior of a single crack proved to be similar to the slow dynamics of the ensemble of numerous cracks in a rock sample [21]. However, an unexpected result was the symmetric reversibility of the logarithmic behavior; i.e., the slopes of the dependences obtained in the course of the activation and after its termination proved to be identical with a high accuracy. This does not agree with the hypothesis of breaking and recovery of some hypothetical bonds (inside the crack). At the same time, in the context of the above discussion of the crack features, the reversible logarithmic behavior immediately follows from the locally cylindrical symmetry of heat flow propagation in the vicinity of the crack. Precisely the quasi-cylindrical geometry is characteristic of the areas of intense heat generation in the regions of stress concentration along the perimeter of the crack and at the line contacts, whose close-to-cylindrical character was independently determined from other considerations (see above). The deformation of the contacts under thermal stresses should lead to consequences similar to the "fast" effects governed by the action of elastic stresses on the contacts and should result in their displacements on the nanometer scale. From simple estimates, one can find that thermal strains can reach comparable values at the expense of temperature inhomogeneities on the order of $\Delta T \sim 0.1$–$1$ K at the crack. Indeed, for a typical coefficient of thermal expansion $\alpha \sim 3 \times 10^{-6}$ K$^{-1}$ and a typical crack size $L \sim 3 \times 10^{-3}$ m, the resulting thermal displacement is $\alpha L \Delta T \sim 10^{-9}$–$10^{-8}$ m. Direct observations [23] of the surfaces of activated cracks by infrared cameras confirmed the possibility of their heating several degrees and higher. The logarithmically slow and time-reversible character of the local heating $\Delta T$ of the center of the heat generation region in the two-dimensional (cylindrical) geometry immediately follows from the solution of the heat conduction equation $\partial T/\partial t - D\Delta_\perp T = Q/(\rho C)$ with a cylindrical source $Q(r, t)$ localized in a region of radius $r \le l$. For heating, the asymptotically logarithmic solution has the form [18]

$$\Delta T \approx \frac{Q_F(k=0)}{4\pi\rho CD}\ln\frac{t}{l^2/D}, \quad \text{for } t \gg l^2/D = \omega_l^{-1}, \quad (7)$$

where $k$ is the spatial harmonic of the Fourier transform $Q_F(k)$ of the cylindrical source with respect to the radial coordinate. This solution is applicable to times up to $t \le L^2/D$. Above this limit, the heat flow from the crack as a whole begins propagating as a heat flow from an object localized in three-dimensional space, and the local heating becomes saturated. For the subsequent cooling after switching off the source $Q(r, t)$ at the instant $t = t_0$ ($t_0 \le L^2/D$), we again arrive at an asymptotically logarithmic solution:

$$\Delta T \approx \frac{Q_F(k=0)}{4\pi\rho CD}\left[\ln\frac{t_0}{l^2/D} - \ln\frac{(t-t_0)}{l^2/D}\right], \quad (8)$$

which is valid for $l^2/D \ll t - t_0 \le t_0$ and has the same coefficient multiplying the logarithmic factor as in Eq. (7). Thus, the observed symmetry of logarithmic activation and relaxation (Fig. 8) and the observed saturation of the logarithmic behavior at activation (within expected times on the order of hundreds of seconds for glass samples) are convincing arguments in favor of the pro-

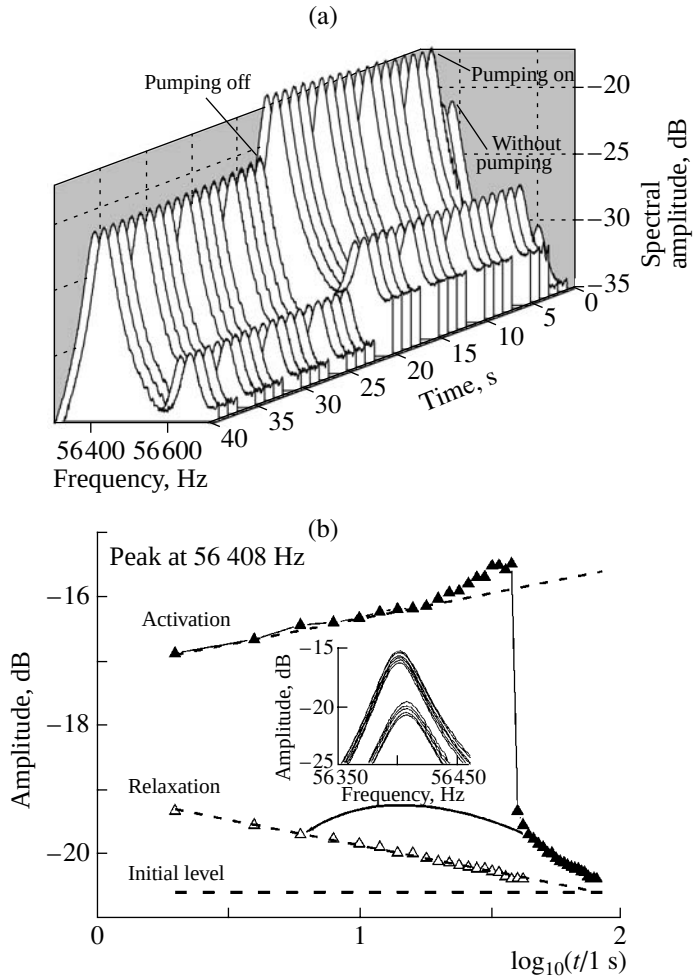


**Fig. 9.** Reversible logarithmic dynamics in the steel sample with a single crack. (a) A sequence of amplitude–frequency curves recorded for two neighboring resonances in the course of acoustic activation and the subsequent relaxation. (b) The amplitude of the peak at $F = 56408$ Hz versus time in the course of activation by the pumping wave and the subsequent relaxation (full triangles; empty triangles show the dependence plotted anew for the relaxation process with the time measured starting from the instant of turning off the pumping). The inset shows the superimposed resonance curves demonstrating that the changes in absorption predominate over the changes in the resonance frequency, as in Figs. 3 and 7 for glass samples.

posed thermoelastic mechanism of the logarithmic slow dynamics.

The universality of this behavior was confirmed by the experiments with a bulk ($36 \times 7 \times 6$ cm) steel sample containing a single crack about 1 cm in size. Figure 9 shows the symmetric and logarithmic-in-time dynamics observed for one of the resonances of the probing wave in this sample. Figure 9a displays a sequence of amplitude–frequency curves recorded for two neighboring resonances at a step of 1 s in the course of the acoustic activation of the sample by the pumping wave and the subsequent relaxation (after the pumping was turned off). Figure 9b shows the time dependences of the amplitude of one of the resonances ($F = 56408$ Hz) with the time measurements starting from the instants of turning on and off the pumping wave for the respective curves. In Fig. 9, as in Fig. 8 for the glass sample, the symmetry of the activation and relaxation processes is clearly pronounced. The characteristic times of the slow processes in Fig. 9 are smaller than those in Fig. 8, which agrees well with the proposed thermoelastic mechanism (in view of the difference in the thermal conductivities of glass and steel).

### *Observation of a Memory in the Nonlinearity of a Crack*

The slow dynamics considered above is actually related to the variations of the linear acoustic properties of the sample with a crack (i.e., its resonance frequencies and $Q$ factors). Attempts to detect slow effects in the nonlinear response (to compare our results with [22]) were hindered by the fact that the variations of nonlinearity-generated harmonics were determined to a considerable extent by variations of the sample resonance parameters, which masked the changes in the

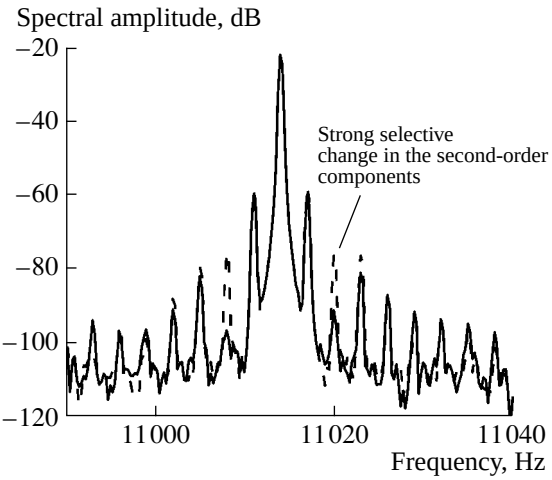


**Fig. 10.** Luxembourg–Gorki cross-modulation spectra of the probing wave for the sample that was preliminarily at rest (the dashed line) and for the same sample that was under the action of the pumping wave for several minutes (the solid line). The noticeable selective changes in the level of the second-order modulation components testify to the change in the character (parity) of the nonlinearity of the crack and to its memory for the activation.

nonlinearity of the crack. Using the Luxembourg–Gorki cross-modulation effect, for one of the glass resonators with a crack, we managed to demonstrate the memory associated with precisely the nonlinearity of the crack for the preceding acoustic activation. Figure 10 shows the cross-modulation spectra of the probing harmonic wave with frequency $f_2$ = 11015 Hz that were obtained immediately after turning on the intense modulated pumping wave (with a carrier frequency $f_2 \approx$ 3800 Hz and a modulation frequency $F$ = 2 Hz) for the sample preliminarily being "at rest" and the spectra obtained for the same sample several minutes after the pumping was turned on. One can see a considerable difference between these spectra in the level of the second modulation component (more than 15 dB), which testifies to a significant change in the character (parity) of nonlinearity. At the same time, the amplitude variations of the fundamental harmonic and other components were insignificant: this suggests that the linear characteristics of the given resonance varied only slightly and, therefore, could not selectively affect the second-order components.

The possibility of a change in the character (parity) of nonlinearity agrees well with the aforementioned nonmonotonicity of the dependence of the average contact width on the pumping amplitude (see the inset in Fig. 7). As long as the amplitude of the modulated (with frequency $F$) pumping does not pass through the minimum of this dependence, the modulation of the average contact width mainly contains the $F$ harmonic. After passing through the minimum, the induced increase in the contact width occurs twice within the modulation period, which leads to a sharp growth of the $2F$ harmonic in the contact modulation. Such a passage of the "operating point" through the minimum may be caused by a change in the pumping amplitude itself or a change in the initial contact compression due to thermoelastic effects at constant pumping amplitude.

## CONCLUSIONS

In the series of experiments with glass and steel samples with cracks, we studied such effects as the time-reversible slow logarithmic dynamics of the elastic and inelastic properties of acoustically activated single cracks, as well as a number of important features of "fast" nonlinear effects: the modulation spectrum transfer of the Luxembourg–Gorki type due to the interaction of acoustic waves at the cracks and the slow dynamics of this effect; the nonmonotonic amplitude behavior and the manifestation of the crack state changes of opposite character for different frequencies of the probing wave (i.e., the simultaneous observation of the induced clarification for some probing modes and absorption for other probing modes). The mechanism of acoustic wave interaction with cracks that was proposed to explain the experimental results is at variance with the commonly accepted idea that the role of thermoelastic effects is insignificant, including the case of the linear (small-amplitude) absorption of elastic waves in rock. The results obtained above give an insight into the physics of both fast and slow wave processes in cracked media. The observed nonlinear acoustic effects, which exhibit a high sensitivity to the presence of cracks in solids, offer considerable promise for the development of new nonlinear-modulation methods for detecting cracks and cracklike defects.

## ACKNOWLEDGMENTS

This work was supported in part by the Russian Foundation for Basic Research (project no. 05-02-17355), the Ministry of Industry and Science (NSh-1641.2003.2), and the Russian Science Support Foundation (V.Z.). The experiments were performed at the Laboratory of Acoustics of Université du Maine (France) under the PAI–Russie and PECO-NEI Programs (project nos. 04521TM and 16366).

## REFERENCES

1. G. M. Mavko and A. Nur, J. Geophys. Res. **83** (B9), 4459 (1978).
2. G. M. Mavko and D. Jizba, Geophysics **59** (1), 87 (1994).
3. V. E. Nazarov, A. V. Radostin, and I. A. Soustova, Akust. Zh. **48**, 85 (2002) [Acoust. Phys. **48**, 76 (2002)].
4. R. B. Gordon and L. A. Davis, J. Geophys. Res. **73** (12), 3917 (1968).

5. R. R. Stewart and M. N. Toksoz, J. Geophys. Res. **88** (B1), 546 (1983).
6. R. W. Carpick, Q. Dai, D. F. Ogletree, and M. Salmeron, Tribol. Lett. **5**, 91 (1998).
7. J. S. Savage, J. Geophys. Res. **71** (16), 3929 (1966).
8. V. Zaitsev, V. Gusev, and B. Castagnede, Phys. Rev. Lett. **89** (10), 105502 (2002).
9. G. Mavko, J. Geophys. Res. **84** (B9), 4769 (1979).
10. V. Zaitsev and P. Sas, Acust. Acta Acust. **86**, 429 (2000).
11. L. D. Landau and E. M. Lifshitz, *Theory of Elasticity* (Nauka, Moscow, 1965; Pergamon, Oxford, 1986).
12. D. Broek, *Elementary Engineering Fracture Mechanics* (Noordhoff, Leyden, 1974; Vysshaya Shkola, Moscow, 1980).
13. E. J. Johnson, *Contact Mechanics* (Cambridge Univ. Press, Cambridge, 1987; Mir, Moscow, 1989).
14. B. D. H. Tellegen, Nature, No. 6, 840 (1933).
15. V. L. Ginzburg, Izv. Akad. Nauk SSSR, No. 12, 253 (1948).
16. A. L. Bagmet, V. E. Nazarov, A. V. Nikolaev, *et al.*, Dokl. Akad. Nauk **346** (3), 390 (1996).
17. V. Zaitsev, V. Gusev, and B. Castagnede, Ultrasonics **40**, 627 (2002).
18. V. Zaitsev, V. Gusev, and B. Castagnede, Phys. Rev. Lett. **90** (7), 075501 (2003).
19. I. Solodov, Ultrasonics **36**, 383 (1998).
20. O. Kolosov and K. Yamanaka, Jpn. J. Appl. Phys. **32**, L1095 (1993).
21. J. A. Ten Cate, E. Smith, and R. A. Guyer, Phys. Rev. Lett. **85** (5), 1020 (2000).
22. I. Solodov and B. Korshak, Phys. Rev. Lett. **88** (1–4), 014303 (2002).
23. L. D. Favro, Xiaoyan Han, Zhong Ouyang, *et al.*, Rev. Sci. Instrum. **71** (6), 2418 (2000).

*Translated by E. Golyamina*

*Acoustical Physics, Vol. 51, Suppl. 1, 2005, pp. S78–S87. Translated from Akusticheskiĭ Zhurnal, Vol. 51, Suppl., 2005, pp. 92–102.*


# Acoustoseismic Wave Fields Generated by Surface Seismic Vibrators

**V. V. Kovalevskiĭ**

*Institute of Computational Mathematics and Mathematical Geophysics, Far East Division, Russian Academy of Sciences, pr. Akademika Lavrent'eva 6, Novosibirsk, 630090 Russia*

*e-mail: kovalevsky@sscc.ru*

Received June 16, 2004

**Abstract**—Results of experimental and theoretical studies of acoustoseismic wave fields generated by surface seismic vibrators are presented. In experiments with high-power seismic vibrators operating in a frequency range of 5–10 Hz, acoustic waves were recorded at distances up to 50 km from the source. The long-range sound propagation from seismic vibration sources was observed in a near-surface waveguide arising due to temperature inversion. The effect of the acoustoseismic induction, i.e., excitation of surface seismic waves by the acoustic wave arriving from the vibrator, was also detected. The results of mathematical modeling of the acoustoseismic field generation by an operating seismic vibrator are presented. They include the modeling of the radiation of a harmonic acoustic wave's by the vibrator, its trapping by the near-surface waveguide, the long-range low-frequency acoustic wave propagation in the presence of the waveguide, and the induction of a surface seismic wave by the arriving harmonic acoustic wave. It is shown that a seismoacoustic wave propagating at the boundary between the elastic earth and the atmosphere is an analog of the Stonely wave that appears in the presence of a near-surface low-temperature layer in the atmosphere. © *2005 Pleiades Publishing, Inc.*

Seismic sources operating on the day surface in contact with two elastic media, namely, the Earth and the atmosphere, generate seismic and acoustic waves interacting at the boundary between these media in the course of their propagation. Many publications are devoted to studying acoustoseismic wave fields. These publications consider both the theoretical aspects of the generation and propagation of waves from different sources and the results of experiments related to monitoring of atmosphere, seismic prospecting, and vibrational probing of the Earth. It is well known that surface explosions give rise to seismic waves, as well as to an intense sound wave propagating along the free surface and inducing a surface seismic wave [1, 2]. The latter is recorded in seismograms with the arrival times equal to the travel time of the sound wave between the explosion and the recording point. Theoretical works [3, 4] considered the processes of acoustic wave radiation by a harmonic source of a force acting on the elastic half-space. The energy estimates were obtained, which showed that the acoustic radiation of real vibrators makes a small part of the seismic radiation energy, and the reception of the acoustic radiation at distances of tens of kilometers was assumed to be impossible.

## 1. EXPERIMENTAL INVESTIGATIONS OF ACOUSTOSEISMIC FIELDS OF VIBRATION SOURCES

The excitation of acoustic waves by a vibration source and their long-range propagation was first detected in geophysical experiments with a GRV-50 hydroresonance vibrator, which were carried out by the Institute of Computational Mathematics and Mathematical Geophysics, Far East Division, Russian Academy of Sciences, near Kamenka, Novosibirsk Region [5, 6]. At a distance of 20 km from the vibrator, three-component seismometers recorded the surface seismic waves induced by the arriving acoustic wave (in what follows, these waves are called seismoacoustic waves). Later, this effect was observed in experiments with high-power low-frequency vibrators, TsV-100 and TsV-40, at distances as far as 50 km [7]. In contrast to the seismic waves, which have constant amplitudes and arrival times, the seismoacoustic waves had large amplitude variations (down to complete disappearance) and noticeable variations of the arrival times (units of seconds).

The radiation of the acoustic waves by the high-power seismic vibrators is caused by the fact that, under the operation of a vibrator at infrasonic frequencies, the ground surface around the source with an area of 100–200 $m^2$ oscillates as a large-scale membrane of an infrasonic acoustic transmitter. These oscillations are synchronous with the variation of the signal frequency radiated by the vibrator and generate acoustic waves in the atmosphere with the same law of frequency variation (sweep-signals) as that in the generated seismic waves.

The propagation of the acoustic waves of infrasonic frequencies (5–10 Hz) over distances of several tens of kilometers is possible due to the refraction of sound

waves in the atmosphere. Two mechanisms of this phenomenon are known: temperature inversion in an air layer near the earth surface and the presence of wind whose velocity increases with height. In the experiments carried out in calm summer weather, when seismoacoustic waves were recorded, a rapid decrease in temperature was observed near the ground at night, which resulted in the formation of a near-surface waveguide. The second mechanism of refraction, related to the presence of wind, appeared in experiments carried out along the Bystrovka–Klyuchi track (a distance of 50 km). In this case, appearing and disappearing seismoacoustic waves correlated with the wind direction from the vibrator or toward the vibrator [7].

The acoustoseismic wave fields generated by the high-power vibrators were investigated in detail during the work on the profile recording of vibrators and explosions from quarries of the Kusbas Basin in the field season of 2001. For temporal and coordinate referencing of the recording systems and the sources, the GPS system was used, which made it possible to exactly determine all distances, both between the vibrator and the seismic array and between the sensors in the array, and, in particular, the orientation of the seismic arrays of the recording systems.

The works were carried out using a TsV-100 vibrator (the vibroseismic test site, Far East Division, Russian Academy of Sciences, at Bystrovka, Novosibirsk Region) and a VIRS-K recording system. Seismoacoustic waves were recorded at three points of the profile: p. Mayak (the distance from the vibrator 28.5 km), p. Stepnoi-2 (31.1 km), and p. Evsino (40.8 km). In all cases, we used a linear seismic array of five three-component SK-1P seismometers with the *X* component oriented along the array, *Y* component oriented across the array, and *Z* component along the vertical; the distance between the sensors was 200 m. At different points of recording, the arrays were differently oriented with respect to the vibrator. At p. Mayak, the direction of the array deviated from the vibrator azimuth by 8 degrees and at p. Stepnoi, by 38 degrees. The layout of the seismic array arrangement is shown in Fig. 1.

The three-component vibration seismograms were obtained at all points of recording and contained two groups of waves: seismic waves and seismoacoustic ones. Figure 2 exhibits seismograms and their fragments for p. Mayak (a distance of 28.5 km). This figure contains the survey seismograms with a duration of 200 s and their 12-s fragments for groups of seismic and seismoacoustic waves. The seismic waves had typical velocities of 5.8–6.4 km/s and arrived at the point of recording within 4.4–5 s, while the seismoacoustic waves arrived within 84–86 s, which corresponds to an acoustic wave velocity of 331–339 m/s. The seismoacoustic waves are recorded only on *X* and *Z* components, and they are absent on the *Y* component. The wave train has a duration of about 2 s and consists of 1–2 peaks of oscillations. The amplitudes of these waves

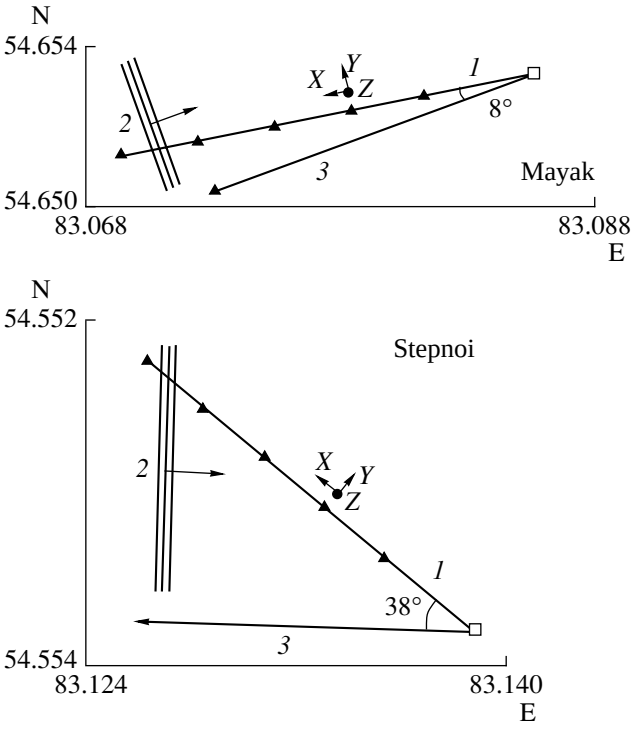


**Fig. 1.** Layout of the seismic array arrangements at p. Mayak at a distance of 28.5 km and at p. Stepnoi at a distance of 31.1 km: (*1*) seismic array with five three-component seismometers, (*2*) front and propagation direction of the acoustic wave, and (*3*) direction to the vibrator; *X*, *Y*, and *Z* are the directions of seismometer components.

are 3–5 times smaller than those of seismic waves. The polarization of seismoacoustic waves has a pronounced elliptic character.

At p. Stepnoi at a distance of 31.1 km, the time of appearance of the seismoacoustic wave on the seismogram is 90–92 s, which corresponds to the velocity of the arriving acoustic wave of 338–345 m/s. At this point, the seismoacoustic waves are recorded on all *X*, *Y*, and *Z* components. It is interesting that, in the measurement session of 2 a.m., the amplitudes of these waves were 2–4 times greater than the seismic wave amplitudes the on the *Z* component and comparable with them on the *X* and *Y* components. The wave has an elliptic polarization in both the *ZX* plane and the *ZY* plane. The appearance of seismoacoustic waves on both horizontal components is related to the deviation of the array direction from the vibrator azimuth by 38 degrees.

The difference in the directivity of the seismic arrays with respect to the direction to the vibrator at distances of 28.5 and 31.1 km (Fig. 3), allowed us to reveal the character of the excitation of the surface seismic wave by the arriving acoustic wave.

Considering the variability in the trains of oscillations in the seismoacoustic wave, one can see the shift of the train as a whole in time from sensor to sensor and the displacement of the maximum amplitude within the

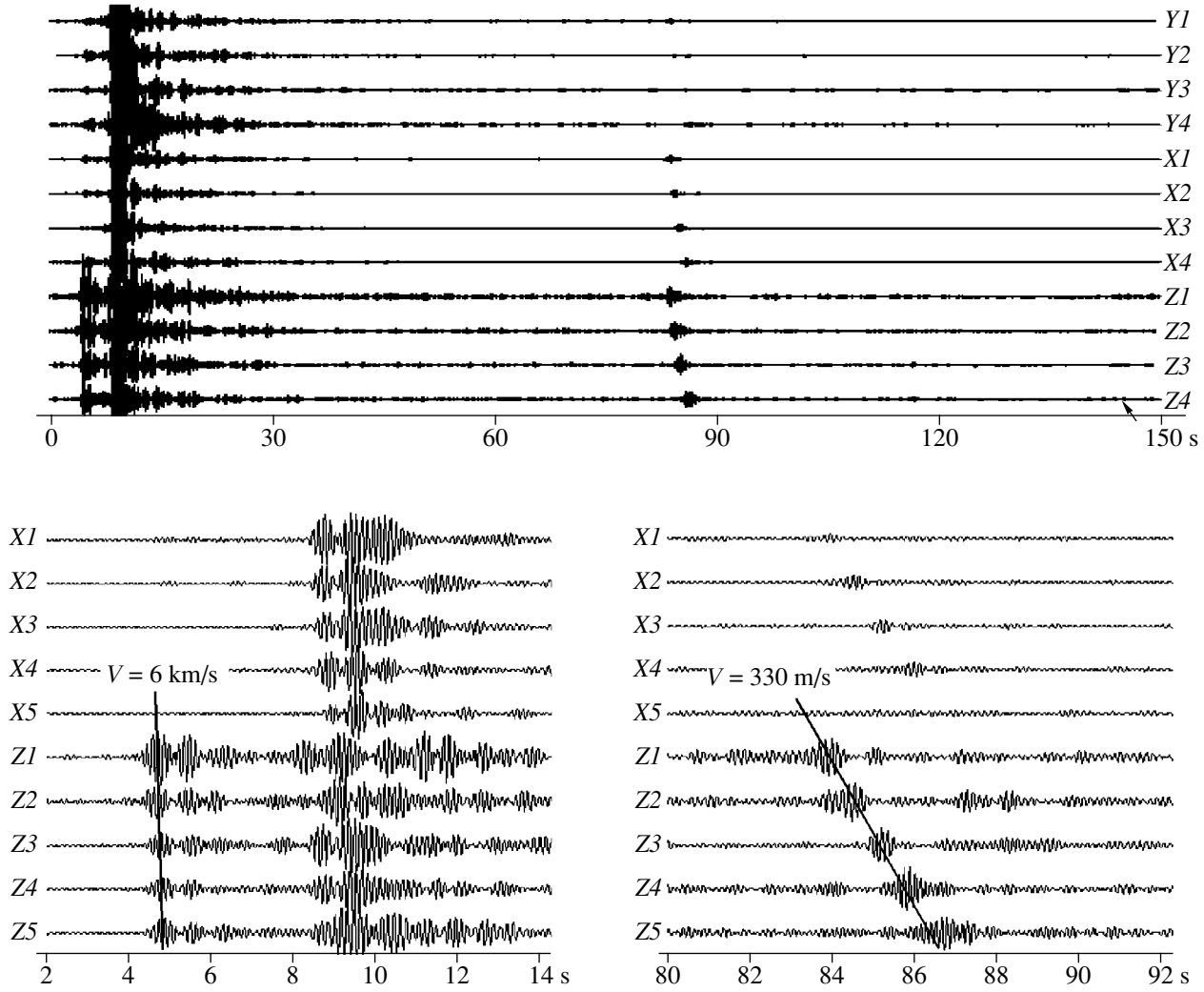


**Fig. 2.** Three-components seismograms at a distance of 28.5 km from the vibrator (top), a fragment of the seismogram for a group of seismic waves (bottom left), and a fragment of the seismogram for a group of seismoacoustic waves (bottom right); *X1–X5*, *Y1–Y5*, and *Z1–Z5* are the components of five seismometers.

train. In addition, the lag of the amplitude maximum in time is evident. Such a character of the propagation of trains of oscillations takes place if the phase and group velocities of a traveling wave are different. The direct determination of the phase velocity by measuring the phases of oscillation for individual sensors is inapplicable in our experiments. The oscillation frequency in the seismoacoustic wave is 6–8 Hz, which corresponds to a wavelength of 40–50 m at a velocity of 330 m/s for the inducing acoustic wave. The separation between sensors is 200 m; i.e., 4–5 wavelengths fit in between them. As a result, an ambiguity of an integer number of periods arises in determining the phase difference between sensors and, therefore, an ambiguity in the determination of the phase velocity. Therefore, for the determination of the phase and group velocities of a seismoacoustic wave, the seismogram envelopes of oscillation trains were analyzed. Figure 4 shows the plots of the envelopes and the envelopes squared of the seismograms for the *Z* component for five sensors of the array located at p. Mayak at a distance of 28.5 km.

For determining the phase velocity, time points of local maxima were found on the amplitude plots for each sensor. With these points, line hodographs were constructed. The phase velocity determined from the hodograph for a seismoacoustic wave is 327–334 m/s.

In order to determine the group velocity, time points of maxima were found on the plots of amplitude squared (energy) for each sensor. A plot of energy for every seismogram has one pronounced maximum. The points for this maximum fall on the line hodograph. Determined from this hodograph, the group velocity of a seismoacoustic wave is 260–275 m/s.

The difference between phase and group velocities in a seismoacoustic wave means the presence of dispersion, as well as that the process of acoustoseismic induction has a two-wave character. An arriving acous-

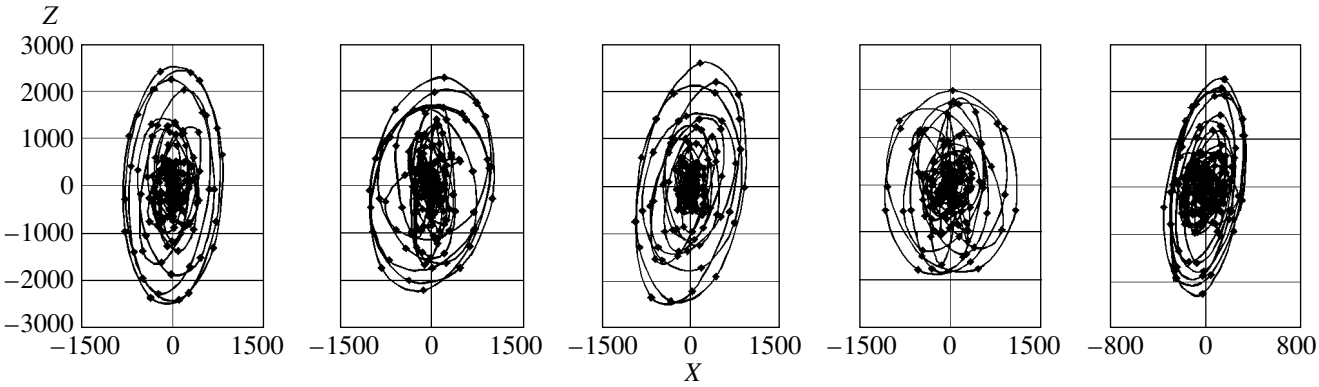


**Fig. 3.** Polarization curves of seismoacoustic waves in the *ZX* plane at a distance of 28.5 km from the vibrator for five three-component seismometers of the seismic array.

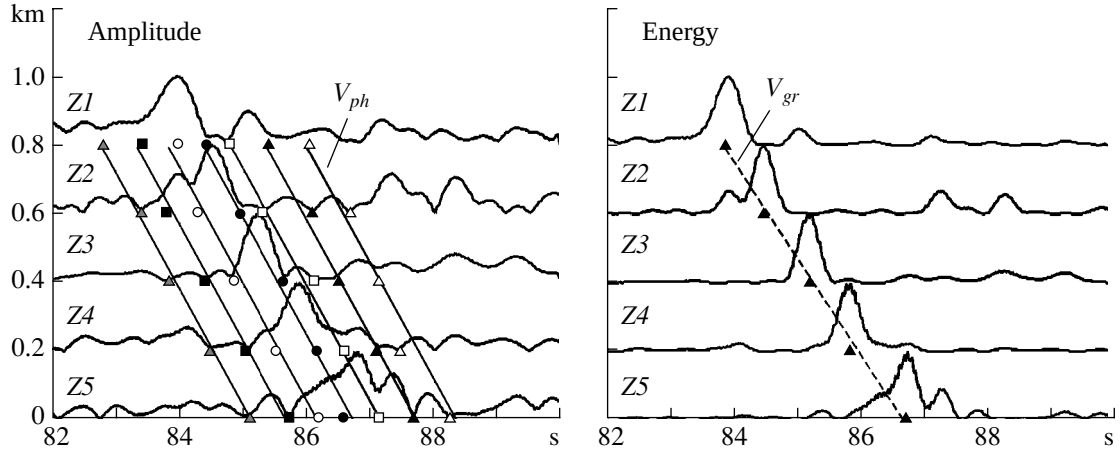


**Fig. 4.** Envelopes (left) and envelopes squared (right) of the seismograms for the *Z* component of five seismometers at a distance of 28.5 km from the vibrator.

tic wave travels along the surface with the velocity of sound in air, i.e., at about 330 m/s (or somewhat greater with a favorable wind). It induces a surface seismic wave of an elliptic polarization (of the Rayleigh wave type), in which the phase characteristics of the oscillation train propagate with the sound velocity while the transfer of the train energy occurs with the velocity of the Rayleigh wave. The latter is determined by the elastic properties of the ground in the upper part of the section.

Similar calculations of phase and group velocities of a seismoacoustic wave were performed for p. Stepnoi (at a distance of 31.1 km). Determined on line hodographs, the phase and group velocities along the array are 437–451 and 317–333 m/s, respectively.

When the directions of the sound wave and the seismic array coincide, the phase velocity of waves at the array coincides with the sound velocity in air, and the group velocity, with the Raylegth wave velocity in the ground. When the directions of the array and the sound wave do not coincide, the phase and group velocities at the array will be inversely proportional to the cosine of the angle between these directions; i.e., it will be higher. Therefore, from the data on the phase and group velocities along the array at p. Stepnoi and the known azimuth of the vibrator, one can determine the velocity of sound and of the Rayleigh wave:

$$c = V_{ph}\cos(\alpha); \quad V_R = V_{gr}\cos(\alpha), \qquad (1)$$

where $V_{ph}$ and $V_{gr}$ are the phase and group velocities along the array, $c$ and $V_R$ are the velocity of sound in air and the Rayleigh wave velocity in the ground, and $\alpha$ is the angle between the direction of the array and the source azimuth.

For the above values of the phase and group velocities at p. Stepnoi, the sound velocity and the Rayleigh wave velocity computed from Eqs. (1) are 345–356 and 250–262 m/s, respectively. For p. Mayak, the sound velocity and the Rayleigh wave velocity almost coincide with the values of the phase and group velocities, respectively, since $\cos(8°) = 0.99$.

**Table 1.** Velocity characteristics of seismoacoustic waves

| $L$, km | $V_{sa}$, m/s | $V_{ph}$, m/s | $V_{gr}$, m/s | $c$, m/s | $V_R$, m/s |
|---|---|---|---|---|---|
| Kamenka, 20 | 339–348 | – | 261–282 | – | 261–282 |
| Mayak, 28.5 | 339–344 | 327–334 | 260–275 | 327–334 | 260–275 |
| Stepnoi, 31.1 | 338–342 | 437–451 | 317–333 | 345–356 | 250–262 |

The data on the velocities charactering the process of acoustoseismic induction and the characteristics of seismoacoustic waves are given in Table 1. The latter also gives the computed velocity of the arriving acoustic wave $V_{sa}$ determined from the distance of the recording point from the vibrator and the travel time of the seismoacoustic wave.

From Table 1, one can see that the data obtained at distances of 20–30 km from the vibrator have much in common. Namely, the velocity of the arriving sound wave that was determined from the travel time of the seismoacoustic wave is equal to or somewhat higher than the sound velocity in air, which is explained by the presence of the wind. The sound velocity at the point of recording correlates with the sound wave velocity along the propagation track: in the absence of the wind, it is equal to the sound velocity (p. Mayak), and in the presence of the wind (p. Stepnoi), it is higher by 5–10 m/s. The fact that the velocity of the arriving acoustic wave is close to the sound velocity points to the near-surface character of its propagation. If this wave propagated with refraction far from the surface, its arrival time would be greater because of the increased path length and decreasing sound velocity due to the decrease in temperature with height. As a result, the velocity of the arriving acoustic wave would be lower.

The values of phase and group velocities at the array depend on the array orientation with respect to the direction of the sound wave propagation (Table 1). The velocity of the surface Rayleigh waves at all three points of recording are close to 250–280 m/s. This is explained by the fact that the region with a radius of 20–40 km from the Bystrov test site has the same geological structure and velocity characteristics in the upper part of the section. In particular, for the grounds of the upper part of the section with the velocity of longitudinal waves $V_p$ =400–500 m/s, the velocity of the surface Rayleigh waves is within $V_s$ = 220–270 m/s, which agrees well with experimental results.

In addition to the very fact of recording seismoacoustic waves at long distances from the vibrator, the result of major interest is the detection of the two-wave character of the acoustoseismic induction process. This result agrees well with the physical concept of this process, i.e., the manifestation of both velocity characteristics of the exciting acoustic wave (the sound velocity in air) and the specific velocity of free surface waves in the ground (the velocity of the Rayleigh wave) in the induced surface wave. The difference between the phase and group velocities points to the nonlinear dispersion law for seismoacoustic waves and requires separate theoretical consideration. However, the basic features of the process of excitation and propagation of the acoustoseismic wave field generated by a vibrator can be obtained from the results of mathematical modeling with rather simple models.

## RESULTS OF MATHEMATICAL MODELING

In studying the acoustoseismic fields generated by high-power seismic vibrators, one can single out three interconnected processes: (i) the process of radiation of acoustic waves by a vibration source operating on the free surface, (ii) the process of long-range acoustic wave propagation from the vibration source along the surface, and (iii) the process of exciting surface seismic waves by a harmonic acoustic wave arriving at the point of recording.

### *Acoustic Wave Radiation by a Vibrator in the Presence of a Near-Surface Low-Velocity Layer*

The mathematical modeling of the processes of infrasonic wave radiation into the atmosphere by operating vibration sources is the subject of a series of works [8–10]. As a model, two homogeneous media are considered: an elastic medium and a gaseous medium contacting along a plane interface. For the elastic half-space, dynamic equations of elasticity with constant parameters (density and longitudinal and transverse wave velocities) are solved, while for the gaseous medium, the wave equation is solved with constant density and sound velocity. The boundary conditions are the equality of normal components of stresses and sound velocities at the interface between the two media. As a source, a harmonic point force is considered, which acts along the normal to the interface of two media. In [8], asymptotics were found for the acoustic and seismic bulk waves in the far zone and the corresponding radiation powers. The solution is given in the form of integral representations, which, for some relationships between the parameters of the media, allows the analytical representation

$$W_a = 3.16\frac{\rho}{\rho_1}\frac{P^2\omega^2}{\pi\rho_1 V_p^3}; \quad W_s = 0.085\frac{P^2\omega^2}{\pi\rho_1 V_p^3}, \qquad (2)$$

where $W_a$ and $W_s$ are the radiation powers of acoustic and seismic waves; $P$ is the force amplitude; $\omega$ is the frequency; $\rho_1$, $V_p$, $V_s$ are the density and the velocities of the longitudinal and transverse waves in the elastic half-space; and $\rho$ is the density of air.

Formulas (2) are valid for the following velocity relationships: $V_p = \sqrt{3}\ V_s = \sqrt{3}\,c$, where $c$ is the sound velocity in air.

The power ratio of seismic and acoustic waves does not depend on frequency and is $W_a/W_s = 0.0186$; i.e., approximately about 2% of the total radiation power is associated with the acoustic waves. Assuming that the parameters of the problem include the vibration source with the force amplitude $P = 100$ t, the density and the sound velocity in gas $\rho = 1.2$ kg/m$^3$ and $c = 340$ m/s, the density and the velocity of longitudinal waves in the ground $\rho_1 = 2000$ kg/m$^3$ and $V_p = 588$ m/s, we obtain $W_s = 94$ W and $W_a = 2.1$ W at a frequency of 6 Hz and $W_s = 261$ W and $W_a = 5.8$ W at a frequency of 10 Hz.

The directional pattern of the acoustic radiation from the vibration source changes noticeably when a near-surface low-velocity air layer appears in the atmosphere due to the temperature inversion or when a layer of cold air with a lower sound velocity appears near the surface. Let us consider the formation of the directional pattern of a point source located near the surface in the ray approximation.

Let a gaseous medium with a low-velocity layer $0 < z < h$ of thickness $h$ with a sound velocity $c_1$ be formed above the elastic half-space $z < 0$ in the cylindrical coordinate system $r$, $\phi$, $z$. A half-space with the sound velocity $c_2$ lies above this layer, and the gas density in the whole gaseous medium is the same $\rho$ (Fig. 5). A point source is located at the point $z = r = 0$.

In the ray approximation, the wave field consists of rays launched from the source and rays refracted and reflected at the boundaries of media. It is known that, in the presence of a low-velocity layer, there exists a limiting angle of reflection and that all rays with grazing angles smaller than this angle undergo total internal reflection in the layer. The value of this angle is determined by Snell's law and depends on the ratio of velocities $c_1$ and $c_2$. The acoustic field at long distances from the source is formed by the waves with grazing angles smaller than the critical one, and they undergo a total internal reflection in the layer. The transmitted waves are inhomogeneous with a real wave vector in the radial direction and an exponential decay along the $z$ axis. The part of the acoustic energy falling into the waveguide is determined in the ray approximation by the ratio of the solid angle, in which waves undergo supercritical reflection, to the solid angle of the half-sphere:

$$\frac{W_c}{W_a} = \frac{h}{R_0} = \sin(\alpha) \approx \sqrt{\frac{2(c_2 - c_1)}{c_2}}, \qquad (3)$$

where $W_a$ and $W_c$ are the total power of acoustic radiation and the power trapped by the waveguide, $R_0$ is the radius from the origin of coordinates to the point of tangency where the wave has the critical angle of reflection from the upper boundary of the layer, $h$ is the thickness of the low-velocity layer, and $c_1$ and $c_2$ are the velocities of sound waves in the layer and the half-space, respectively.

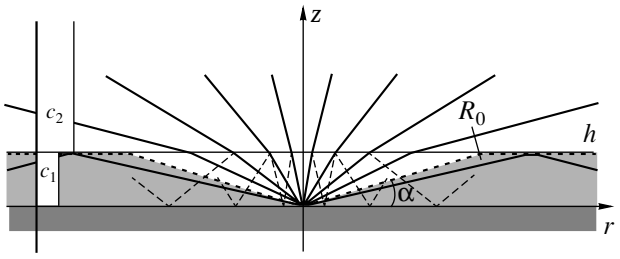


**Fig. 5.** Schematic diagram of calculating the energy of acoustic field in the near-surface layer.

As seen from Eq. (3), the value of the wave energy in the layer does not depend on its thickness and is determined only by the ratio of the sound velocities.

In spite of the fact that the coefficient in Eq. (3) is small for small sound velocity differences, the presence of the waveguide affects the acoustic wave amplitudes at long distances from the source. Comparing the acoustic wave amplitude at the distance $R$ in the half-space without the waveguide and that with the waveguide, with allowance for the cylindrical symmetry of the channel, we obtain

$$W_a = A_0^2(R)2\pi R^2, \quad W_c = A_c^2(R)2\pi Rh,$$
$$\frac{A_c^2(R)}{A_0^2(R)} = \sqrt{\frac{2(c_2 - c_1)}{c_2}}\frac{R}{h}, \qquad (4)$$

where $A_0$ is the amplitude of the acoustic wave at the distance $R$ in the half-space and $A_c$ is the amplitude of the wave in the waveguide at the same distance $R$.

Table 2 presents the numerical values of the velocities, the ratio of powers, and the ratio of amplitudes at a distance of 30 km from the source for two temperature differences in the layer, 5 and 10°C, and for three values of the layer thickness, 25, 50, and 100 m. The temperature coefficient of the sound velocity in air is 0.59 m/s deg, and the sound velocity is 331 m/s at 0°C.

As seen from Table 2, for the temperature difference of 5–10°C, the limiting angle of reflection is 8–11 deg and the waveguide can trap from 13 to 20% of the acoustic power. This is a considerable value if we take into account that this power remains in the waveguide. As follows from the geometry of the problem and Eqs. (3), the value of the acoustic power in the layer does not depend on the layer thickness but is determined by the velocity (or temperature) difference. It should be noted that the amplitude ratio at the point of recording with (or without) the waveguide has greater values for smaller layer thickness. This is explained by

**Table 2.** Power and amplitude ratios for the acoustic wave at a distance of 30 km from the source

| $\Delta T$, °C | $c_1$, m/s | $c_2$, m/s | $h$, m | $\alpha$ | $W_c/W_0$ | $R_0$, m | $R$, km | $A_c/A_0$ |
|---|---|---|---|---|---|---|---|---|
| 5 | 331 | 334 | 10 | 7.8 | 0.13 | 75 | 30 | 19.9 |
| 5 | 331 | 334 | 25 | 7.8 | 0.13 | 188 | 30 | 12.6 |
| 5 | 331 | 334 | 50 | 7.8 | 0.13 | 376 | 30 | 8.9 |
| 5 | 331 | 334 | 100 | 7.8 | 0.13 | 752 | 30 | 6.3 |
| 10 | 331 | 337 | 10 | 11 | 0.19 | 53 | 30 | 23.6 |
| 10 | 331 | 337 | 25 | 11 | 0.19 | 133 | 30 | 14.9 |
| 10 | 331 | 337 | 50 | 11 | 0.19 | 267 | 30 | 10.5 |
| 10 | 331 | 337 | 100 | 11 | 0.19 | 534 | 30 | 7.4 |

the fact that, the smaller the layer thickness, the smaller the distance to the point of the waveguide formation ($R_0$) is and the smaller the distance at which the law of amplitude decay corresponding to cylindrical geometry of the waveguide $\frac{1}{\sqrt{R}}$ begins to work instead of $\frac{1}{R}$ for the spherical geometry without the waveguide. This explains a fact known from acoustics: the rapid formation of a near-surface waveguide when only a slight cooling occurs near the surface. The same is true for the experiments with vibrators.

### *Propagation of Acoustic Waves in the Near-Surface Waveguide*

The long-range propagation of acoustic waves from a vibrator is related to the presence of waves that retain their energy in the waveguide without radiation into the overlying half-space. The modeling is simplified by the fact that, at long distances from the source, the spherical wave field is locally plane and permits a two-dimensional modeling.

Let us consider the two-dimensional problem for the above model of a gaseous half-space with a low-velocity layer overlying a rigid half-space. The gaseous medium occupies the upper half-space $0 < z$ and contains a low-velocity layer $0 < z < h$ of thickness $h$. The sound velocity in the layer is $c_1$, in the half-space above the layer, $c_2$; the gas density in both the layer and the half-space is $\rho$.

The wave equations for the pressure in the layer and the half-space and the relation between the velocities and pressures have the form

$$\begin{aligned} &\frac{1}{c_1^2}\frac{\partial^2 p_1}{\partial t^2} - \Delta p_1 = 0; \quad \rho\frac{\partial \mathbf{u}_1}{\partial t} + \nabla p_1 = 0 \\ &\frac{1}{c_2^2}\frac{\partial^2 p_2}{\partial t^2} - \Delta p_2 = 0; \quad \rho\frac{\partial \mathbf{u}_2}{\partial t} + \nabla p_2 = 0, \end{aligned} \tag{5}$$

where $p_1(z, x, t)$ and $p_2(z, x, t)$ are the pressures in the layer and the half-space and $\mathbf{u}_1(x, y, z)$ and $\mathbf{u}_2(x, y, z)$ are the vectors of the velocities in the layer and the half-space, respectively.

The boundary conditions are as follows: at the boundary with the rigid half-space, the zero value of the normal component of the velocity, and at the boundary between the layer and the upper half-space, the equality of the pressures and the normal velocity components in the first and second media:

$$\begin{aligned} u_{z1}(z, x, t)\big|_{z=0} &= 0 \\ u_{z1}(z, x, t)\big|_{z=h} &= u_{z2}(z, x, t)\big|_{z=h} \\ p_1(z, x, t)\big|_{z=h} &= p_2(z, x, t)\big|_{z=h}, \end{aligned} \tag{6}$$

where $u_{z1}(z, x, t)$ and $u_{z2}(z, x, t)$ are the vertical components of the velocity vectors.

The solution can be represented as the superposition of plane homogeneous waves in the layer with real wave vectors and an inhomogeneous wave in the upper half-space with a real wave vector directed along the $x$ axis and an exponential amplitude decay along the $z$ axis:

$$\begin{aligned} p_1(z, x, t) &= \exp(i\omega t - ikx) \\ &\times (a_1\exp(-ik_1 z) + a_2\exp(-ik_1 z)); \\ p_1(z, x, t) &= b_1\exp(i\omega t - ikx)\exp(-\alpha z), \end{aligned} \tag{7}$$

where $a_1$ and $a_2$ are the amplitudes of plane waves in the layer, $b_1$ is the wave amplitude in the half-space $h < z$, $\omega$ is the frequency, $k$ is the projection of the wave vector on the $x$ axis, $k_1$ is the projection of the wave vector on the $z$ axis, and $\alpha$ is the attenuation coefficient along the $z$ axis in the upper half-space.

From wave equations (5) with allowance for boundary conditions (6) and the form of the solution, we obtain the relation between the wave vectors and the

**Table 3.** Numerical values of the wave numbers and attenuation coefficients for the half-space and the layer

| $\Delta T$, °C | $c_1$, m/s | $c_2$, m/s | $h$, m | $f$, Hz | $k$, 1/m | $k_1$, 1/m | $\alpha$, 1/m | $2\pi/k$, m | $2\pi/k_1$, m | $1/a$, m |
|---|---|---|---|---|---|---|---|---|---|---|
| 5 | 331 | 334 | 10 | 6 | 0.113 | 0.015 | 0.002 | 55.1 | 417 | 441 |
| 5 | 331 | 334 | 25 | 6 | 0.113 | 0.014 | 0.005 | 55.1 | 440 | 188 |
| 5 | 331 | 334 | 50 | 6 | 0.113 | 0.012 | 0.008 | 55.1 | 506 | 113 |
| 5 | 331 | 334 | 100 | 6 | 0.113 | 0.009 | 0.012 | 55.1 | 681 | 82 |
| 10 | 331 | 337 | 10 | 6 | 0.113 | 0.021 | 0.004 | 55.1 | 300 | 225 |
| 10 | 331 | 337 | 25 | 6 | 0.113 | 0.019 | 0.009 | 55.1 | 330 | 102 |
| 10 | 331 | 337 | 50 | 6 | 0.113 | 0.015 | 0.014 | 55.1 | 408 | 67 |
| 10 | 331 | 337 | 100 | 6 | 0.113 | 0.01 | 0.018 | 55.1 | 595 | 53 |

frequency, i.e., the dispersion equations characteristic of the waveguides:

$$\frac{\omega^2}{c_1^2} = k^2 + k_1^2; \quad \frac{\omega^2}{c_2^2} = k^2 - \alpha^2;$$
$$\frac{k_1}{\sqrt{\dfrac{\omega^2(c_2^2 - c_1^2)}{c_1^2 c_2^2} - k_1^2}} = \cot(k_1 h). \tag{8}$$

The relationships of the wave amplitudes in the layer and the half-space are given by the expressions

$$a_1 = a_2;$$
$$a_1 e^{-ik_1 h} + a_2 e^{ik_1 h} = b_1 e^{-\alpha h}; \tag{9}$$
$$\frac{k_1}{\rho\omega}(a_1 e^{-ik_1 h} - a_2 e^{ik_1 h}) = b_1 \frac{\alpha}{i\rho\omega} e^{-\alpha h}.$$

Equation (8) can be solved numerically. The results of calculations with the layer parameters taken from Table 2 and at a frequency of 6 Hz are given in Table 3.

As follows from Table 3, for small velocity differences, an almost plane wave is formed in the layer. The values of the wave number $k_1$ and the attenuation coefficient $\alpha$ are close one another and much smaller than the horizontal wave number $k$. The corresponding wavelengths and typical dimensions also differ widely. On the whole, the following tendencies are observed: the greater the velocity difference between the layer and the half-space and the greater the layer thickness, the smaller the penetration of the inhomogeneous wave into the half-space (i.e., the parameter $1/\alpha$). Quantitative estimates show that, at temperature differences of 5–10°C, the energy of the acoustic field is concentrated in the region within 100–200 m above the earth surface, in the low-velocity layer and in the half-space near the layer boundary. The maximum energy density is concentrated in the low-velocity layer, and the maximum pressure amplitude of the acoustic wave is reached near the lower boundary of the layer, at the surface of the elastic half-space.

*The Process of the Excitation of Seismoacoustic Waves*

According to solution (7), in the low-velocity layer, an almost plane wave propagates with a velocity close to the sound velocity in air. The effect of the sound wave propagating in the layer on the underlying elastic half-space consists in that pressure wave (7) travels along the interface $z = 0$ and induces a strain wave. The problem of generating a surface seismic wave in the elastic half-space by the acoustic wave propagating in air can be considered using the model of an elastic half-space with a free boundary at which normal stress is given in the form of a traveling wave [11].

Consider the plane problem for a homogeneous isotropic elastic half-space $z > 0$ with parameters $\lambda$, $\mu$ and $\rho$. The acoustic wave propagating along the boundary in the direction of the $x$ axis is taken into account in the boundary conditions for the normal stress at the surface of the elastic half-space (at $z = 0$). It is a harmonic acoustic wave with a constant velocity $c$ equal to the sound velocity in air and with the pressure amplitude $p$ and frequency $\omega$.

It is necessary to solve the Lame equations with the boundary conditions

$$(\lambda + \mu)\mathrm{grad}\,\mathrm{div}u + \mu\Delta u - \rho\frac{\partial^2 u}{\partial t^2} = 0, \tag{10}$$

$$t_{xz}\big|_{z=0} = 0, \quad t_{zz}\big|_{z=0} = p\exp i(\omega t - kx). \tag{11}$$

Here, $k = \omega/c$ is the wave number of the acoustic wave, $c$ is the sound velocity in air, $u$ is the displacement field, and $t_{xz}$ and $t_{zz}$ are the tangential and normal components of the stress tensor.

The solution to problem (10) with boundary conditions (11) can be represented in the form of plane waves. Introducing the notations $\gamma = V_s/V_p$ and $\theta = c/V_s$,

we represent the solution for the displacement field components $u_x$ and $u_z$ in the form

$$u_x = -ikC[(2-\theta^2)e^{-kz\sqrt{1-\gamma^2\theta^2}} - 2\sqrt{1-\theta^2}\sqrt{1-\gamma^2\theta^2}e^{-kz\sqrt{1-\theta^2}}]e^{i(\omega t-kx)}, \quad (12)$$

$$u_z = kC\sqrt{1-\gamma^2\theta^2}[(\theta^2-2)e^{-kz\sqrt{1-\gamma^2\theta^2}}]e^{i(\omega t-kx)},$$

where

$$C = \frac{p}{k^2\rho V_s^2 R(\theta)}, \quad R(\theta) = (2-\theta^2)^2 - 4\sqrt{1-\gamma^2\theta^2}\sqrt{1-\theta^2}. \quad (13)$$

Solution (12) depends on the relative values of the velocities of longitudinal and transverse waves in the ground and the velocity of the acoustic wave. It is possible to single out three regions of parameters that determine different types of solutions.

Region I: $V_p < c$, $1 < \gamma\theta < \theta$. Solution (11) is the superposition of constant-amplitude longitudinal and transverse waves propagating under different angles to the free surface and transferring the energy in the direction of the wave vectors. The polarization of the displacement field at the half-space surface has the form of degenerate ellipses with variable slope:

$$u_x|_{z=0} = Ck[(2-\theta^2) + 2\sqrt{\theta^2-1}\sqrt{\gamma^2\theta^2-1}] \times \sin\omega\left(t-\frac{x}{c}\right), \quad (14)$$

$$u_z|_{z=0} = -Ck\theta^2\sqrt{\gamma^2\theta^2-1}\sin\omega\left(t-\frac{x}{c}\right).$$

Region II: $V_s < c < V_p$, $\gamma\theta < 1 < \theta$. Solution (11) is the superposition two waves: a surface wave, which propagates with the velocity $c$ along the $x$ axis and has an amplitude exponentially decaying with depth, and a transverse wave, which has a constant amplitude and propagates downward under an angle. The polarization of the displacement field at the half-space surface remains elliptic with a variable slope of the ellipse:

$$u_x|_{z=0} = Ck\left[(2-\theta^2)\sin\omega\left(t-\frac{x}{c}\right) - 2\sqrt{\theta^2-1}\sqrt{1-\gamma^2\theta^2}\cos\omega\left(t-\frac{x}{c}\right)\right], \quad (15)$$

$$u_z|_{z=0} = Ck\theta^2\sqrt{1-\gamma^2\theta^2}\cos\omega\left(t-\frac{x}{c}\right).$$

Region III: $0 < c < V_s$, $\gamma\theta < \theta < 1$. The acoustic wave propagates above the half-space in which the velocities of longitudinal and transverse waves are greater than the sound velocity in air. In this case, a surface wave propagating with the velocity of the acoustic wave is induced in the half-space. The displacement field amplitudes exponentially decay with $z > 0$, and the energy flux along the $z$ axis in the region of $z > 0$ is absent. The induced surface wave is elliptically polarized. In this region of parameters, $V_s$ and $V_p$ have the values at which the sound velocity coincides with the velocity of the Rayleigh surface wave. Solution (11) has a singularity at this point, since the Rayleigh function entering into the denominator of the coefficient $C$ is equal to zero. As the parameters of the half-space approach these values, the displacement field amplitude increases infinitely. Physically, this corresponds to the resonance excitation of a surface wave with a constant influx of energy from the acoustic wave:

$$u_x|_{z=0} = Ck[2-\theta^2-2\sqrt{1-\gamma^2\theta^2}\sqrt{1-\theta^2}]\sin\omega\left(t-\frac{x}{c}\right)$$
$$u_z|_{z=0} = Ck\theta^2\sqrt{1-\gamma^2\theta^2}\cos\omega\left(t-\frac{x}{c}\right). \quad (16)$$

This suggests that, when an acoustic wave propagates above the rigid half-space (with high velocities of longitudinal and transverse waves compared to velocity $c$), a surface wave propagating with the sound velocity in air is induced. In the case of a half-space in which the Rayleigh wave velocity is equal to the sound velocity in air, a resonance absorption of the acoustic wave energy takes place and a resonance build-up of amplitude occurs for the surface wave propagating along the $x$ axis. In the case of a pressure-release half-space (with low values of $V_p$ and $V_s$ compared to $c$), both the surface wave and the waves propagating at an angle to the free surface and transporting the energy from the acoustic wave into the half-space are induced.

Figure 6 shows the polarization curves obtained from solution (7) for air with a low-velocity layer near the surface and from solution (12) for the three aforementioned regions with different relative values of the sound velocity in the layer and the velocities of the longitudinal and transverse waves in the elastic half-space. The scale of polarization ellipses in the elastic half-space was increased for clarity. In the low-velocity layer, an almost plane wave propagates with a linear polarization. In the upper half-space, the polarization is also elliptic with a small value of the elliptic $Z$ axis and with an exponential decay along the vertical. In the elastic half-space, the polarization varies from linear (region I) to elliptic (regions II and III). A stationary wave in $X$ direction is observed only in region III. This wave can be considered as a variant of the Stonely wave in the case of the presence of a low-velocity gaseous layer near the boundary of the elastic half-space. In the two other regions, plane waves propagating downward at different angles are present.

In conclusion, we note that the solution to problem (10) with boundary conditions (11) is the superposition of the solutions to an inhomogeneous system of

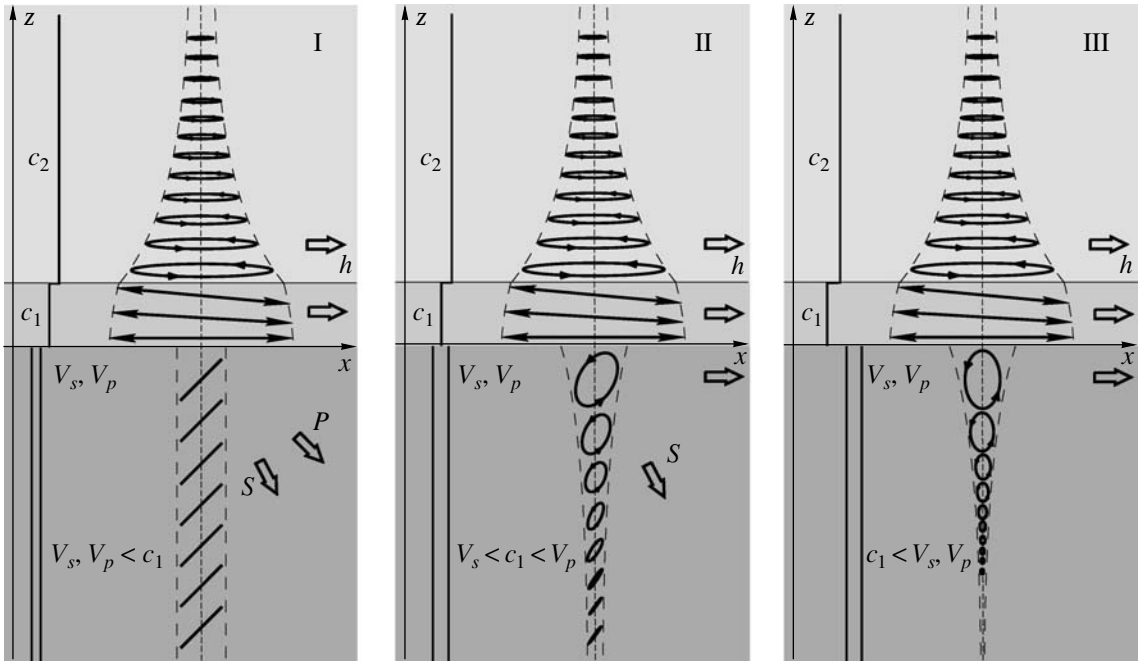


**Fig. 6.** Polarization curves for the acoustic wave propagating in air with a low-velocity layer near the surface and for the surface wave induced in the elastic half-space.

equations with a nonzero right-hand side and a homogeneous system of equations with a zero right-hand side. The solution to the inhomogeneous system is presented above: it describes the induced surface wave that propagates with the velocity of the sound wave $c$ along the surface. As is known, the solution to the homogeneous system of equations is the Rayleigh wave with the velocity $V_R$.

Thus, in the general case, in the characteristics of the seismoacoustic wave generated by the acoustic wave due to the interaction with the elastic half-space, one can expect manifestations of a two-wave process, i.e., the relation of its characteristics to the sound velocity in air $c$ and to the velocity of the Rayleigh wave $V_R$. This result of modeling is confirmed by experiments recording the surface waves induced by the acoustic radiation of a vibrator, the data of which are presented above.

## ACKNOWLEDGMENTS

This work was supported by the Russian Foundation for Basic Research, project no. 03-05-64177.

## REFERENCES

1. I. N. Gupta and R. A. Hartenberger, Bull. Seismol. Soc. Am. **71** (6), 1731 (1981).
2. I. I. Gurvich, *Seismic Prospecting* (Nedra, Moscow, 1970) [in Russian].
3. Yu. M. Zaslavskiĭ, Izv. Akad. Nauk SSSR, Fiz. Zemli, No. 9, 86 (1982).
4. A. V. Razin, Fiz. Zemli, No. 2, 73 (1993).
5. A. S. Alekseev, B. M. Glinskiĭ, V. V. Kovalevskiĭ, *et al.*, *Trudy Vychisl. Tsentr Sibir. Otdel. Ross. Akad. Nauk, Mat. Model. Geofiz.* (VTs SO RAN, Novosibirsk, 1994), pp. 3–11.
6. A. S. Alekseev, B. M. Glinskiĭ, V. V. Kovalevskiĭ, *et al.*, Dokl. Akad. Nauk **346** (5), 664 (1996).
7. B. M. Glinskiĭ, V. V. Kovalevskiĭ, and M. S. Khaĭretdinov, Geol. Geofiz. **40** (3), 431 (1999).
8. Yu. M. Zaslavskiĭ, Izv. Akad. Nauk SSSR, Fiz. Zemli, No. 9, 86 (1982).
9. A. V. Razin, Izv. Akad. Nauk SSSR, Fiz. Zemli, No. 12, 100 (1991).
10. Yu. M. Zaslavskiĭ, Akust. Zh. **49**, 626 (2003) [Acoust. Phys. **49**, 529 (2003)].
11. V. V. Kovalevskiĭ, *Trudy Vychisl. Tsentr Sibir. Otdel. Ross. Akad. Nauk, Mat. Model. Geofiz.* (VTs SO RAN, Novosibirsk, 1994), pp. 12–18.

*Translated by Yu. Lysanov*

*Acoustical Physics, Vol. 51, Suppl. 1, 2005, pp. S88–S101. Translated from Akusticheskiĭ Zhurnal, Vol. 51, Suppl., 2005, pp. 103–117.*


# Nonlinear Acoustic Spectroscopy of Local Defects in Geomaterials

**A. V. Lebedev, L. A. Ostrovskiĭ, and A. M. Sutin**

*Applied Physics Institute, Russian Academy of Sciences, ul. Ul'yanova 46, Nizhni Novgorod, 603950 Russia*

*e-mail: swan@hydro.appl.sci-nnov.ru*

Received September 15, 2004

**Abstract**—General approaches to solving the problem of nonlinear acoustic spectroscopy of defects in geomaterials are considered. Expressions that relate the nonlinear response (scattering at combination frequencies) to the position, orientation, and nonlinear characteristics of narrow cracks are obtained. The expressions describe a broad class of nonlinear interactions at a crack. The nonlinearity caused by the contact of uneven rough edges of a crack is analyzed in detail. The results of the analysis are compared with the results obtained earlier from considering micromechanical models and with experimental data. The satisfactory agreement between the theoretical and experimental values of Landau's moduli suggests that the mechanism of contact nonlinearity may manifest itself in the process of fracture of polycrystalline rock, when narrow cracks with uneven edges are formed. Numerical examples demonstrate the possibility of determining the orientation and position of a narrow crack. The procedure of solving the problem of crack localization is illustrated by the example of a crack in a thin rod. The importance of taking into account the phase data in the determination of the crack coordinate is pointed out. © *2005 Pleiades Publishing, Inc.*

## INTRODUCTION

Today, the nonlinear diagnostics of defects in materials and structures is the subject of numerous publications (for example [1, 2]). In comparison with homogeneous solids (metals, glass, and crystal bodies), structurally inhomogeneous geomaterials (rocks) differ by the high level of nonlinearity and a vast variety of nonlinear effects [1]. It was demonstrated that nonlinear effects, such as harmonic generation and intermodulation, can be more sensitive to the presence of potentially dangerous defects like cracks than the changes in the linear parameters of a system, for example, the velocities of wave propagation, $Q$ factors of oscillations, etc. As a rule, experiments are directed at the demonstration of the feasibility of defect detection without determining its size and location within a sample. Basically, to localize a defect, methods analogous to those used in the problems of pulsed ranging and acoustic tomography can be applied [3–5]. For example, in [6, 7], the position of a crack with large wave dimensions was determined by measuring the linear backscattering at different location angles [6] or the scattering at a combination frequency [7]. In the latter case, it was possible to separate the scattering by a linear inclusion and by a crack.

Evidently, nonlinear effects manifest themselves to the greatest extent with increasing strain amplitudes. The strain amplitude reaches its peak at the natural frequencies of a sample, which correspond to the resonances of vibration modes. In this paper, we consider the general approach to solving the problem of nonlinear mode spectroscopy. We assume that nonlinear distortions and mode interaction occur at the inclusions of the crack type and that the elastic matrix itself represents a linear elastic body (below, we explain why this assumption is justified). In this case, nonlinear effects should be considered as the effects caused by processes of nonlinear scattering of elastic waves by inclusions. It is possible to calculate the scattering field by considering it as a field generated by the reaction forces. The amplitudes of these forces must satisfy the solution to a self-consistent problem with corresponding boundary conditions [8, 9]. The vibration response of a finite-size body to the forces applied to it can be calculated using the Green function formalism for the region external with respect to the inclusion [10, 11]. It is important in this case that nonlinear distortions be absent in this region and the matrix be considered as a linear elastic solid (see the above assumption). Therefore, in the case of a known Green function, the determination of linear and nonlinear scattering needs the determination of the secondary force producing this scattering field. The Green function itself, in the general case, can be represented in the form of a series in the mode contributions (see [10], Chapter 13), which are determined from the solution to the linear problem of acoustic spectroscopy [12, 13].

In the problems of fracture mechanics, the division of a solid volume containing a crack into three regions is used [14] (Fig. 1). The stress in the zone of the process is nonlinear and determined by the adhesion

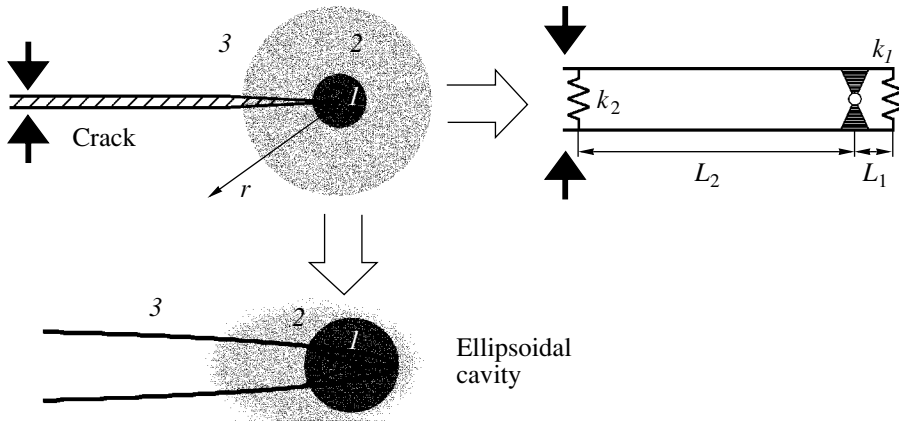


**Fig. 1.** Separation of the region near the crack tips into three subregions (see also [14], Fig. 4). Region *1* corresponds to the process region or the adhesion region. Region *2* is the universal region of elasticity. Region *3* is the external region of elastic deformations. At the left, the equivalent spring–lever model is shown (see explanations in the text). The elliptical geometry provides a correct description of the strain field in regions *2* and *3*. The singularity near the crack tips (region *1*) is restricted by the presence of a "beak" (the Khristianovich hypothesis [16]).

forces, which can be of various origins [15, 16]. The dimensions of this zone can be estimated by the spatial scale within which the stress exceeds the elasticity threshold in the surrounding matrix and a microplasticity is observed (see [14], p. 10). The term "universal region of elasticity" means that the variation of stress has a universal character and is inversely proportional to the square root of the distance to the process region, which is the source of deformations (Fig. 1). The value of singularity depends on the character of the crack load, symmetry, etc. [15, 16], analogously to the distribution of the stress field in the vicinity of the points of dislocation fixation (see [11], Chapter 4).

Thus, the concentration of stress near a crack tip is local and provides an opportunity to consider a solid in region *3* (Fig. 1) as a linear elastic body obeying Hooke's law. The growth of stress near the crack tip can be described quantitatively if the crack is changed for an elliptical hole in the solid. Inglis was the first to indicate this opportunity (see [14], Sections 2 and 3). The ratio of the stress peak to the stress at infinity (applied to a crack) is equal to the ratio of the ellipse semiaxes. Therefore, the well-known property of a crack as a concentrator of stress [14, 15] is described mathematically within the framework of the model of an elliptically shaped hole. The stress amplification at the tip of a crack can also be described by a simple lever–spring model that is demonstrated in Fig. 1 at the left. The spring $k_1$ describes the force arising in the case of deformation of the crack tip, and the spring $k_2$ describes the stiffness of the material filling the crack (in the case of a hole, $k_2 = 0$). The ratio $L_2/L_1$ is equal to the ratio of the ellipsoid semiaxes and determines the amplification factor. The difference of the stiffness $k_2$ from zero limits the amplification factor (in the limit $k_2 \longrightarrow \infty$, the deformation of the "crack" tips becomes infinitely small, and the nonlinear effects vanish).

If the wave dimensions of the crack are small and the observation point is in the far wave field of the scatterer, a simplified description is possible. In this case, the crack reaction can be changed (in what sense will be explained below) for the force vector applied to the crack center. After the determination of the value and direction of the vector, it is easy to calculate the perturbations in the elastic matrix, which are generated by the crack, if the Green function is known. The nonlinear properties of the scatterer apparently can be taken into account using the characteristics of the filling (the spring $k_2$).

The paper is organized as follows. In the first section, we consider the general theory of scattering of elastic waves by cracks. The cracks are simulated by oblate ellipsoids. The expressions obtained provide an opportunity to describe a wide class of nonlinear interactions, which is important for describing a complex nonlinear reaction of geomaterials. In the second section, we treat the particular case of a contact nonlinearity that may occur in the contact of rough surfaces resulting from a local fracture of a heterogeneous medium, such as rock. A comparative analysis of the expressions from the first sections and those obtained earlier is presented, and the features of the general character are indicated. A comparison with the measurement data for the third-order elasticity moduli in the Westerly granite allows us to assume the presence of a contact nonlinearity in this type of granite. Further calculations are performed for the parameters of the Westerly granite. In the third section, we consider an example of crack localization in a thin rod and indicate the general principles of solving the problem of defect localization.

## SCATTERING OF ELASTIC WAVES AT NARROW CRACKS

The general structure of the scattering field of a monochromatic wave in the case of an arbitrary geometry of the inclusion can be written in the form of an integral expression [17]:

$$\Delta u_k(\mathbf{x}) = \int_V \Big[\omega^2(\tilde{\rho}-\rho)v_i(\xi)G_{ki}(\mathbf{x}|\boldsymbol{\xi}) - (\tilde{\mathscr{C}}_{ijpq}-\mathscr{C}_{ijpq})\frac{\partial v_p}{\partial \xi_q}\frac{\partial G_{ki}(\mathbf{x}|\boldsymbol{\xi})}{\partial \xi_j}\Big]d\boldsymbol{\xi}, \quad (1)$$

where $\Delta\mathbf{u}(\mathbf{x})$ is the vector of the additional displacement at the point with the coordinate $\mathbf{x}$ because of the scattering by the inclusion concentrated within the volume $V$, $\mathbf{v}(\boldsymbol{\xi})$ is the displacement vector within the inclusion, $\rho$ is the density of the medium, $\mathscr{C}_{ijpq}$ is the elasticity tensor [11], and $G_{ki}(\mathbf{x}|\boldsymbol{\xi})$ is the Green function describing the displacement component $k$ in the case of the force action in the $i$ direction. The quantities marked with tilde correspond to the material parameters of the inclusion. If the inhomogeneity is small, $\mathbf{v}(\boldsymbol{\xi})$ may be changed for the displacement vector in the incident wave (the Born or Rayleigh approximation), which provides an opportunity to obtain closed expressions for the scattered field.

The first term in Eq. (1) determines the dipole scattering caused by the excess or lack of mass in the volume $V$. The second term is associated with the change of the volume $V$, and in the case of a liquid medium it would correspond to monopole (isotropic) scattering. Equation (1) is analogous to Eq. (23.64) in [18], which describes the sound scattering at an elastic inclusion in a liquid. Nonlinear effects manifest themselves more strongly the higher the amplitude of deformation of the volume $V$. Therefore, of most interest is the case of $\tilde{\mathscr{C}}_{ijpq} \ll \mathscr{C}_{ijpq}$. Here, as in the acoustics of liquids [18], the second term in Eq. (1) makes the major contribution to the scattering field.

Various crack models [19] actually differ in the way of representation of $\tilde{\mathscr{C}}_{ijpq}$ through the shear and bulk moduli of the inclusion with allowance for its geometry. Bearing in mind the convenience of representation of integral (1), we use the Eshelby results [20] that were obtained for quasi-static deformations of a crack.

Eshelby suggested trying the solution in the form of sections, lacings, and superpositions of deformations caused by these virtual states. The total strain is represented in [20] in the form of the superposition of the strain transformation tensor $e_{ij}^T$ in the absence of the matrix and the restrictive strain tensor $e_{ij}^C$ determined by the presence of the matrix. The latter quantity is homogeneous inside and outside the ellipsoidal inhomogeneity. Thus, in the presence of exterior strains $e_{ij}^A$ produced by a distant source, the quantity $e_{ij}^A + e_{ij}^C$ describing the total strain is continuous at the passage through the inhomogeneity boundary. The stress inside and outside the inhomogeneity must be balanced, which leads to the condition

$$\lambda_1(e^A+e^C)\delta_{ij} + 2\mu_1(e_{ij}^A+e_{ij}^C) = \lambda(e^A+e^C-e^T)\delta_{ij} + 2\mu(e_{ij}^A+e_{ij}^C-e_{ij}^T), \quad (2)$$

where $e^{A,C,T} = e_{11}^{A,C,T} + e_{22}^{A,C,T} + e_{33}^{A,C,T}$, $\lambda$ and $\mu$ are the Lame coefficients of the matrix, and $\lambda_1$ and $\mu_1$ are the Lame coefficients of the inclusion (they determine the stiffness $k_2$ in Fig. 1).

An advantage of Eshelby's model is the fact that the bulk reaction force $\mathbf{f}$ acting from the inclusion upon the elastic matrix is expressed with the help of the tensor $e_{ij}^T$ according to the expression

$$f_i = \frac{\partial \sigma_{ij}^T}{\partial x_j}, \quad (3)$$

where

$$\sigma_{ik}^T = (\lambda e^T \delta_{ik} + 2\mu e_{ik}^T). \quad (4)$$

Thus, the scattering given by Eq. (1) and determined by the change of the volume is expressed as

$$\Delta u_k(\mathbf{x}) = F_i(\boldsymbol{\xi}_0)G_{ki}(\mathbf{x}|\boldsymbol{\xi}_0), \quad (5)$$

where $F_i(\boldsymbol{\xi}_0) = V_0 f_i(\boldsymbol{\xi}_0)$ is the reaction force and $V_0$ is the volume occupied by the crack. In the case of a circular crack with the radius $r_0$, which is simulated by an oblate ellipsoid with the ratio of semiaxes $\alpha \ll 1$, we have $V_0 = 4\pi r_0^3 \alpha/3$. In Eq. (5), $\boldsymbol{\xi}_0$ corresponds to the crack "center" and the fact that the crack has small wave dimensions is explicitly taken into account.

One can see from Eq. (2) that the expression for stress is inhomogeneous for the internal and external regions. The meaning of this notation is that part of strains ($e_{ij}^T$) for the external region is not related to any stress in the external region and reflects the fact of the presence of the inhomogeneity with a preset geometrical shape. In other words, it is assumed that the processes of fracture results in the violation of continuity of the medium and a cavity is formed, which is stable with respect to infinitely small deformations. The strain $e_{ij}^T$ itself also may be considered as the one needed for restoring the continuity of the medium (the crack collapse). The processes of fracture are, evidently, inelastic in their nature. Therefore, in Hooke's law, the strains in the external medium are $e_{ij}^A + e_{ij}^C - e_{ij}^T$. A more detailed discussion can be found in [20].

The major problem in the procedure of solution [20] lies in searching for the relation between the strains $e_{ij}^C$ and $e_{ij}^T$. Eshelby demonstrated that, in the coordinate

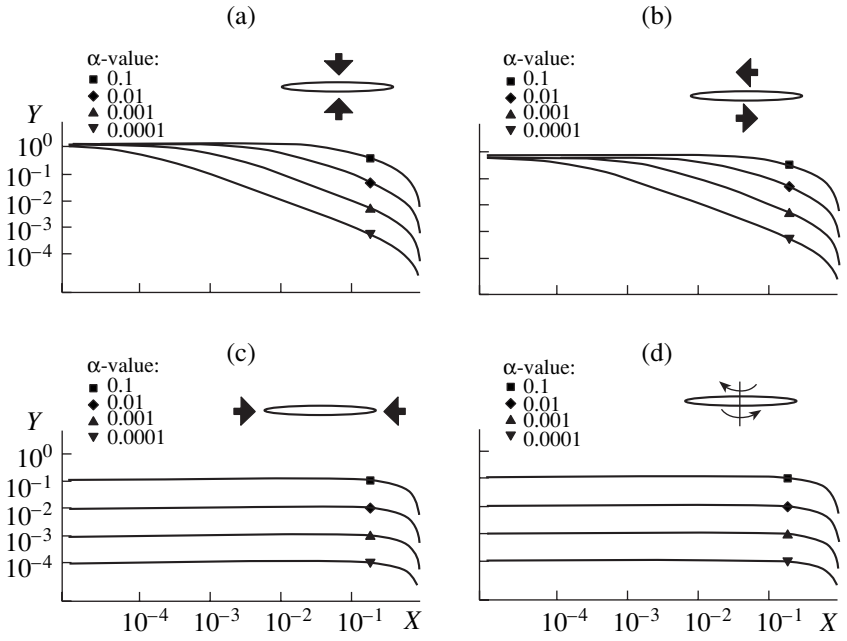


**Fig. 2.** Quantity $Y = \alpha e_{ij}^T / e_{ij}^A$ as a function of $X = \mu_1/\mu = \lambda_1/\lambda$ for different ratios of the ellipsoid semiaxes (specified in the left upper corner for each of the plots). The ordinates show the ratio $\alpha e_{ij}^T / e_{ij}^A$ for $ij$ = (a) 33, (b) 13, (c) 11, and (d) 12. The external forces applied to the crack through $e_{ij}^A$ are schematically indicated for each of the plots. The scattering vanishes at $X = 1$ (the absence of singularities in the elastic moduli).

system connected with an ellipsoidal inhomogeneity, this relation is linear and has the form

$$e_{ij}^C = S_{ijkl} e_{kl}^T, \tag{6}$$

where the nonzero values of the fourth-order tensor $S_{ijkl}$ are elliptical integrals (see [20], Eq. (3.8)) and equal to [19]:

$$S_{11} = S_{22} = QI_{aa} + RI_a, \quad S_{12} = S_{21} = QI_{ab} - RI_a,$$
$$S_{13} = S_{23} = QI_{ac}\alpha^2 - RI_a, \quad S_{31} = S_{32} = QI_{ac} - RI_c,$$
$$S_{33} = Q\left(\frac{4\pi}{3} - 2I_{ac}\alpha^2\right) + I_c R, \tag{7}$$
$$S_{66} = QI_{ab} + RI_a,$$
$$S_{44} = S_{55} = \frac{Q(1+\alpha^2)I_{ac} + R(I_a + I_c)}{2}.$$

In Eq. (7), standard two-index notations are used [11, 19]: $11 \Rightarrow 1$, $22 \Rightarrow 2$, $33 \Rightarrow 3$, $23 \Rightarrow 4$, $31 \Rightarrow 5$, and $12 \Rightarrow 6$. The quantities in Eq. (7) are as follows: $I_a = \frac{2\pi\alpha(\arccos\alpha - \alpha S_a)}{S_a^3}$, $I_c = 4\pi - 2I_a$, $I_{ac} = \frac{I_c - I_a}{3S_a^2}$, $I_{aa} = \pi - 3I_{ac}/4$, $I_{ab} = I_{aa}/3$, $S_a = \sqrt{1-\alpha^2}$, $R = \frac{1-2\nu}{8\pi(1-\nu)}$, $Q = \frac{3R}{1-2\nu}$, and $\nu = \frac{\lambda}{2(\lambda+\mu)}$. The quantity $\alpha$ is the ratio of the semiaxes of an oblate ellipsoid (it is assumed that the section across the smaller semiaxis is a circle). Equations (7) are written down under the assumption that the $x_3$ axis is directed along the normal to the crack simulated by an oblate ellipsoid.

Most interesting is the analysis of very thin cracks with $10^{-4} \le \alpha \le 10^{-2}$, which are formed in the case of brittle fracture [15, 21–23]. In the limit $\alpha \longrightarrow 0$, the nonzero quantities $S_{ij}$ are $S_{33} \simeq 1$, $S_{31} = S_{32} \simeq \frac{\nu}{1-\nu}$, and $S_{44} = S_{55} \simeq \frac{3-2\nu}{4(1-\nu)}$. This means that compression–tension strains across the normal to a narrow crack and torsional strain of such a crack do not play any significant role. One can see this also from Fig. 2, where the relations between the strains $e_{ij}^T$ and $e_{ij}^A$ are shown as functions of $\alpha$ and relative stiffness of filling $\lambda_1/\lambda = \mu_1/\mu$.

Equations (2) with allowance for Eqs. (6) and (7) are solved for $e_{ij}^T$ at preset values of $e_{ij}^A$, $\lambda_1$, $\mu_1$, $\lambda$, and $\mu$. Equations (7) are valid for $0 \le \alpha \le 1$, which makes it possible to study the effect of the crack shape on the linear and nonlinear scattering. The case $\alpha = 1$ corresponds to a spherical inclusion.

A nonlinear response from an inclusion can be treated as a small perturbation of the boundary conditions given by Eqs. (2), if nonlinear distortions are relatively small [24]. Let us assume that the equation of state allows us to determine the functions $\lambda_1(e_{ij})$ and $\mu_1(e_{ij})$, where $e_{ij} = e_{ij}^C + e_{ij}^A$ correspond to linear deformation of a crack (zero approximation). In this case, using the Born approximation for describing the nonlinear distortions, Eq. (2) for perturbations is represented in the form

$$\begin{aligned}&(\lambda(\breve{e}^C - \breve{e}^T) - \lambda_1\breve{e}^C)\delta_{ij}\\ &+ 2(\mu(\breve{e}_{ij}^C - \breve{e}_{ij}^T) - \mu_1\breve{e}_{ij}^C) = c_{ijkl}\times(e_{kl}^C + e_{kl}^A),\end{aligned} \tag{8}$$

where the quantities marked with $(\breve{\cdot})$ correspond to the perturbations caused by nonlinear distortions. The right-hand side of Eq. (8) contains the quantity $e_{kl}^C$ obtained by solving the linear problem. In the general case, the quantities in the tensor $c_{ijkl}$ may depend on both the amplitude and the strain rate (nonlinear hysteresis) [2, 25]. If we restrict ourselves to analyzing the quadratic nonlinearity, the fourth-order tensor $c_{ijkl}$ is a linear form, $c_{ijkl} = c_{ijklmn}\times(e_{mn}^C + e_{mn}^A)$. The examples considered below only refer to the case of quadratic nonlinearity.

The reaction force $\breve{\mathbf{f}}$ responsible for the nonlinear scattering and applied to the elastic matrix is apparently determined by Eq. (3) in the case of changing $\sigma_{ij}^T$ for $\breve{\sigma}_{ij}^T$, where $\breve{\sigma}_{ij}^T = \lambda\breve{e}^T\delta_{ij} + 2\mu e_{ij}^T$. The nonlinear scattering field is determined by Eq. (5) with substitution of $f_i$ for $\breve{f}_i$.

The above expressions are written in the coordinate system connected with the crack. To take into account the crack orientation in the solid, it is necessary to represent these expressions in the coordinate system connected with the solid. To make further analysis more convenient, it is expedient to write down Eqs. (2) and (8) in the matrix forms and use the matrix unitary transformations of rotation.

Let us introduce two auxiliary matrices written down with two-index notations: $\hat{\mathbf{a}}_{ij} = (\lambda_1 - \lambda) + 2(\mu_1 - \mu)\delta_{ij}$, $\hat{\mathbf{b}}_{ij} = \lambda + 2\mu\delta_{ij}$ for $i, j \leqslant 3$ and $\hat{\mathbf{a}}_{ij} = 2(\mu_1 - \mu)\delta_{ij}$, $\hat{\mathbf{b}}_{ij} = 2\mu\delta_{ij}$ for $3 < i, j \leq 6$. Equations (2) and (8) are represented as follows:

$$(\hat{\mathbf{a}}\hat{\mathbf{S}} + \hat{\mathbf{b}})\mathbf{e}^T = -\hat{\mathbf{a}}\mathbf{e}^A, \tag{9}$$

$$(\hat{\mathbf{a}}\hat{\mathbf{S}} + \hat{\mathbf{b}})\breve{\mathbf{e}}^T = -\hat{\mathbf{c}}(\hat{\mathbf{S}}\mathbf{e}^T + \mathbf{e}^A)^2, \tag{10}$$

where the matrix elements $\hat{\mathbf{S}}$ are determined by Eqs. (7) and the elements of the matrix $\hat{\mathbf{c}}$ describe the quadratic nonlinear perturbations in the strain tensor $e_{ij}^T$. The strain tensors are represented as the vectors composed of the quantities $e_{ij}^{T,A}$ written down using standard two-index notations. Multiplying the left- and right-hand sides of Eqs. (9) and (10) by the inverse matrix $(\hat{\mathbf{a}}\hat{\mathbf{S}} + \hat{\mathbf{b}})^{-1}$, we obtain a solution in the form (the inverse matrix exists if the shear modulus $\mu$ in the solid surrounding the defect is nonzero; see the discussion below)

$$\mathbf{e}^T = \hat{\mathbf{T}}_0^{(4)}\mathbf{e}^A, \tag{11}$$

$$\breve{\mathbf{e}}^T = \hat{\mathbf{T}}_0^{(6)}\mathbf{e}^A\hat{\mathbf{T}}_c^{(4)}\mathbf{e}^A, \tag{12}$$

where the fourth- and sixth-order transfer matrices are

$$\hat{\mathbf{T}}_0^{(4)} = -(\hat{\mathbf{a}}\hat{\mathbf{S}} + \hat{\mathbf{b}})^{-1}\hat{\mathbf{a}}, \tag{13}$$

$$\hat{\mathbf{T}}_0^{(6)} = -(\hat{\mathbf{a}}\hat{\mathbf{S}} + \hat{\mathbf{b}})^{-1}\hat{\mathbf{c}}\hat{\mathbf{T}}_c^{(4)}, \tag{14}$$

$$\hat{\mathbf{T}}_c^{(4)} = (\hat{\mathbf{S}}\hat{\mathbf{T}}_0^{(4)} + \hat{\mathbf{I}}), \tag{15}$$

and $\hat{\mathbf{I}} = \mathbf{I}_{ijkl} = \delta_{ij}\delta_{kl}$ represents a unit diagonal matrix. The product of the matrices $\hat{\mathbf{T}}_c^{(4)}\mathbf{e}^A$ determines the strain tensor inside the crack.

Equations (11) and (12) are written down in the coordinate system with the axes coinciding with the principal axes of the ellipsoid. To describe the crack rotation with respect to the global coordinate system connected with the sample, it is necessary to use the unitary transformations of rotation. It seems that the simplest technique is the rotation of the local coordinate system connected with the crack in such way that the direction of the axes coincide with the direction of the axes of the global coordinate system and then, after solving Eqs. (11) and (12), to perform the inverse transformation of rotation. The local coordinates $x_i'$ in Eqs. (2) and (8) depend linearly on the global coordinates, $x_i' = \hat{\mathbf{R}}_{ij}x_j$, where the matrix $\hat{\mathbf{R}}$ describes the unitary transformation of rotation. The rule for the transformation of the stress and strain tensors has the form [19]

$$e_{ij}' = \hat{\mathbf{U}}_{ijkl}e_{kl}, \tag{16}$$

where $\hat{\mathbf{U}}_{ijkl} = \hat{\mathbf{R}}_{ik}\hat{\mathbf{R}}_{jl}$.

Details concerning the transformation of rotation can be found in many books (see [12], p. 41, and [19], p. 14). The transformation of the clockwise rotation of the crack normal about the $x_2$ axis through an angle $\vartheta$ is described by the expression

$$\hat{\mathbf{R}} = \begin{pmatrix}\cos\vartheta & 0 & \sin\vartheta\\ 0 & 1 & 0\\ -\sin\vartheta & 0 & \cos\vartheta\end{pmatrix}. \tag{17}$$

In a more general case, the matrix $\hat{\mathbf{R}}$ is the product of matrices of the form of Eq. (17), which describe rotation in the three Euler angles [26].

Equations (11) and (12) taking into account the transformations of rotation formally remain the same, but the transfer matrices have to be redetermined:

$$\mathbf{e}^T = \hat{\mathbf{T}}^{(4)}\mathbf{e}^A, \tag{18}$$

$$\check{\mathbf{e}}^T = \hat{\mathbf{T}}^{(6)}\mathbf{e}^A\hat{\mathbf{T}}_c^{(4)}\hat{\mathbf{U}}\mathbf{e}^A, \tag{19}$$

where $\hat{\mathbf{T}}^{(4)} = \hat{\mathbf{U}}'\hat{\mathbf{T}}_0^{(4)}\hat{\mathbf{U}}$ and $\hat{\mathbf{T}}^{(6)} = \hat{\mathbf{U}}'\hat{\mathbf{T}}_0^{(6)}\hat{\mathbf{U}}$. By virtue of the unitary property of the transformation of rotation (Eq. (17)), the matrix of the inverse transformation $\hat{\mathbf{U}}'$ is the transposed matrix $\hat{\mathbf{U}}$.

The matrix equations (18) and (19) determine the strains $\mathbf{e}^T$ and $\check{\mathbf{e}}^T$ in the global coordinate system connected with the solid containing the crack. The tensor of external deformations $\mathbf{e}^A$ and its gradients are assumed to be known and preset in the global coordinate system. Taking into account Eq. (4), the quantities $\partial\sigma_{ij}^T/\partial x_j$ are determined by differentiating Eqs. (18) and (19) with respect to the global coordinates $x_j$:

$$\frac{\partial\boldsymbol{\sigma}^T}{\partial x_j} = \hat{\mathbf{b}}\hat{\mathbf{T}}^{(4)}\frac{\partial\mathbf{e}^A}{\partial x_j}, \tag{20}$$

$$\frac{\partial\check{\boldsymbol{\sigma}}^T}{\partial x_j} = \hat{\mathbf{b}}\hat{\mathbf{T}}^{(6)}\left(\frac{\partial\mathbf{e}^A}{\partial x_j}\hat{\mathbf{T}}_c^{(4)}\hat{\mathbf{U}}\mathbf{e}^A + \mathbf{e}^A\hat{\mathbf{T}}_c^{(4)}\hat{\mathbf{U}}\frac{\partial\mathbf{e}^A}{\partial x_j}\right). \tag{21}$$

Equations (20) and (21) determine the vector of bulk reaction force (3) and scattering field (5) with allowance for the position, orientation, and filling characteristics of the inhomogeneity. The transfer matrix $\hat{\mathbf{T}}^{(4)}$ in Eq. (20) may be treated as a *T*-matrix in the general theory of scattering [9]. This means that, in the general case, in describing the scattering by a crack with finite wave dimensions, it is possible to use the procedure proposed above with just the only difference that the transfer matrix must be determined according to [9].

It is necessary to note that the analysis of the limiting case $\mu, \lambda_1, \mu_1 \longrightarrow 0$ is impossible within the framework of the quasi-static solution of Eq. (2), since, in this case, the added stiffness is equal to zero and $e_{ij}^T \longrightarrow \infty$. This singularity arises due to two factors. First, there is the impossibility of a stable existence of the cavity in the absence of shear rigidity of the medium and stiffness of the inhomogeneity. Second, the absence of inertial terms (added mass) at $\mu = \mu_1 = 0$ and $\lambda_1 \longrightarrow 0$ leads to the infinite growth of the oscillation amplitude at a finite value of the acting force (the value of the input impedance of the inhomogeneity relative to the acting force tends to zero). At $\mu > 0$, the inverse matrix $(\hat{\mathbf{a}}\hat{\mathbf{S}} + \hat{\mathbf{b}})^{-1}$ involved in Eqs. (11) and (12) exists and $e_{ij}^T$ is finite.

Figure 2 presents a linear response of the inhomogeneity for important particular cases of deformation. The following values for the Lame coefficients were used for calculation: $\lambda = 14$ GPa and $\mu = 24$ GPa. They correspond to the Westerly granite (see below). The scattered field is proportional to the volume $V_0$ occupied by the inhomogeneity (Eq. (5)). Therefore, the quantities $e_{ij}^T$ given in Fig. 2 were multiplied by $\alpha$ to exclude the dependence on $V_0$ in the case of variation of $\alpha$.

Since the relation is linear (Eq. (11)), the reaction force in the case of a plane wave $e_{ij}^A\exp(-i\omega t + i\mathbf{kr})$ is equal to the value of $e_{ij}^T$ multiplied by the volume $V_0$ and the wave number $k = \omega/c$, where $c$ is the propagation velocity of the wave. Therefore, the reaction force for the strains $e_{33}$, $e_{13}$, and $e_{23}$ has the same order of magnitude as for a spherical cavity of the same radius (Figs. 2a and 2b). One can see that a thin crack almost does not "notice" other types of deformations (Figs. 2c and 2d). This explains the well-known fact of the strong dependence of the elastic properties of solids on the concentration of thin cracks and the appearance of elastic anisotropy in the case of oriented cracks [21, 27, 28]. One can see that the finite value of inhomogeneity stiffness limits $e_{ij}^T/e_{ij}^A$, as well as the parameter $\alpha$.

The values of $e_{ij}^T/e_{ij}^A$ presented in Fig. 2 are multiplied by $\alpha$, and $\alpha \ll 1$ in the case of brittle fracture. Therefore, the strains within the crack may be $1/\alpha \gg 1$ times greater than the strains in the incident wave $e_{ij}^A$. This allows us to assume the existence of a nonlinear response in the case of crack deformation caused by nonzero $e_{33}^A$ and $e_{13}^A = e_{23}^A$. The physical reasons for the appearance of nonlinearity in the process of crack deformation may be different. It can be microplasticity in the process zone, roughness of the contact surface at crack edges, surface tension in the liquid inside the crack, etc. [15]. Without going into the details of these processes, it is possible to develop their phenomenological description by presetting the dependences $\lambda_1(\mathbf{e}, \dot{\mathbf{e}})$ and $\mu_1(\mathbf{e}, \dot{\mathbf{e}})$ and assuming the medium around a crack to be linear. Further, we will consider the nonlinearity arising at the contacts of rough edges of a crack [29]. In this case, the nonlinear response is apparently proportional to the number of contacts. The number of contacts also determines the linear compressibility of the crack and is characterized by the ratios $\lambda_1/\lambda$ and $\mu_1/\mu$. As one can see from Fig. 2, the crack filling reduces the coefficient of strain amplification, which has the order of magnitude of $1/\alpha$ in the absence of filling. Thus, we have two competing mechanisms and, therefore, we

can expect a peak of contact nonlinearity at $\lambda_1/\lambda \sim \alpha$ and $\mu_1/\mu \sim \alpha$.

## CONTACT-TYPE NONLINEARITY

Acoustic nonlinearity at the contacts of rough surfaces was considered in [30], where the case of homogeneous deformations in a thin rod was analyzed, and in [31] for three-dimensional deformations of a general form. If the contact area is much smaller than the area of the crack and the deformations of contacts are linear, it is possible to use Hertz's theory [29]. In this case, a power dependence of stress on strain takes place. Both models [30, 31] have one common disadvantage: the reaction of a crack to a shift is not taken into account. This corresponds to a situation where the crack edges are as if fixed with respect to shear deformations. As a result, both models take into account only bulk deformations of a crack [30, 31]. On the other hand, as one can see from Fig. 2, the shear strains $e_{13}$ and $e_{23}$ are also important.

The classical approach to analyzing the effects of anharmonicity consists in consequently taking into account the terms of the potential energy expansion, which are proportional to the third, fourth, etc., powers of strain [11, 32]. If the material filling the crack is isotropic, the free energy (accurate to cubic terms) is

$$\mathcal{E} = \frac{\lambda_1 e^2}{2} + \mu_1 e_{ij}^2 + \frac{\mathbf{A}}{3} e_{ij} e_{jk} e_{ki} + \mathbf{B} e_{ij}^2 e + \frac{\mathbf{C}}{3} e^3, \quad (22)$$

where **A**, **B**, and **C** are Landau's moduli [11]. It is assumed that the quantities are $\mathbf{A}, \mathbf{B}, \mathbf{C} \gg \lambda, \mu$ and that, in the process of determination of the strain tensor, there is no need in distinguishing the points before and after the deformation (see [11], Sections 1 and 26), $e_{ij} = \frac{1}{2}\left(\frac{\partial u_i}{\partial x_j} + \frac{\partial u_j}{\partial x_i}\right)$. In this case, the "physical nonlinearity" [24] prevails.

Let us write down the right-hand side of Eq. (8) in the form $\breve{\sigma}_{ij} = c_{ijklmn}(e_{kl}^C + e_{kl}^A)(e_{mn}^C + e_{mn}^A)$ and use the thermodynamic relation for the variation of free energy $d\mathcal{E} = \sigma_{ij} de_{ij}$. As the result, we obtain six independent coefficients

$$\begin{cases} c_{111111} = \mathbf{A} + 3\mathbf{B} + \mathbf{C}, \\ c_{111122} = 2\mathbf{B} + 2\mathbf{C}, \\ c_{112233} = 2\mathbf{C}, \\ c_{111313} = \mathbf{A} + \mathbf{B}, \\ c_{112323} = \mathbf{B}, \\ c_{122331} = \mathbf{A}. \end{cases} \quad (23)$$

The coefficients of the form of $c_{111223}$ with an uneven number of identical indices are equal to zero. Other nonzero quantities, $c_{ijklmn}$, can be obtained from the spherical symmetry (the isotropy of the elastic properties of the crack filling) by a cyclic rearrangement of the indices and a substitution of the form of $11 \Leftrightarrow 22$. It is necessary to note that the terms $c_{121212}$, $c_{232323}$, and $c_{131313}$ are equal to zero; i.e., shear strains, as one would expect proceeding from the ideas of symmetry, are not accompanied by quadratic nonlinear distortions. Equation (22) describes a nonlinear interaction between three shear strains ($c_{122331}$), between shift and expansion–compression ($c_{112323}$ and $c_{111313}$), and between the expansion–compression waves. The interaction of the form $12 \Rightarrow 12$ manifests itself in the case of taking into account the terms cubic with respect to the dependence $\sigma_{ij}(e_{mn})$.

To calculate the nonlinear response of a crack, it is necessary to set realistic values for the Landau's moduli **A**, **B**, and **C**. These values can be determined from the theoretical model based on the micromechanics of interaction of small components with a further integration with corresponding distribution functions and from the experiment. The first case needs knowledge of the contact geometry, the distribution function for the shapes of these contacts, and the heights of roughness. Since there is no reliable information on these values, various idealizations are used [30, 31], and the error of the final result is totaled from the errors of all used approximations. Therefore, it is preferable to determine the values of **A**, **B**, and **C** from experimental data. Below, we reproduce some results of [31] to demonstrate how it is possible to obtain a theoretical estimate for the value of **C** and how this value is related to the considerations of the previous section and to experimental data.

The starting point for the analysis in [31] is the assumption on the crack reaction only to the deformations connected with variation of the volume. In this case, the variation of the crack volume is written down as the Taylor series with respect to the stress applied along the normal to the crack ($\alpha \ll 1$), $\Delta V/V_0 = a\sigma_{33} + b\sigma_{33}^2/2 + \ldots$, where $V_0 = 4\pi r_0 \alpha/3$ is the volume occupied by the elliptical inhomogeneity. These strains must be added to the strains of the medium around the crack, $\Delta e_{ij} \simeq (\Delta V/V_0)\delta_{3i}\delta_{3j}$ (Fig. 2a). Ignoring intermediate transformations, we write down an equation for the unperturbed stress $\sigma_{33}$ as a function $e_{33} = e_{33}^{(0)}$ (the term $\propto \Delta e_{33}$ corresponds to linear scattering):

$$a = \frac{4(1-\nu^2)}{3\pi K(1-2\nu)(1+d_0/l)} = \frac{4(1-\nu^2)}{\pi E(1+d_0/l)}, \quad (24)$$

$$b = \frac{64}{27\pi^2 K^2 \alpha}\left(\frac{1-\nu^2}{1-2\nu}\right)^2 \frac{r_0 d_0}{l^2} \frac{1}{(1+d_0/l)^3}, \quad (25)$$

$$\sigma_{33} = (\lambda + 2\mu)e_{33} - \frac{b(\lambda+2\mu)^3}{2} e_{33}^2 = (\lambda + 2\mu)e_{33} - \frac{32K(1-\nu)^5 r_0 x}{\pi^2(1+\nu)(1-2\nu)^2 \alpha l (1+x)^3} e_{33}^2, \quad (26)$$

where $K = \lambda + 2\mu/3$ is the bulk modulus, $E = 3K(1 - 2\nu)$ is the Young modulus, $r_0$ is the crack radius, $l$ is the average height of the inhomogeneity, $d_0$ is the average value of the distance between the crack edges, $d_0 = 4\alpha r_0/3$, and $x = d_0/l$. Exact numerical values in Eq. (25) depend on the shapes of contacting inhomogeneities, the distribution functions, etc. [31]. Therefore, the dependence on the average height of inhomogeneities $l$ and the ratio of semiaxes $\alpha$ are of major interest.

Taking into account Eq. (23) we obtain

$$\mathbf{C} = -\frac{32K(1-\nu)^5 r_0 x}{\pi^2(1+\nu)(1-2\nu)^2\alpha l(1+x)^3}. \qquad (27)$$

One can readily see that the maximum of **C** takes place at $x = 1/2$ [31].

It is interesting to clarify what value of $\lambda_1/\lambda$, $\mu_1/\mu$ (Fig. 2) corresponds to $x = 1/2$. Let us treat the crack filling as a spring with the stiffness $k_2 = \bar{E}\mathcal{S}/(1-\nu^2)d_0$, where $\mathcal{S} = \pi r_0^2$ is the crack area and $\bar{E}$ is the Young modulus corresponding to $\lambda_1$ and $\mu_1$. The inequality $\bar{E} \le E$ is valid, since the area of a real contact for rough surfaces is a small part of $\mathcal{S}$. We use Eq. (24) and write down an expression for $\bar{E}$: $\bar{E}/E = 3\pi\alpha/8 \simeq 1.18\alpha \approx \alpha$. Hence, the maximum at $x = 1/2$ corresponds to balancing the springs $k_1$ and $k_2$ in the lever–spring model shown in Fig 1. The condition $\bar{E}/E \approx \alpha$ also means that the area of real contact is $\alpha \ll 1$ times smaller than the crack area $\mathcal{S}$, since the inhomogeneities apparently have the same elastic parameters as the matrix.

The ratio of the average height of inhomogeneities $l$ to the size of the defect $r_0$ almost does not depend on $r_0$ (scale invariance takes place) [23] and is $10^{-4} \le l/r_0 \le 10^{-2}$. Thin cracks are formed in the case of brittle fracture of crystalline or polycrystalline solids. The Poisson ratio in polycrystalline rocks is $\nu \simeq 0.1$–$0.2$ [33]. Then, Eq. (27) may be additionally simplified ($\nu = 0.15$, $\alpha = 8l/3r_0$, $x = 1/2$):

$$\mathbf{C} \sim -1.5K \times (10^3 - 10^7). \qquad (27')$$

This quantity is noticeably greater than the modulus of **C** for pure metals, alloys, etc., excluding those with structural inhomogeneities (see [34], Table IV, and [35], Table VI, last column). It is interesting to compare the value given by Eq. (27') with the measured data [34], where experimental values for all three Landau's moduli in rock samples were obtained. Among the data given in [34], we choose those corresponding to Westerly granite. The reasons for this choice are as follows.

In the general case, cracks in rocks are oriented chaotically [21, 22]. Therefore, it is difficult to evaluate **A**, **B**, and **C** for a single crack proceeding from the experimental data obtained for an ensemble of cracks. However, Westerly granite has an internal structure formed due to the scaling of biotite [36] and the presence of oriented cracks. This fact allows us to assume that the major part of cracks is oriented in one direction. In this case, the values of the Landau's moduli [34] must be divided by the volume concentration of cracks to obtain the estimates for the moduli **A**, **B**, and **C** for a single crack (see table).

Evaluation of the Landau's moduli for a single crack in Westerly granite. The data are obtained by multiplying **A**, **B**, and **C** (see [34], Table IV) by 100, which corresponds to the volume concentration of cracks equal to 1% [*ibid.*]. The scatter in the values of **C** within the model given in [31] corresponds to the variation of the parameters $\alpha = 10^{-2}$–$10^{-4}$ and $l/r_0 = 10^{-2}$–$10^{-4}$ in the case of brittle fracture of granite

| $K$ (GPa) | $\mu$ (GPa) | **A** (GPa)$\times 10^5$ | **B** (GPa)$\times 10^5$ | **C** (GPa)$\times 10^5$ |
|---|---|---|---|---|
| 29.9 | 23.6 | –14 | –20 | –1.2 |
| Expected value (27′): | | | | $-4.5\times(10^{-1}$–$10^3)$ |

Taking into account the strong dependence of the modulus **C** on $\alpha$ and $l/r_0$ in Eq. (27) and also the significant variations of these parameters [22, 23], we can state that a satisfactory qualitative agreement between the data of [34] and the estimate given by Eq. (27') is observed. Thus, we may assume that the nonlinearity observed in [34] was caused by contact phenomena, and the moduli **A** and **B** describe the effects caused to the shift, which was not taken into account in simple models [30, 31].

There are many possibilities for the separation of the nonlinear response [1, 7, 37–41]. The most effective methods are based on analyzing the combination frequencies [7, 39–41]. We will use the signal of intermodulation to determine the nonlinear scattering at a crack.

The calculation was performed in the following way. It was assumed that two monochromatic plane waves with frequencies $f_1$ and $f_2$ and parallel wave vectors propagate in an infinite solid containing a crack. The wave frequencies were set in such a way that $f_2/f_1 = 1.01$ (the specific value of this ratio in the case of an infinite solid does not matter). Both waves lead to crack deformation. The amplitudes of external strains in both waves were set $e_{ij}^A = 10^{-8}$, which is typical of ultrasonic measurements. The material parameters of the solid corresponded to Westerly granite (table). The relative stiffness of the inclusion was set $\lambda_1/\lambda = \mu_1/\mu = \alpha$, which corresponds to the maximum nonlinear response (Eq. (27)). The bulk reaction force corresponding to linear scattering is determined according to Eqs. (3) and (20) for the frequency $f_1 = 1$ kHz. The bulk reaction force corresponding to nonlinear scattering is determined by Eqs. (3) and (21) for the difference frequency $f_2 - f_1$. The total value of the reaction force is proportional to the volume occupied by the inhomogeneity. Therefore, for definiteness, the crack radius was set to $r_0 = 1$ mm and $\alpha = 10^{-3}$.

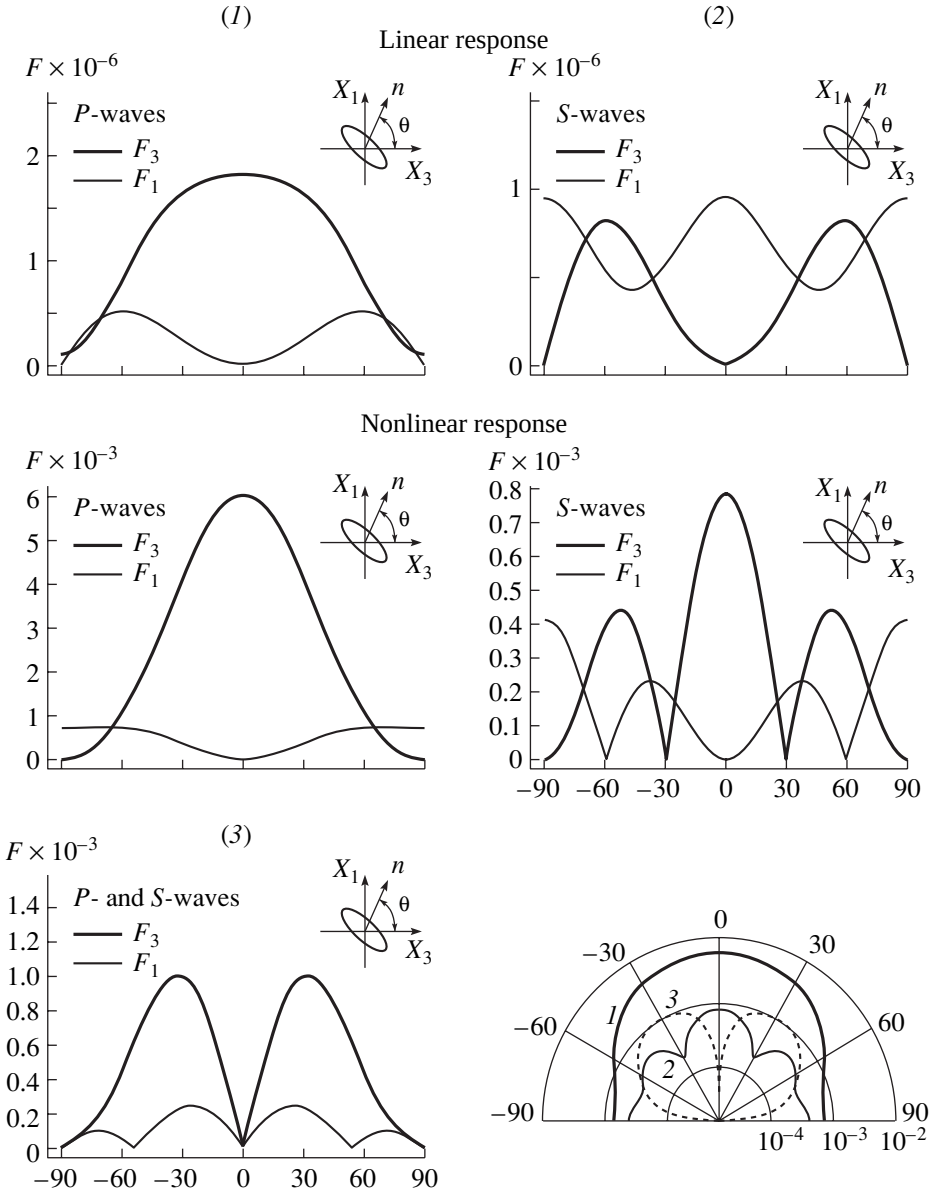


**Fig. 3.** Angular dependence of the reaction force. The angle $\vartheta$ corresponds to the inclination of the crack with respect to the $x_3$ axis, as it is shown in the right upper corner of each of the plots. The waves propagate along the $x_3$ axis. The ratio of the ellipsoid semiaxes is $\alpha = 10^{-3}$. The radius is $r_0 = 1$ mm. The polar diagram demonstrates the dependence of the induced force amplitude $\sqrt{\breve{F}_1^2 + \breve{F}_2^2 + \breve{F}_3^2}$ on the angle $\vartheta$. Indices *1–3* refer to the three cases considered.

The dependence of the reaction force on the angle of incidence of plane waves is given in Fig. 3. The projections $\breve{F}_2 \equiv \breve{f}_2 V_0$ for nonlinear scattering are negligibly small with respect to $\breve{F}_3 \equiv \breve{f}_3 V_0$, and, therefore, they are not presented in the plots. In the case of linear scattering, only two projections $F_1$ and $F_3$ are nonzero, which follows from the symmetry of the problem: the wave vector of a plane wave is orthogonal to the $x_2$ axis for any $\vartheta$.

Linear and nonlinear scattering is proportional to the amplitude of the external strain $e_{ij}^A$ to the power corresponding to Eqs. (20) and (21). As one can see from Fig. 3, the reaction force responsible for the nonlinear scattering may be greater than the linear reaction force even in the case of moderate strains. However, it is necessary to note that the calculation was performed for the "optimal" value of the filling stiffness ($k_1 = k_2$, Fig. 1, see also the discussion after Eq. (27)). We can also see that both the amplitude (polar diagram in Fig. 3) and the

direction of the vector of the reaction force (Fig. 3, curves *1–3*) depend on the angle $\vartheta$. This allows us to expect a good "sensitivity" of nonlinear scattering to the parameter $\vartheta$ in solving the problems of nonlinear resonance spectroscopy in the three-dimensional case.

As one can see from Fig. 3, the nonlinear reaction force has a magnitude of $10^{-3}$ N at the frequencies ~$10^{-3}$ Hz. In [42], the mechanical characteristics of a sample of Westerly granite were measured. A laboratory sample was a cylinder with a diameter of 50 mm, length of 100 mm, and mass of about 519 g. Sample strains were $10^{-8}$ under a force of $10^{-2}$ N in the frequency range of $10^4$ Hz. The dynamic range of measurements [42] was about 60 dB. Therefore, the value of the reaction force $\breve{F}_i \sim 10^{-3}$ (Fig. 3) must ensure a reliable detection of the nonlinear response of a laboratory sample with the same dimensions and mass as in [42].

## CRACK LOCALIZATION WITHIN A THIN ROD

Let us consider longitudinal vibrations of a thin rod with free ends as an example for the application of the expressions obtained above. The equations of motion for this vibrating system has the form (the $x_3$ axis is directed along the rod) [43]

$$\rho S\frac{\partial^2 u_3}{\partial t^2} = ES\frac{\partial^2 u}{\partial x_3^2} + F_3(x_3, t) \quad (28)$$

with the boundary conditions

$$ES\frac{\partial u_3}{\partial x_3}\bigg|_{x_3 = 0, L} = 0, \quad (29)$$

where $\rho$ is the density of the rod material, $S$ is the cross-section area, $E$ is the Young modulus of the rod material, $L$ is the rod length, and $u_3(x, t)$ are the displacements along the rod, which are assumed to be uniform in the cross-section. The force $F_3(x_3, t)$ in Eq. (28) corresponds to either an external force exciting rod vibrations or the reaction forces due to inhomogeneities.

Let us assume that rod vibrations are excited by a concentrated force with unit amplitude that is applied in the section $x_{3F}$ of the rod, $F_3(x_3, t) = \cos(\omega t)\delta(x_3 - x_{3F})$, where $\delta(x)$ is the Dirac delta function. Applying a standard technique of integral transformations (for example, see [44], Eq. (45)), we obtain an expression for the Green function of Eq. (28) with the boundary conditions given by Eq. (29):

$$\mathbf{G}(x_{3F}|x_3) = -\mathrm{Re}\left\{\frac{\cos(\omega t)\cos kx'_{3F}\cos kx'_3}{\rho c_l S\omega\sin kL}\right\}, \quad (30)$$

where $k = \omega/c_l(1 - i\eta/2)$; $c_l$ is the phase velocity of the longitudinal wave: $\rho c_l^2 = E$ and $\eta$ is the tangent of the loss angle [43, 44], which corresponds to linear attenuation in the rod material ($\eta \ll 1$). The quantities marked with $(\cdot)'$ are ($x_3 \ll x_{3F}$): $x'_{3F} = L - x_{3F}$, $x'_3 = x_3$, and ($x_3 \geq x_{3F}$): $x'_{3F} = x_{3F}$, $x'_3 = L - x_3$. The Green function of Eq. (30) does not contain a dependence on the transverse coordinates of the force $x_{1F}$ and $x_{2F}$ if the rod is thin with respect to the longitudinal wavelength: $\max(|x_1|), \max(|x_2|) \ll c_l/\omega$.

The strain tensor in the rod is $e_3^A = \partial u_3/\partial x_3$ and $e_{1,2}^A = -\nu e_3^A$ (the Poisson effect [11]). Shear strains are apparently absent, and $e_j^A = 0$ for $j = 4, 5, 6$. The nonzero values of $\partial e_j^A/\partial x_n$ in Eqs. (20) and (21) correspond to $j = 1, 2, 3$ and $n = 3$. Therefore, the two quantities

$$e_3^A = \mathrm{Re}\left\{\frac{k\cos(\omega t)\cos kx'_{3F}\sin kx'_3}{\rho c_l S\omega\sin kL}\right\}\frac{\partial x'_3}{\partial x_3}, \quad (31)$$

$$\frac{\partial e_3^A}{\partial x_3} = \mathrm{Re}\left\{\frac{k^2\cos(\omega t)\cos kx'_{3F}\cos kx'_3}{\rho c_l S\omega\sin kL}\right\}, \quad (32)$$

completely determine the reaction forces acting on the rod in the section of crack localization $x_{3c}$. Multiplying the Green function by the corresponding reaction forces $F_3 \equiv f_3 V_0$ and $\breve{F}_3 \equiv \breve{f}_3 V_0$, where $f_3 = \partial\sigma_{3j}^T/\partial x_j$ (Eq. (20)) and $\breve{f}_3 = \partial\breve{\sigma}_{3j}^T/\partial x_j$ (Eq. (21)), we determine the displacements caused by the scattering.

Let us consider the excitation of rod vibrations by two tonal force sources $F_3^{(1)}$ and $F_3^{(2)}$ applied to the rod end $x_{3F} = 0$. For definiteness, we assume the force frequencies satisfy the condition $\omega_2 > \omega_1$. We also assume that, in our imaginary experiment, a sensor detects the acceleration of the rod end $x_3 = L$ (Fig. 4, diagram at the top). The amplitude of rod vibrations at the combination frequency $\omega_3 = \omega_2 \pm \omega_1$ is determined by the values of the reaction forces (Eq. (21)) and the Green function (Eq. (30)) at the point of crack localization:

$$A(\omega_3) \sim k_1 k_2 \frac{(k_2\sin(z_1)\cos(z_2) + k_1\cos(z_1)\sin(z_2))\cos(z_3)\cos(k_3 L)}{\sin(k_1 L)\sin(k_2 L)\sin(k_3 L)}, \quad (33)$$

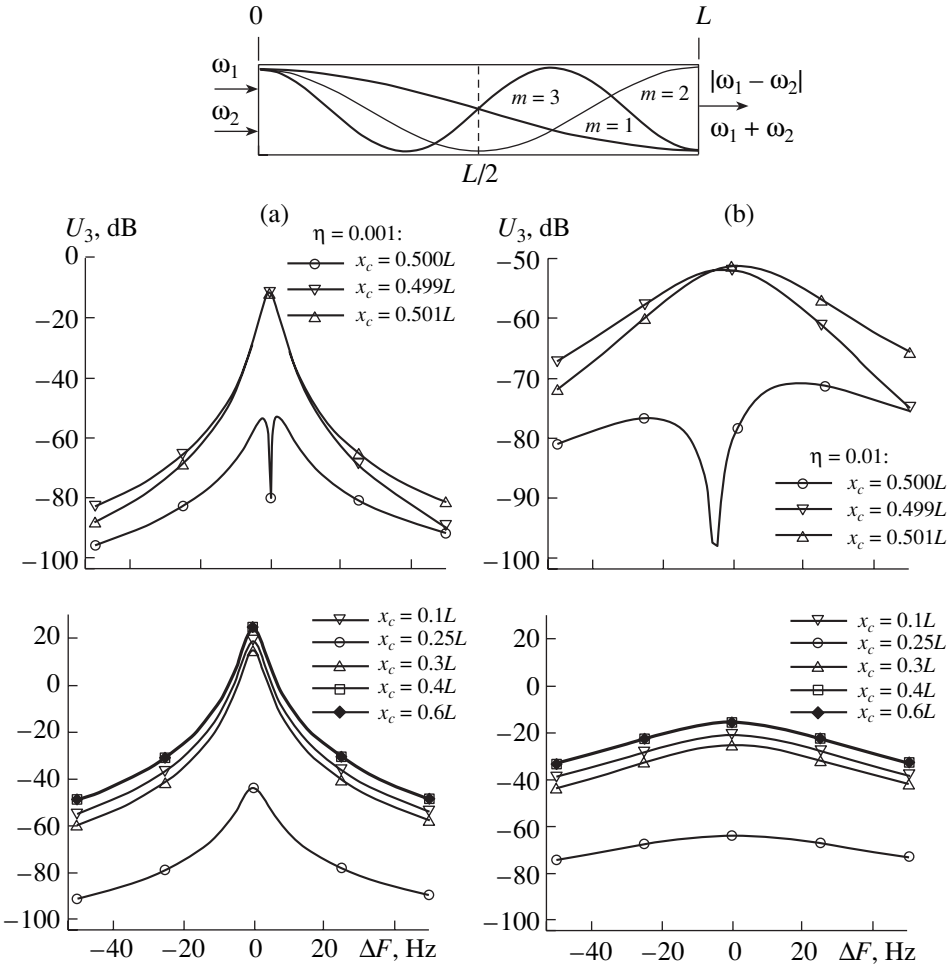


**Fig. 4.** Frequency response in the vicinity of the second mode resonance ($m = 2$). The calculation is performed for different coordinates $x_{3c}$ of the crack position along the rod. The plots correspond to the loss factor $\eta$ = (a) 0.001 and (b) 0.01. The ordinate gives the acceleration at the difference frequency relative to acceleration at the first mode resonance $\omega_1 = \pi c_l/L$. The amplitudes of external forces are $F_3^{(1,2)} = 1$ N. The rod length is $L = 1$ m. The material parameters are the same as those used in calculations of Fig. 3. The angle of crack inclination to the rod axis is $\vartheta = 0$.

where $z_j = k_j x_{3c}$ and $k_j = \omega_j/c_l$, $j = 1, 2, 3$.

The boundary conditions given by Eq. (29) are homogeneous. The distribution of displacements at the resonance frequencies $k_j L = \pi n$ ($\omega_n = \pi n c_l/L$) is symmetric with respect to the rod center for the modes with even numbers and antisymmetric for the modes with odd numbers. Simple transformations of the trigonometric functions involved in Eq. (33) demonstrate that, in the case of nonlinear interaction of resonance modes with the same parity, the response $A(\omega_3)$ is symmetric for a crack equidistant from the rod center $x_3 = L/2$. In the case of interaction of modes with different parity, $A(\omega_3)$ differs in its sign.

The next two figures demonstrate examples of calculation for the rod response at the difference frequency $\omega_3 = \omega_2 - \omega_1$. In numerical experiments, the frequency $\omega_1$ was fixed and coincided with the resonance frequency of the first mode $\omega_1 = \pi c_l/L$. The frequency $\omega_2$ was varied in the vicinity of the resonance frequency of the third (Fig. 4) and fourth (Fig. 5) modes: $\omega_2 = \pi n c_l/L + \Delta\omega$, where $n = 3, 4$ and $\Delta\omega \ll \pi n c_l/L$ is the value of frequency mismatch.

In the case of nonlinear interaction of the first and third modes, the vibration corresponding to the resonance of the second mode is excited. One can see from Eq. (33) (the term in parentheses in the numerator) that the amplitude of the reaction force tends to zero in the case of crack localization exactly at the rod center. In this case, one can see in Fig. 4 a deep gap at the resonance frequency of the second mode ($\Delta\omega = 0$). The gap is the narrower and deeper the higher the $Q$ factor of rod vibrations is. The values of the Landau's moduli **A**, **B**, and **C** used in the calculation are large relative to $\lambda$ and $\mu$ (table). Therefore, the maximum displacements of the crack position from the rod center lead to a signifi-

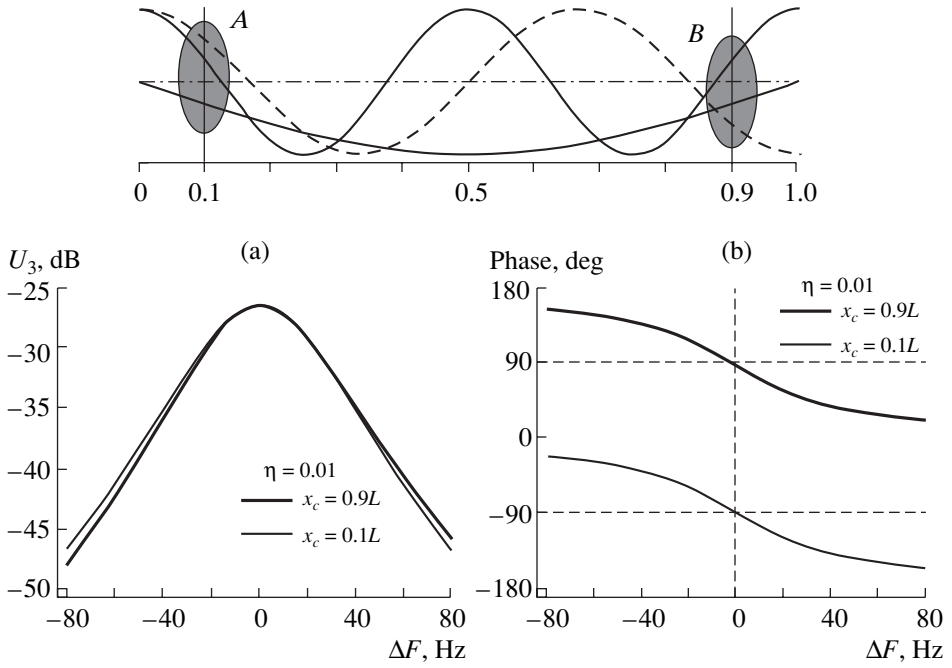


**Fig. 5.** The possibility to determine the crack position relative to the rod center at homogeneous boundary conditions. The dependence of the values of $\sin z_1$, $\cos z_2$, and $\cos z_3$ involved in Eq. (33) on the crack position is shown at the top. The quantity $A(\omega_3)$ has different signs in the hatched regions *A* and *B*. This provides an opportunity to use the phase data for refining the defect position.

cant increase in the response at the resonance frequency.

The response $A(\omega_3)$ is also minimal in the case of the crack position at the displacement node of the second mode, $x_{3c} = L/4$, $3L/4$, when the value of the Green function (Eq. (30)) is minimal. A reduction of the nonlinear response in this case and the symmetry of the amplitude response at an equal distance from the crack to the rod center are clearly visible in Fig. 4.

As one can see from Eq. (33), the amplitude of the nonlinear response $A(\omega_3)$ is proportional to the product of three resonance factors (the denominator of Eq. (33)). A strong dependence of $A(\omega_3)$ on the vibration decrement is illustrated by the plots given at the left and right in Fig. 4. Note that the values of acceleration at the difference frequency that are given in Fig. 4 are normalized to the resonance response of the first mode. Therefore, in the case of one-order-of-magnitude growth of the vibration decrement, the amplitude of the nonlinear response decreases by two orders of magnitude.

As we have already noted above, a nonlinear interaction of modes with different parity provides an opportunity to eliminate the ambiguity of the crack position with respect to the rod center. This is shown in Fig. 5, which corresponds to the interaction of the first and fourth modes. Solid thick lines in Fig. 5 demonstrate the distribution of the quantities $e_{33}^A(x_3)$ and $\partial e_{33}^A(x_3)/\partial x_3$ involved in Eq. (21). Two versions of the crack location symmetric with respect to the rod center, $x_{3c} = 0.1L$ and $0.9L$, are marked with vertical lines. The dot-and-dash horizontal lines correspond to zero values. The broken line demonstrates the distribution of displacements in the mode excited as the result of nonlinear interaction. This term is present in Eq. (30) and determines the mode amplitude. The quantity $A(\omega_3)$ has different signs in the hatched regions.

Hence, the frequency dependence of the vibration phase differs for $x_{3c} = 0.1L$ and $0.9L$. The phase of vibrations at the difference frequency in this case is determined with respect to the phase of vibrations in the first mode, whose frequency is constant and coincides with the resonance one.

The amplitude dependence of the response at the difference frequency for two versions of the crack position is given in Fig. 5a. There are no significant differences in the amplitude dependences. The frequency dependence of the phase at the difference frequency is given in Fig. 5b. The phase response differs for the two versions, which can be used to eliminate the ambiguity in the determination of the crack position.

Thus, analyzing the nonlinear interaction of many mode pairs, it is possible to obtain exhaustive information on the position of a crack. The above simple example of longitudinal vibrations of a thin rod allowed us to demonstrate the general procedure of solving the problem of nonlinear acoustic spectroscopy.

## CONCLUSIONS

In this study, we have considered approaches to solving the problem of nonlinear acoustic spectroscopy of local defects. A theoretical model is proposed, which provides an opportunity to describe a broad class of problems on the nonlinear interaction of elastic waves in solids at narrow cracks with the minimal amount of *a priori* information. The problem of determining the position, orientation, and material parameters of a crack is reduced to determining the application point, magnitude, and direction of the vector of the induced force or the reaction force of the crack to an elastic matrix, which can be considered as a linear elastic solid.

Both the magnitude and the direction of the reaction force vector exhibit a strong dependence on the type of interacting waves and their wave vectors with respect to the normal to the crack. This allows us to expect a high sensitivity of the method of nonlinear acoustic spectroscopy in measuring the corresponding parameters. The value of the reaction force for the Westerly granite is estimated using the published experimental data. It is demonstrated by a numerical example that, at small strains on the order of $10^{-8}$, which are typical of acoustic measurements, and at frequencies of about $10^3$ Hz, the amplitude of the nonlinear reaction force at optimal conditions is such that it is possible to reliably detect the nonlinear vibration response of a laboratory sample.

The problem of nonlinear resonance interaction of longitudinal waves propagating in a thin rod is considered as an example of crack localization. This example, permitting an analytical solution, illustrates the method for reconstructing the crack position. In addition, it is demonstrated that the phase data allow one to eliminate the ambiguity arising in the case of symmetric boundary conditions.

## ACKNOWLEDGMENTS

This work was supported in part by the Russian Foundation for Basic Research (project no. 03-05-64933), the Project for Supporting the Scientific Schools of Russia (grant no. 1641.2003.2), and State Contract no. 40.020.1.1.1171.

## REFERENCES

1. R. A. Guyer and P. A. Johnson, Phys. Today **52** (4), 30 (1999).
2. L. A. Ostrovskiĭ and P. A. Johnson, Riv. Nuovo Cimento **24** (7), 1 (2001).
3. W. H. Munk, P. Worcester, and C. Wunsch, *Ocean Acoustic Tomography* (Cambridge Univ. Press, Cambridge, 1995).
4. E. V. Malyarenko and M. K. Hinders, J. Acoust. Soc. Am. **108**, 1631 (2000).
5. J. G. Berryman, P. A. Berge, and B. P. Bonner, J. Acoust. Soc. Am. **107**, 3018 (2000).
6. J. D. Achenbach, L. Adler, D. K. Lewis, and H. McMaken, J. Acoust. Soc. Am. **66**, 1848 (1979).
7. V. V. Kazakov, A. M. Sutin, and P. A. Johnson, Appl. Phys. Lett. **81**, 646 (2002).
8. H. Hönl, A. Maue, and K. Westpfahl, *Theorie der Beugung* (Springer, Berlin, 1961; Mir, Moscow, 1964).
9. P. C. Waterman, J. Acoust. Soc. Am. **45**, 1417 (1969).
10. Ph. Morse and H. Feschbach, *Methods of Theoretical Physics* (McGraw-Hill, New York, 1953; Inostrannaya Literatura, Moscow, 1960), Vol. 2.
11. L. D. Landau and E. M. Lifshitz, *Theory of Elasticity* (Nauka, Moscow, 1986; Pergamon, Oxford, 1986).
12. A. Migliori and J. L. Sarrao, *Resonant Ultrasound Spectroscopy: Applications to Physics, Materials Measurements, and Nondestructive Evaluation* (Wiley, Chichester, 1997).
13. L. A. Ostrovsky, A. V. Lebedev, A. L. Matveyev, *et al.*, J. Acoust. Soc. Am. **110**, 1770 (2001).
14. J. Fineberg and M. Marder, Phys. Rep. **313**, 1 (1999).
15. B. Lawn, *Fracture of Brittle Solids* (Cambridge Univ. Press, Cambridge, 1993).
16. G. I. Barenblatt, Prikl. Mat. Mekh. **23** (3), 434 (1959).
17. A. K. Mal and L. Knopoff, J. Inst. Math. Appl. **3**, 376 (1967).
18. E. Skudrzyk, *The Foundations of Acoustics: Basic Mathematics and Basic Acoustics* (Springer, New York, 1971; Mir, Moscow, 1976).
19. G. Mavko, T. Mukeji, and J. Dvorkin, *The Rock Physics Handbook. Tools For Seismic Analysis in Porous Media* (Cambridge Univ. Press, Cambridge, 1998).
20. J. D. Eshelby, Proc. R. Soc. London **241**, 376 (1957).
21. R. L. Kranz, Tectonophysics **100**, 449 (1983).
22. K. Hadley, J. Geophys. Res. **81**, 3484 (1976).
23. W. L. Power, T. E. Tullis, and J. D. Weeks, J. Geophys. Res. **93**, 15 268 (1988).
24. K. A. Naugol'nykh and L. A. Ostrovskiĭ, *Nonlinear Wave Processes in Acoustics* (Nauka, Moscow, 1990; Cambridge Univ. Press, Cambridge, 1998).
25. J. W. Macki, P. Nistri, and P. Zecca, Soc. Ind. Appl. Math. Rev. **35**, 94 (1993).
26. G. A. Korn and T. M. Korn, *Mathematical Handbook for Scientists and Engineers* (McGraw-Hill, New York, 1968; Nauka, Moscow, 1984).
27. D. L. Anderson, B. Minster, and D. Cole, J. Geophys. Res. **79** (26), 4011 (1974).
28. O. Nishizawa, J. Phys. Earth **30**, 331 (1982).
29. K. Johnson, *Contact Mechnaics* (Cambridge Univ. Press, Cambridge, 1985; Mir, Moscow, 1989).
30. V. E. Nazarov and A. M. Sutin, J. Acoust. Soc. Am. **102**, 3349 (1997).
31. A. V. Lebedev and V. E. Nazarov, Fiz. Zemli **1**, 50 (2000).
32. K. Brugger, Phys. Rev. **133**, 1611 (1964).
33. *Handbook of Physical Quantities*, Ed. by I. K. Kikoin (Atomizdat, Moscow, 1976) [in Russian].

34. K. W. Winkler, J. Acoust. Soc. Am. **100**, 1392 (1996).

35. F. Birch, Phys. Rev. **71**, 809 (1947).

36. C. H. Scholz and T. A. Koczynski, J. Geophys. Res. **84**, 5535 (1979).

37. A. É. Ekimov, A. V. Lebedev, L. A. Ostrovskiĭ, and A. M. Sutin, Akust. Zh. **42**, 61 (1996) [Acoust. Phys. **42**, 51 (1996)].

38. E. D. Smith and J. A. TenCate, Geophys. Res. Lett. **27**, 1985 (2000).

39. K. Van Den Abeele, P. A. Johnson, and A. M. Sutin, Res. Nondestruct. Eval. **12**, 17 (2000).

40. K. Van Den Abeele, A. M. Sutin, J. Carmeliet, and P. A. Johnson, NDT&E Int. **34**, 239 (2001).

41. D. Donskoy, A. Sutin, and A. Ekimov, NDT&E Int. **34**, 231 (2001).

42. A. V. Lebedev, V. V. Bredikhin, I. A. Soustova, *et al.*, J. Geophys. Res. **108** (B10), EPM11(1–12) (2003).

43. E. Skudrzyk, *Simple and Complex Vibratory Systems* (Pennsylvania State Univ. Press, Philadelphia, 1968).

44. E. Skudrzyk, J. Acoust. Soc. Am. **67**, 1105 (1980).

*Translated by M. Lyamshev*